RADIO ASTRONOMY

Journal of the Society of Amateur Radio Astronomers
September - October 2024

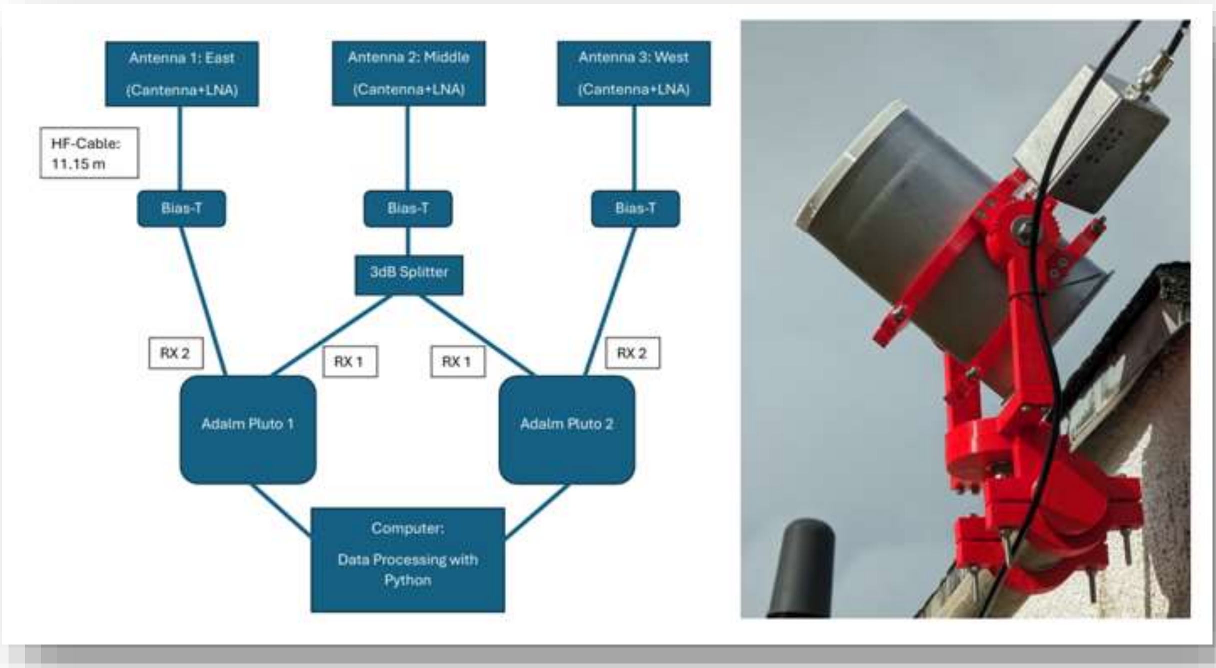

Three Cantenna Interferometer

Dr. Richard A. Russel
SARA President and Editor

Bogdan Vacaliuc
Contributing Editor

Radio Astronomy is published bimonthly as the official journal of the Society of Amateur Radio Astronomers. Duplication of uncopyrighted material for educational purposes is permitted but credit shall be given to SARA and to the specific author. Copyrighted materials may not be copied without written permission from the copyright owner.

Radio Astronomy is available for download only by SARA members from the SARA web site and may not be posted anywhere else.

It is the mission of the Society of Amateur Radio Astronomers (SARA) to: Facilitate the flow of information pertinent to the field of Radio Astronomy among our members; Promote members to mentor newcomers to our hobby and share the excitement of radio astronomy with other interested persons and organizations; Promote individual and multi station observing programs; Encourage programs that enhance the technical abilities of our members to monitor cosmic radio signals, as well as to share and analyze such signals; Encourage educational programs within SARA and educational outreach initiatives. Founded in 1981, the Society of Amateur Radio Astronomers, Inc. is a membership supported, non-profit [501(c) (3)], educational and scientific corporation.

Cover Photo:
Vanessa Annika Schulz

Contents

President's Page

New SARA Features:

1) New video editor provides translations in French, German, and Spanish. We are proceeding to translate some of the popular You Tube videos.

2) The BYTE section by the SARA VP, Marcus Fischer provides updates on software techniques and tools.

Membership Renewals

- We are continuing to process 2025 membership renewals.
- Our SARA MailChimp database has been updated to account for all memberships. The database contains 678 members. We have 352 members who have not renewed for 2025. The plan is to remove members from the mailing list who have not renewed by December 31.

2025 Western Conference

- The Western Conference will be held at the Very Large Array at Socorro, N.M. in March 2025. More info as we get it.
- Call for papers and presentations
- Coordinators: Ken Redcap (pacder@hotmail.com) & Wayne McCain (wayne.mccain@athens.edu)
-

2025 Eastern Conference

- The Eastern Conference will be held at the Green Bank Observatory, June 7 (Sat) – June 11 (Wed) 2025
- We will combine the conference with the Radio Jove Team.
- Coordinator: SARA VP, Marcus Fisher (marcus.s.fisher@gmail.com)

Rich

SARA President

Editor's Notes

We are always looking for basic radio astronomy articles, radio astronomy tutorials, theoretical articles, application and construction articles, news pertinent to radio astronomy, profiles and interviews with amateur and professional radio astronomers, book reviews, puzzles (including word challenges, riddles, and crossword puzzles), anecdotes, expository on "bad astronomy," articles on radio astronomy observations, suggestions for reprint of articles from past journals and other publications, and announcements of radio astronomy star parties, meetings, and outreach activities.

Subscribe to the SARA YouTube Channel

SARA has a YouTube channel at: https://www.youtube.com/@radio-astronomy

Don't forget to LIKE the videos! It helps with the YouTube distribution algorithm.

We are also looking to add content to the site. Anyone who wants to help produce a series of 5 - minute videos relating to radio astronomy technology or observations please contact me. (drrichrussel@netscape.net)

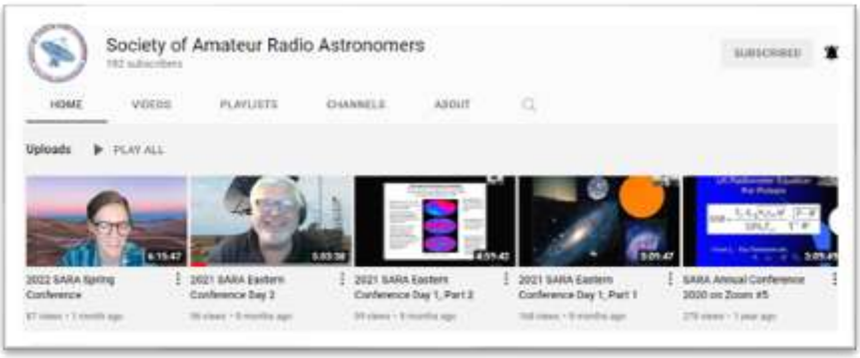

Observation Reports

We are now accepting 1-2 page observation reports. These reports should include the astronomical object's RA/DEC plus UTC of the observation. Also include the telescope configuration, process used to observe the object and results. Picture of the setup and plots of the observation are a plus to the report.

If you would like to write an article for Radio Astronomy, please follow **the newly updated Author's Guide** on the SARA web site:
http://www.radio-astronomy.org/publicat/RA-JSARA_Author's_Guide.pdf.

Let us know if you have questions; we are glad to assist authors with their articles and papers and will not hesitate to work with you. You may contact your editors any time via email here: edit@radio-astronomy.org.

The editor(s) will acknowledge that they have received your submission within two days. If they do not reply, assume they did not receive it and please try again.

Please consider submitting your radio astronomy observations for publication: any object, any wavelength. Strip charts, spectrograms, magnetograms, meteor scatter records, space radar records, photographs; examples of radio frequency interference (RFI) are also welcome.
Guidelines for submitting observations may be found here: http://www.radio-astronomy.org/publicat/RA-JSARA_Observation_Submission_Guide.pdf

NEW The BYTE

A new section is being added to the bimonthly SARA journal focused on system software applicable for amateur radio astronomy (RA).

Society of Amateur Radio Astronomers (SARA) **2025 SARA Eastern Conference**	

Block off your calendars and start thinking about your travels for next summer! We have teamed up with the Radio Jove group and are holding a combined conference next year!

- 2025 SARA Eastern Conference and Radio Jove
- June 7 (Sat) – June 11 (Wed) 2025
- Green Bank Observatory (GBO) West Virginia (WV)

Conference committee members include:

- Rich Russel
- Tom Jacobs
- Ciprian "Chip" Sufitchi
- Kammie Russel
- Don Latham
- Dennis Farr
- Jay Wilson
- Tom Hagen
- Dave Lacko
- Gary Memory
- Chuck Higgins

Planning is underway and more information will be coming as it develops. Any comments and/or suggestions please reach out to the committee chair Marcus Fisher (vicepresident@radio-astronomy.org)

SARA Student & Teacher Grant Program

All, SARA has a grant program that is, sad to say, very underutilized. We will provide kits or money to students and teachers including college students to help them with a radio telescope project. SARA can supply any of the following kits:

[1] SuperSID
[2] Scope in a Box
[3] IBT (Itty Bitty Telescope)
[4] Radio Jove kit
[5] Inspire
[6] Sky Scan

We can also provide up to five hundred dollars ($500.00 USD) for an approved radio telescope project.

We have on occasion provided more money based on the merits of the project and the SARA Grant Committee approval.

More information on the grant program can be found at the URL below.
SARA Student and Teacher Project Grants | Society of Amateur Radio Astronomers (radio-astronomy.org)

All that is required is the SARA grant request form be filled out and sent in. If it needs more work for approval, we will work with the students to help ensure their success.

Please pass the word that SARA will fund any legitimate radio telescope project anywhere in the world.

If you have a question, contact me at crowleytj@hotmail.com .
Tom Crowley - SARA Grant Program Administrator

Drake's Lounge Australia

This new zoom forum is geared to the Melbourne, Australia time zone (UTC+10) in order to improve coordination with our Australia, New Zealand, and Japanese members. The meetings are scheduled for the 4th Friday of every month, 9 AM Melbourne time. A zoom announcement will be sent out to all SARA members before the meeting.

Radio Telescope Observation Party (RTOP)

RTOP is designed to demonstrate how to take observations using various radio telescopes. It will also cover how to record and analyze data.
RTOP is every month on the 1st Sunday at 2 pm Eastern time (1800 UTC). ZOOM email notifications will be sent to all members.

Drake's Lounge

Join the SARA community as we discuss the latest astronomy and radio astronomy news. The lounge also provides a forum to share and get advice on your radio astronomy projects from very experienced amateur radio astronomers.

Drake's Lounge is every month on the 3rd Sunday at 2 pm Eastern time (1800 UTC). ZOOM email notifications will be sent to all members.

News: (September - October 2024)

Comet Tsuchinshan-ATLAS

(Image credit: B. Vacaliuc, Hillsborough NH, USA) – 10/12 23:24 UTC

(Image credit: B. Vacaliuc, Oak Ridge TN, USA) – 10/15 00:02 UTC

(Image credit: B. Vacaliuc, Kingston TN, USA) – 10/20 00:10 UTC

Bob King ~ Get Ready for Comet Tsuchinshan-ATLAS — The Best Is Yet to Come!
https://skyandtelescope.org/astronomy-news/get-ready-for-comet-tsuchinshan-atlas-the-best-is-yet-to-come/
Comet C/2023 A3 (Tsuchinshan-ATLAS) LightCurve/Observations/Ephemeris Data
https://cobs.si/comet/2410/

The Virtual Telescope Project ~ Comet C/2023 A3 Tsuchinshan-ATLAS at perihelion: online observation
https://www.youtube.com/watch?v=cVo_wfqwmS8

Joe Rao ~ The dazzling Comet Tsuchinshan-ATLAS is emerging in the night sky: How to see it
https://www.space.com/comet-tsuchinshan-atlas-bright-night-sky

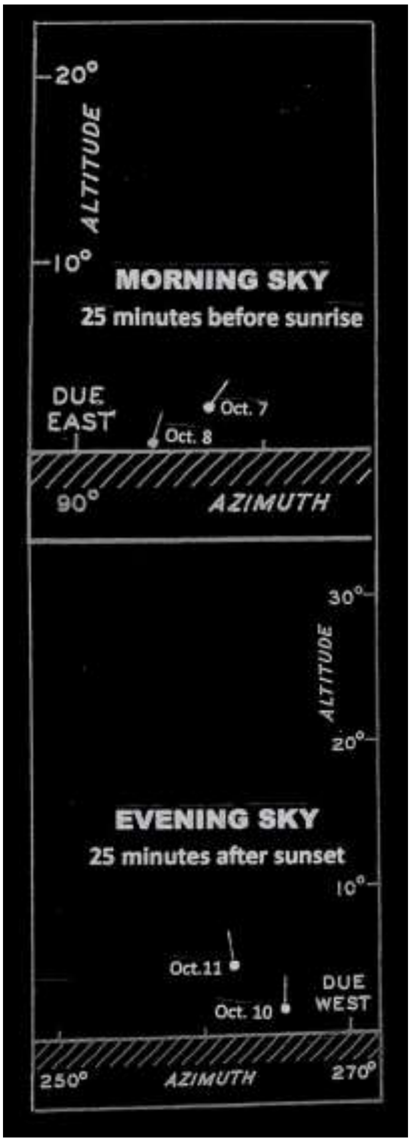

(Image credit: Joe Rao)

(Image credit: Mike Olason)

Meredith Garofalo ~ Comet Tsuchinshan-ATLAS photobombs SOHO spacecraft during powerful solar flare (video)
https://www.space.com/comet-tsuchinshan-atlas-soho-solar-flare-video

(Image credit: ESA/NASA/SOHO)

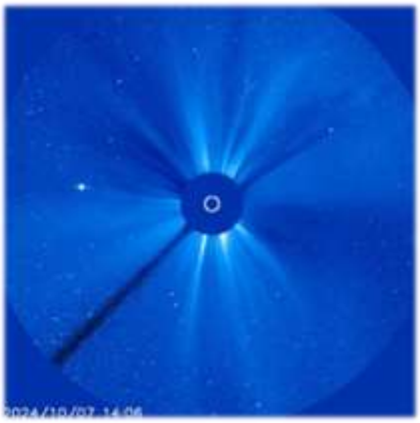

https://soho.nascom.nasa.gov/data/Theater/ (*select S3, start date 2024-10-07; the comet first begins to show in the frame on 2024-10-07 14:06 on the right edge*)

(Image credit: ESA/NASA/SOHO)

Harry Baker ~ Rare illusion gives 'once-in-a-lifetime' comet a seemingly impossible 2nd tail after closest approach to Earth for 80,000 years
https://www.livescience.com/space/comets/rare-illusion-gives-once-in-a-lifetime-comet-a-seemingly-impossible-2nd-tail-after-closest-approach-to-earth-for-80-000-years

(Image credit: Michael Jäger)

Victoria Corless ~ Astronaut captures stunning timelapse of Comet Tsuchinshan-ATLAS from ISS (video)
https://www.space.com/comet-tsuchinshan-atlas-matthew-dominick-iss-photo

Credit: Matthew Dominick
https://x.com/dominickmatthew/status/1836916069870751825

Bob King ~ Comet Tsuchinshan-ATLAS Climbs, Brightens and Delights!
https://skyandtelescope.org/astronomy-news/comet-tsuchinshan-atlas-climbs-brightens-and-delights/

Embedded near the end of the article is this impressive time-lapse video:

(Amateur astronomer Suresh Sreenivasan of Hopkins, Minnesota, created this video of the comet as it sets through cloud bands on October 13th. Video details: Nikon D7200, 50-mm f/1.8, ISO 320, 5-second exposures. Video is 101 frames at 10 fps.)

Miles Hatfield, Rachel Lense ~ NASA Discovers a Long-Sought Global Electric Field on Earth

https://science.nasa.gov/science-research/heliophysics/nasa-discovers-long-sought-global-electric-field-on-earth/
http://dx.doi.org/10.1038/s41586-024-07480-3 (sharing token provided by NASA)
(Credit: NASA's Goddard Space Flight Center/Lacey Young)

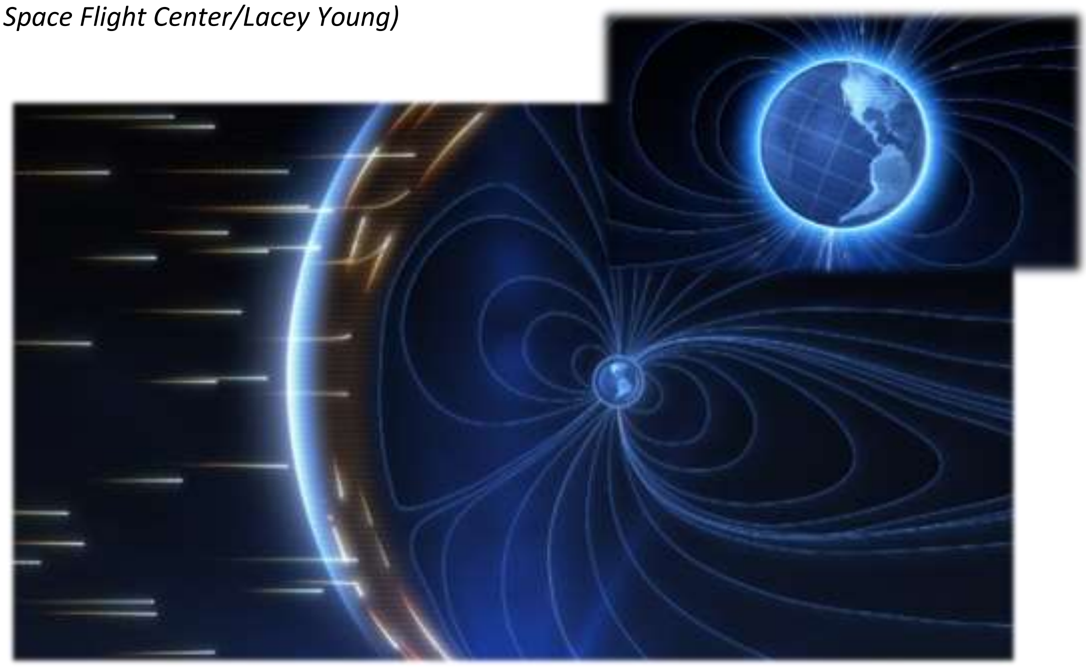

video: https://www.youtube.com/watch?v=UCM1MaYC5lM
Downloadable files: https://svs.gsfc.nasa.gov/14628

Ben Turner ~ One of the universe's biggest paradoxes could be even weirder than we thought, James Webb telescope study reveals
https://www.livescience.com/space/cosmology/one-of-the-universe-s-biggest-paradoxes-could-be-even-weirder-than-we-thought-james-webb-telescope-study-reveals

https://arxiv.org/abs/2408.06153 Wendy L. Freedman, et. al., "Status Report on the Chicago-Carnegie Hubble Program (CCHP): Three Independent Astrophysical Determinations of the Hubble Constant Using the James Webb Space Telescope", Cosmology and Nongalactic Astrophysics (astro-ph.CO)

(Image Credit: NASA/CXC/JPL-Caltech/STScI/NSF/NRAO/VLA)

Ethan Siegel ~ 10 insights about the expanding Universe from a Nobel Laureate
https://bigthink.com/starts-with-a-bang/10-insights-expanding-universe-nobel-laureate/

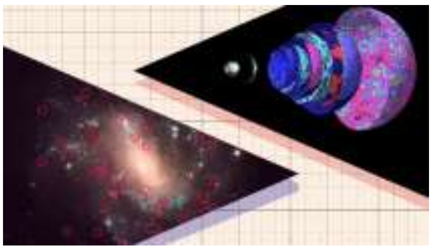

https://arxiv.org/abs/2408.11770 Adam G. Riess, et. al. "JWST Validates HST Distance Measurements: Selection of Supernova Subsample Explains Differences in JWST Estimates of Local H0", Cosmology and Nongalactic Astrophysics (astro-ph.CO))

(Image Credit: Annelisa Leinbach / NASA, Adobe Stock)

Juan Siliezar ~ New mass spectrometry technology could transform tiny sample analysis
https://phys.org/news/2024-09-mass-spectrometry-technology-tiny-sample.html

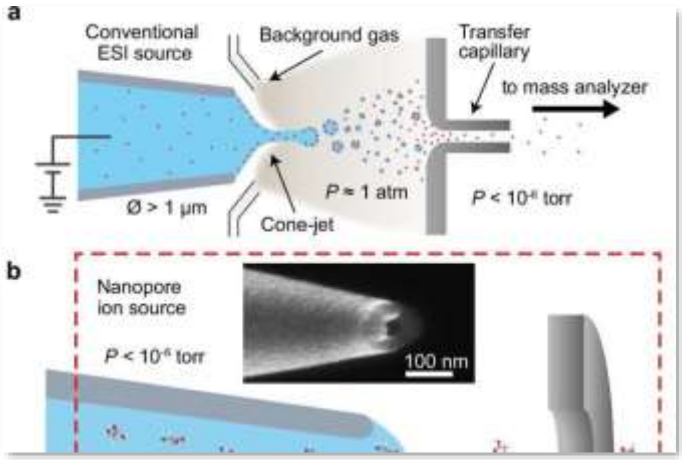

(Credit: Nature Communications (2024). DOI: 10.1038/s41467-024-51455-x)

ESA/Hubble Information Centre ~ Hubble and Chandra find supermassive black hole duo
https://dx.doi.org/10.3847/1538-4357/ad6b91

(Credit: NASA, ESA, Anna Trindade Falcão (CfA))

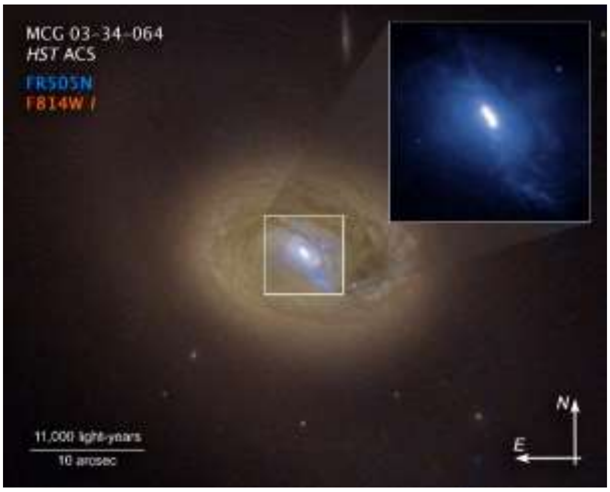

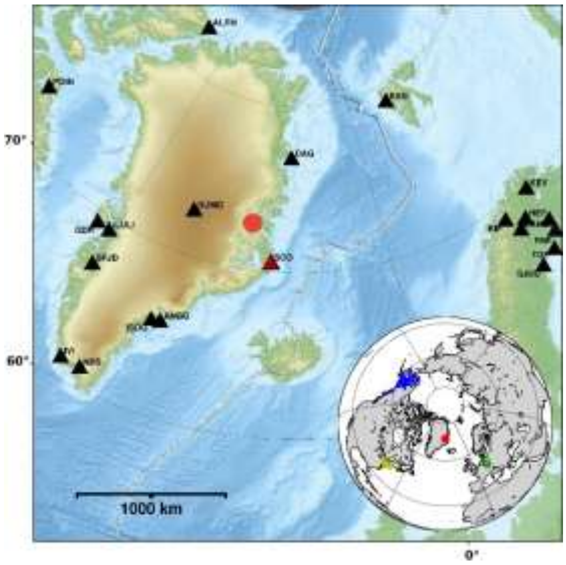

Seismological Society of America ~ 650-Foot Run-Up: Megatsunami in Greenland Sends Seismic Waves Worldwide
https://scitechdaily.com/650-foot-high-megatsunami-in-greenland-sends-seismic-waves-worldwide/

https://doi.org/10.1785/0320240013
(Credit: Angela Carillo Ponce et al.)

Astronomy & Astrophysics ~ Second-gen Starlink satellites leak 30 times more radio interference, threatening astronomical observations
https://phys.org/news/2024-09-gen-starlink-satellites-leak-radio.html

https://www.astron.nl/starlink-satellites/
https://doi.org/10.1051/0004-6361/202451856

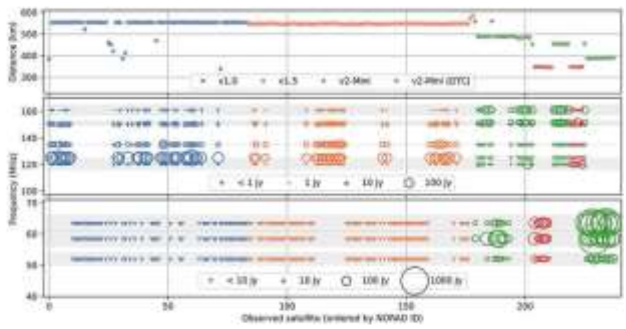

(Credit: Astronomy & Astrophysics (2024). DOI: 10.1051/0004-6361/202451856)

Simons Foundation ~ New Habitable Zone Planet Found in Unusual Star System
https://scitechdaily.com/new-habitable-zone-planet-found-in-unusual-star-system/

https://doi.org/10.3847/1538-3881/ad1d5c
https://www.zooniverse.org/projects/nora-dot-eisner/planet-hunters-tess/about/research

Matt Kelly ~ If it flares, 'blaze star' T Corona Borealis will be clearly visible
https://phys.org/news/2024-09-flares-blaze-star-corona-borealis.html

Recurrent Nova T CrB: Coming Soon to a Sky Near You
video: https://youtu.be/1Zfg67Q-szU

From:
U. Munari, S. Dallaporta, G. Cherini, "*The 2015 super-active state of recurrent nova T CrB and the long term evolution after the 1946 outburst*", New Astronomy vol 47, pg 7 (2016) https://arxiv.org/abs/1602.07470

The paper ends with the words:
"Is therefore everything in place for a new nova outburst in 2026, again ~80 years past the last eruption?"

And so, we wait and observe...

AAVSO Finder Charts for T CrB
https://www.aavso.org/t-crb-finder-charts

Tomisin Olujinmi ~ DeepRad is a cheap, modular SDR receiver based on the RTL-SDR (Crowdfunding)
https://www.cnx-software.com/2024/09/12/deeprad-cheap-modular-sdr-receiver-based-rtl-sdr/
https://www.crowdsupply.com/deepsea-developments/deeprad

Matt Williams ~ The Ultraviolet Habitable Zone Sets a Time Limit on the Formation of Life
https://www.universetoday.com/167714/the-ultraviolet-habitable-zone-sets-a-time-limit-on-the-formation-of-life-1/

https://doi.org/10.1093/mnrasl/slae064

(Credit: NASA/Kepler Mission/Dana Berry)

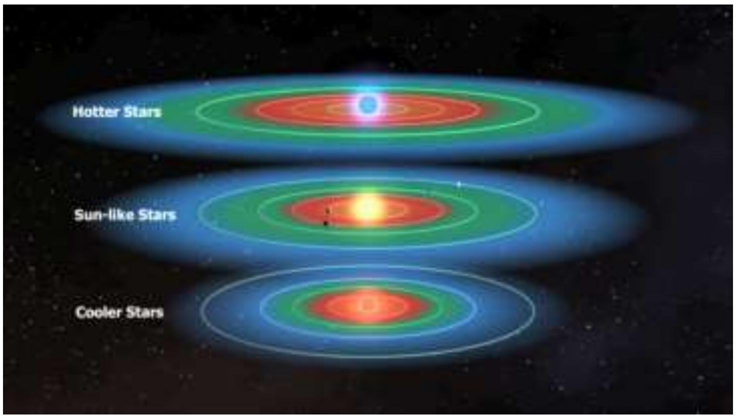

Shubhangi Dua ~ Tough plastics broken down sustainably with common chemical, sunlight, air
https://interestingengineering.com/science/tough-plastics-sustainably-broken-down
https://doi.org/10.1002/marc.202400358

(Credit: UNSW / Maxime Michelas and Cyrille Boyer)

Bob Yirka ~ Odds of asteroid 99942 Apophis striking Earth slightly higher than thought
https://phys.org/news/2024-09-odds-asteroid-apophis-earth-slightly.html
https://dx.doi.org/10.3847/PSJ/ad644d
(Credit: The Planetary Science Journal (2024). DOI: 10.3847/PSJ/ad644d)

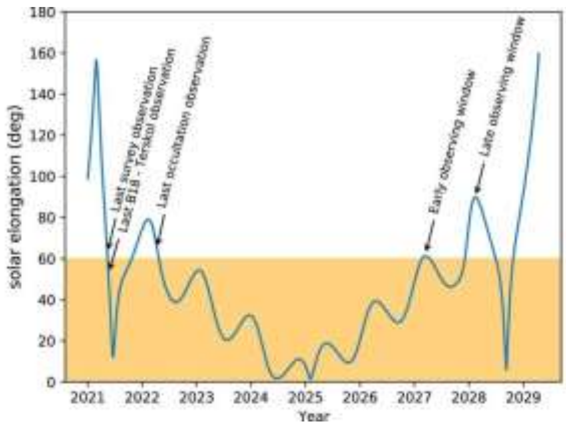

Robert Lea ~ Black hole blasts largest jet ever seen at 23 million light-years long
https://www.space.com/black-hole-jets-longest-23-million-light-years
https://www.nature.com/articles/s41586-024-07879-y
(Credit: E. Wernquist / D. Nelson (IllustrisTNG Collaboration) / M. Oei)
Ben Turner ~ Earth's new 'mini moon' will orbit our planet for the next 2 months
https://www.livescience.com/space/asteroids/earths-new-mini-moon-will-orbit-our-planet-for-the-next-2-months

https://dx.doi.org/10.3847/2515-5172/ad781f

(Credit: Ellenoor Shameli/BBC Studios)
video: https://www.bbc.com/reel/video/p0jsl446/the-science-behind-the-mini-moon-entering-earth-s-orbit

Charles Q. Choi ~ A 'primordial' black hole may zoom through our solar system every decade
https://www.space.com/black-holes-solar-system

Jennifer Chu ~ Close Encounters with Dark Matter: MIT Study Finds Detection Possible Through Mars' Wobble
https://scitechdaily.com/close-encounters-with-dark-matter-mit-study-finds-detection-possible-through-mars-wobble/

(Credit: Image by Benjamin Lehmann, using SpaceEngine @ Cosmographic Software LLC)

Robert Lea ~ Black hole 'bullets' fired at Mars could reveal more about dark matter
https://www.space.com/mars-black-hole-bullets-dark-matter

(Image credit: Robert Lea (created with Canva)/NASA)

https://doi.org/10.1103/PhysRevD.110.063533 (Tung X. Tran, Sarah R. Geller, Benjamin V. Lehmann, and David I. Kaiser, "Close encounters of the primordial kind: A new observable for primordial black holes as dark matter", Phys. Rev. D 110, 063533, 17 September 2024

Stefanie Waldek ~ ESA's JUICE spacecraft confirmed Earth is habitable. Here's why
https://www.space.com/esa-juice-confirms-earth-is-habitable
https://www.esa.int/Science_Exploration/Space_Science/Juice/Juice_confirms_that_Earth_is_habitable

(Credit: ESA/Juice/JMC)

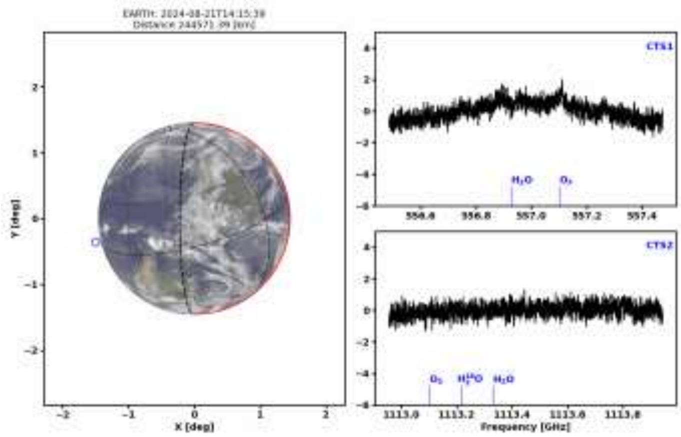

Mark Kaufman ~ As spacecraft zooms to Venus, it peers back at humble Earth and the moon
https://mashable.com/article/earth-moon-spacecraft-juice-images

(Credit: ESA)

Steven Vaughan-Nichols ~ 20 years later, real-time Linux makes it to the kernel - really
https://www.zdnet.com/article/20-years-later-real-time-linux-makes-it-to-the-kernel-really/

(Credit: Steven Vaughan-Nichols)

Michelle Starr ~ Listen to The Eerie 'Sound' From A Black Hole, Captured by NASA
https://www.sciencealert.com/listen-to-the-eerie-sound-from-a-black-hole-captured-by-nasa
(Credit: NASA/CXC/SAO/E.Bulbul, et. al.) video: https://youtu.be/ioR5np1fmEc
https://chandra.harvard.edu/photo/2014/perseus/

Eric Ralls ~ Deep space radio signal reaches Earth after 8 billion years
https://www.earth.com/news/deep-space-radio-signal-reaches-earth-after-8-billion-years-frb-20220610a/

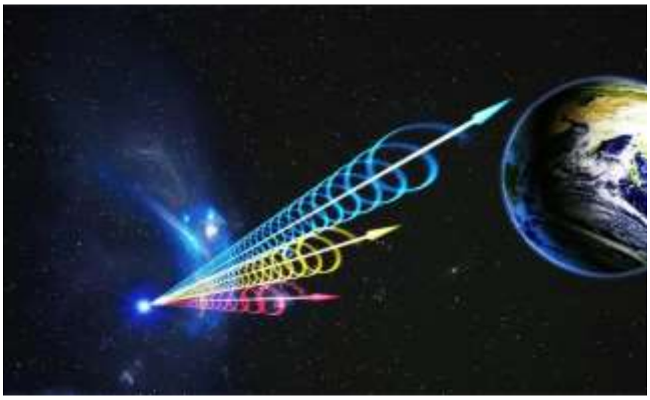

(Credit: Eric Ralls/earth.com)
https://doi.org/10.1126/science.adf2678

Ben Brubaker ~ New Evidence Shows Heat Destroys Quantum Entanglement
https://www.quantamagazine.org/computer-scientists-prove-that-heat-destroys-entanglement-20240828/

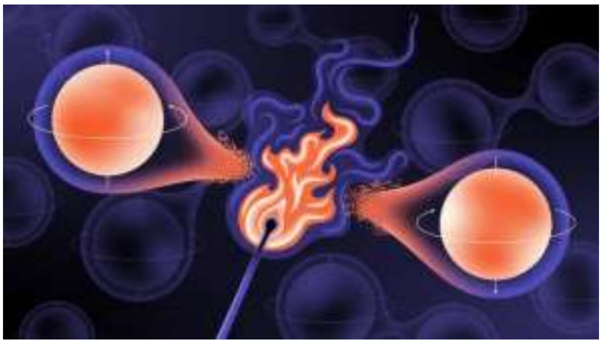

(Credit: Kristina Armitage/Quanta Magazine)

Wired Video ~ Quantum Computing Expert Explains One Concept in 5 Levels of Difficulty
(Credit: Dr. Talia Gershon/IBM Quantum Research)

Stevens Institute of Technology ~ Thought to Be Impossible: Scientists Propose Groundbreaking Method to Detect Single Gravitons
https://scitechdaily.com/thought-to-be-impossible-scientists-propose-groundbreaking-method-to-detect-single-gravitons/
(Credit: Pikovski Research Group)
https://www.nature.com/articles/s41467-024-51420-8

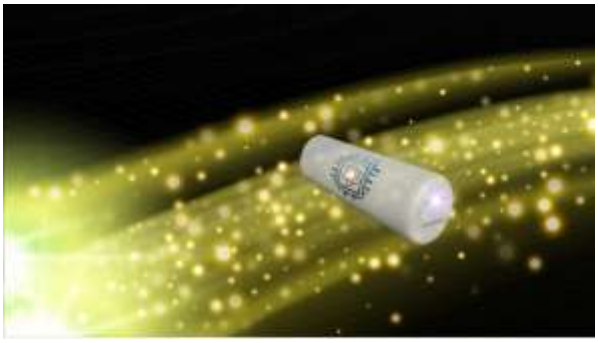

Jamie Carter ~ Space photo of the week: Entangled galaxies form cosmic smiley face in new James Webb telescope https://www.livescience.com/space/astronomy/space-photo-of-the-week-entangled-galaxies-form-cosmic-smiley-face-in-new-james-webb-telescope-image

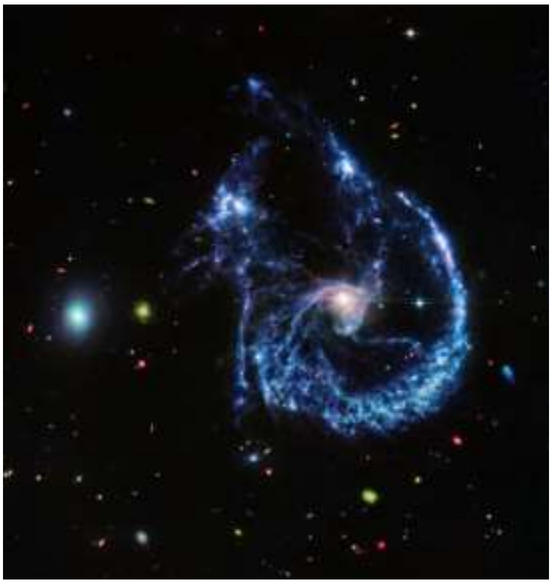

(Credit: NASA, ESA, CSA, STScI, url: https://esawebb.org/images/weic2423b/)

Robert Lea ~ James Webb Telescope goes 'extreme' and spots baby stars at the edge of the Milky Way (image)
https://www.space.com/james-webb-space-telescope-extreme-outer-galaxy

(Credit: NASA, ESA, CSA, STScI, M. Ressler (JPL))
https://iopscience.iop.org/article/10.3847/1538-3881/ad4e2e
https://dx.doi.org/10.48550/arXiv.2407.07822

Keith Cooper ~ 2nd Kuiper Belt? Our solar system may be much larger than thought
https://www.space.com/second-kuiper-belt-solar-system-larger-than-thought

(Credit: NASA/SOFIA/Lynette Cook)
https://arxiv.org/pdf/2407.21142

NSN Webinar Series: Europa Clipper: First NASA Mission to an Ocean World with Dr. Bonnie Buratti
video: https://youtu.be/V-Y9cpKvWZ8

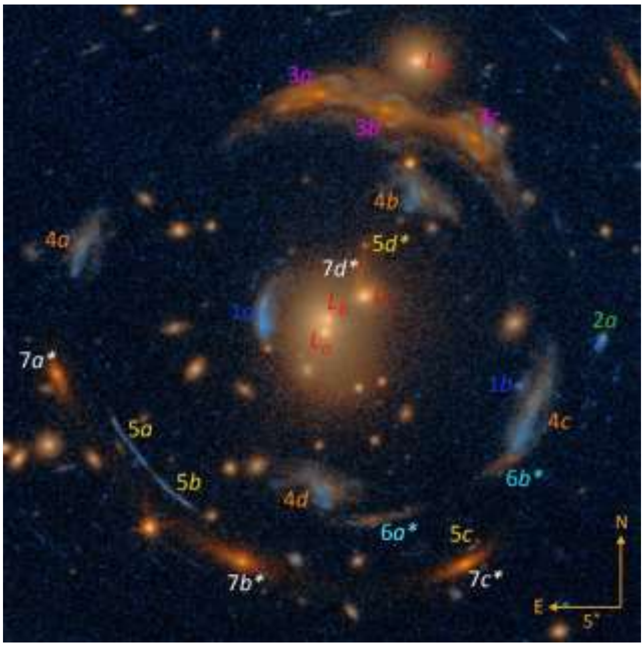

Marsha Fenner ~ "Amazingly Lucky" Gravitational Lens Reveals New Insights into Dark Matter and Dark Energy
https://scitechdaily.com/amazingly-lucky-gravitational-lens-reveals-new-insights-into-dark-matter-and-dark-energy/

(Credit: William Sheu (UCLA) using Hubble Space Telescope data)

https://iopscience.iop.org/article/10.3847/1538-4357/ad65d3

Technical Knowledge and Education: (September-October 2024)

Terence Dickinson, Alan Dyer ~ The Backyard Astronomer's Guide

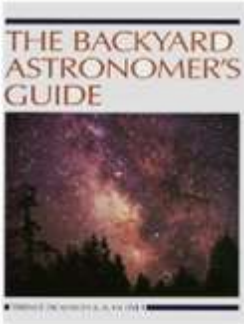

https://www.goodreads.com/book/show/1672322.The_Backyard_Astronomer_s_Guide

The International Astronomical Union - Minor Planet Center
https://minorplanetcenter.net/
https://minorplanetcenter.net/iau/info/Astrometry.html
(Guide to Minor Body Astrometry)

SARA ~ ezRA – Easy Radio Astronomy Analysis Tutorials:
- *Simple Overview: https://youtu.be/sgid9zn9KkY*
- *Analysis 1- Introduction and Data Collectors*: https://youtu.be/ig_jPTuS8ZA
- *Analysis 2- Spreadsheet Analysis*: https://youtu.be/HkrIN9d6Hd8
- *Analysis 3- Signal Progression*: https://youtu.be/VIp7L6gIZPY
- *Analysis 4- More Plots and ezb file*: https://youtu.be/K02MADafOhc
- *Analysis 5- Interference Filters*: https://youtu.be/FeFk9EvITtc
- *Analysis 6- ezSky*: https://youtu.be/UNwS0f9X7kE
- *Analysis 7- AntXTVT and VLSR* : https://youtu.be/0ezig90GNBc
- *Analysis 8- ezGal*: https://youtu.be/i0St2X7ODKM

SARA ~ *Radio Astronomy Video Series: Constants, Variables and Formulas, Radio Astronomy Formulas:*
- *Introduction to Radio Astronomy: https://youtu.be/AOgvjRXnins*
- *Lesson 1- Parabolic Dish Gain*: English (Espanol)
- *Lesson 2 -Parabolic Dish Half Power Beamwidth*: English (Espanol)
- *Lesson 3 -Thermal Noise*: English (Espanol)
- *Lesson 4 -Focal Length and f/D*: English (Espanol)
- *Lesson 5 -Feed Illumination Angle*: English (Espanol)
- *Lesson 6 -Pointing Offset Gain Loss*: https://youtu.be/dQ8wAaTtm40
- *Lesson 7 -Measuring System Temperature (TSys)*: https://youtu.be/4gVUFFxra-U
- *Lesson 8 -Coax Attenuation Interpolation*: https://youtu.be/3B8hV6vFyo8
- *Lesson 9 -Pulsar math including electron density, distance, and age*: https://youtu.be/Bymdp--_3JU
- *Lesson 10 -Distance Math - AU, Parallax, Parsecs and Light Years*: https://youtu.be/6fo0y3fDOZs
- *Lesson 11 -Doppler Frequency and Relative Velocity Calculations*: https://youtu.be/8zKloAVpnJc
- *Lesson 12 -Pointing to the Milky Way using a Compass and Protractor*: https://youtu.be/33xeUSji94U
- *Lesson 13 -Radiometer Equation Basics*: https://youtu.be/vAyypJ8f2z8
- *Lesson 14 -Noise Figure and Noise Factor Calculations*: https://youtu.be/GD6wZhW5NPA
- *Lesson 15 -Interpreting Stokes Parameters*: https://youtu.be/wUVsbfURIsg
- *Lesson 16 -Velocity Factor, Speed of Light in a Coax Cable: https://youtu.be/WWuqRyb4Ad8*
- *Lesson 17 -Interferometry Fringe Spacing: https://youtu.be/rYhUKFn7IWg*

SuperSID

SuperSID
Collaboration of Society of Amateur Radio Astronomers and Stanford Solar Center

- Stanford provides data hosting, database programming, and maintains the SuperSID website
- Society of Amateur Radio Astronomers (SARA) sells the SuperSID monitors for 48 USD to amateur radio astronomers and the funds are then used to support free distribution to students all over the world (image below as of Fall 2017)
-
- Jonathan Pettingale at SARA is responsible for building and shipping the SuperSID monitor kits: SuperSID@radio-astronomy.org
- SuperSID kits may be ordered through the SARA SuperSID webpage: http://radio-astronomy.org/node/210
- Questions about the SuperSID project may be directed to Steve Berl at Stanford: steveberl@gmail.com
- Jaap Akkerhuis at Stanford is responsible for the SuperSID software and SARA has provided financial support for his efforts
- SuperSID website hosted by Stanford: http://solar-center.stanford.edu/SID/sidmonitor/
- SuperSID database: http://sid.stanford.edu/database-browser/
- The data is searchable by time, station, date, and multiple plots may be placed on the same graph for comparison.

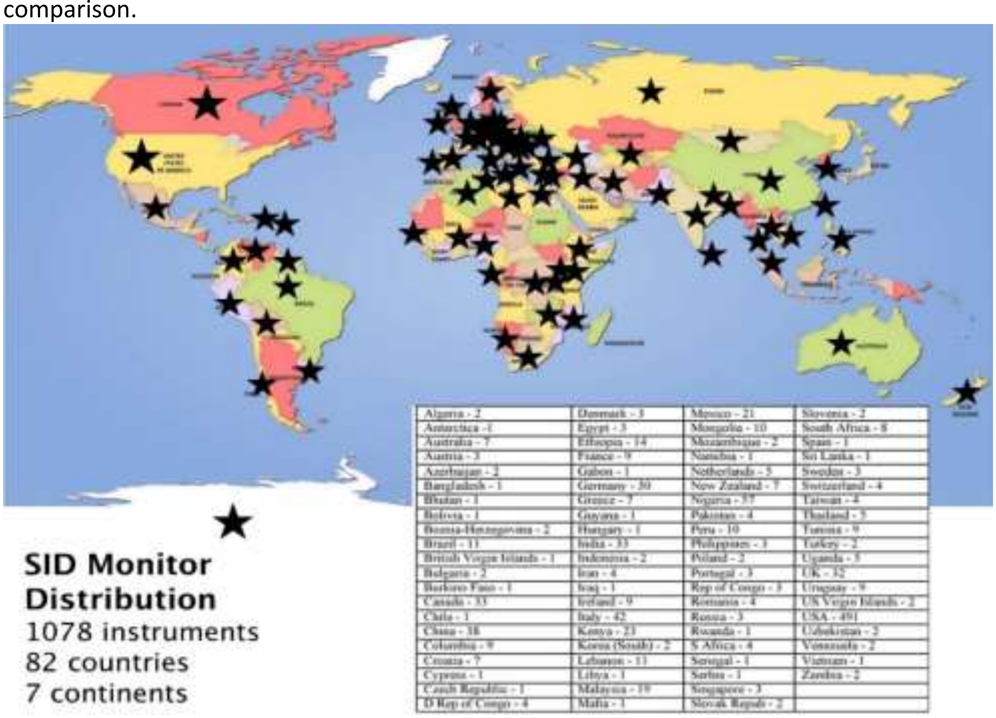

-

For official use only
Monitor assigned: __________
Site name: ________________
Country: ___________________

SuperSID Space Weather Monitor

Request Form

	Your information here		
Name of site/school *(if an institution)*:			
Choose a site name: *(3-6 characters) No Spaces*			
Primary contact person:			
Email:			
Phone(s):			
Primary Address:	Name School or Business Street Street City State/Province Country Postal Code		
Shipping address, if different:	Name School or Business Street Street City State/Province Country Postal Code		
Shipping phone number:			
Latitude & longitude of site:	Latitude: ____________________________ Longitude: ___________________________		

I understand that neither Stanford nor the Society of Amateur Radio Astronomers is responsible for accidents or injuries related to monitor use. I will assure that a surge protector and other lightning protection devices are installed if necessary.

Signature: ____ **Date:** ______________________________

I will need:

What	*Cost*	*How many?*
SuperSID distribution USB Power	$48 (assembled)	
USB Sound card 96 kHz sample rate *(or provide this yourself)*	$40 *(optional)*	
Antenna wire (120 meters) *(or you can provide this yourself)*	$23 *(optional) with connectors attached and tested*	
RG 58 Coax Cable (9 meters) *(or provide this yourself)*	$14 *(optional) with connectors attached and tested*	
Shipping	US $12 Canada & Mexico $40 all other $60	
	TOTAL	$

____ **I have included a $____________ check** (payable to SARA)
____ **I will make payment thru** www.paypal.com to treas@radio-astronomy.org

or

____ If you are a Minority-serving institution, in a Developing or economically deprived nation, and/or you are using the monitor with students for educational purposes, you may qualify for obtaining a monitor at reduced or no cost. Check here if you wish to apply for this designation. Then tell us how you want to use the SuperSID monitor. Include type of site, number of students involved, whether public or private school, grade levels, etc. and describe your program. The goal of the SuperSID project is to provide as many students with systems as possible. If you are able to pay for a system, even if you qualify for a free one, please do so and help support our goal.

For more details on the Space Weather Monitor project, see: **http://sid.stanford.edu**

To set up a SuperSID monitor you will need:

1 Access to power and an antenna location that is relatively free of electric interference (could be indoors or out)

2 A **PC**** with the following minimal specifications:
   a. A sound card that can record (sample) up to 96 kHz, or a USB port to connect such a sound card (for North and South America)
      i. All other countries can use AC97 sound card with 48 kHz record (sample) rate. Most computers made after 1997 will have AC97.
   b. Windows 2000 or more recent operating system
   c. 1 GHz Processer with 128 mb RAM
   d. Ethernet connection & internet browser (desirable, but not required)
   e. Standard keyboard, mouse, monitor, etc.

3 An inexpensive antenna that you build yourself. You'll need about 120 meters (400 feet) of **insulated** wire. Solid wire is easier to wind than stranded. Magnet wire will work but be more fragile. You can use anything from #18 to #26 size wire. The antenna frame can be made of wood, PVC pipe, or similar materials. We'll provide instructions. You can purchase the wire from us or obtain your own.

4 RG58 coax cable with a BNC connector at one end to run from the antenna to the SuperSID receiver. 9 meters is recommended, but the length will depend on where you place the antenna. You can purchase the coax from us or obtain your own.

5 Surge protector and other protection against a lightning strike

---

Return this form to: SuperSID@radio-astronomy.org
or mail to:

SARA Treasurer
c/o Thomas Jacobs
P. O. Box 4245
Wilmington, NC 28406.

Announcing Radio JOVE 2.0

The Radio JOVE Team

Radio JOVE students and amateur scientists from around the world observe and analyze natural radio emissions of Jupiter, the Sun, and our galaxy using their own easy to construct radio telescopes.

Our Project announces Radio JOVE 2.0, where participants assemble a 16-24 MHz radio spectrograph to observe solar, Jupiter, Galactic, and Earth-based natural radio emissions and share their observations with fellow participants.

In the Beginning

Radio JOVE started as a NASA sponsored educational outreach project in 1999. We developed a radio telescope kit suitable for receiving signals from Jupiter, the Sun, the Galaxy, and Earth-based radio emissions. The original kit comprised a radio receiver (RJ1.1) and a dual dipole antenna for 20.1 MHz. An important goal was to teach electronic principles including how to build, solder, and assemble the radio receiver and antenna.

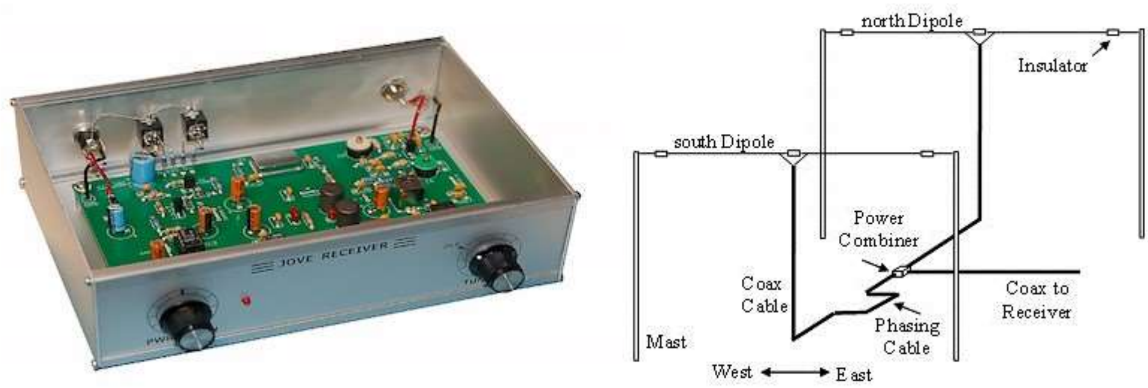

Figure 1. A Radio JOVE RJ1.1 receiver and a schematic of the dual-dipole antenna.

In addition to the hardware, three software packages were developed. These were Radio Jupiter Pro (Jupiter emission prediction program), Radio-SkyPipe (strip chart program) and Radio Sky Spectrograph (control and display of radio spectrograph data).

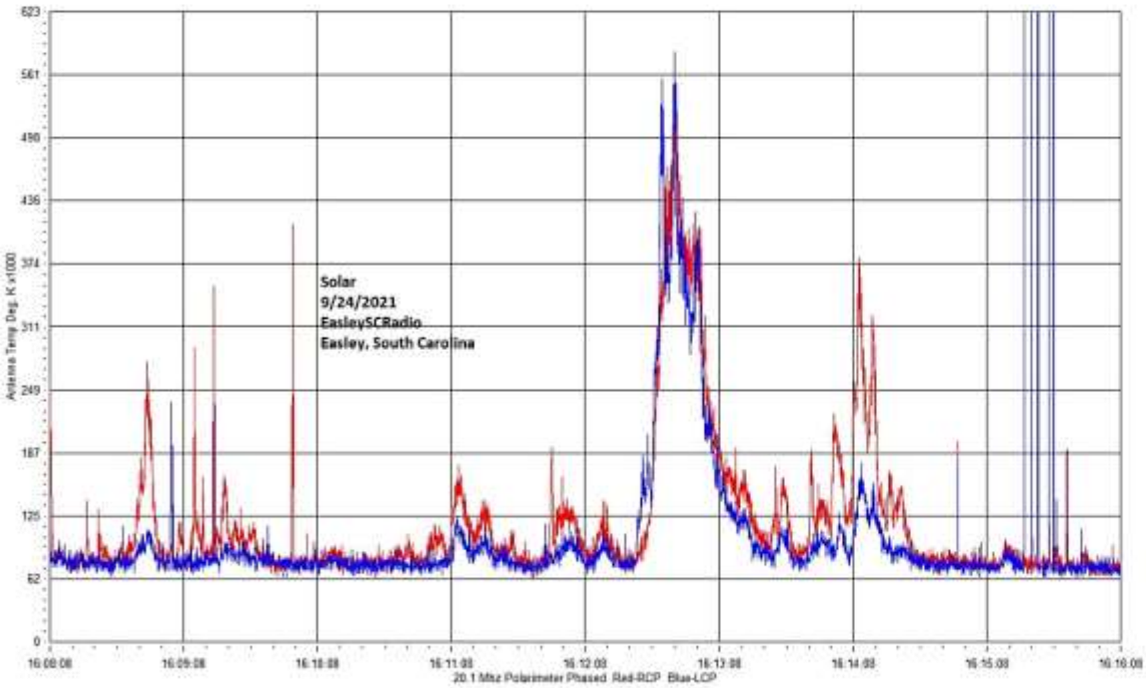

Figure 2. A SkyPipe strip chart showing multiple solar bursts using a JOVE receiver. John Cox, SC.

The Growth of Radio JOVE

As of Autumn 2021, over 2,500 kits have been sold at cost to schools and individuals around the world. Thousands of data submissions from observers have been made to the Radio JOVE data archive.

The Radio JOVE web site has always provided a wealth of information describing observation methods and various educational materials intended to teach radio astronomy techniques and scientific methods. Biannual newsletters are produced, and several telephone help sessions are held each year.

A sub-group of experienced observers known as the Spectrograph Users Group (SUG) evolved from the core JOVE group. These observers developed data collection and analysis techniques using more advanced equipment and techniques. SUG members have contributed to articles published in peer-reviewed scientific journals. This group remains active under the Radio JOVE listserv at https://groups.io/g/radio-jove/.

Moving Forward with New Technology

In the past, Radio JOVE provided the hands-on experience of building a radio kit. We have many RJ1.1 receivers in operation successfully contributing scientifically valuable data. It has, however, become increasingly difficult to obtain parts for the RJ1.1 receiver kits and we therefore decided to replace the RJ1.1 receiver with a new SDR-based design for the receiver portion of our radio telescope kits. While we continue to support the hardware and software for the original RJ1.1 receivers, the only kits now available for purchase from Radio JOVE contain this newly designed system.

In recent years, new technologies have made software defined radios (SDRs) ever more affordable. These radios can operate on a single frequency like the original JOVE receiver but can also generate spectrograms which depict radio activity as a function of both time and frequency. Such displays offer new insights into our studies of the Sun, Jupiter, the Galaxy, and both natural and artificial Earth-based radio emissions.

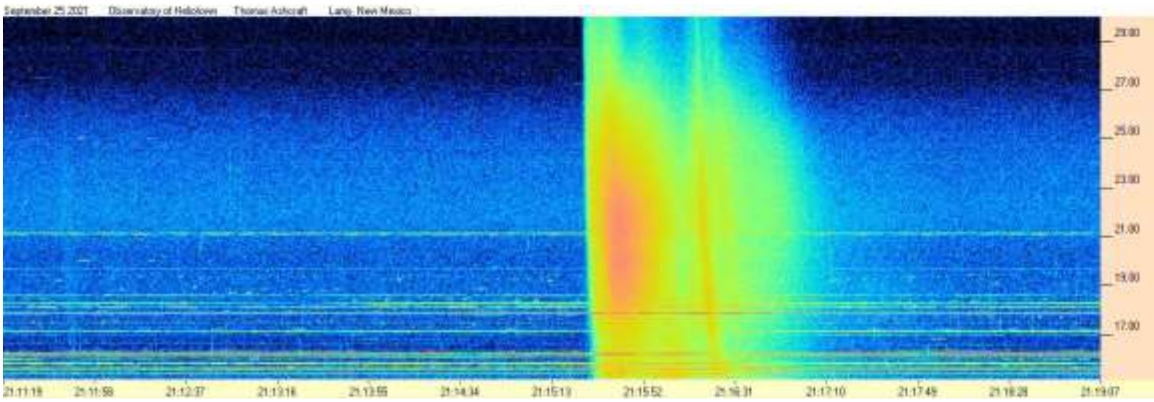

Figure 3. Radio spectrogram showing multiple solar bursts received by Tom Ashcraft in New Mexico. Horizontal scale is time, and the vertical scale is frequency. Amplitude is displayed using different colors corresponding to the strength of signals.

Radio JOVE continues to sell radio telescope packages including an antenna, receiver, and software; however, the receiver is now a commercially built SDR.

Figure 4. The JOVE team has had considerable success with the SDRPlay RSP1A unit and will provide support for using this instrument for our radio astronomy program. Not all SDR types can be supported, but it is our intent to provide support for some other SDRs as they become available during this period of rapid SDR development.

It continues to be our goal to introduce new observers to the scientific method and help them experience the thrill of receiving cosmic radio signals. Through a series of educational training modules and observing and analysis projects we aim to guide new observers to levels where they can contribute to Citizen Science projects.

We continue to support our large user base that uses JOVE RJ1.1 receivers – both in terms of technical support for the receivers but also with new and exciting observing projects for both RJ1.1 and SDR users.

We welcome both new and experienced observers to the JOVE 2.0 program as we share the excitement of receiving, studying, and understanding radio signals from our corner of the galaxy.

Please see the Radio JOVE web site at https://radiojove.gsfc.nasa.gov for more information.

RADIO JOVE 2.0 RADIO TELESCOPE KIT ORDER FORM

Order Online using PayPal™

* * * Please allow 2 to 3 weeks for delivery. * * *

IMPORTANT: Before you order the Jove receiver kit and/or the antenna kit, we suggest that you read the on-line manuals. You will need to provide additional materials and tools to complete the antenna. The cost of additional materials for the antenna support structure (masts, etc.) may be in the range of US$75 to US$100. Also note that the optimal antenna height can be up to 20ft, depending upon your latitude.

Item # RJK2u – Complete 2.0 Kit: Receiver + Unbuilt Antenna Kit + Software This kit includes an SDRplay RSP1A, USB Cable, SMA/BNC cable, F-adapter, unbuilt Antenna Kit (RJA), printed assembly manuals, and Radio-Sky Spectrograph (RSS) software. Note: Kit does not include antenna support structure. **Price: $215 + Shipping (See reverse for shipping)**	**Item # RJK2p** – Complete 2.0 Kit: Receiver + Professionally Built Antenna Kit + Software This kit includes an SDRplay RSP1A, USB Cable, SMA/BNC cable, F-adapter, Professionally Built Antenna Kit (RJA2), printed assembly manuals, and Radio-Sky Spectrograph (RSS) software. Note: Kit does not include antenna support structure. **Price: $384 + Shipping (See reverse for shipping)**
Item # RJA – Unbuilt Antenna Kit The RJA Radio JOVE Antenna Kit includes a printed construction manual, stranded copper easy-to-solder antenna wire, ceramic insulators, RG-59 easy-to-solder coax cable, screw-on F connectors, and a power combiner. Note: Kit does not include antenna support structure. Assembly requires a soldering gun and other tools. **Price: $90 + Shipping (See reverse for shipping)**	**Item # RJA2** – Professionally Built Antenna Kit The RJA2 Radio JOVE Antenna Kit includes a printed installation manual, two professionally assembled dipole antennas constructed of #14 Copperweld wire with Budwig center insulators and center support rope attachment points, high quality RG-6 coax with pre-installed commercial grade connectors, and a power combiner. Note: Kit does not include antenna support structure. **Price: $249 + Shipping (See reverse for shipping)**
Item # LTJ2 – Listening to Jupiter, 2nd Ed. by R. S. Flagg PDF download of Richard Flagg's book "Listening to Jupiter, 2nd Ed., 2005". The file is downloaded from a secure website. **Price: $10 + $0 shipping (PDF file download)**	**Item # RJR2** – Radio JOVE 2.0 Receiver-Only Kit This kit includes one SDRplay RSP1A SDR receiver, USB Cable, SMA/BNC cable, and F-adapter, printed assembly manuals, and Radio-Sky Spectrograph (RSS) software. **Price: $135 + Shipping (See reverse for shipping)**

RADIO JOVE 2.0 RADIO TELESCOPE KIT ORDER FORM (continued)

Order Online at
https://radiojove.net/kit/order_form.html OR
Complete this form and mail with payment

Payment may be made by Credit Card via PayPal™, U.S. Check, U.S. Money Order, International Money Order in U.S. funds drawn on a U.S. bank, or Western Union Money Transfer made payable to **The Radio JOVE Project**. No bank-to-bank wire transfers are accepted. Purchase Orders are accepted from U.S. Institutions.

Send to: The Radio JOVE Project
1301 East Main St
MTSU Box 412
Murfreesboro, TN 37132, USA
email: chiggins@mtsu.edu
FEIN: 20-5239863

Item	Description	Quantity	Item Price	Shipping (see below)	Subtotal
RJK2u	Complete Radio JOVE 2.0 Kit Receiver + unbuilt Antenna		$215		
RJK2p	Complete Radio JOVE 2.0 Kit Receiver + Professionally Built Antenna		$384		
RJA2	Professionally Built Antenna-Only Kit		$249		
RJA	Unbuilt Antenna-Only Kit		$90		
RJR2	Receiver-Only Kit		$135		
LTJ2	Listening to Jupiter, 2nd Ed., by R.S. Flagg (PDF download)		$10	$0	
				Total:	

Shipping Fees for Radio JOVE: We ship all packages using USPS Priority Mail flat rate boxes.
U.S.A.: $17.00
Canada: $57.00
All Other International Shipping: $85.00

Ship to: (Please print clearly)

Name: ____

Address: ____

City, State, Postal Code: ____

Province, Country: ____

Email: ____

Visit the Radio JOVE web site and fill out the team application form at https://radiojove.net/sign_up_form.php even if you are just an interested individual so that you can receive important information about kit updates, online services, and activities within the project as they occur!

The British Astronomical Association
A company limited by guarantee
Registered Charity No. 210769
Founded in 1890
PO Box 702, Tonbridge, TN9-9TX 020-7734 4145
www.britastro.org

Please send questions, reports, and observations to John Cook: jacook@jacook.plus.com

BAA Radio Astronomy Section, Director: Paul Hearn

RADIO SKY NEWS **2024 JULY**

VLF SID OBSERVATIONS

July has been another very active month; 173 classified events being recorded as SIDs. There was only one X-class flare, with 65 M-class and 107 C-class. Eighty-one of the SIDs recorded did not have X-ray classifications in the SWPC satellite data or were not included in the list. The SWPC list did include a large number of events without classifications, these are shown in the timing tables as '*,' some of which appear to be quite strong. Two of these on the 26th were recorded by five observers. Events marked '?' were not listed.

The X-ray background level was just below or at M-level for part of the month, so smaller flares did not produce SIDs. The density of M-flares also hides many C-flares that we would otherwise record. The 23.4kHz German signal was switched off for the first half of the month.

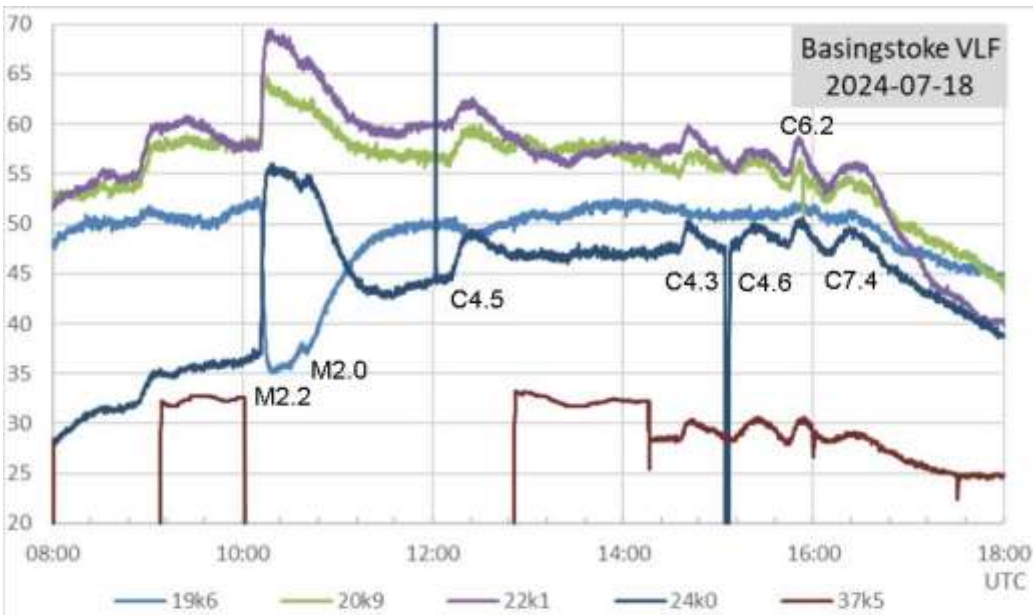

This recording from July 18th by Paul Hyde shows a pair of M-class flares that have almost merged into a single SID. My own recording shows just a single SID, other observers also recording it as a single event. The SWPC shows that both flares were from AR13751, a fairly large and complex sunspot group. The flares in the afternoon were much smaller, producing clear SIDs on most of the signals in Paul's recording.

The two unclassified events on the 26th are clearly seen in the recording by Mark Prescott:

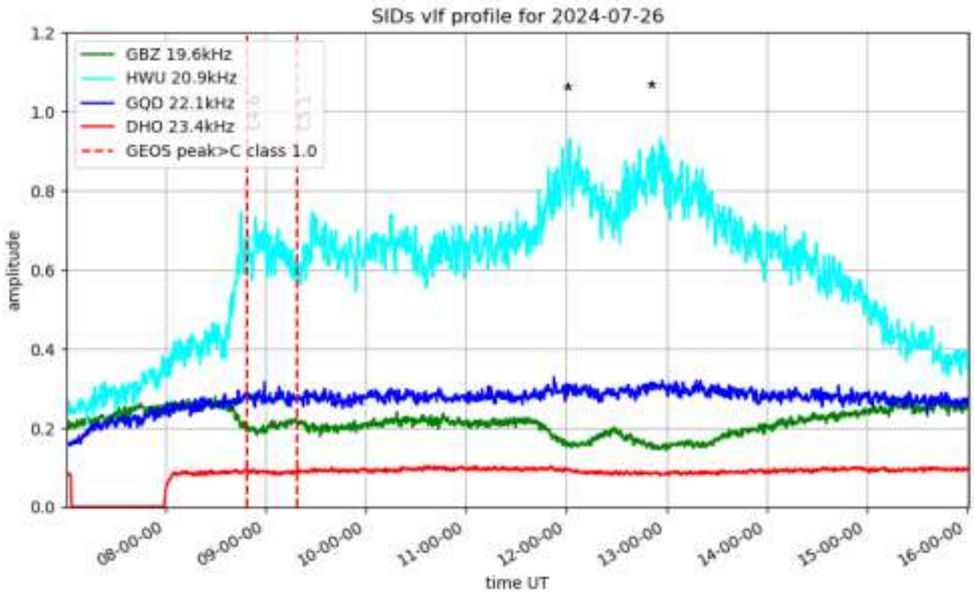

They show on both 20.9kHz and 19.6kHz, while 22.1 and 23.4kHz have not responded. The C4.6 and C5.1 flares earlier in the day have produced smaller SIDs, showing that the unclassified pair were at least C4 or C5 in strength.

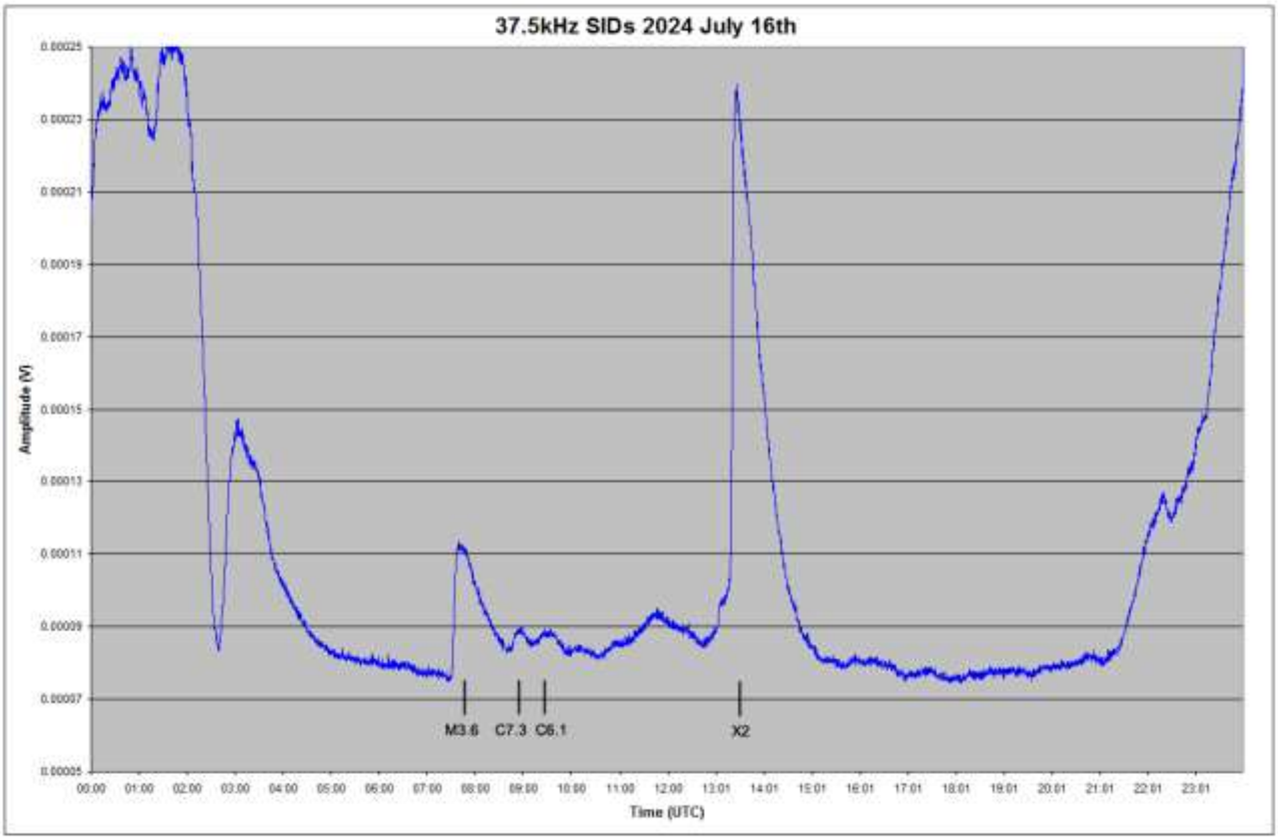

The strongest flare recorded was the X1.9 on the 16th. Mark Edwards' recording shows a very strong response at 37.5kHz and includes the smaller flares earlier in the morning. The 23.4kHz signal had come back on air earlier in the day, but then went off again just as the X1.9 flare started.

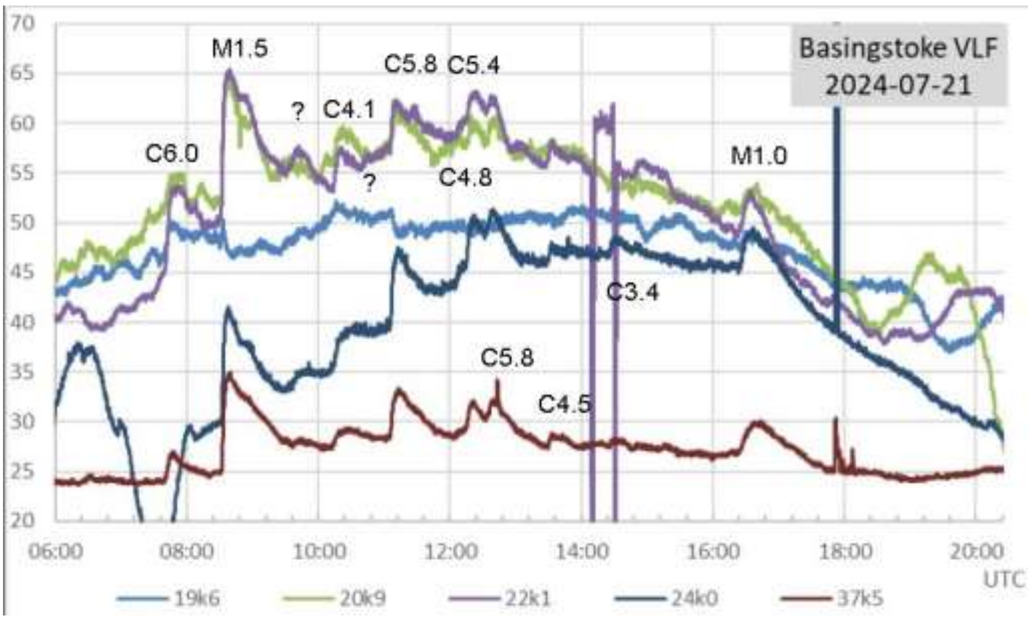

Paul Hyde's recording from the 21st shows near continuous flaring through the day. I have attempted to label the SIDs as clearly as I can, but many of them overlap and some are barely visible. The SID from the M1.5 flare shows a double peak on some signals, but not all of them. The trio of C4.8, C5.4 and C5.8 have also merged into a single SID, the weaker C4.8 just about visible on the 22.1kHz signal. The day ended with a C4.7 flare at 20:14UT, just at the end of the chart.

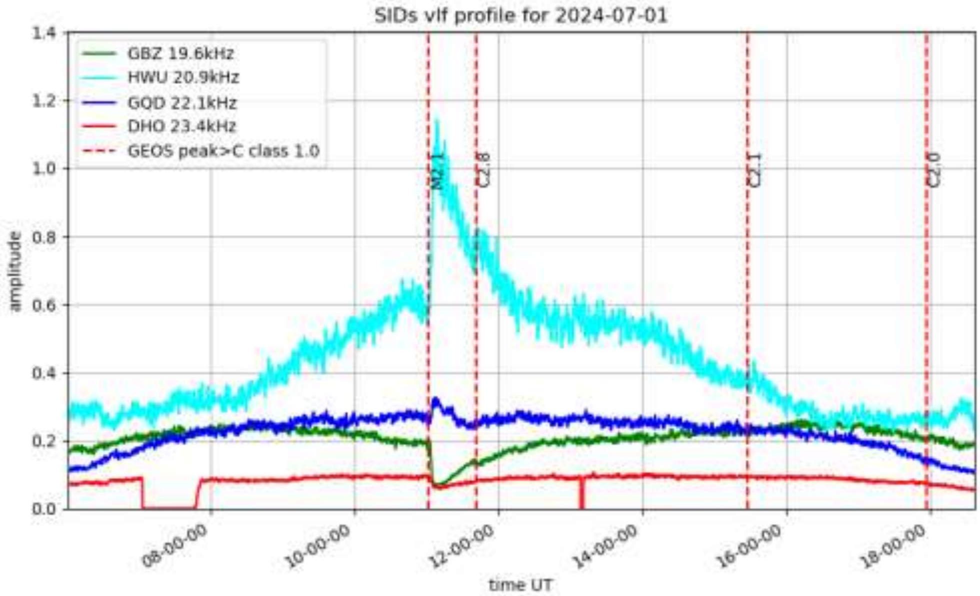

Activity on the 1st was much lower, Mark Prescott's recording showing just four flares, only two of which were recorded as SIDs. The C2.8 flare occurred just 40 minutes after the peak of the M2.1, and so the production of a SID was quite a surprise. It shows well at 19.6kHz but is not present at 23.4kHz.

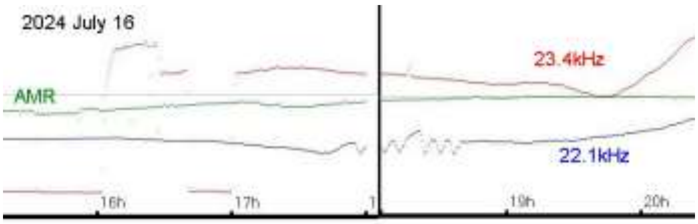

My own recording from the 16th shows some oscillation in the 22.1kHz signal from about 17:40 to 18:50 UT.

The break just after 18:00 is where the data was downloaded and the logger restarted. The cause of the oscillation is not clear, as it does not show at 23.4kHz.

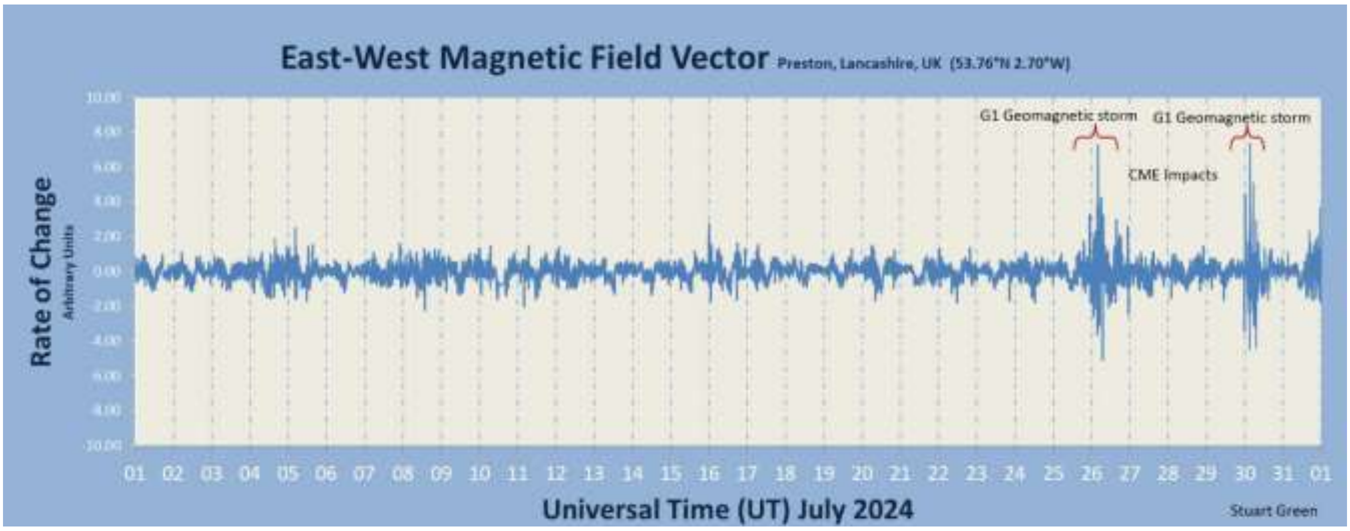

Stuart Green's monthly summary of magnetic activity shows a very quiet start to July, with two storms in the last week of the month. Our SID recordings show that there was plenty of solar activity right through the month with plenty of strong flares. The STCE reports also include plenty of CMEs, but once again they mostly seem to have not been Earth-directed. The strong triple flare on the 29th may have produced a small SFE aligned with the M8.7. My recording shows the magnetometer (AMR) along with the VLF signals. The SFE is marked '^,' timed at 12:55UT. It could easily be from local interference, so difficult to interpret. Roger Blackwell also has a transient in his recording, although it appears to be a few minutes after 13:00.

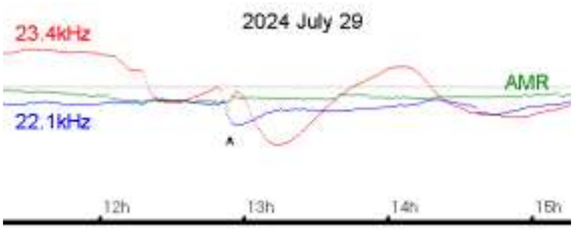

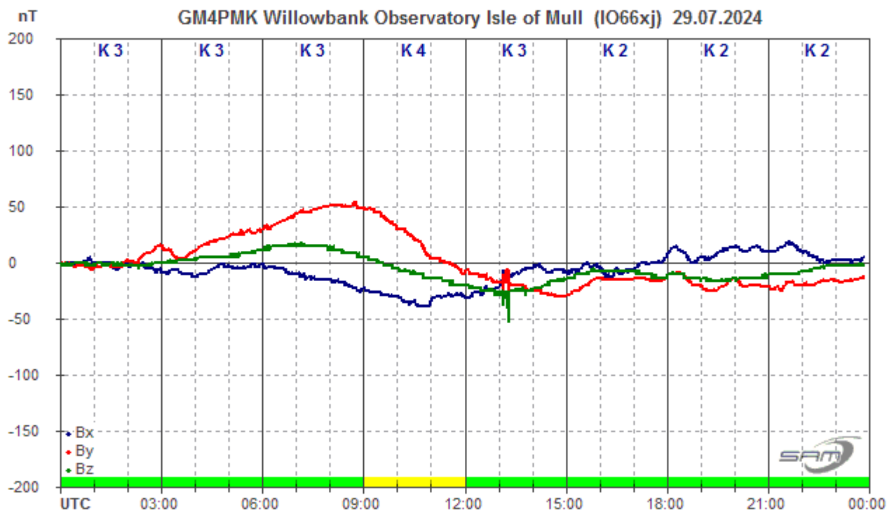

The first of the stronger storms was on the 26th, recorded by Thomas Mazzi in Italy:

This seems to have been from a combination of weak CMEs and a change in the solar wind. Callum Potter's recording from Orkney shows the storm in a little more detail:

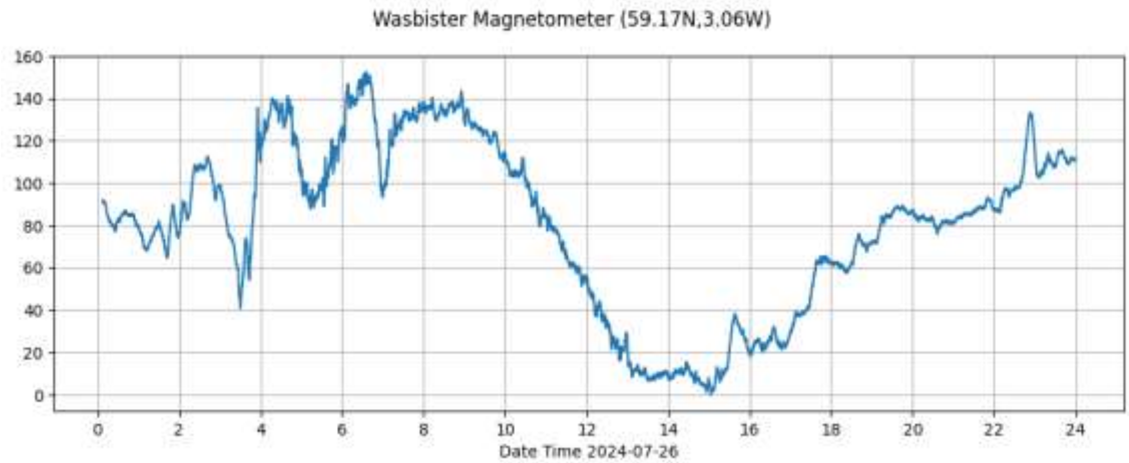

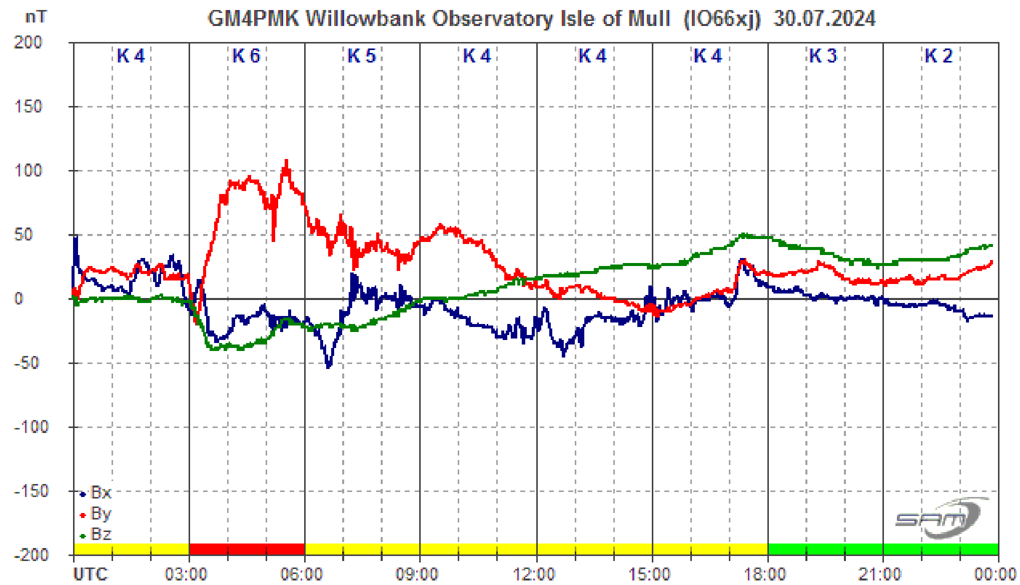

Activity was lower on the 27th...29th, increasing again in the morning of the 30th, shown in Roger Blackwell's recording. Most of the 31st was also fairly quiet but became more active in the late afternoon.

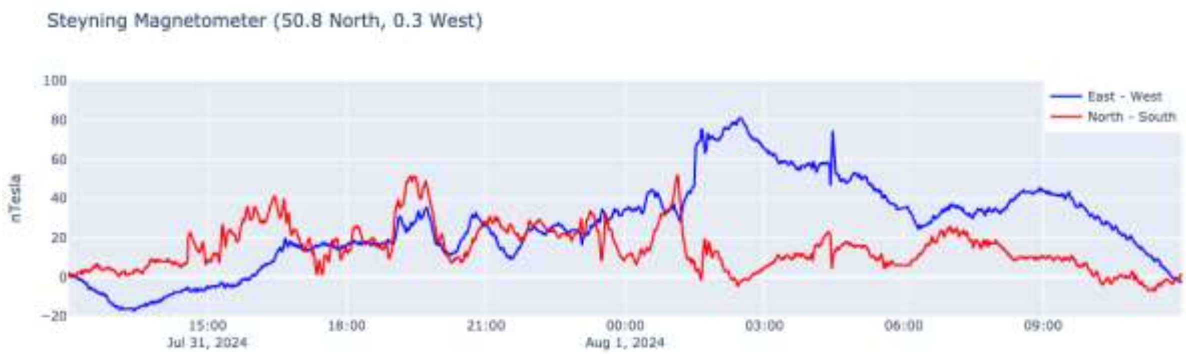

Nick Quinn's recording shows a disturbed period stating just before 15UT, continuing into August 1st. There is also evidence of an SFE around 05UT on the 1st, more on that next month.

Magnetic observations received from Roger Blackwell, Stuart Green, Thomas Mazzi, Callum Potter, Nick Quinn, and John Cook.

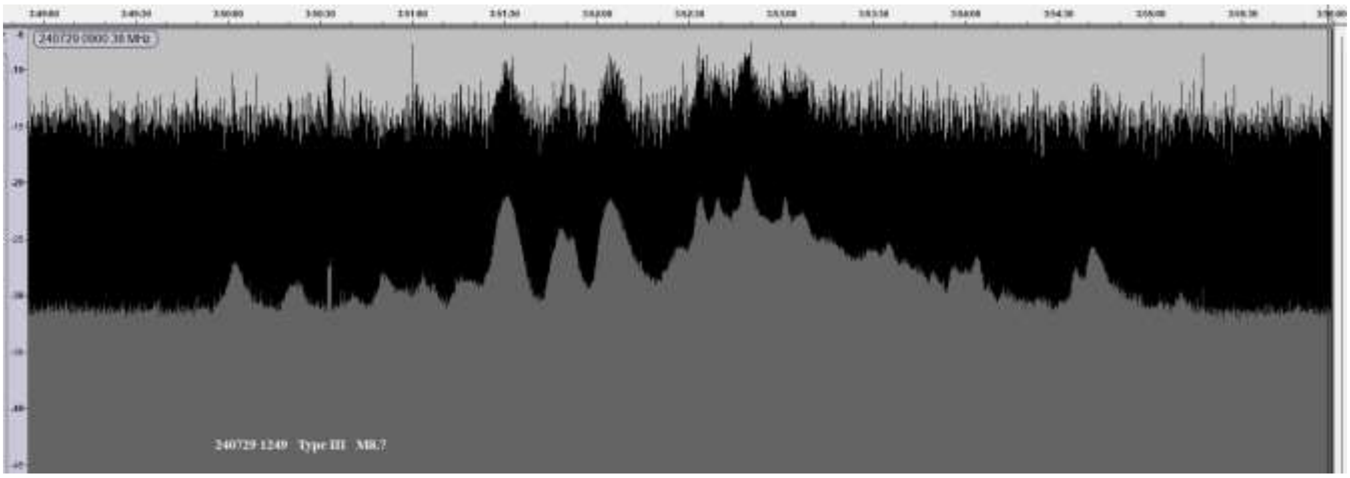

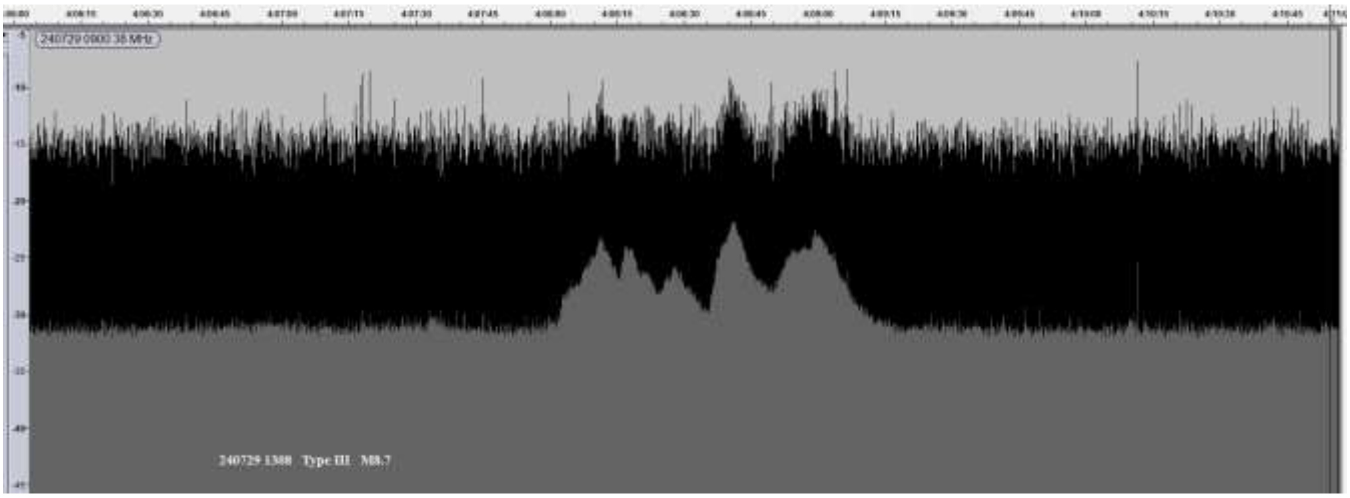

The strong triple flare on the 29th also produced some 38MHz emissions, recorded by Colin Briden. The first chart shows a type III emission starting at 12:49, the impulsive rise of the M8.7 flare. The second chart is from 13:08, during the decay phase of the flare. They have an amplitude of about 12dB, the first being a little stronger and much more complex. Colin Clements also recorded strong VHF emissions:

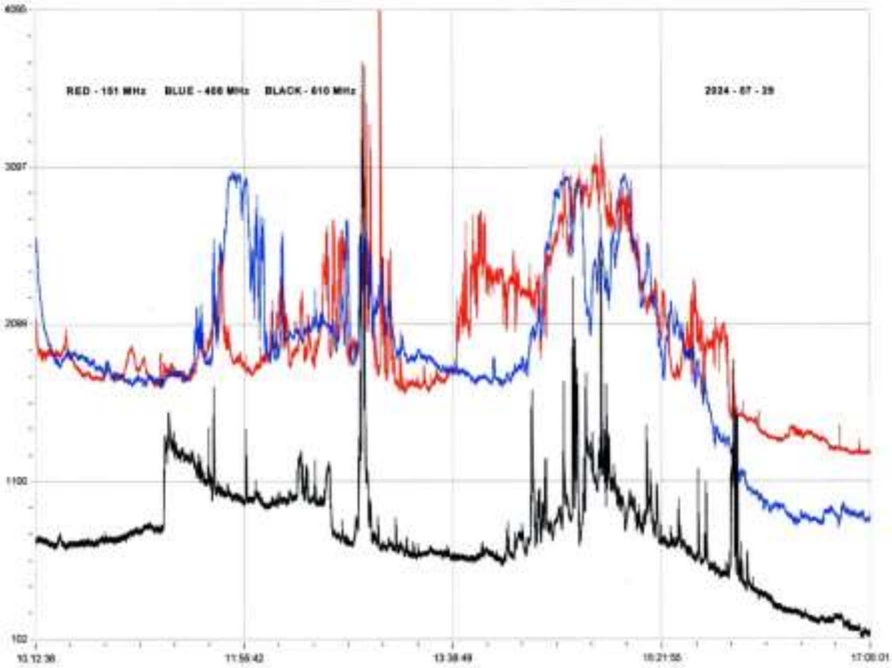

The strong spike on all three frequencies is at about 12:51UT, also matching the rise of the M8.7 flare. That is followed by a gap before the signal level rises again at about 13:40. The decay phase of the flare did last a long time, with the M4.2 flare peaking at 14:46 adding to the noise level. The SWPC X-ray data does show some unclassified flares around 11:30 to 12UT, that may be responsible for the earlier noise burst in Colin's recording.

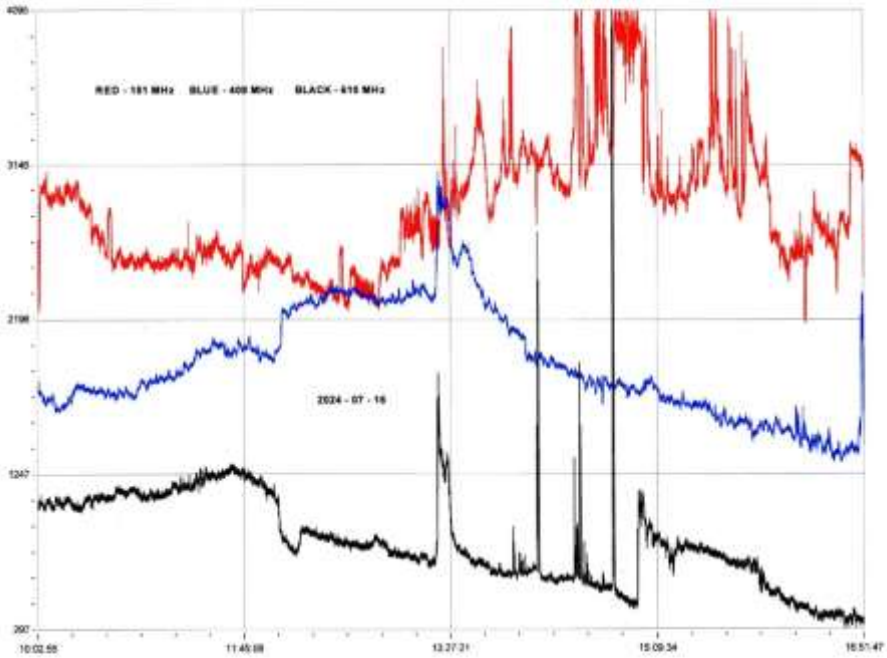

The X1.9 flare on the 16th also generated some strong VHF emissions, mostly during its decay phase. Short spikes at 610MHz (black) and 408MHz (blue) mark the start of the flare. 151MHz (red) has a slower rise in signal level, but then remains very active well into the afternoon.

MUONS

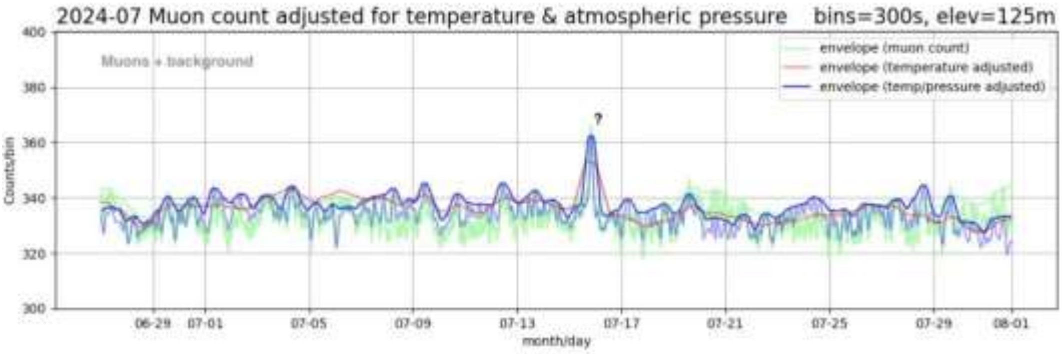

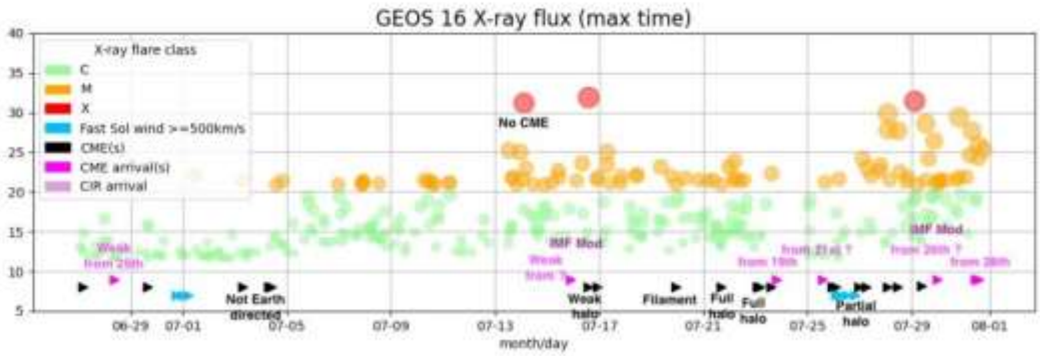

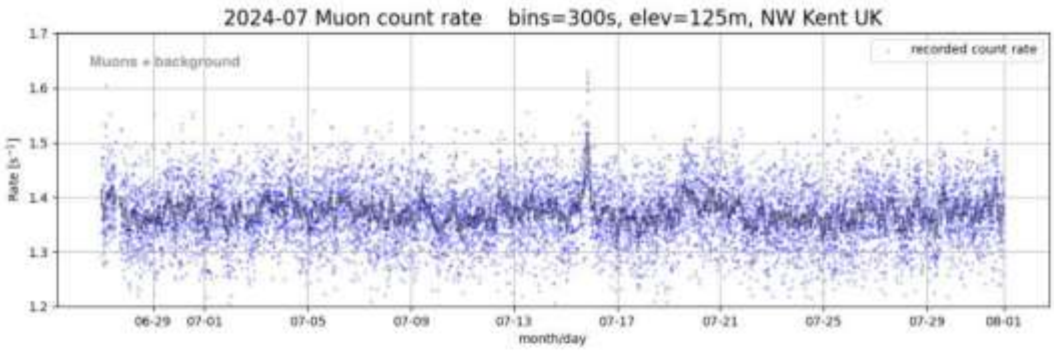

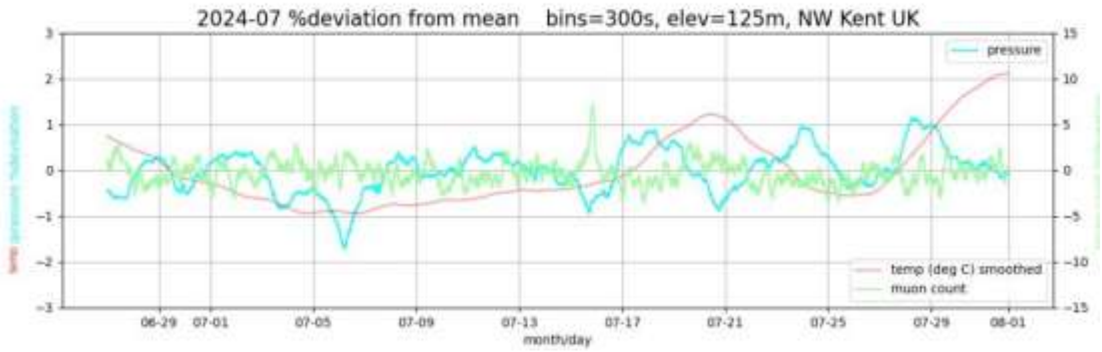

Mark Prescott's Muon charts show a fairly calm month, apart from a sharp spike on the 15th / 16th. The source of this is not clear, although there was a weak magnetic disturbance around that time. Measuring the chart, the peak seems to be before the X1.9 flare on the 16th. The small dip in the Muon counts after this follow the increase in M-flares and CMEs.

VLF SID OBSERVATIONS

Solar activity again remained high in August, with another 168 classified flares recorded. There were four of X-class that were suitably timed for us to record. The background X-ray flux level also remained high for much of the month, hiding some of the smaller flares. There were also plenty of multi-peaked and simultaneous flares, making many of the SIDs difficult to assign to specific flares. There were also plenty of unclassified events listed in the SWPC weekly bulletins. Those that were listed but without magnitudes are shown as '*,' while those not listed are shown as '?'.

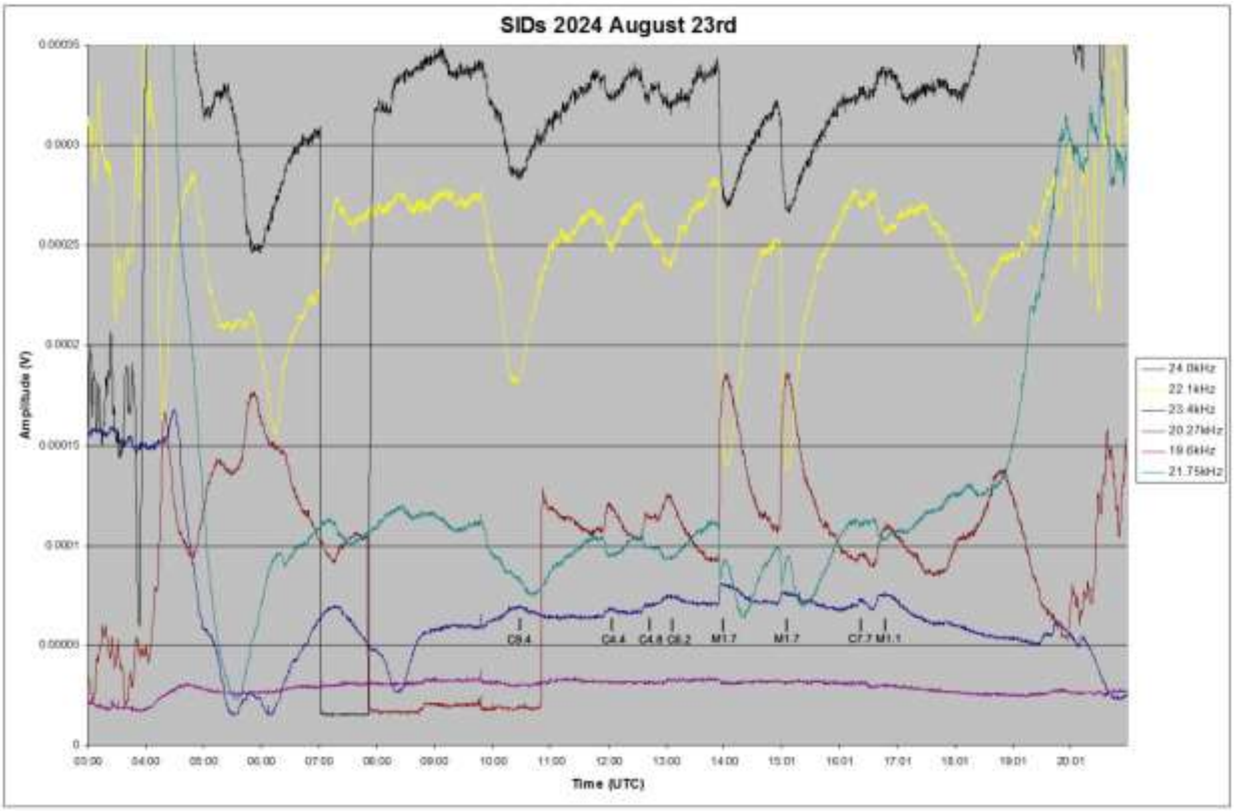

Mark Edwards' recording from the 23rd shows how many of the SIDs have merged, making analysis difficult. Mark has identified the stronger flares, but there are plenty of smaller peaks visible in the chart. The small difference in flare magnitudes is due to using different sources of X-ray data.

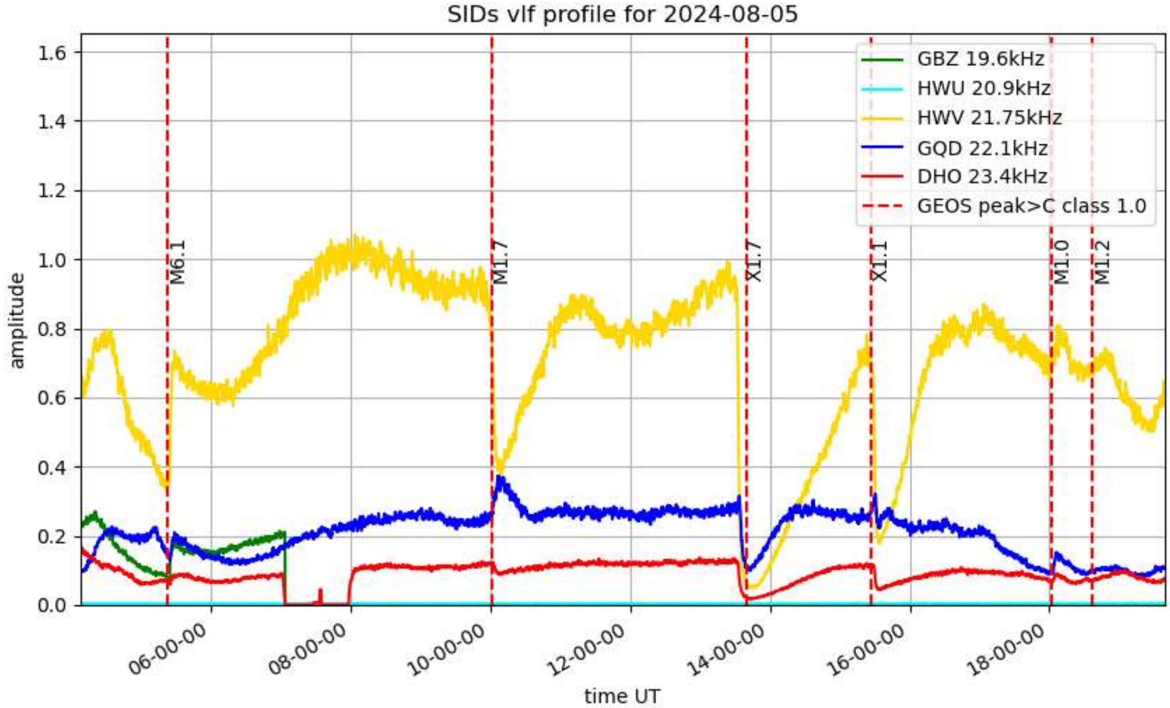

Mark Prescott's recording from the 5th shows the two strong X-flares. The first has merged into the second at 21.75kHz, which has then merged into the sunset period. The 22.1kHz trace is interesting in that the M1.7 SID has a rising peak while the X1.7 shows a falling peak. The X1.1 SID looks like a small 'peak and wave' type, and the later M1.0 again shows a rising peak. The 21.75kHz path is southward into France while the 22.1kHz path is north towards the Solway Firth.

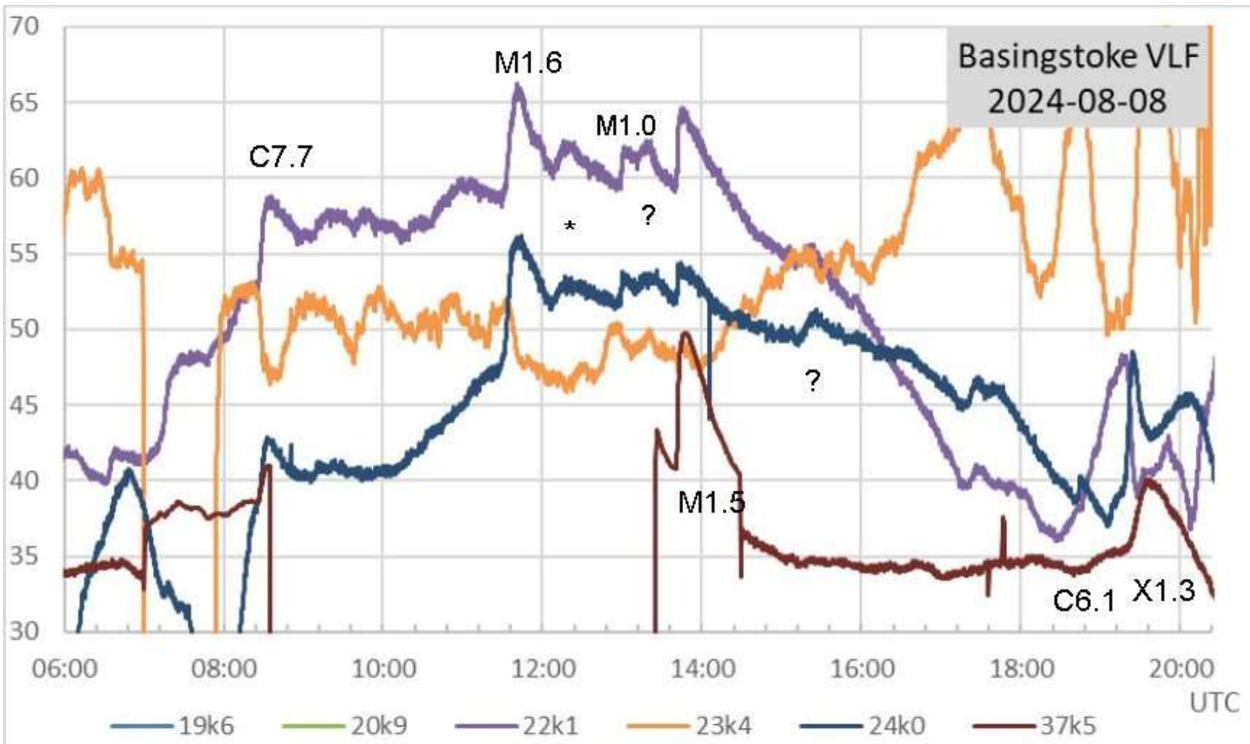

The third of the X-flares was late in the afternoon of the 8th, recorded on the Trans-Atlantic signals by Paul Hyde. The Grindavik signal went off air due to more volcanic activity later in the month, but was still operating on the 8th, showing a clean SID. 24kHz seems to show a 'spike and wave' shape. The chart also shows some of the unclassified events during the day, giving a very complex pattern.

The fourth of the X-flares was early on the 14th, peaking at about 06:45UT, and produced quite strong SIDs on both signals in the recording by Colin Clements. The two M-flares are also well recorded. There were several smaller unclassified events during the day, but not visible in the general background noise on these signals.

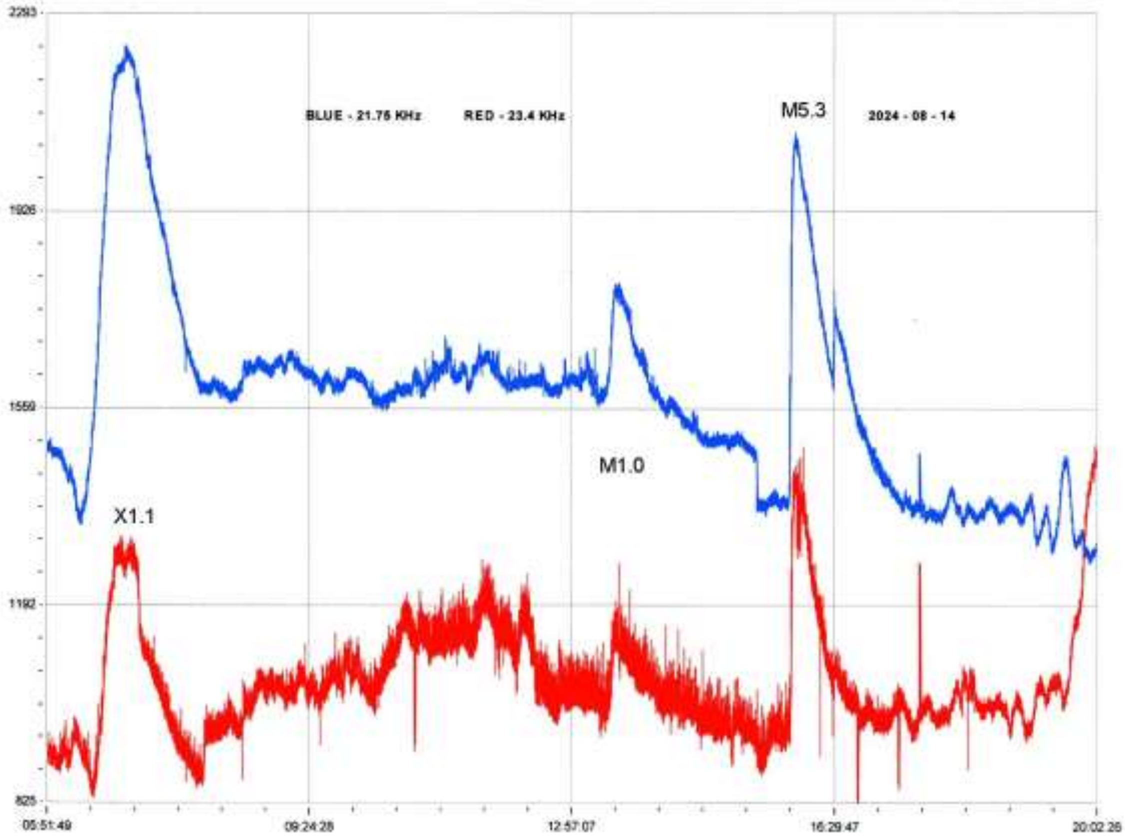

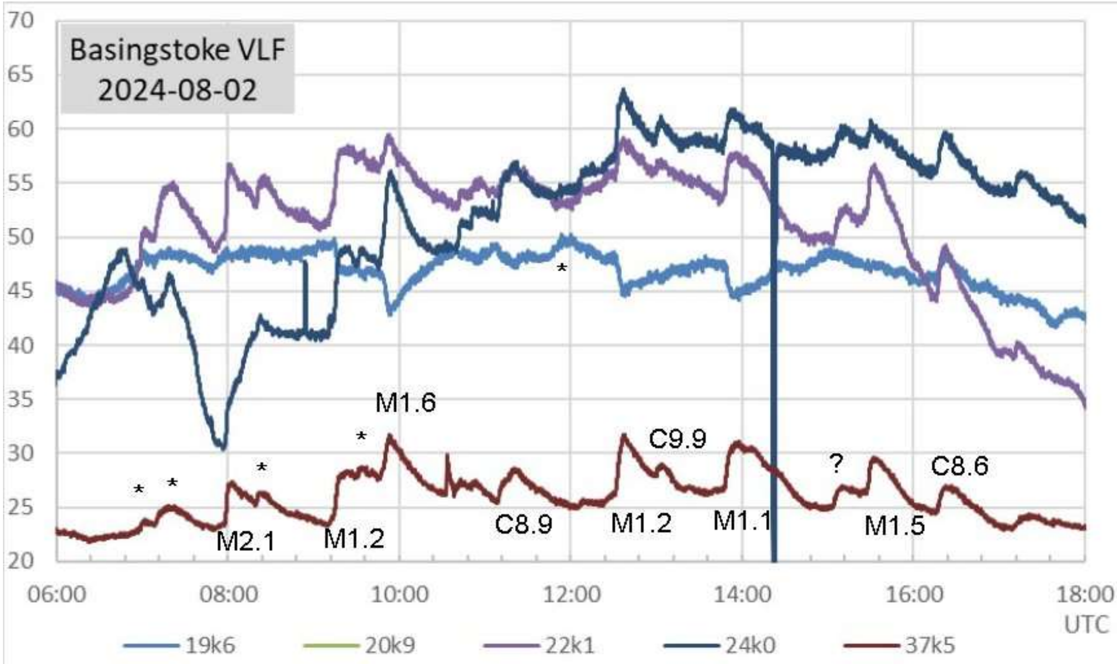

Paul Hyde's recording from the 2nd shows a day full of SIDs, quite well defined at 37.5kHz. I have attempted to label the unclassified events, some of which are quite distinct and show on most of the signals. Strong activity continued through most of August, although with more C-flares later in the month.

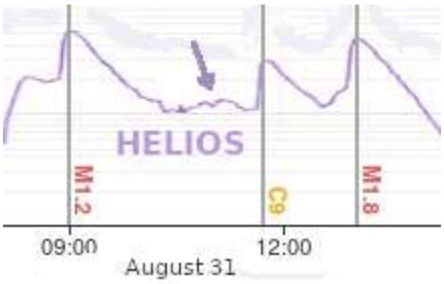

Thomas Mazzi also noted one of these unclassified events with his Helios system. It does match a peak in the X-ray charts, although I do not have the precise timing.

MAGNETIC OBSERVATIONS

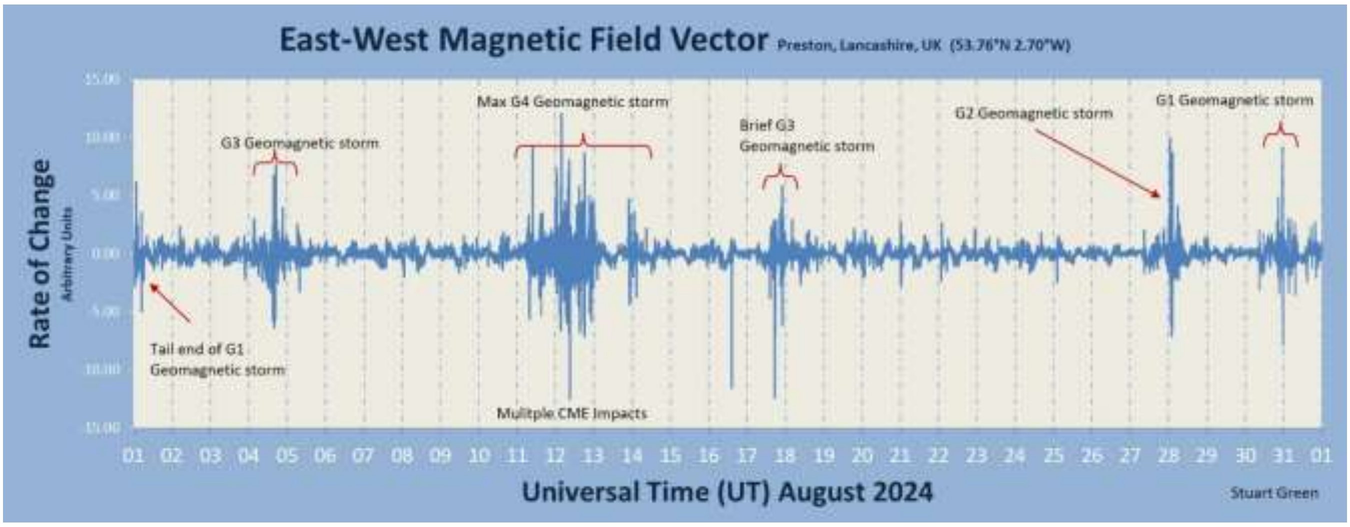

Stuart Green's summary of the month's magnetic activity shows some strong storms, including a G4 storm on the 11th to 14th. August started with the tail end of a storm at the end of July. In the July report I included a magnetic chart by Nick Quinn that included an SFE as a sharp spike. I have expanded my own recording to show the SFE with the M4.0 flare that produced it.

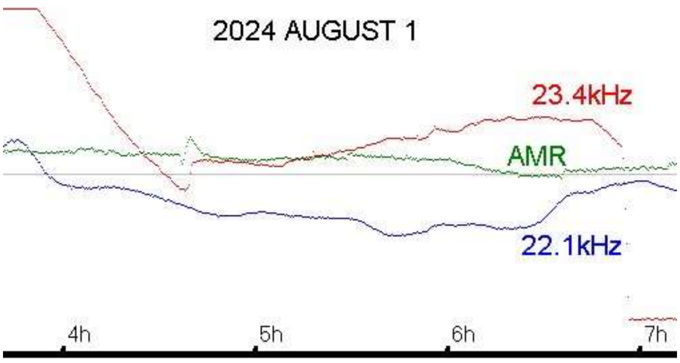

The flare is just visible in the 23.4kHz signal, together with the SFE in the green magnetometer trace. It peaks at 04:41UT and has a magnitude of 43nT. Roger Blackwell's recordings show a similar amplitude. The disturbance was short-lived, fading out by midday.

The major storm starting on the 11th seems to have been the result of several CMEs combining, so the actual source is not clear. Our SID observations show plenty of strong flares over the previous few days. Callum Potter's recording for the 11th and 12th shows the activity:

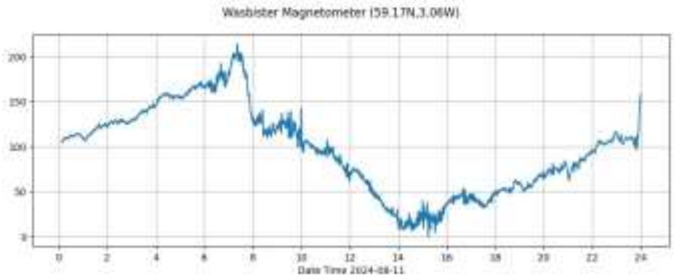

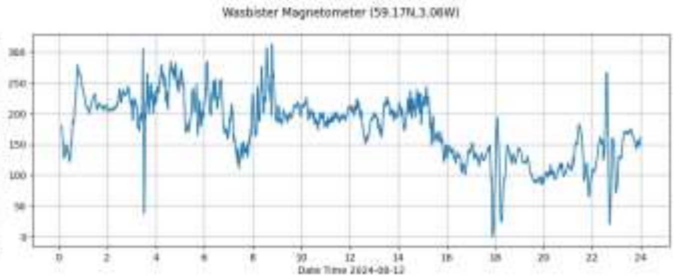

The disturbance is fairly mild on the 11th but increases rapidly at midnight. Note that the vertical scale changes on the 12th to show the greater amplitude during the day. Activity faded over the next few days.

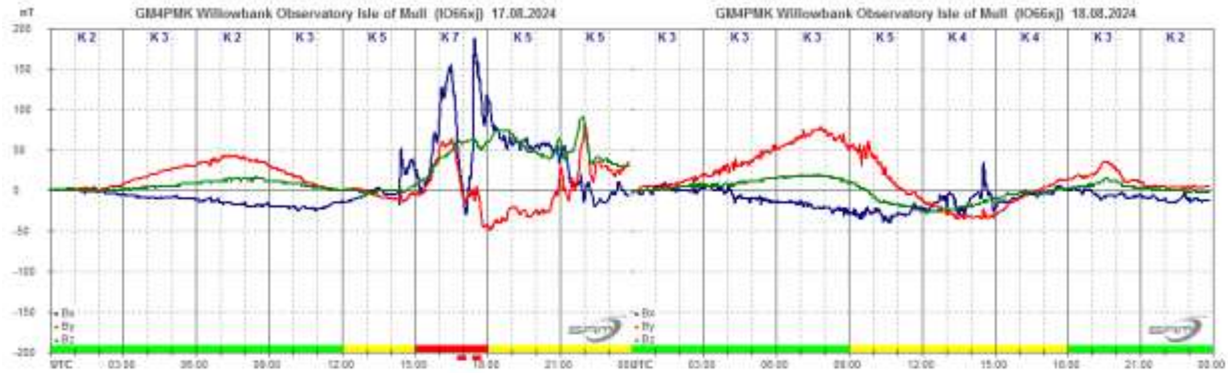

Roger Blackwell recorded the less active storm on the 17th and 18th, starting with a CME impact at about 14:20 on the 17th. The STCE bulletin lists a CME from the X1.4 flare early on the 14th arriving at 13:30. If this is the same event, then it was a very slow CME, taking over three days to reach Earth. The disturbance was much weaker after midnight, with a low amplitude turbulence in the morning of the 18th.

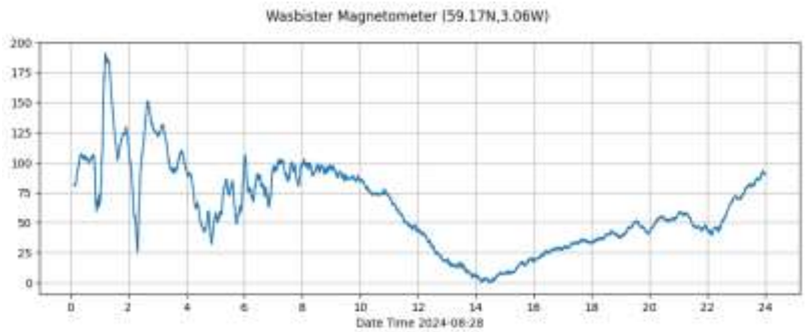

The two minor storms at the end of August were much weaker, Callum Potter's chart from the 28th showing activity starting at midnight and fading out before midday. Activity on the 31st was weaker and faded out quite quickly. The source seems to have been a stronger solar wind from a pair of coronal holes.

Magnetic observations received from Roger Blackwell, Stuart Green, Callum Potter, Nick Quinn, and John Cook.

SOLAR EMISSIONS

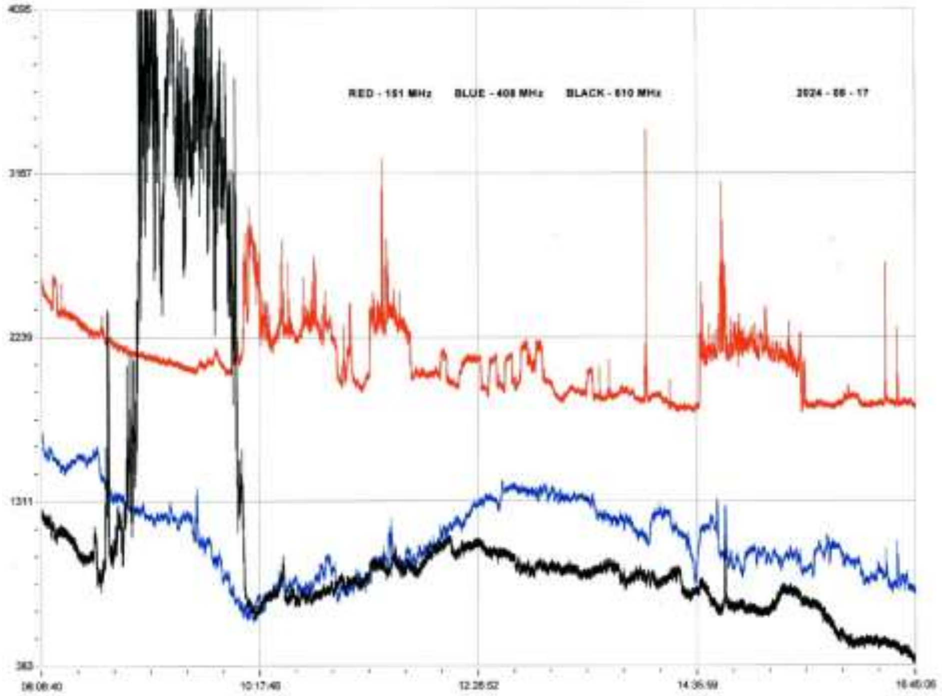

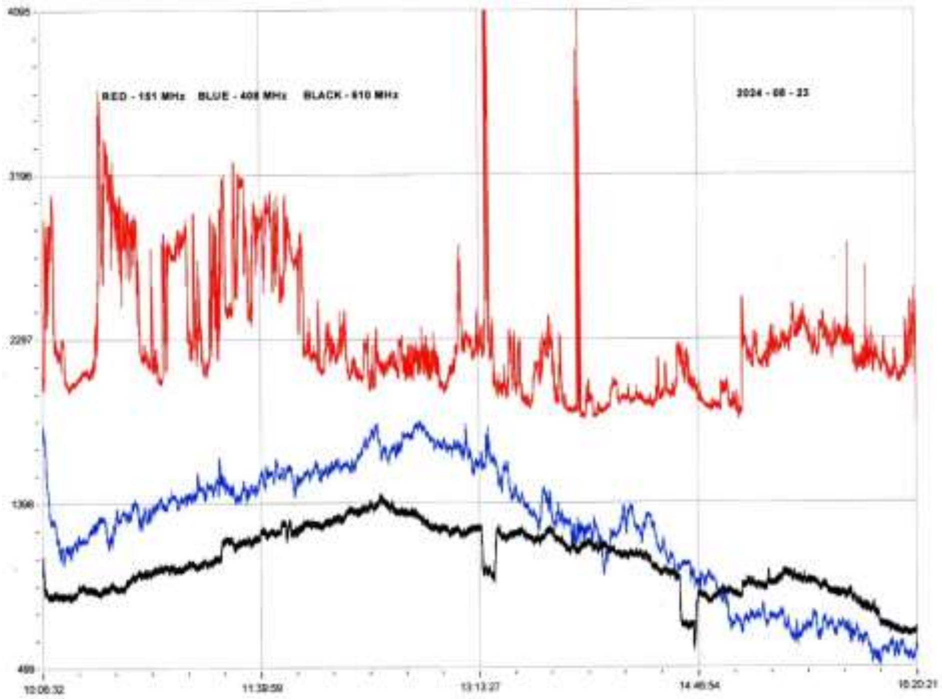

Colin Clements recorded radio emissions on several days in August. The 17th (top chart) shows some 151MHz (red) emissions matching the M1.6 and M1.1 flares, along with some of the unclassified events later in the afternoon. The strong 610MHz (black) burst may match some of the early unclassified flares but is rather odd. On the 23rd there is long period of 151MHz emission matching the strong C-flares in the morning, as well as a pair of short spikes around 13:15-13:30, perhaps from the afternoon C-flares. 408MHz (blue) has remained quiet on both days. Emissions were also recorded on the 5th, 16th, 19th,30th and 31st.

MUONS

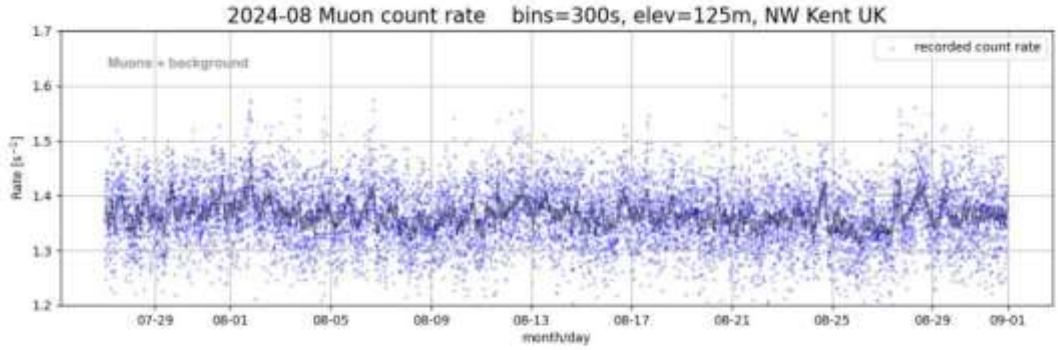

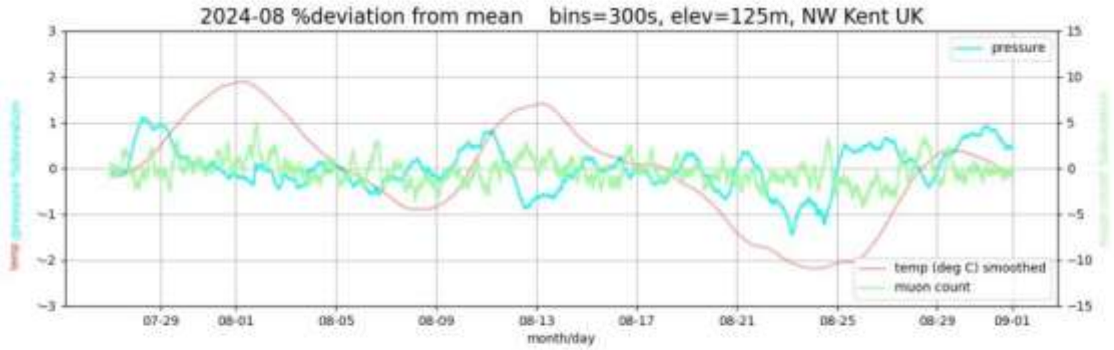

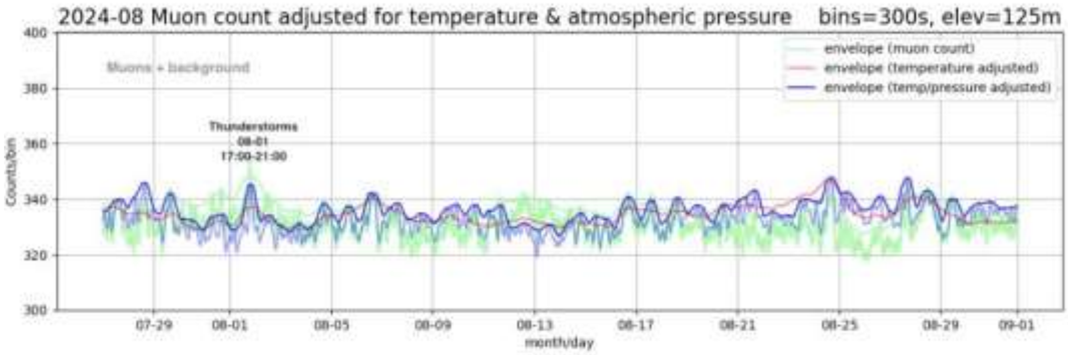

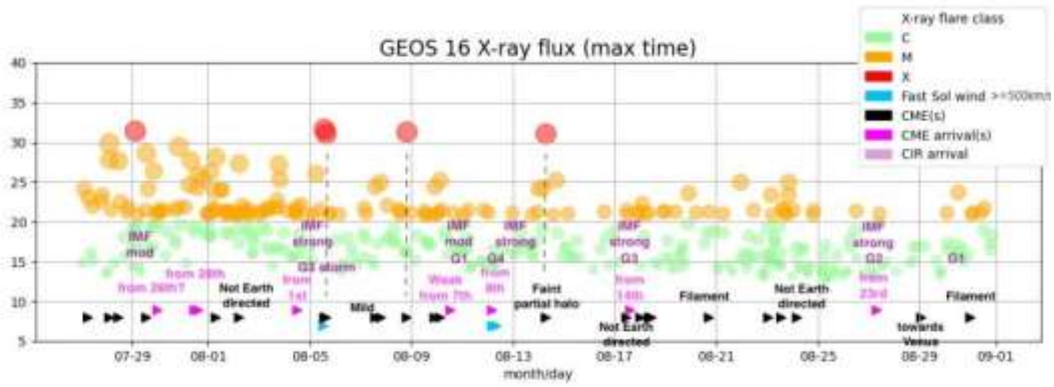

There were plenty of thunderstorms around the UK in August, Mark Prescott seeing one on the 1st. It has created a small increase in his Muon counts. This sits in the middle of a period of lower counts during the high density of M-flares in late July / early August. The large magnetic storm starting on the 11th produced a drop in the muon count lasting four days. There are also some small drops matching other minor magnetic activity.

PERSEIDS

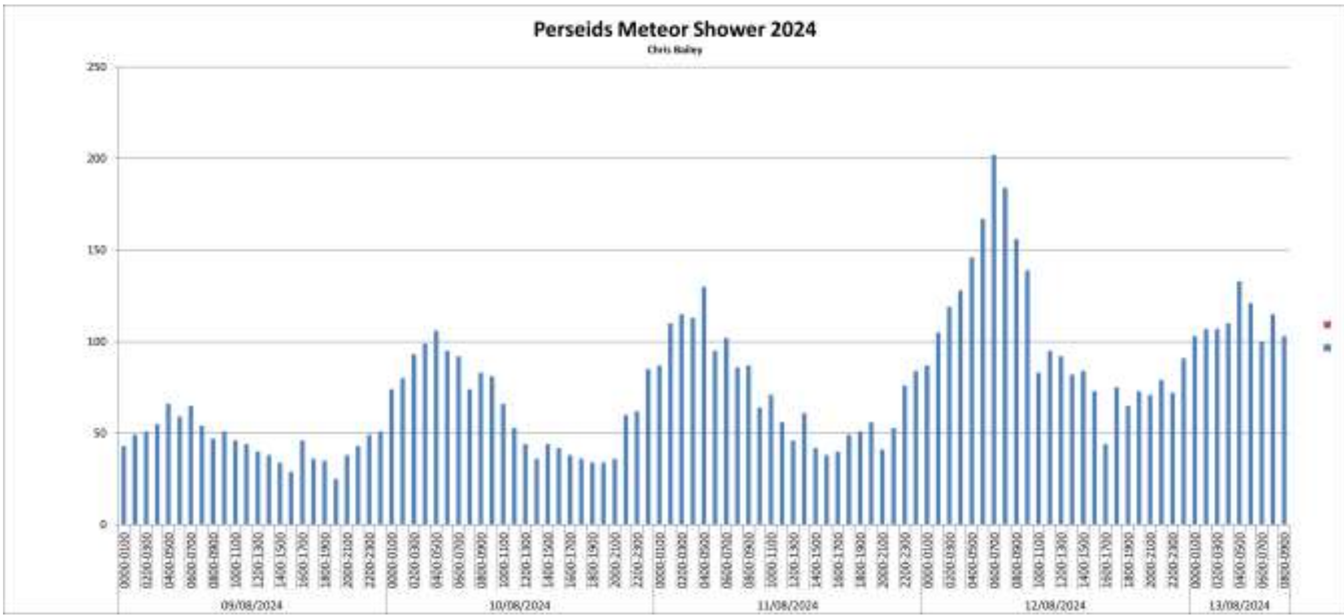

Chris Bailey's chart of Perseid echoes runs from the 9th to 09:00UT on the 13th. There is a clear peak between 06 and 07UT on the 12th. The afternoon and evening counts are also fairly high, much as predicted in the BAA handbook. Counts were also quite high in the early hours of the 11th and 13th.

The weather was generally nice and warm on the night of the 12th, so I was able to make a visual count between 22:00 and 23:00, seeing 7 Perseids (plus a few satellites and aeroplanes!) looking to the northeast away from the worst of the local lighting. I was also aware of a faint auroral glow at the time, an unexpected addition from the strong magnetic storm. Observers from my local library astronomy group had similar counts.

A late report from Nick Quinn includes the mild magnetic disturbance at the end of August:

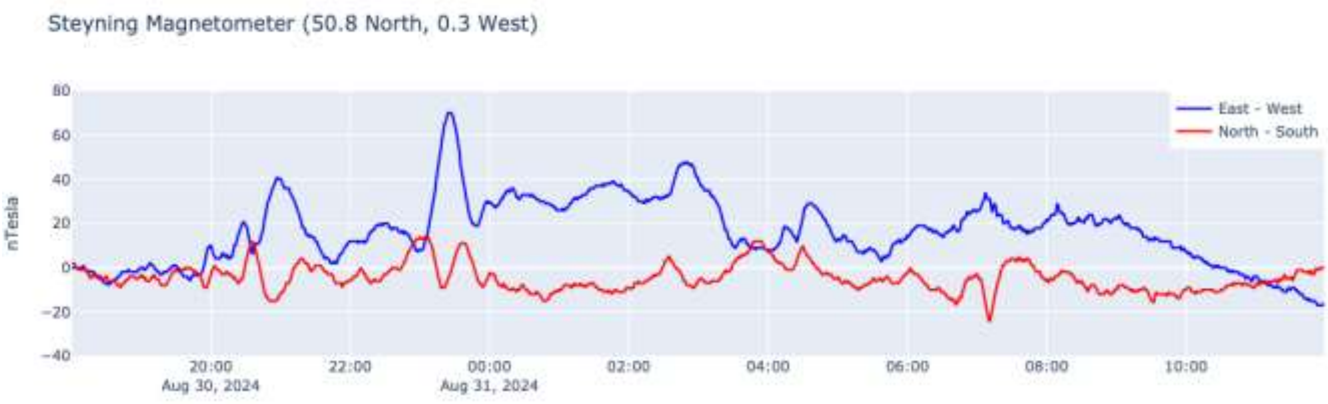

BARTELS CHART

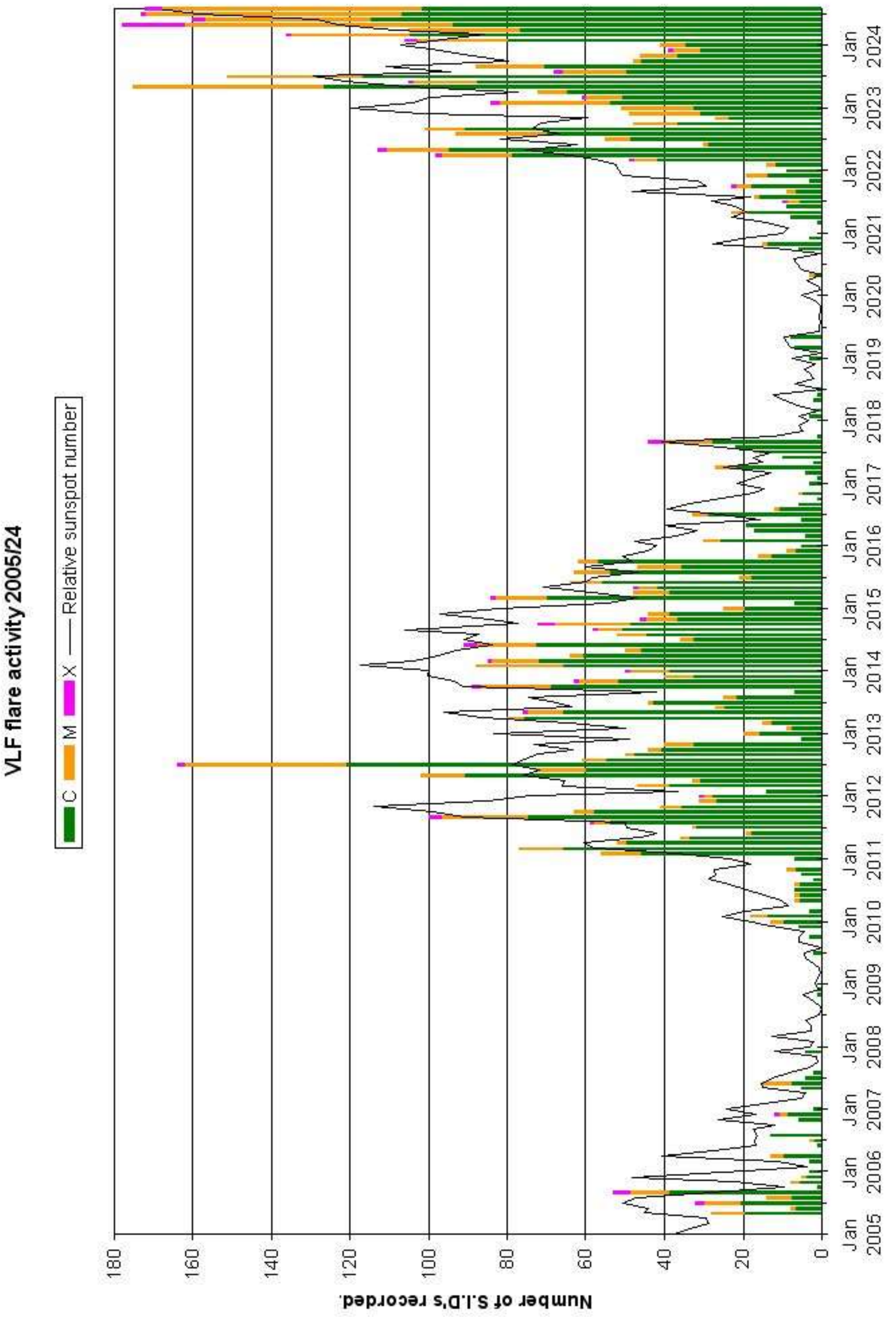
VLF flare activity 2005/24
C
M
X
Relative sunspot number
Number of S.I.D's recorded.
0
20
40
60
80
100
120
140
160
180
Jan 2005
Jan 2006
Jan 2007
Jan 2008
Jan 2009
Jan 2010
Jan 2011
Jan 2012
Jan 2013
Jan 2014
Jan 2015
Jan 2016
Jan 2017
Jan 2018
Jan 2019
Jan 2020
Jan 2021
Jan 2022
Jan 2023
Jan 2024

BAA RA Section programme 2024

British Astronomical Association
Supporting amateur astronomers since 1890
Radio Astronomy Section


Director: Paul Hearn

The Radio Astronomy Section aspires to encourage and support the construction of radio telescopes by amateurs, their use for observing programmes, and the development of a deeper understanding of the science underlying what is being observed. Programmes can be aimed at any radio astronomical phenomenon, at any radio frequency. This encouragement will be through the operation of continuing group programmes, and through building communication and information exchange between individuals and groups pursuing their own projects. The main purpose of the Group is to act as a reservoir and clearing house for information on radio telescope design, construction and debugging, and how to use these instruments effectively. This will include the discussion of observing techniques and data analysis. Members should be able to exchange ideas, give advice and help each other. Establishing a pool of design information and software suitable for use in observing and data processing is a priority.

BAA Radio Astronomy Section Seminar programme.

Cosmic ray muon measurement at a global scale and the associated applications

Professor Xiaochun He - Department of Physics & Astronomy, Georga State University

Friday 1st November 19:30 (19:30 UTC)

The development of a global network for Cosmic ray muon detection is described. The focus of the presentation will be on the detector development and the expansion of the detector network worldwide which will be mainly used for monitoring the dynamic changes in the space and terrestrial weather in real-time at global scale.

Binary Stars and Stellar Cannibalism

Dr. Noel Castro-Segura University of Warwick Astronomy and Astrophysics Group

Friday Nov 8th 19:30 BST (19:30 UTC)

Stars are the building blocks of the universe. The majority of the stars in our galaxy spend their lives associated with a stellar companion, bound by the gravitational pull between them. The population of so-called binary stars encompasses up to 80% of the stars in the galaxy, and approximately half of these systems have an orbital period short enough to induce mass transfer between the two celestial objects at some point in their evolution.

Many of these interacting binaries contain a compact stellar remnant, which accretes material stripped from the surface of its companion star, thus providing an ideal laboratory to study physical bodies with extreme gravity such as white dwarfs and neutron stars. Furthermore, they offer a unique opportunity to infer the presence of one of the most exotic objects in the universe: black holes. This allows us to learn how they interact with their environment while shaping the universe we observe.

Here, I will review the basics of binary evolution and provide an overview of the phenomena observed in these systems. Additionally, I will highlight how amateur astronomers and citizen scientists can contribute to advancing science.

SARA are always invited, anyone not on the mailing list can contact me – paul@hearn.org.uk

Videos

- Python for Muons #4 – Presenting findings using Jupyter notebooks and the web.
  2024 May 16
- SKA precursors, the Zooniverse and some machine learning...
  2024 May 7
- Python for Muons #3 – Analysis & Charting muon data using python.
  2024 May 7
- Python for Muons #2 – Reading muon data using python.
  2024 Apr 23
- The October 14, 2023, Solar Eclipse Effects on VLF Radio Propagation Observed in Alaska
  2024 Apr 16

More Videos

- Contact the Director

Section Pages

- RAZoom Programme 2024
- Radio Astronomy Basics
- Current Projects Observations
- VLF Archive Reports - 2005-2024
- BAA RA Zoom Conference Meetings Archive
- BAA RA Training Workshops & Archive
- BAA RA 21 Day Conference - Saturday, 2021, October 16 - 10:00 to 17:00
- Resources
- Archived RAGazine and Circulars
- Muon Project

The Byte – Marcus Fisher

The BYTE Society of Amateur Radio Astronomers Bimonthly Journal	01010011 01101111 01100011 01101001 01100101 01110100 01111001 00100000 01101111 01100110 00100000 01000001 01101101 01100001 01110100 01100101 01110101 01110010 00100000 01010010 01100001 01100100 01101001 01101111 00100000 01000001 01110011 01110100 01110010 01101111 01101110 01101111 01101101 01100101 01110010 01110011

This section of the bimonthly SARA journal focuses on system software applicable for amateur radio astronomy (RA). Given that it is SARA's mission to facilitate the flow of information, promote observing programs, enhance the technical abilities of its members, to name just a few, we feel it is pertinent to dedicate a section of the journal around software articles that enables our members and pushes us forward as a group.

Considering the entire radio astronomy landscape, from designing to building the systems, to making observations and controlling/tracking the objects being observed, to data processing and analysis various system software is utilized to help make our endeavors more efficient and effective. As such, we plan to use this section of the journal to report on software topics of interest such as:

- Programming embedded systems
- Programming languages
- Planning observations
- Control systems and tracking
- Data analysis and processing
- Testing software
- Use of Artificial Intelligence (AI) and Machine Learning (ML)

Please reach out to the vice president (vicepresident@radio-astronomy.org) if you are interested in contributing to this section of the journal or if you have specific requests for topics to be written about.

Software Topics:

- Cybersecurity Awareness Month (October) - understanding your security risks is important and can seem either overwhelming or you can be overly confident, "no way I can be hacked into". Here is a minimum set of activities for you to consider:
    - Create a digital footprint (aka network topology / network architecture), where you inventory all your digital assets, their locations, what they are connected to
    - Identify all ENTRY and EXIT points in your architecture … do not make any assumptions – a common issue I always find is rooted in the assumption that computer A is not connected or is "air gapped", so no one can "hack into it".
    - Conduct a basic threat assessment against your digital footprint that you created in the first step and apply a threat assessment model against it to understand potential vulnerabilities
        - STRIDE approach (https://en.wikipedia.org/wiki/STRIDE_model)
        - MITRE ATT&CK approach (https://attack.mitre.org/)
        - Additional tools can be used to automate scanning your systems looking for known vulnerabilities (Nessus, Nmap, OpenVAS) but at a minimum you should conduct a paper assessment against your system
    - Look at all your potential threats and consider what your mitigation strategies can be to buy down some of the risk
        - Example Threat - Content Injection where a bad actor gains access to your system not by getting you to click on a malware infested email but instead finds data-transfer channels somewhere in your network that can be hijacked or spoofed. For example,

where you are moving data from one system to another. In evaluating your network, look for avenues of data transfer and especially with external systems that you do not authenticate with.

    - Common attacks against Server Message Block (SMB) protocol to transfer files between systems utilizes some of the following mitigation strategies:
        - Utilizes segmented networks and encryption between segments
        - Restrict file transfers
        - Scan all file transfers
  - Install and utilize open-source intrusion detection tools
    - As an example - Snort (https://www.snort.org/)
- Something Embedded
  - Control Your Telescope Using Stellarium and Arduino (https://www.instructables.com/Control-Your-Telescope-Using-Stellarium-Arduino/)
    - Several control systems are available using Arduino, I believe we need an article evaluating all the different open-source projects that are out there.
  - Radio astronomers are adopting accelerated computing and AI on NVIDIA (https://blogs.nvidia.com/blog/seti-institute-ai-fast-radio-bursts/?ncid=em-even-345641-l8&nvweb_e=&mkt_tok=MTU2LU9GTi03NDIAAAGWEUNurbJCz6V6ch89y7GtMKI87zHD7KpfF6hKwcziwHsAL8J_tqvL6w1BB1aXv_s-WPzPI3cyOOtNta2pjAASbRinNTEqIN78xzwPcq1itss9qMzgLA)
  - Nvidia platforms are quite powerful, affordable and are a logical next step for the hobbyist after the Arduino and Raspberry Pi
    - https://developer.nvidia.com/embedded-computing
    - https://blogspot.tenettech.net/2019/09/13/interfacing-software-define-radio-sdr-with-nvidia-nano-jetson-development-kit/
    - https://developer.nvidia.com/embedded/community/jetson-projects/assisted_astronomy
    - https://www.rtl-sdr.com/gpu-accelerated-rtl-sdr-radio-interferometer-code-for-radio-astronomy/
- Some Software News
  - Mozilla released the Firefox 131.0.2 update in response to a zero-day vulnerability in the browser (https://www.pcworld.com/article/2485961/update-firefox-131-now-to-patch-a-critical-zero-day-security-flaw.html)
  - Python 3.13 was published October 7, 2024 … check out some of the new features (https://realpython.com/python313-new-features/)
  - Java Development Kit (JDK) 23 is Now Available (https://inside.java/2024/09/17/jdk-23-available/?elq_mid=258786&sh=1426924682118819229152423192 47&cmid=DEVT240613P00013C00004)
    - https://www.youtube.com/watch?v=ymuv5aUzWu0
  - Problems Quantum Computers Will (and Won't) Solve: (https://mailchi.mp/quantamagazine.org/why-colliding-particles-reveal-reality-2493261?e=cd5ca53eb3)
  - PyCharm vs Jupyter Notebook (https://blog.jetbrains.com/pycharm/2024/09/pycharm-vs-jupyter-notebook/)
  - Planetary radio interferometry and Doppler experiment as an operational component of the Jupiter Icy Moons Explorer mission (https://arxiv.org/abs/2408.14965)
  - SKAO Observation Execution Tool: Designing for concurrent, responsive observations (https://arxiv.org/abs/2407.17149)
  - PDR: The Planetary Data Reader (https://joss.theoj.org/papers/10.21105/joss.07256)

- Tutorial on web scraping using Python (https://www.geeksforgeeks.org/python-web-scraping-tutorial/)
- Workshop on Astropy (https://github.com/astropy/astropy-workshop)
- Top 5 Machine Learning Algorithms for Beginners (https://pub.towardsai.net/top-5-machine-learning-algorithms-for-beginners-cd380c7810f7)
- Beginning Exploratory Data Analysis (https://machinelearningmastery.com/from-data-to-insights-a-beginners-journey-in-exploratory-data-analysis/?utm_source=drip&utm_medium=email&utm_campaign=MLM+Newsletter+September+21%2C+2024&utm_content=5+Real-World+Machine+Learning+Projects+To+Build+%E2%80%A2+Concise+Guide+to+Feature+Engineering

- Compiled Listing of Astronomy Software (good sites to bookmark)
  - Astronomy Software (http://www.midnightkite.com/index.aspx?URL=Software)
  - NASA's High Energy Astrophysics Science Archive Research Center (HEASARC) Software Repository (https://heasarc.gsfc.nasa.gov/docs/software.html)
  - Sky and Telescope (https://skyandtelescope.org/astronomy-resources/astronomy-software-public-domain-freeware-and-shareware/)
  - Astronomy Online (https://astronomyonline.org/AstronomySoftware.asp)
  - Wikipedia list of software for astronomy research and education (https://en.wikipedia.org/wiki/List_of_software_for_astronomy_research_and_education)
- Remotely Operated Telescopes
  - Pictor Telescope (https://pictortelescope.com/)
  - Wikipedia list of radio telescopes (https://en.wikipedia.org/wiki/List_of_radio_telescopes)

This was the first publication of the software section for the journal. I am seeking ideas on what our members would like to see on a bi-monthly basis, please send me a note with suggestions.

Marcus Fisher (vicepresident@radio-astronomy.org)

Solar flare observations with a cantenna interferometer

by Vanessa Annika Schulz, June 2024

Introduction:

For radio-astronomers to reach a similar resolution of arcseconds as the optical and X-ray astronomers, they would need massive single-dish radio telescopes with a diameter of several kilometers. However, at the same time, they would like to keep the steerability of the telescope, which ultimately results in the 100 m diameter-limit of Greenbank and Effelsberg. Therefore, the idea of radio interferometry is to use several smaller dishes with large baselines to synthesize a large dish by using tens to hundreds of smaller, easy to manufacture dishes.

As a master thesis project, a simple East-West-transit-interferometer with variable baselines will be used to create a new lab course experiment for the University of Bonn at the Astropeiler Stockert e.V. The project is aiming to understand the basics of interferometry and how to handle data reduction with a simple and cost-effective setup.

In this project, the Sun will be studied at 1419 MHz at different E-W baselines aimed South. It is quite interesting to study the Sun as its radio emission can be complex since it shows variations on different timescales from ms to solar cycles. The Sun is currently in the 25th solar cycle since extensive recordings began in 1755 [10], it is expected to reach its maximum in July 2025 [1]. When nearing these maxima, the sunspot number and activity increases resulting in the observation of solar flares and coronal mass ejections. While at mm and cm wavelengths the flare emission is caused by incoherent gyrosynchrotron radiation mechanisms, at dm to m wavelengths the emission is caused by coherent plasma radiation. The transition between these two mechanisms ranges between 1 and 3 GHz, where this setup is operating [2].

Therefore, we were quite lucky, when we detected solar flares originating from sunspots AR13663 and AR13664 on May 8th and May 9th with our cantenna interferometer, especially since some of them were very energetic and connected to coronal mass ejections (CME) aimed towards Earth, resulting in northern lights which were visible in the night of May 10th to May 11th [3]. This allowed us to study the linearity of the system's response and the influence on the fringe period which is a measure of resolution.

In this article we will first present the setup of the interferometer. Afterwards, the X-ray results from the solar flare observations on May 8th and 9th will be explained. Finally, solar flare observations will be presented and compared to "normal" observations (quiet sun). Lastly, for one solar flare observation day (May 9th) the linearity of the system and the influence on the fringe period will be shown.

Interferometer Setup:

The setup consists of 3 "cantennas" (circular waveguides), which are put on a red 3D printed mount that is manually adjustable in both axes (azimuth and elevation). In addition, they all have a white 3D printed lid to protect it from weather. The advantage of these cantennas is a large opening angle allowing us to observe the Sun from morning to early evening (UTC roughly 6 to 17, which in our time zone is from 8 am to 7 pm). Therefore, one can already spot the variation in baseline, without moving the antennas, as we are observing with the projected baseline, which changes depending on the Sun's declination. For the observations presented here, the antennas were aligned towards South at a declination of 50°.

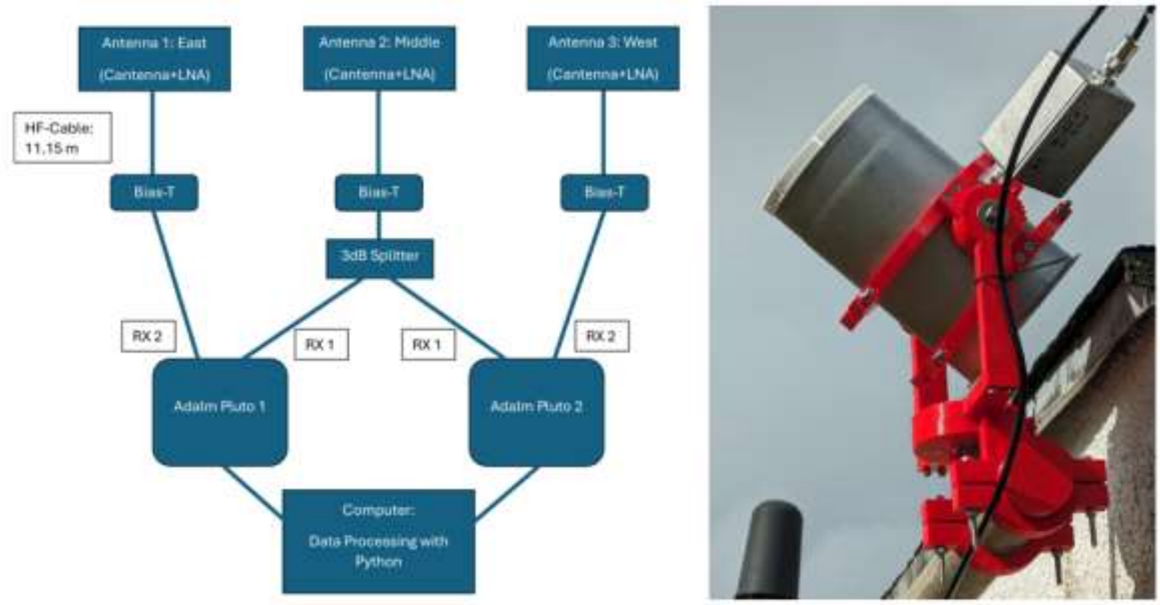

Figure 1: On the left, the interferometer setup is presented; on the right, one of the three cantennas on its 3D printed mount can be seen.

These cantennas are then put on a pipe, which is mounted to the backside of the garage at the Astropeiler site, so they can be easily moved along this pipe allowing to measure at different baselines. For the measurements performed here, 2 different baselines were available 2.2 m between the middle and West antennas and 7.7 m between the East and middle antennas. Directly connected to the antennas are the low noise amplifiers with integrated filters (Nooelec SAWbird+ H1 [6]). Then 3 equal lengths coaxial cables bring the signal back to the electronics box inside the garage. The signal of the middle antenna is then split (as the goal is to have 3 baselines available, but the two SDRs have a time offset, so the signals from the middle antenna need to be auto-correlated to estimate the time offset and correct for it), all these four signals are then connected to the two channel modified ADALM-PLUTO SDRs [7], which were set to observe at 1419 MHz with a bandwidth of 10 MHz on these observation days. These PLUTOs then send the complex power data (IQ-data) to the PC, where the signals are stored and processed.

In a python script, the following data products are calculated from the IQ-values: the power of each antenna, for each antenna set the vectorial addition of the signals (adding interferometer) and for each baseline the complex correlation. This results in a set of fringes (real and imaginary part), from which one can go on and determine the visibility, phase and fringe period.

Solar flares May 8th and May 9th: background to sunspots and flares:
On May 8th and 9th, sunspots AR13663 and AR13664 [3] were very active and responsible for the detected solar flares. In this section, some facts will be listed to these two sunspots on the observation dates [3]. On May 8th sunspot complex AR13663 consisted of 10 active sunspots and had a size of 400 millionths of a solar hemisphere (MH), while sunspot complex AR13664 showed 62 individual sunspots and had a size of 1200 MH. On May 9th complex AR13663 again consisted of 10 sunspots but spanned a smaller size of 300 MH and complex AR13664 had 81 active sunspots which had a size of 1090 MH. Sunspot region AR13664 was almost as big as the Carrington's sunspot

from August/September 1859, where a series of intensive flares and CMEs resulted in geomagnetic storms which set fire to the telegraph offices and sparked auroras from Cuba to Hawaii [3].

In the following, other radio and X-ray observations will be used to compare and analyze the data recorded with the cantenna interferometer. This can be done since there are different stations in the radio and X-ray regime that do solar observations to monitor and forecast Space weather and its influences on Earth.

To compare to X-ray data, the databank STIX [4] was used. They have a list for each day containing all registered and confirmed solar flares, mentioning the UTC of the peak and the intensity measured by GOES. GOES are Geostationary Operational Environmental Satellites operated by NASA and NOAA [8], which observe in soft X-ray regime (0.1 to 0.8 nm) and measure solar flare intensities. These solar intensities are classified into five categories according to [3]:

A: $10^{-8}\ W/m^2$; B: $10^{-7}\ W/m^2$; C: $10^{-6}\ W/m^2$; M: $10^{-5}\ W/m^2$; X: $10^{-4}\ W/m^2$

To validate the quality of our data recorded, radio observations at 1415 MHz from the Geodetic Observatory Wettzell [9] were used. Their focus is to analyze the impact of space weather on satellite navigation; therefore, they cover different frequency bands. They observe at 1415 MHz to study the influence on GNSS, which will be used here since it is the closest frequency available to ours. Their measured data already is calibrated offering us the solar flux in solar flux units (1SFU= 10 000Jy). [9]

Normal observation day:
To compare the solar flare observation to normal days, the measurement of the complex correlator for the 2.2 m baseline is illustrated here, where the fringes are better visible than the 7.7 m baseline fringes since they are very close together. The complex correlation consists of a set of fringes, the real and imaginary part, which are plotted in red and blue.

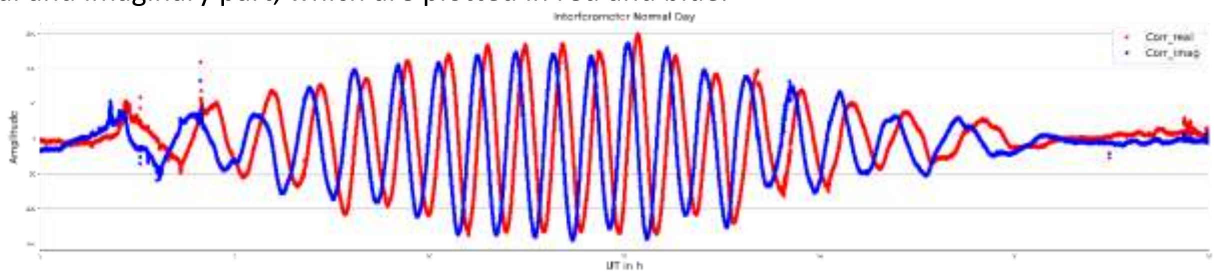

Figure 2: This plot shows the output of the complex correlator (red: real part and blue: imaginary part) for normal observation days for the 2.2 m baseline with time in UTC on the x-axis and amplitude in arbitrary units on the y-axis.

In this plot it is important to note that the maximum amplitude is at approximately 150 a.u. (arbitrary units). One can also see that the fringes at the beginning and end appear a little “wobbly”, this might be due to trees blocking the field of view in the morning and evening, when the sun rises or sets. In addition, the peaks are wider in the morning and afternoon than at noon, this is due to the Sun’s movement across the sky and the change in the baseline. In the morning and evening, the baseline is the shortest, which means we can observe a larger fringe period than at noon, when the baseline is the longest. This will be seen in a later plot when comparing the fringe period on normal days to the solar flare events.

Solar flares on May 8th:

On May 8th, during the observation time with the cantenna interferometer (UTC 6:00 to 16:00) 30 solar flares of different intensities were measured with GOES [4]. In the graph, in black the power signal of one antenna is visible, the colored dashed vertical lines illustrate the maximum of the X-ray detected solar flares with their peak intensity. Normally, the maximum power we measure is at about 2000 (unitless), but during one very intense flare at noon it goes up to almost 35000 (unitless), the flux of the sun normally ranges between 80 to 120 solar flux units (1SFU= 10 000Jy), but on May 8th it goes up to 32 000 SFU during an M8.7 flare at UTC 12:04, which was connected to a CME [3]. In general, one can note that not all these flares were detected by the cantennas, especially the flares in the afternoon after this very intense one, which have a much lower intensity. However, it is interesting to note that in the morning there were several flares of similar intensity as the early afternoon flares, which were detected. From this phenomenon, one can conclude that it is not a question of sensitivity if we can detect these smaller flares, but the emission processes for X-ray and radio flare detections differ. One can clearly note that the flare detection stops after the major flare causing a CME, while in the X-ray regime there are still some flares which also reduce in intensity over time.

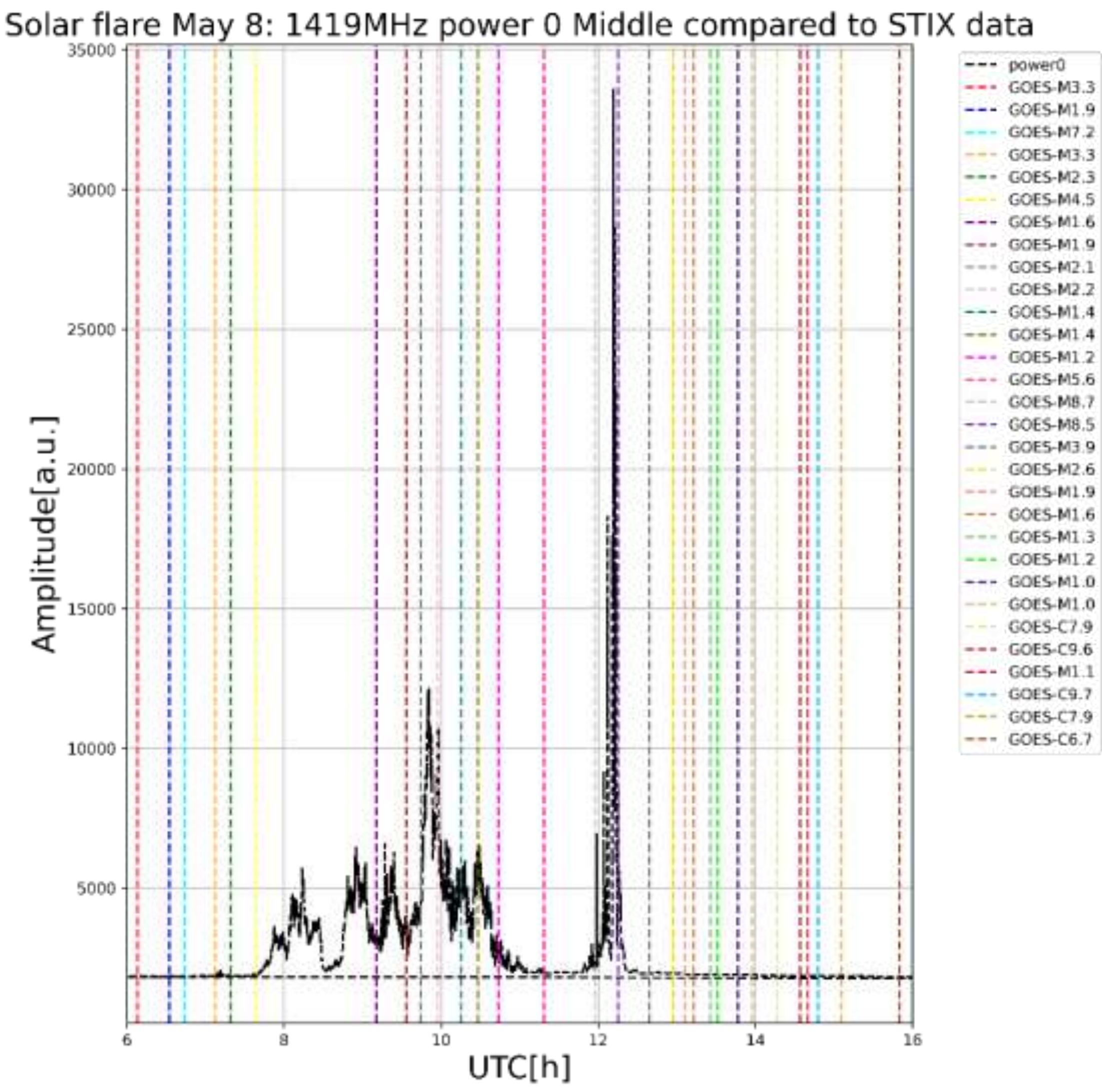

Figure 3: In black the power signal of the middle antenna is illustrated, the colored vertical dashed lines show the time maximum of the X-ray solar flares, the intensity can be seen in the legend on the right.

Solar flares on May 9th:

On May 9th, during the observation time with the cantenna interferometer (UTC 8:00 to 16:00) 29 solar flares of different intensities were measured with GOES [4]. Again, in the afternoon the intensity of the solar flares is lower than in the morning and these flares were not detected with the cantenna interferometer.

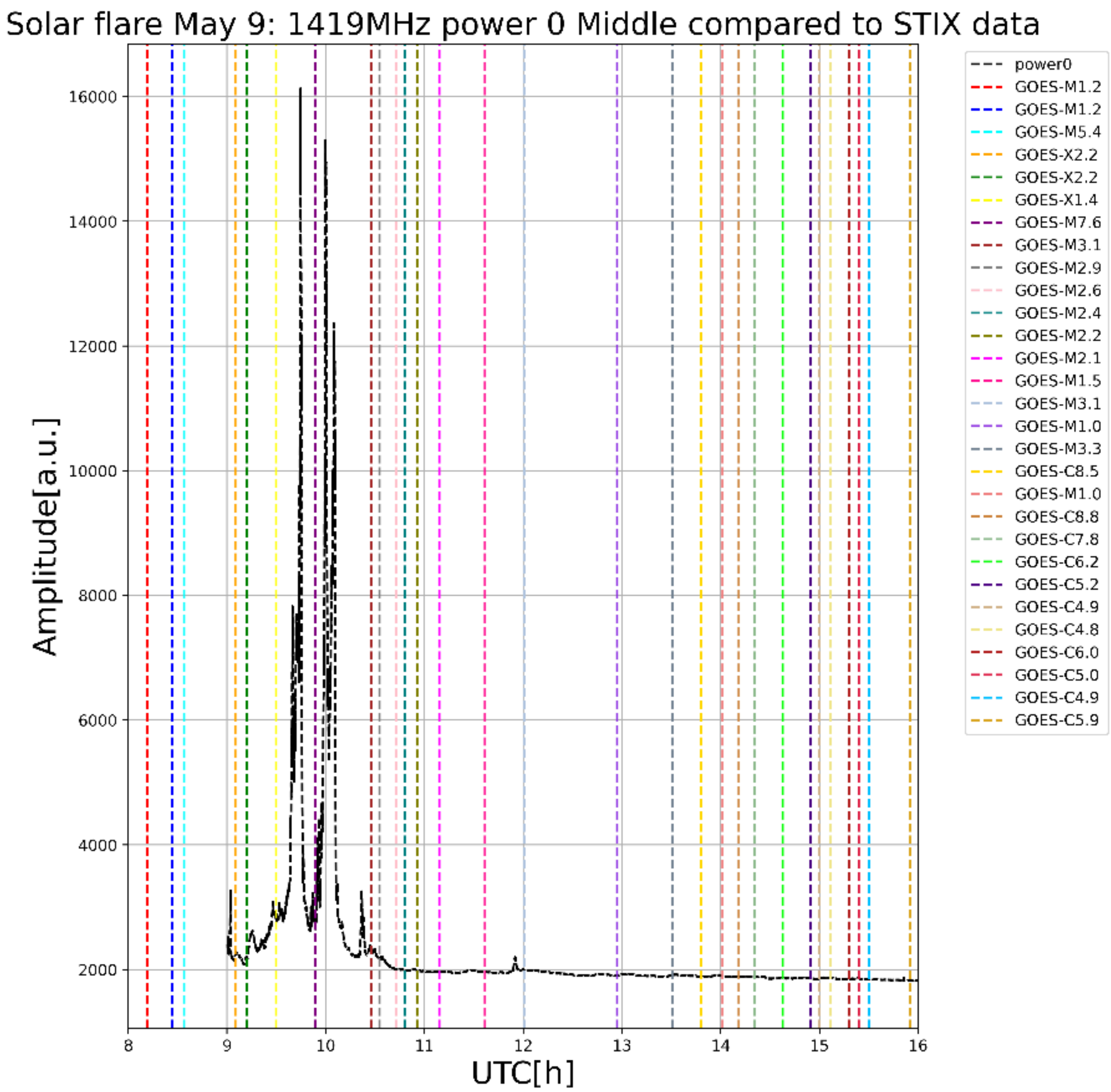

Figure 4: like Figure 3, the power signal of the middle antenna and the X-ray solar flare peaks are presented.

Linearity of the system:

These strong solar irradiation offers the unique opportunity to investigate the linearity of the interferometer's response across a wide flux range. In this part we no longer take the power signal of a single antenna, but the amplitude of the visibility from the fringe set, which can be obtained from the real and imaginary part of the complex correlator this way:

$$|V| = \sqrt{real^2 + imag^2}$$

In the plot, on the y-axis is the solar flux measured by the Geodetic Observatory Wettzell [9] and on the x-axis is the cantenna visibility data. In addition, the data points got a time stamp. We can clearly see that a linear function can be fit to the data (goodness of fit is described by $\chi^2_{red} = 16996$ and linear correlation coefficient by $r = 0.976$), however for high intensities, there is a large scattering, which might be due to the fact, that the timing between both observations did not match perfectly and we needed to define time bins with its corresponding mean intensities on both axes.

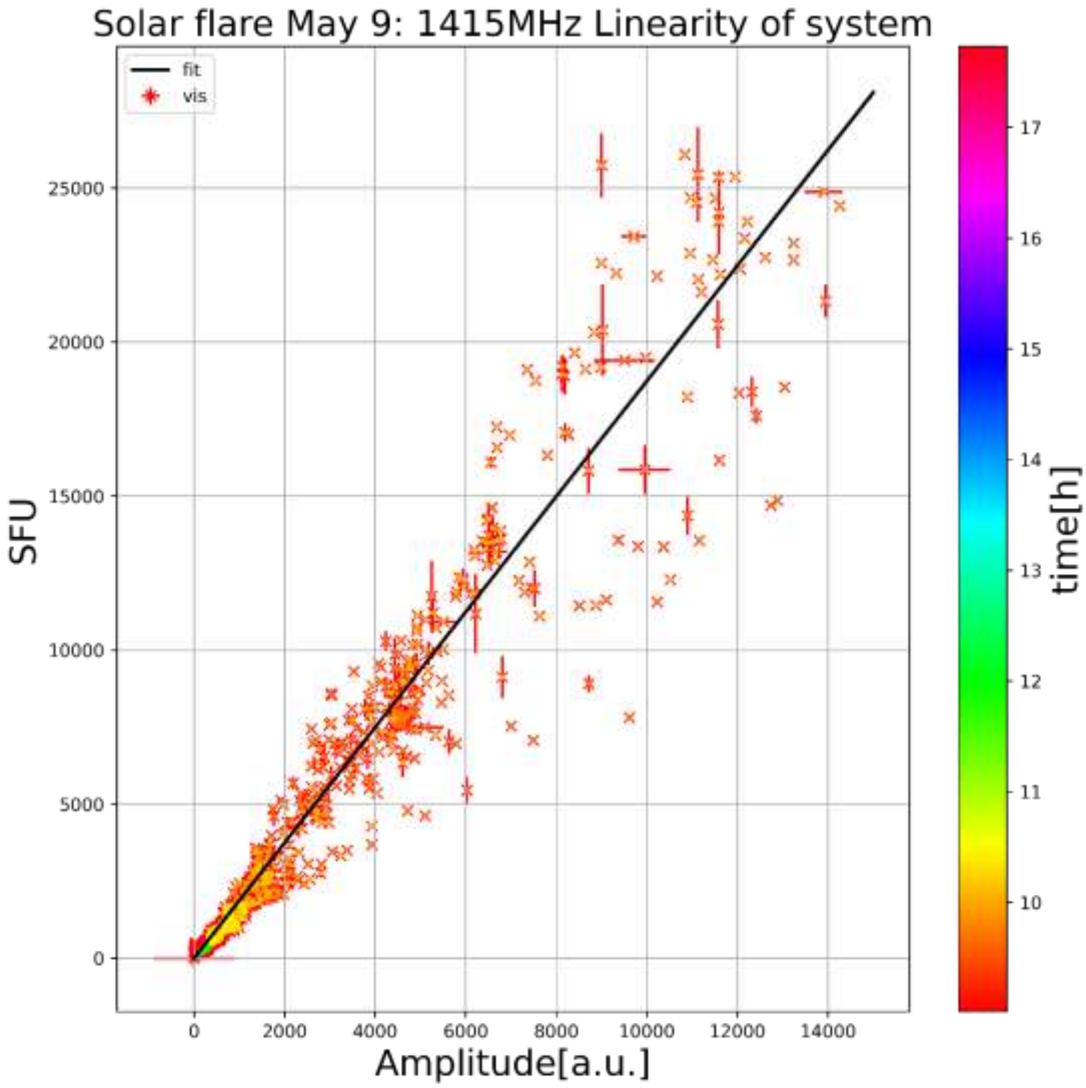

Figure 5: On the y-axis of this plot is the solar flux measured by the Geodetic Observatory Wetzell [9] against the amplitude of the visibility in arbitrary units (a.u.) on the x-axis highlighting the linearity of the interferometer's response.

Influence of solar flares on the fringe period:

As the fringe period is a measure for angular resolution, it is quite interesting to compare on the one hand side different baselines and on the other hand side solar flare events to quiet solar days. The fringe period can be deduced from either the real or imaginary part of the correlation, here the real part was used. The fringe period is taken as the time difference between two consecutive peaks. In the plot this is represented for both baselines. In brown the quiet solar day for the 2.2 m baseline and in green the solar flare day for the 2.2 m baseline is illustrated. In blue the quiet solar day for the 7.7 m baseline and in red the solar flare day for the 7.7 m baseline is presented. In black a fit curve is applied to the quiet solar observation days. This fit follows an inverse cosine function, as the natural fringe rate follows this relationship:

$$\nu_f = \frac{B}{\lambda}\omega_e \cos(\delta) \quad \text{and} \quad T = \frac{1}{\nu_f}$$

Where B is the baseline, λ the observed wavelength, ω_e the earth rotation and δ the declination of the observed object. In the plot we can clearly see the difference between the different baselines, for a smaller baseline the fringes are wider which ultimately results in a larger fringe period and therefore a rough resolution. For the 7.7 m baseline, we have much narrowly spaced fringe period and therefore higher angular resolution.

If we now want to compare the quiet solar days to the solar flare days, then one can see that the fringe period during ongoing solar flares differs from the brown or blue data set. However, there is no pattern detectable that the fringe period gets shorter or longer (and therefore the resolution improves or worsens) when solar flares occur, since there are deviations below and above the quiet solar data points. But one can draw the conclusion that we observed an object of a different size, i.e. the sunspot responsible for the flare.

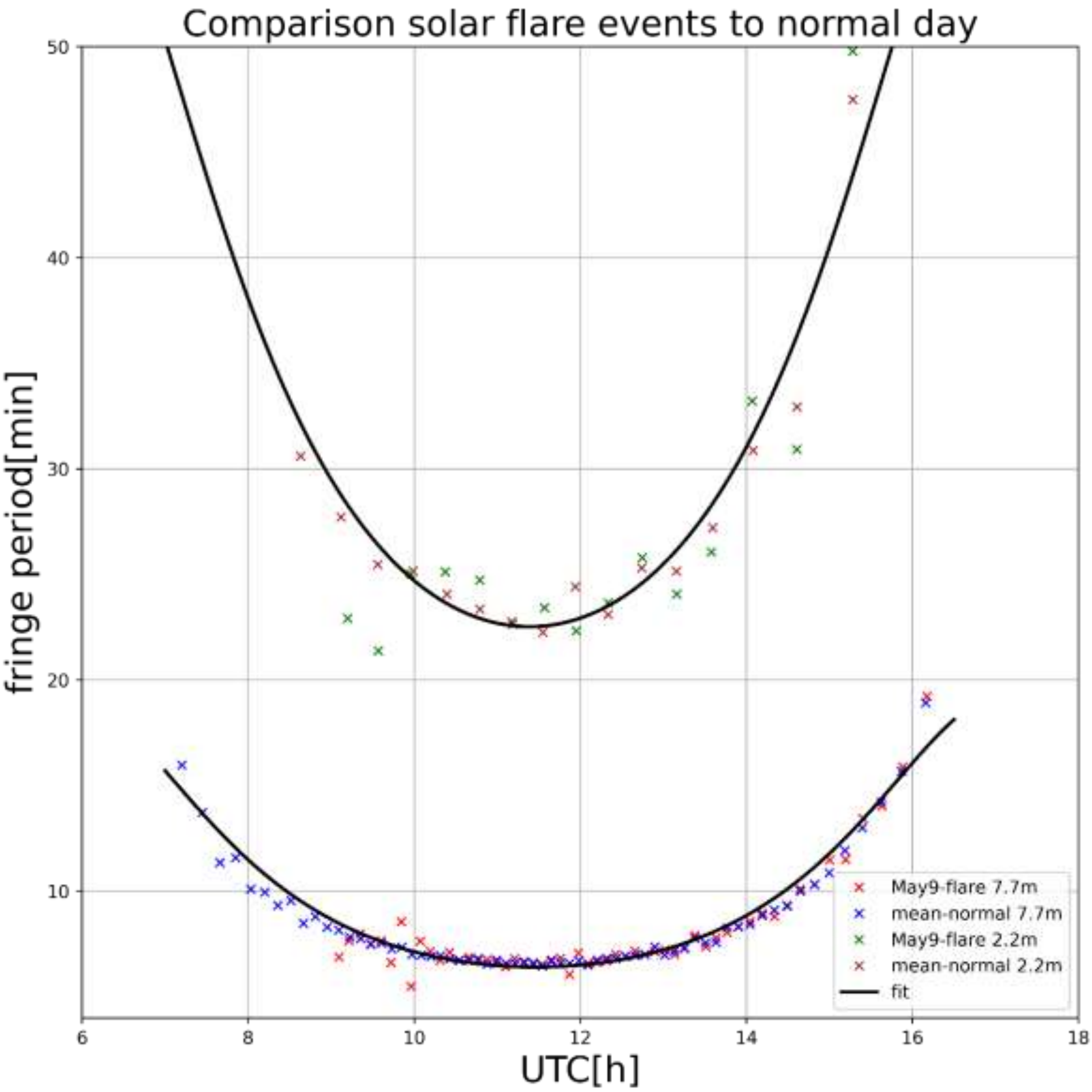

Figure 6: For two baselines (2.2 and 7.7 m) the change of the fringe period throughout one observation day and the impact of solar flares is illustrated.

Outlook:

These very intense solar flares allowed us to study the system's response and the influence of solar flare events on the fringes. We also observed smaller solar flares from April until June 2024, but their intensity and duration were weaker and shorter than the observations presented here, therefore no valuable information could be extracted from them. But since we are only at the starting of the maximum of the 25th solar cycle, it will be interesting to see whether there will be flares of similar or higher intensity.

References:

[1] Solar Cycle Progression, Space Weather Prediction Center NOAA, (June 2024) https://www.swpc.noaa.gov/products/solar-cycle-progression

[2] Vesselina Kalinova, Solar observations with the Small Radio Telescope, Bulgarian Astronomical Journal, Vol. 15, p. 107, 2011

[3] Dr. Tony Phillips, (June 2024) https://www.spaceweather.com/archive.php?view=1&day=08&month=05&year=2024https://xras.ru/en/sun_flares.html?m=5&d=8&y=2024 https://www.spaceweather.com/archive.php?view=1&day=09&month=05&year=2024

[4] Säm Krucker, G. J. Hurford, et al., The Spectrometer/Telescope for Imaging X-rays (STIX), A&A, volume 642 (2020), DOI: https://doi.org/10.1051/0004-6361/201937362

Hualin Xiao, Shane Maloney, Säm Krucker, et al.,The data center for the Spectrometer and Telescope for Imaging X-rays (STIX) on board Solar Orbiter, A&A in 2023, volume 673, A142, DOI: https://doi.org/10.1051/0004-6361/202346031

[5] Sunspot region 3664, major flares and CMEs!, (June 2024) https://www.spaceweatherlive.com/en/news/view/531/20240508-sunspot-region-3664-major-flares-and-cmes.html

[6] Nooelec (June 2024) https://www.nooelec.com/store/sdr/sdr-addons/sawbird/sawbird-h1.html

[7] Analog Devices (June 2024) https://www.analog.com/en/resources/evaluation-hardware-and-software/evaluation-boards-kits/adalm-pluto.html#eb-overview

[8] NASA, (June 2024) https://science.nasa.gov/mission/goes

[9] Federal Agency for Cartography and Geodesy, (May 2024), https://weltraumwetter.bkg.bund.de/#data-archive-access

[10] Peixin Luo and Baolin Tan, Long-term evolution of solar activity and prediction of the following solar cycles, Research in Astronomy and Astrophysics in 2024, https://arxiv.org/abs/2402.13173

Observation of G09.621+0.196 methanol maser 6.7 GHz

by Dimitry Fedorov UA3AVR

This report is about observations of G09.621+0.196 methanol maser 6.7 GHz in September 2024 with small single dish radio telescope 2.4 m. Detected line corresponds to the molecular transition $5_1 \rightarrow 6_0$, A^+ methanol molecule type, accurate frequency 6668.5192 MHz [1]. This maser belongs to class II, i.e. it is pumped to the inverse state by the infrared radiation from nearby objects. The maser is located in southern celestial hemisphere, RA 18:6:14, DEC –20:31:33 (J2000), and is seen from the observation site 55°46'00.5"N 37°49'25.8"E with low elevations (up to 14° over the horizon). This is strongest 6.7 GHz maser in the Galaxy and occupies top 1st position in the list of brightest masers 6.7 GHz by Eduard Mol [2].

More info about the maser

A typical spectrum from database [3] is shown at Figure 1, left. There are two lines (features) in the spectrum with different brightness (4000-6000 Jy and about 1000 Jy); they are positively correlated usually. The data shows relative stability of the maser, see a time plot for distinguished features at Figure 1, right; just periodic rises (flares) in the brightness up to 1000-2000 Jy are seen. Figure 1, right notes a multiplicity of distinguished features, but only two of them mentioned above dominate significantly and well seen on the spectra.

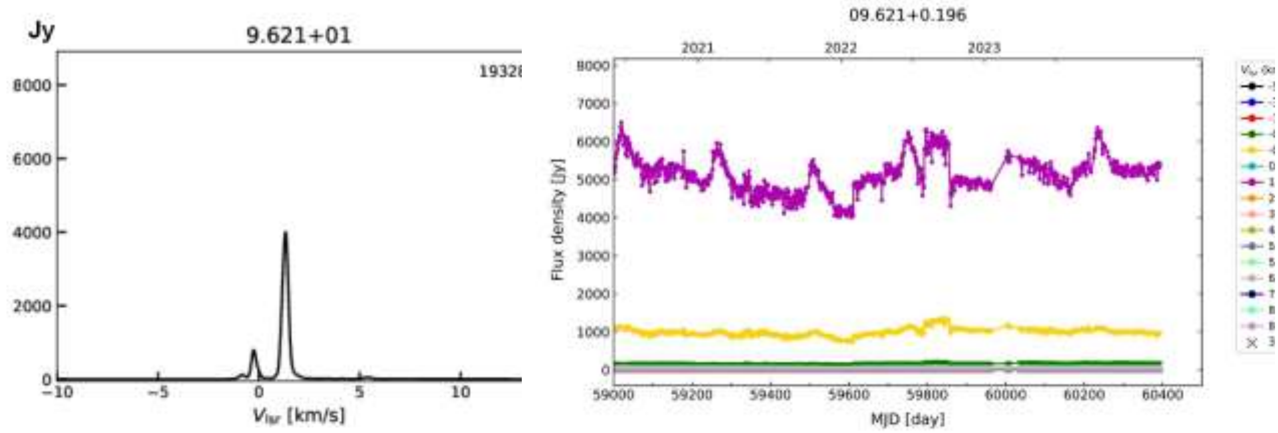

Figure 1. Ibaraki iMet data for G09.621+0.196 [3]: left – a typical spectrum, right – peak flux densities for lines (features) of the maser.

The maser belongs to class II; the methanol cloud is excited and pumped by infrared radiation from nearby stellar object or protostar. Evidences of excitation spots from the maser location in a wide wavelength range are shown on Figure 2; pictures were taken from [4]. The radiation of short mm-waves could excite the methanol molecules as well as shorter wavelengths radiation. Presence of short wavelength infrared spots indicates how hot exciting object is.

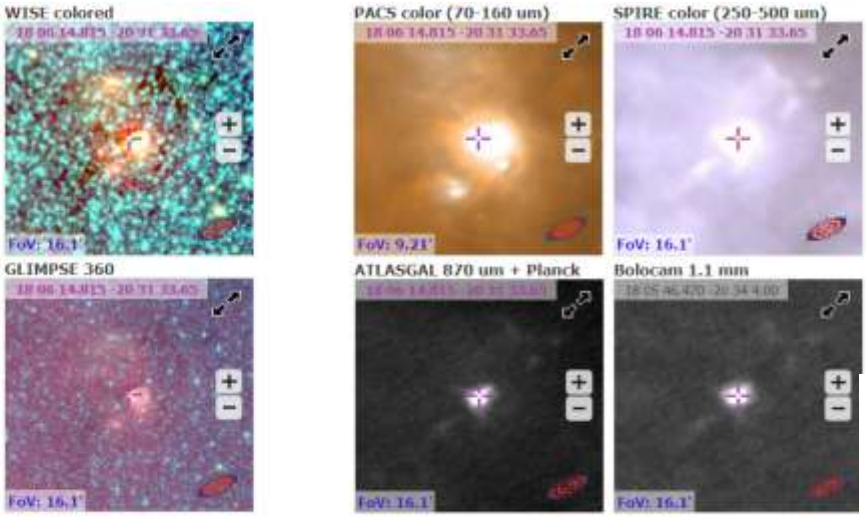

Figure 2. Seen radiation spots in the G09.621+0.196 location [4]; left – short wavelength infrared (WISE – up to 22 µm, GLIMPSE – up to 8 µm), right spots – long wave infrared, sub mm-waves, and short mm-waves.

Instrumentation

Observations at 6.7 GHz were made using 2.4 m small single dish telescope, see Figure 3.

Dish size: **D** = 2.4 m.

Telescope characteristics:

η_A = 0.65 – Aperture Efficiency by solar measurements [5] and Learmonth observatory solar data [6] interpolated to 6.7 GHz. Antenna Half Power Beam width δ_{HPBW} = 1.3° is comparable with the Sun angular size δ_{sun}=0.53°; hence, the Beam filling factor $=1-2\left(\frac{\delta_{sun}}{\delta_{HPBW}}\right)^2$ was included in calculations ([7], ch. 8.2.3 and [8]), dish sensitivity (forward gain) Γ = 0.001 K/Jy;

$\mathbf{T_{sys}}$ = 110 K – from Y-factor Moon measurements [9], $\mathbf{T_{sys}}$ = 120 K, obtained from known receiver NF and estimated spillover;

SEFD = $\mathbf{T_{sys}}/\Gamma$ = 112690 Jy (with $\mathbf{T_{sys}}$ = 120 K);

Minimal detectable peak flux density ≈ 113 Jy (RBW=2.5 kHz, 1 hour of integration).

Linear polarization.

Source automatic tracking during all the integration time (with F1EHN software).

Outdoor downconverter:

Terrasat 6.4-7.1 GHz RX module (LO 5.7 GHz) + LNA (NF=1.2 dB). Indoor IF receiver: USRP B200mini, receiver resolution – 2.5 kHz by noise bandwidth (about 0.1 km/s in velocity units), total receiver bandwidth – 1.5 MHz. The indoor IF receiver USRP B200mini is controlled using LabVIEW software with on-fly averaging of spectra (no intermediate data are stored), see more details about IF receiver and post-processing procedures in [10-12].

Figure 3. 2.4 m dish mounted on the roof of apartment building (55°46'00.5"N 37°49'25.8"E) with 6.7 GHz RX downconverter at the focus. The dish was designed by Sergei Zhutyaev RW3BP for mm-waves initially.

Results

Observed spectrum of the maser is shown at Figure 4. Integration time was 1 hour, but presence of the source is seen immediately on the receiver screen with less than 0.5-1 min of integration. It is possible the levels are underestimated in comparison to Ibaraki iMet data, see Figure 1 and [3].

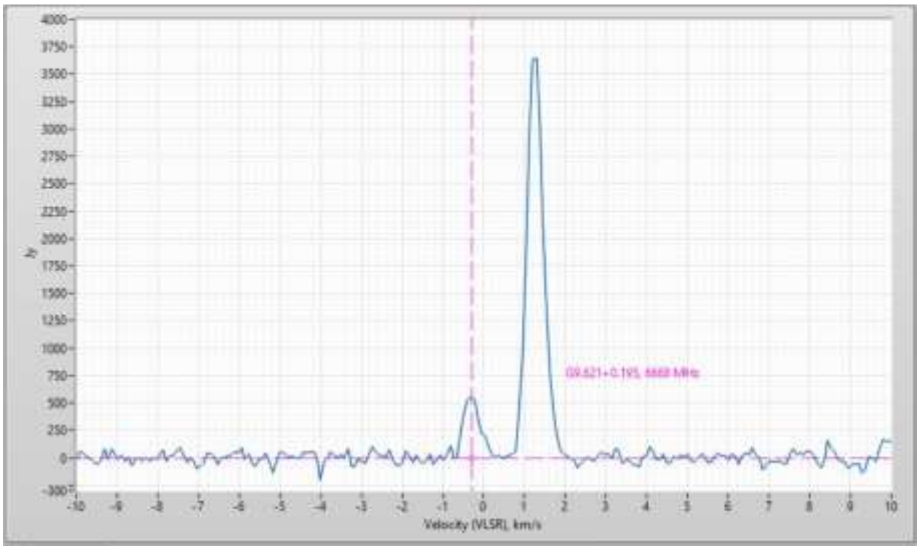

Figure 4. Observed G09.621+0.196 methanol spectrum 6.7 GHz, 2024-09-04, integration 1 hour.

Acknowledgments
A lot of thanks to Sergei Zhutyaev RW3BP for access to his 2.4 m dish, Figure 3 and valuable help in observations.

References

[1] H.S.P. Mueller et al, *Accurate rest frequencies of methanol maser and dark cloud lines*, arXiv:astro-ph/0408094 (2004).
[2] Eduard Mol, *Catalogue of the brightest astrophysical maser sources*, Radio Astronomy, Journal of the Society of Amateur Radio Astronomers, March – April 2023, page 90.
[3] Ibaraki iMet database, G09.621+0.196 data, https://vlbi.sci.ibaraki.ac.jp/iMet/data/9.621+01/.
[4] Database of astrophysical masers maserDb.net, object G9.621+0.195, https://maserdb.net/object.pl?object=G9.621+0.195.
[5] Wolfgang Herrmann, *Refurbishing an SRT, Part 4: Characterization and Observation Examples*, Radio Astronomy, Journal of the Society of Amateur Radio Astronomers, September – October 2022, p. 42.
[6] Learmonth solar observatory, radio flux, https://www.sws.bom.gov.au/Solar/3/4.
[7] T.L. Wilson, K. Rohlfs, S. Hüttemeister, *Tools of Radio Astronomy*, 6th ed, Springer, 2013.
[8] Joachim Köppen DF3GJ, *A Closer Look at Filling Factors*, DUBUS 4/2021, v 50, p 15.
[9] D. Fedorov UA3AVR, *System temperature Tsys by measurements the Moon radiation*, Radio Astronomy, Journal of the Society of Amateur Radio Astronomers, January – February 2024, p. 62.
[10] D. Fedorov UA3AVR, *Methanol maser lines 12 GHz observations*, Radio Astronomy, Journal of the Society of Amateur Radio Astronomers, September – October 2022, page 71.
[11] D. Fedorov UA3AVR, *Notes on building a maser receiver*, Radio Astronomy, Journal of the Society of Amateur Radio Astronomers, March – April 2024, p. 71.
[12] D. Fedorov UA3AVR, *Antenna unit for 6.7 GHz methanol maser telescope*, Radio Astronomy, Journal of the Society of Amateur Radio Astronomers, May – June 2024, p. 89.

About the author

Dimitry Fedorov was first licensed as radio amateur since 1982, as UA3AVR since 1983. In 1990 graduated as MS in electronics in Moscow Power Engineering University. Now works as research and development engineer in wireless industry, LTE/5G NR, RF and microwave modules development. Previous scientific experience in nuclear and particle physics, worked in Moscow State University, Institute of Nuclear Physics and Universität Tübingen, Institut für Theoretische Physik, see profile blog at https://www.researchgate.net/profile/Dimitry-Fedorov-2. Radio Astronomy hobby since 2012, mainly in applications for weak signals reception. You can contact the author at ua3avr@yandex.ru.

H1 Galaxy Observations Using the Green Bank 20 Meter Skynet Dish

By Jason Burnfield
18 October 2024

Observation Settings

- L-Band
- High Resolution
- 1 second "ON"
- 1 second "OFF"
- 10 repetitions for a total of 10 seconds each (for smaller signals I used 5 or 10 second intervals for a total of 50 or 100 seconds total)

This method of "on target" and "off target" data collection allows the empty sky near the galaxy in question to be used for a calibration reference which also removes almost all of the interference from the local Milky Way hydrogen signal because it is nearly the same for on and off target data sets so cancels out.

Here is a step-by-step explanation of how I made my observations using the 20 Meter Telescope

Open your browser and go to https://www.skynet.unc.edu.

Log-in using the SARA username and password which you can get by emailing Stephen Tzikas at: Tzikas@alum.rpi.edu.

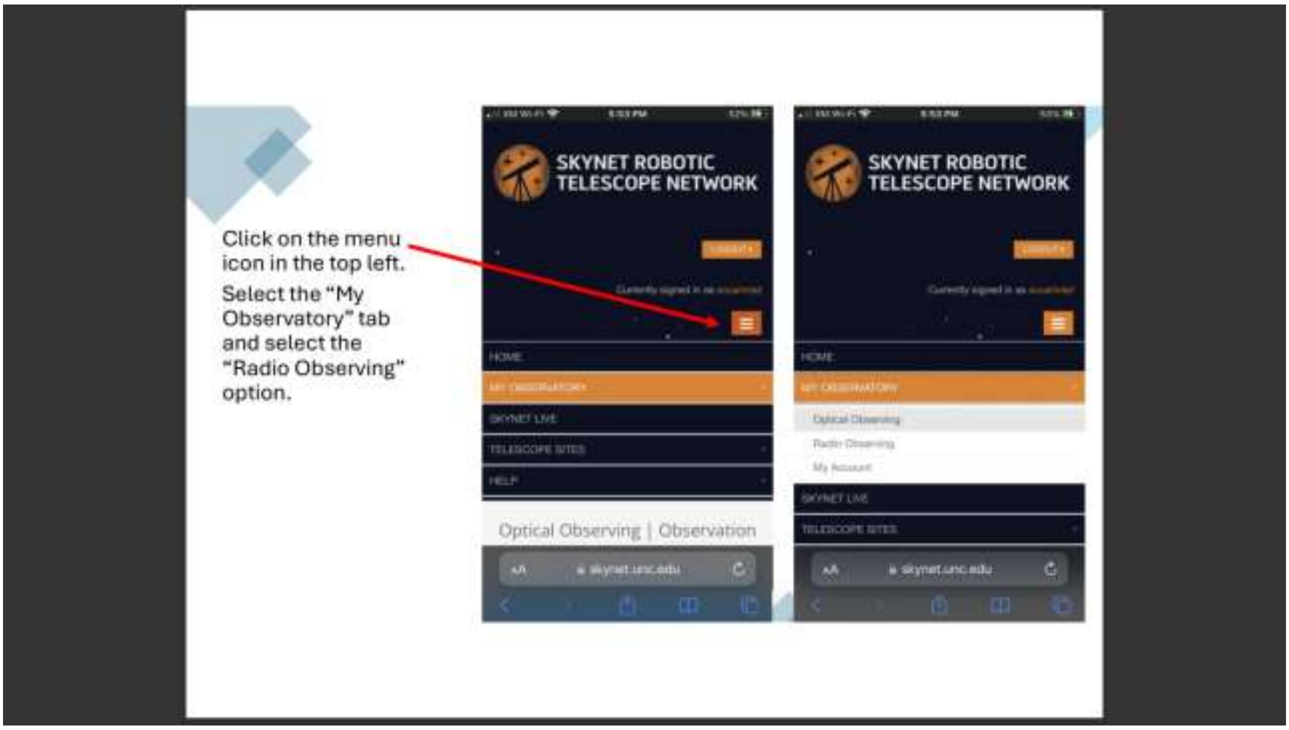
Click on the menu icon in the top left.
Select the "My Observatory" tab and select the "Radio Observing" option.
SKYNET ROBOTIC TELESCOPE NETWORK
SKYNET ROBOTIC TELESCOPE NETWORK
Optical Observing | Observation
skynet.unc.edu
skynet.unc.edu

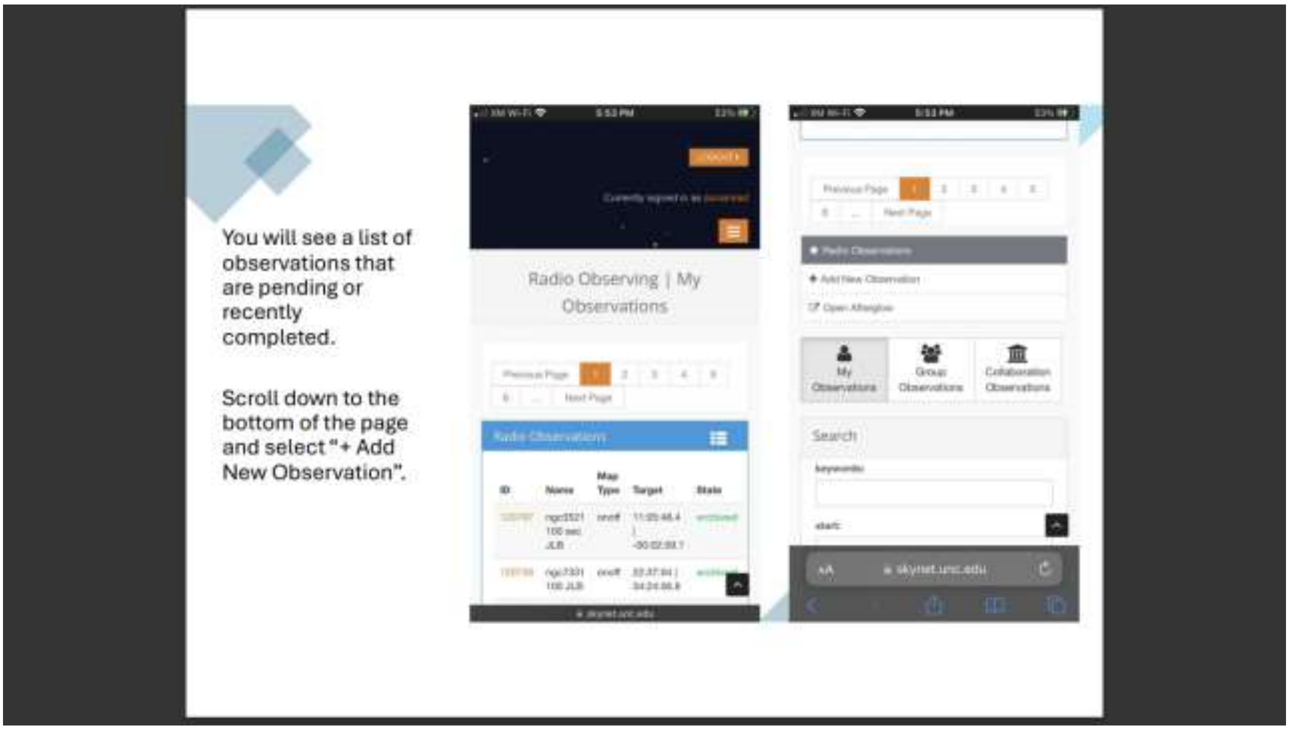
You will see a list of observations that are pending or recently completed.
Scroll down to the bottom of the page and select "+ Add New Observation".
Radio Observing | My Observations
Radio Observations
Search
skynet.unc.edu

Scroll down the page until you see the "keywords:" box and type in the designation or name of the galaxy you want to observe.

You can also enter coordinates exactly instead of using the keyword search.

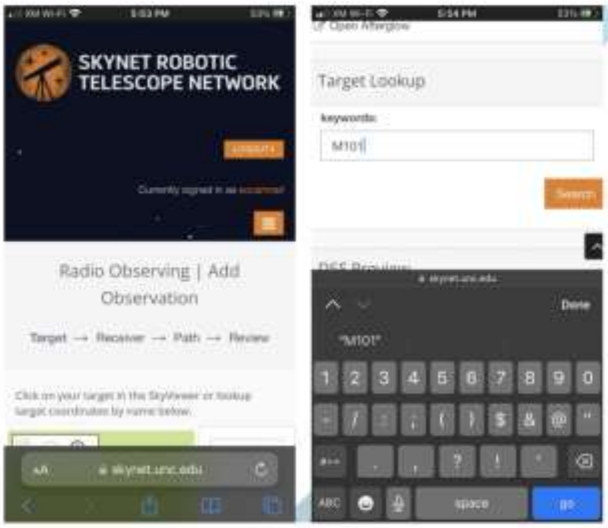

Scroll up to the top and you should see the coordinates already populated for the object you entered.

Edit the Observation Name to add your initials.

You can change the Min Sun Separation and Min Target Elevation as desired.

A chart will show when the object will be in range of the observation settings you selected.

Hit "Save and Continue" to go to the next screen.

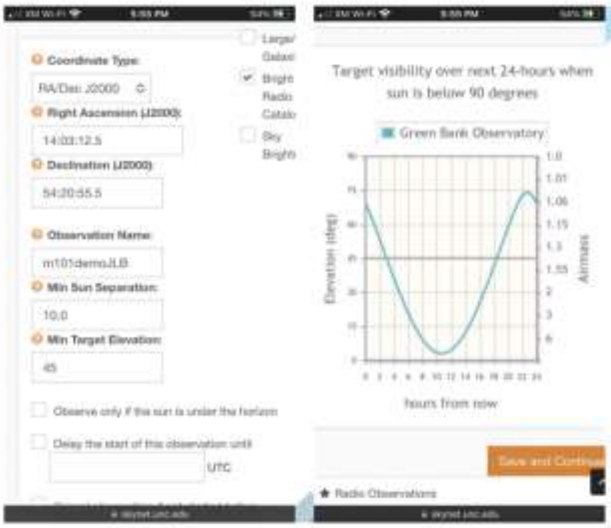

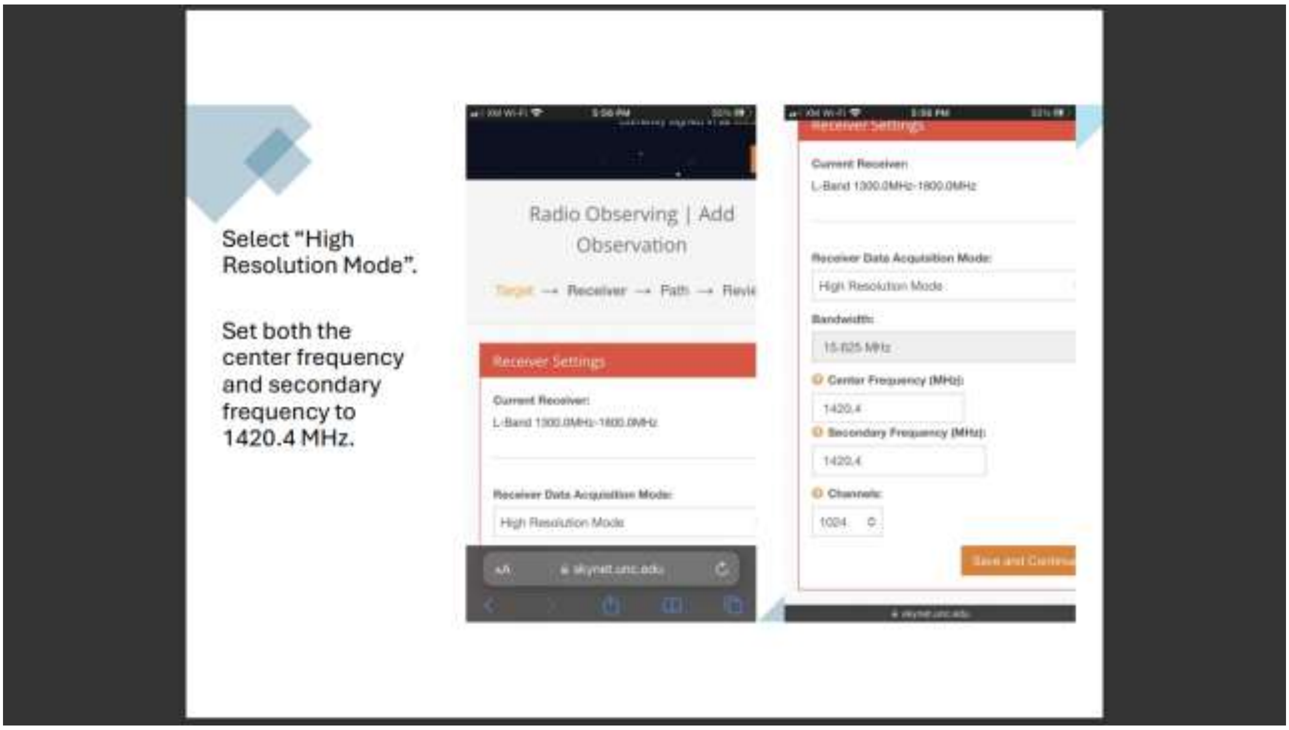
Select “High Resolution Mode”.
Set both the center frequency and secondary frequency to 1420.4 MHz.
Radio Observing | Add Observation
Receiver Settings
Current Receiver:
L-Band 1300.0MHz-1800.0MHz
Receiver Data Acquisition Mode:
High Resolution Mode
Bandwidth:
Center Frequency (MHz):
1420.4
Secondary Frequency (MHz):
1420.4
Channels:
1024
Save and Continue

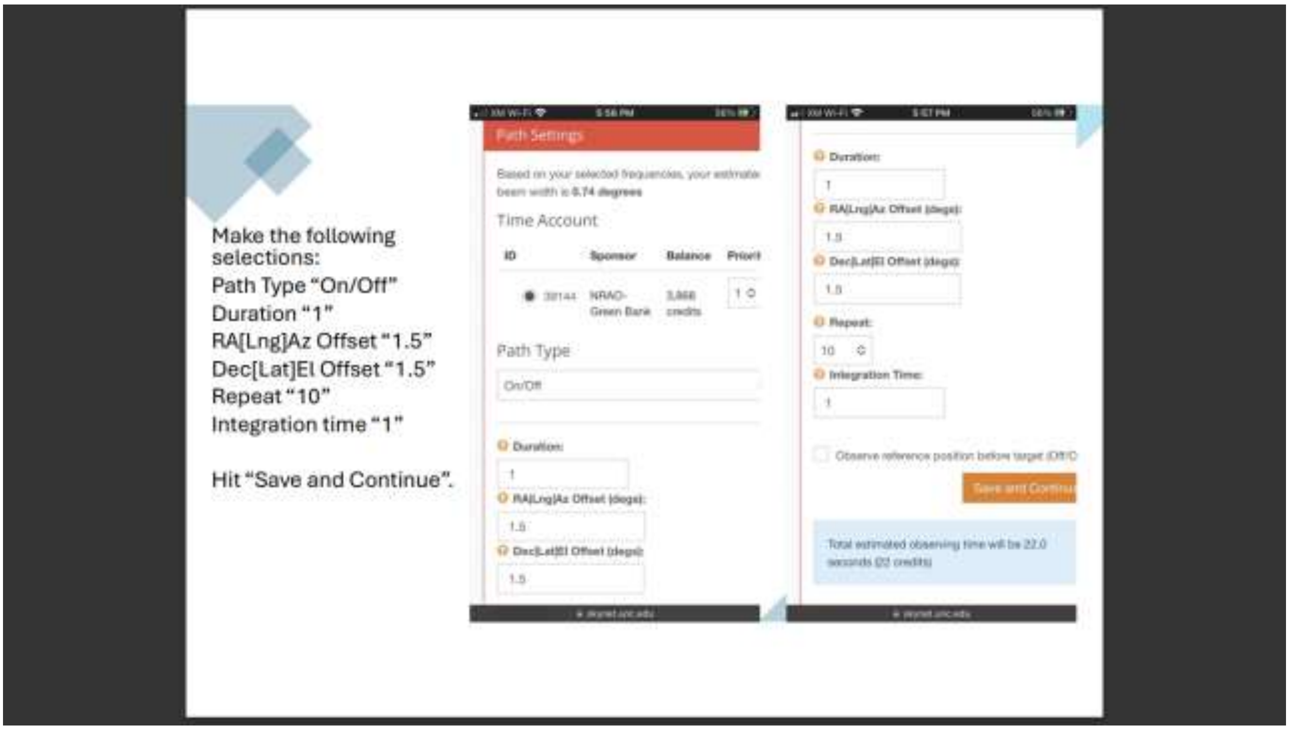
Make the following selections:
Path Type “On/Off”
Duration “1”
RA[Lng]Az Offset “1.5”
Dec[Lat]El Offset “1.5”
Repeat “10”
Integration time “1”
Hit “Save and Continue”.
Path Settings
Time Account
Path Type
On/Off
Duration:
1
1.5
1.5
Repeat:
10
Integration Time:
1
Save and Continue


Double-check all of your selections and if they look correct, hit "Submit".
Radio Observing | Add Observation
OBSERVATION NAME: m101demoJLB
COORDINATE TYPE: RA_DEC_COORD
RA|LNG|AZ: 14:03:12.4
DEC|LAT|EL: 54:20:55.5
MIN SUN SEPARATION: 10.0 degrees
MIN TARGET 45.0 degrees
DURATION: 1.0 secs
INTEGRATION TIME: 1.0 secs
REPEAT: 10 secs
TIME ACCOUNT: 39144 - NRAO-Green Bank
BALANCE: 3,868 credits
TOTAL COST: 22 credits
ENDING BALANCE: 3,846 credits

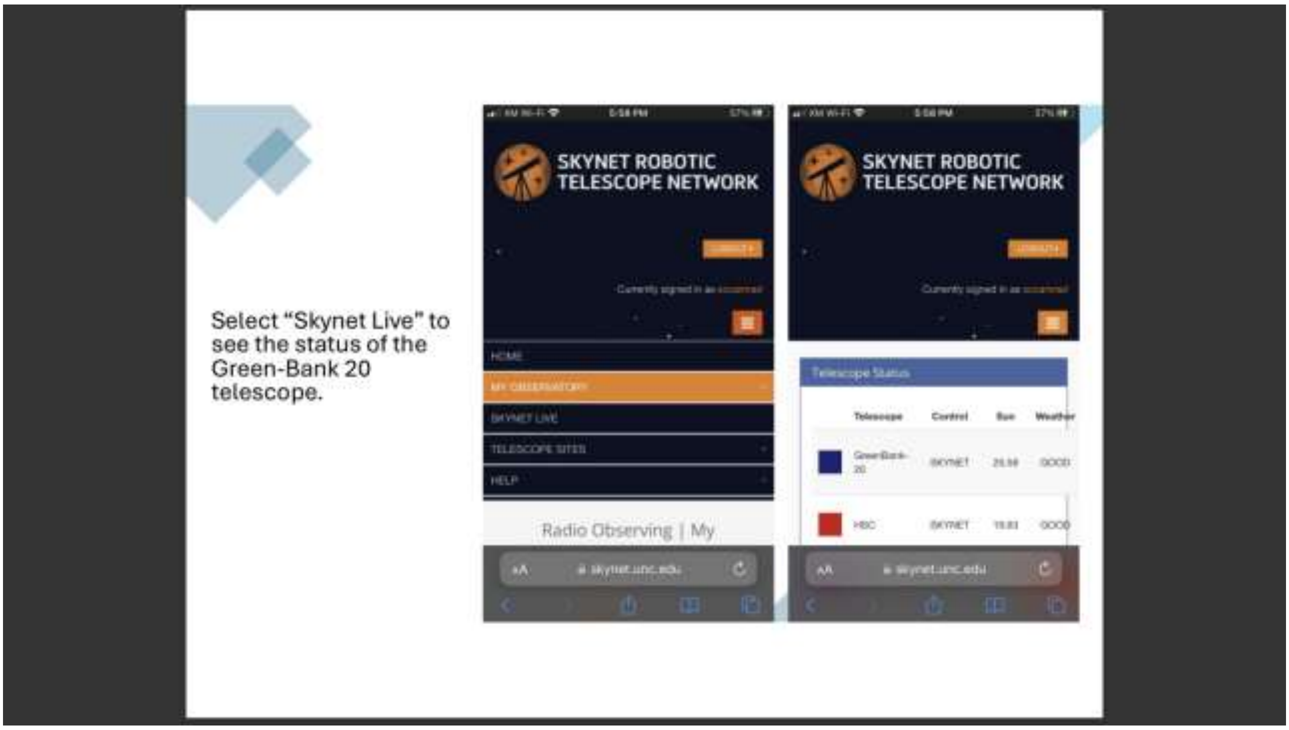
Select "Skynet Live" to see the status of the Green-Bank 20 telescope.
SKYNET ROBOTIC TELESCOPE NETWORK
SKYNET ROBOTIC TELESCOPE NETWORK
Radio Observing | My

From here, you can watch the observation status in progress.

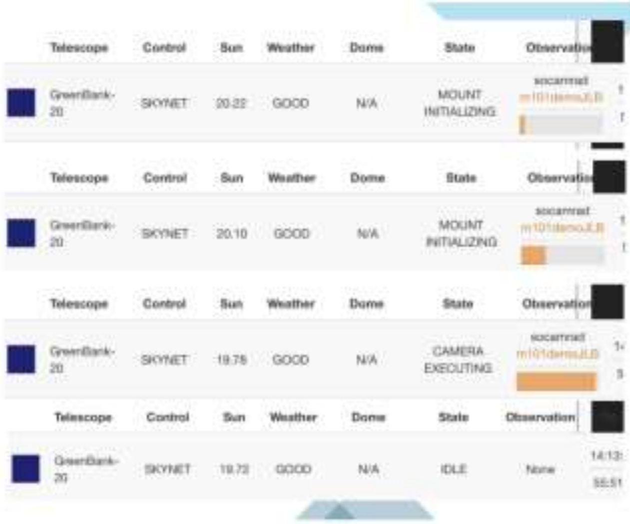

Select "Radio Observing" again and you will see that the status is "archived" which means your observation results are now ready to view and/or download.

When you click on the ID of the observation you will see a link to view and download your data.

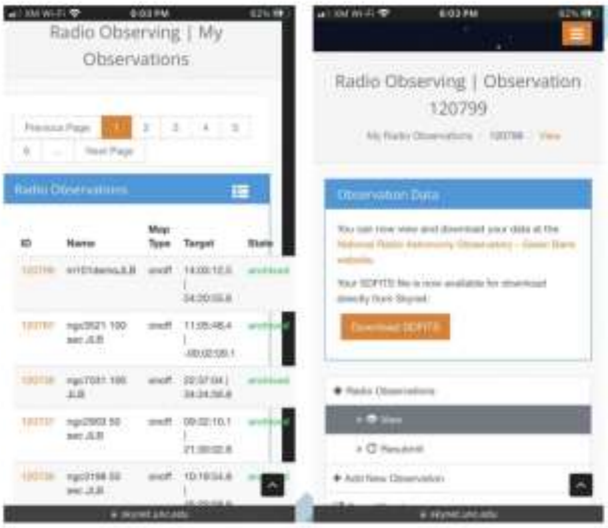

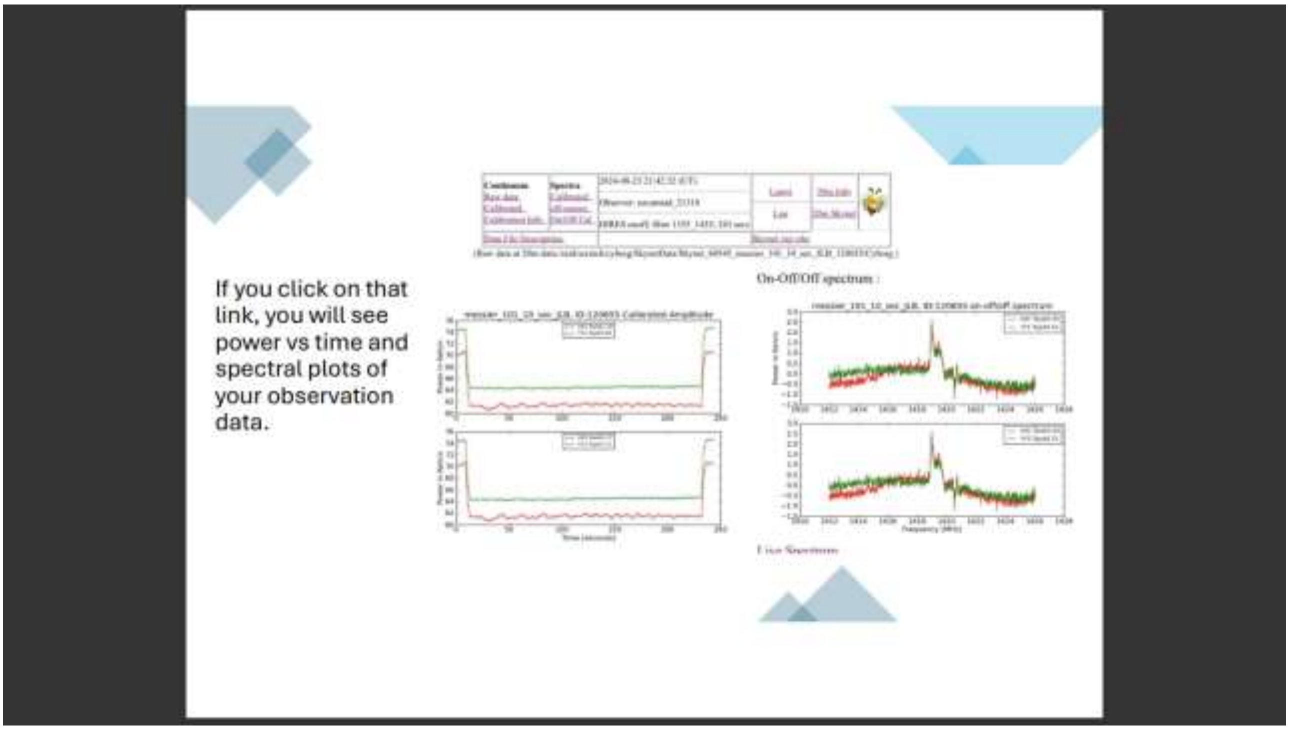
If you click on that link, you will see power vs time and spectral plots of your observation data.
On-Off/Off spectrum :

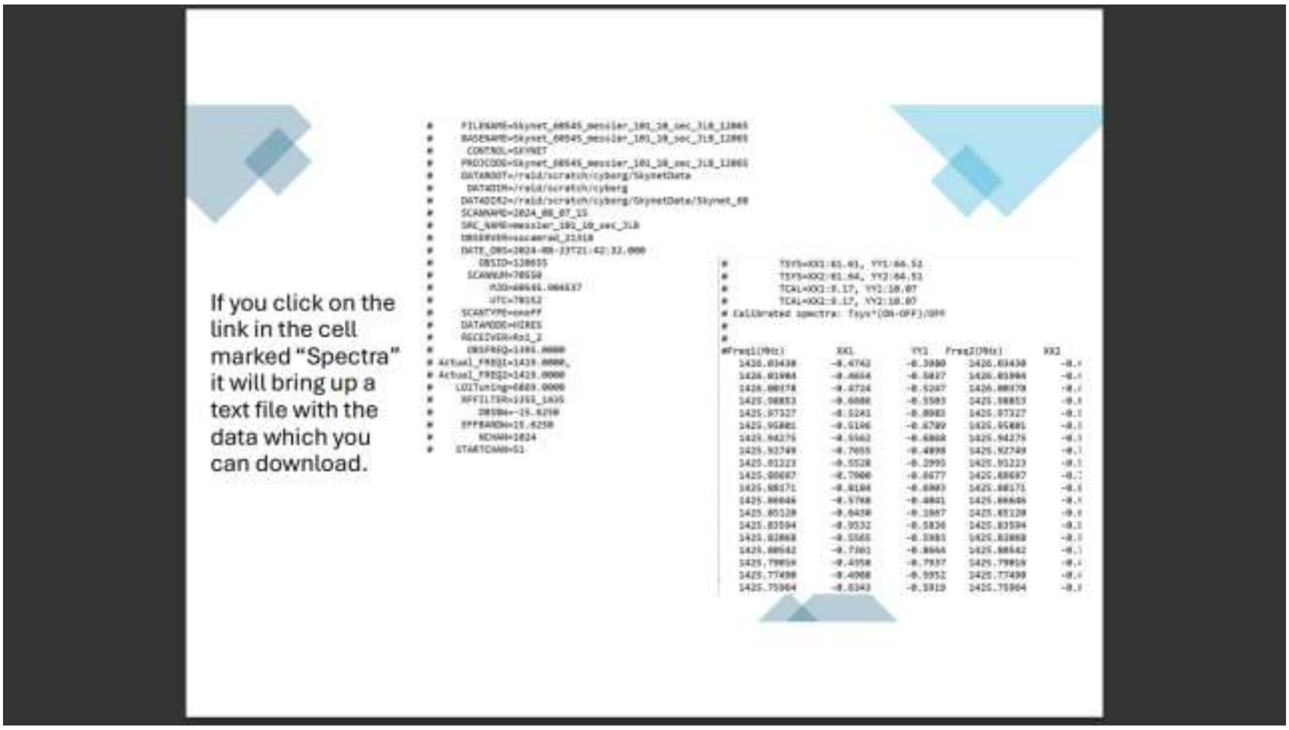
If you click on the link in the cell marked "Spectra" it will bring up a text file with the data which you can download.

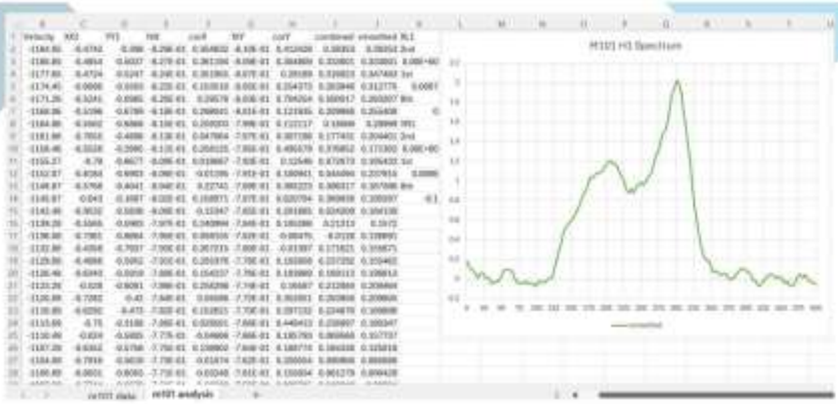

I dump my data results into an excel spreadsheet to flatten the background and display the resulting spectrum in a nice plot with velocity on the x-axis instead of frequency.

There are templates and user guides for my analysis spreadsheets available.

The following slides are hydrogen spectra from 30 nearby galaxies using the method I just described.

They are in order from strongest to weakest signal strength.

These spectra were verified using published spectral plots from professional surveys (cited at the end).

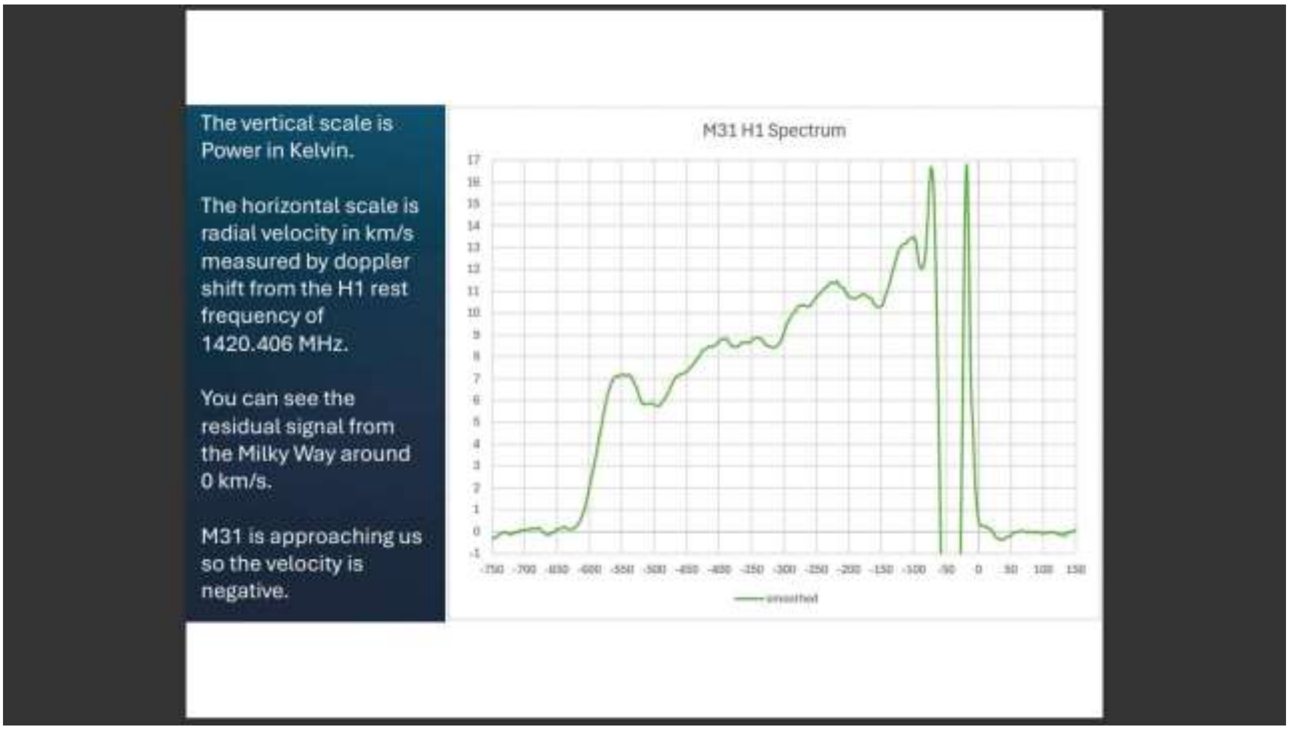
The vertical scale is Power in Kelvin.
The horizontal scale is radial velocity in km/s measured by doppler shift from the H1 rest frequency of 1420.406 MHz.
You can see the residual signal from the Milky Way around 0 km/s.
M31 is approaching us so the velocity is negative.
M31 H1 Spectrum
smoothed

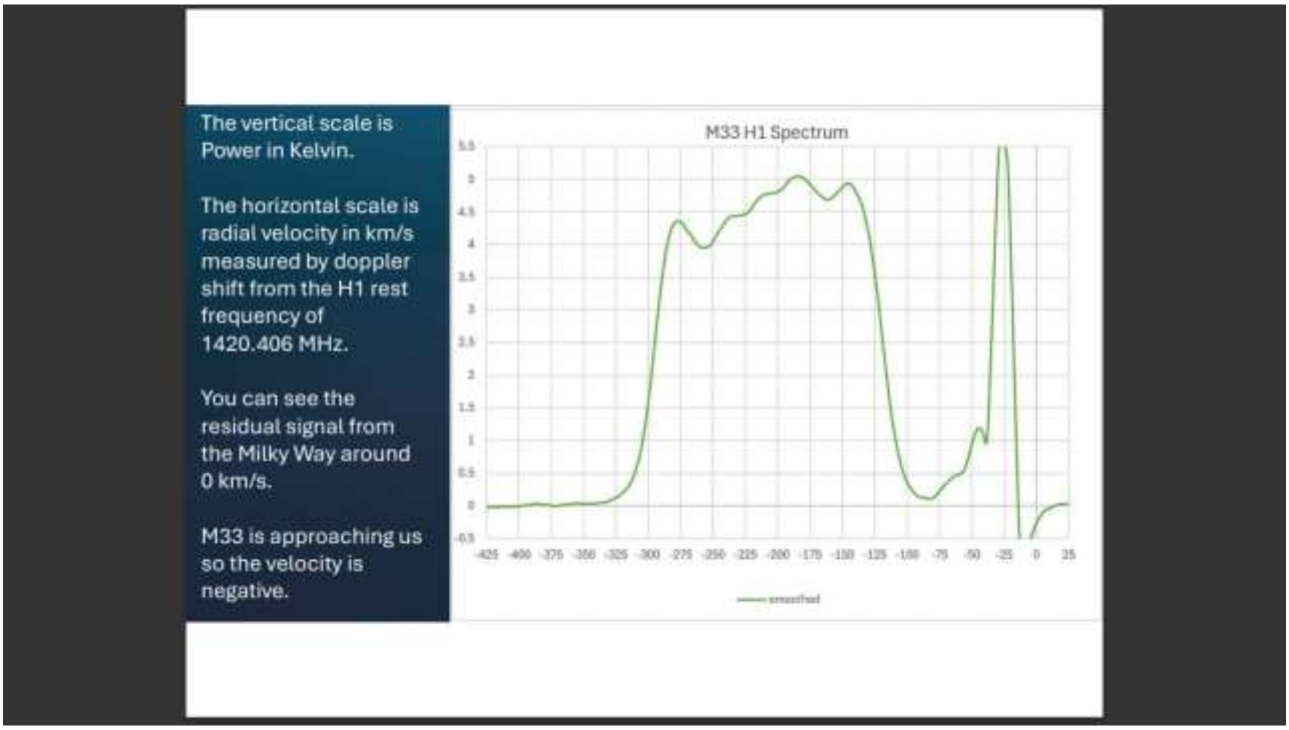
The vertical scale is Power in Kelvin.
The horizontal scale is radial velocity in km/s measured by doppler shift from the H1 rest frequency of 1420.406 MHz.
You can see the residual signal from the Milky Way around 0 km/s.
M33 is approaching us so the velocity is negative.
M33 H1 Spectrum
smoothed

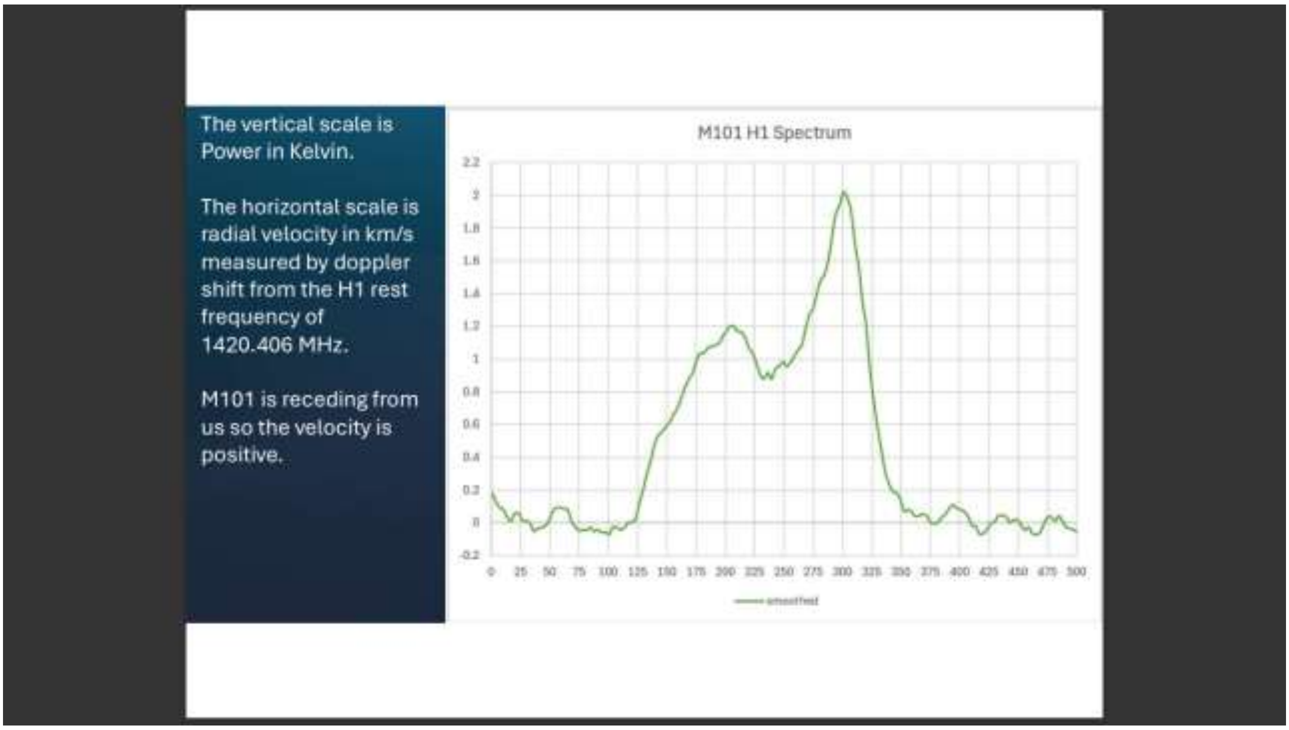
The vertical scale is Power in Kelvin.
The horizontal scale is radial velocity in km/s measured by doppler shift from the H1 rest frequency of 1420.406 MHz.
M101 is receding from us so the velocity is positive.
M101 H1 Spectrum

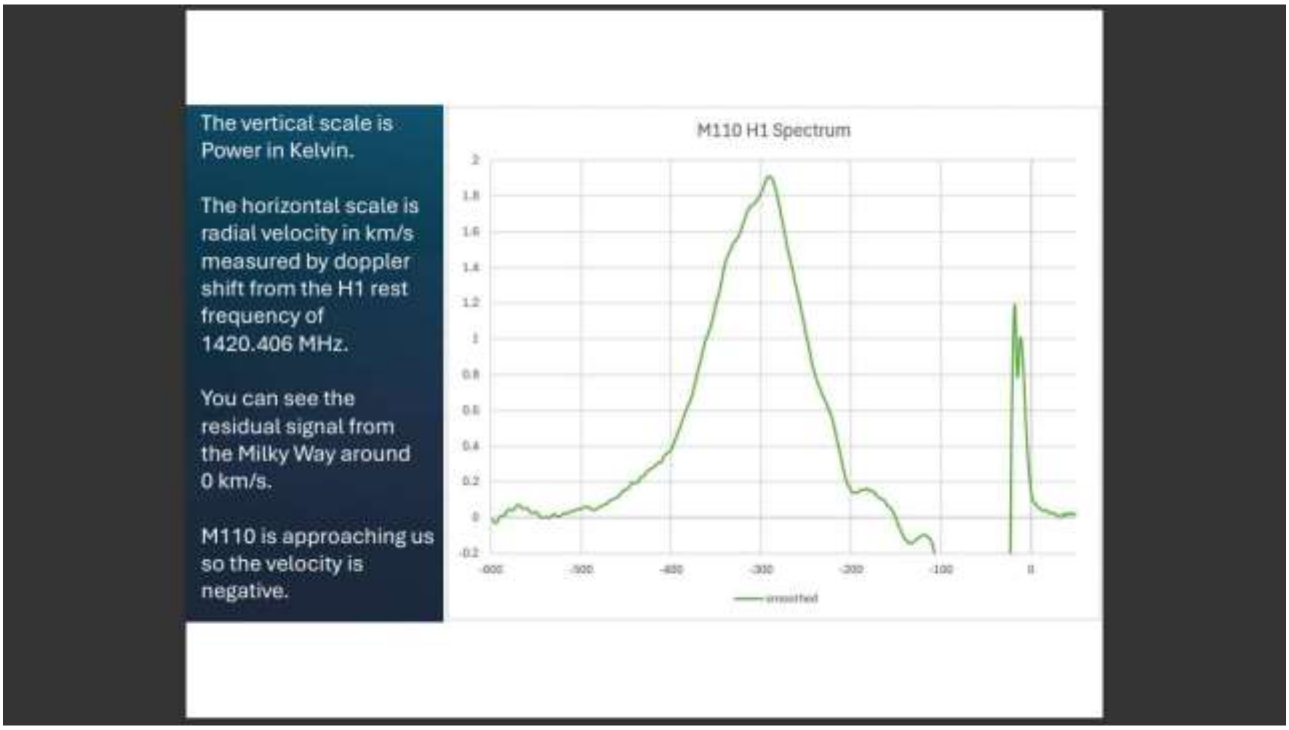
The vertical scale is Power in Kelvin.
The horizontal scale is radial velocity in km/s measured by doppler shift from the H1 rest frequency of 1420.406 MHz.
You can see the residual signal from the Milky Way around 0 km/s.
M110 is approaching us so the velocity is negative.
M110 H1 Spectrum

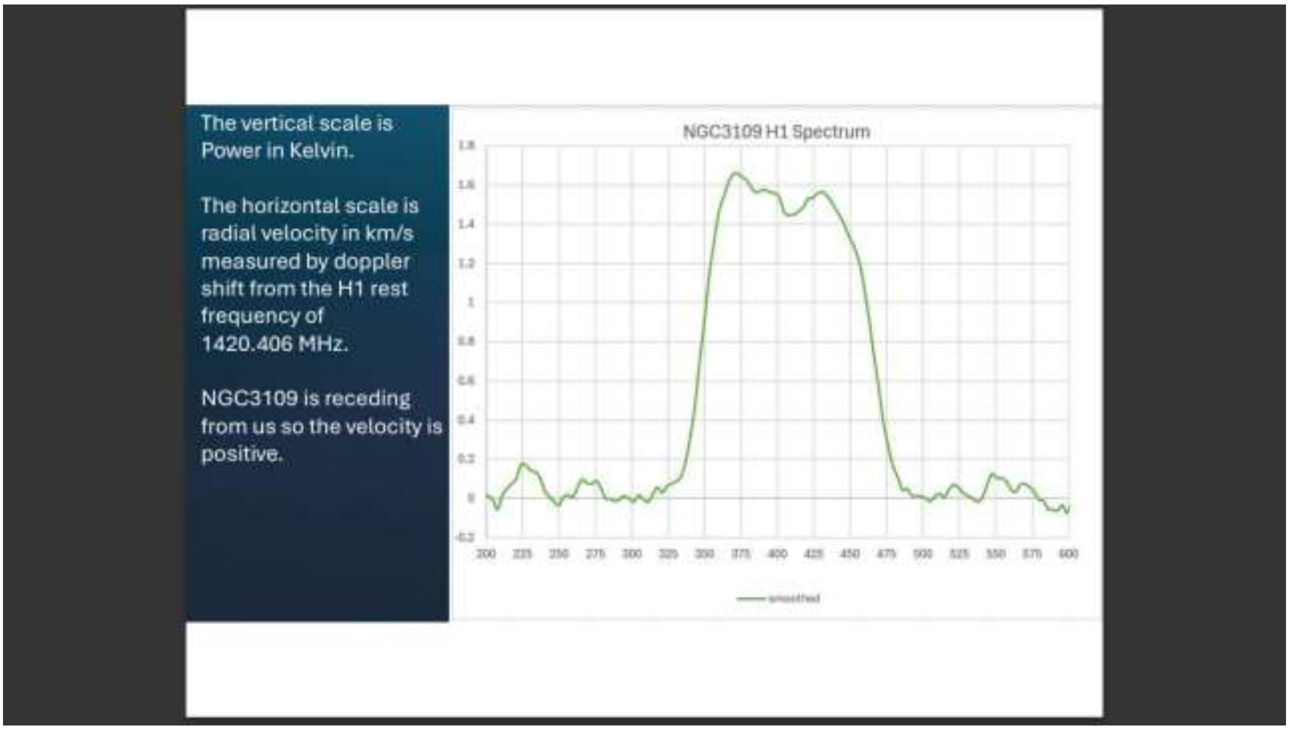
The vertical scale is Power in Kelvin.
The horizontal scale is radial velocity in km/s measured by doppler shift from the H1 rest frequency of 1420.406 MHz.
NGC3109 is receding from us so the velocity is positive.
NGC3109 H1 Spectrum

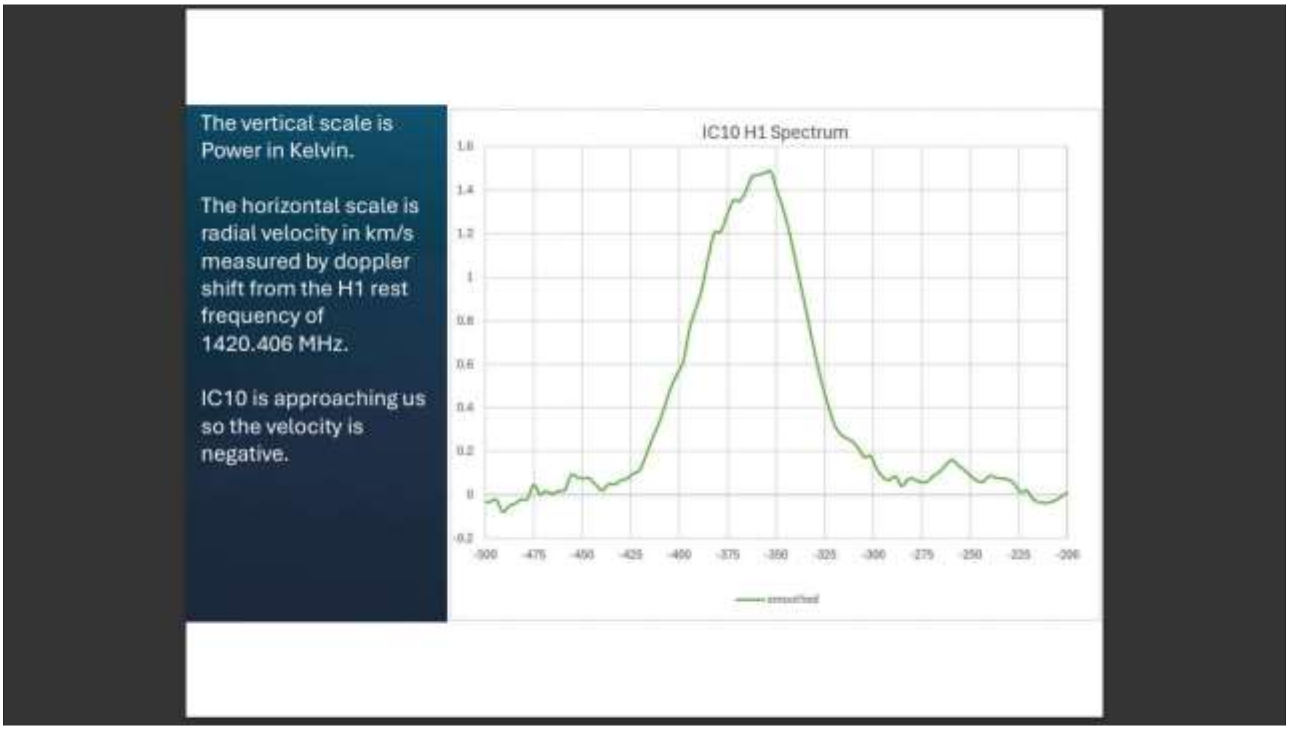
The vertical scale is Power in Kelvin.
The horizontal scale is radial velocity in km/s measured by doppler shift from the H1 rest frequency of 1420.406 MHz.
IC10 is approaching us so the velocity is negative.
IC10 H1 Spectrum

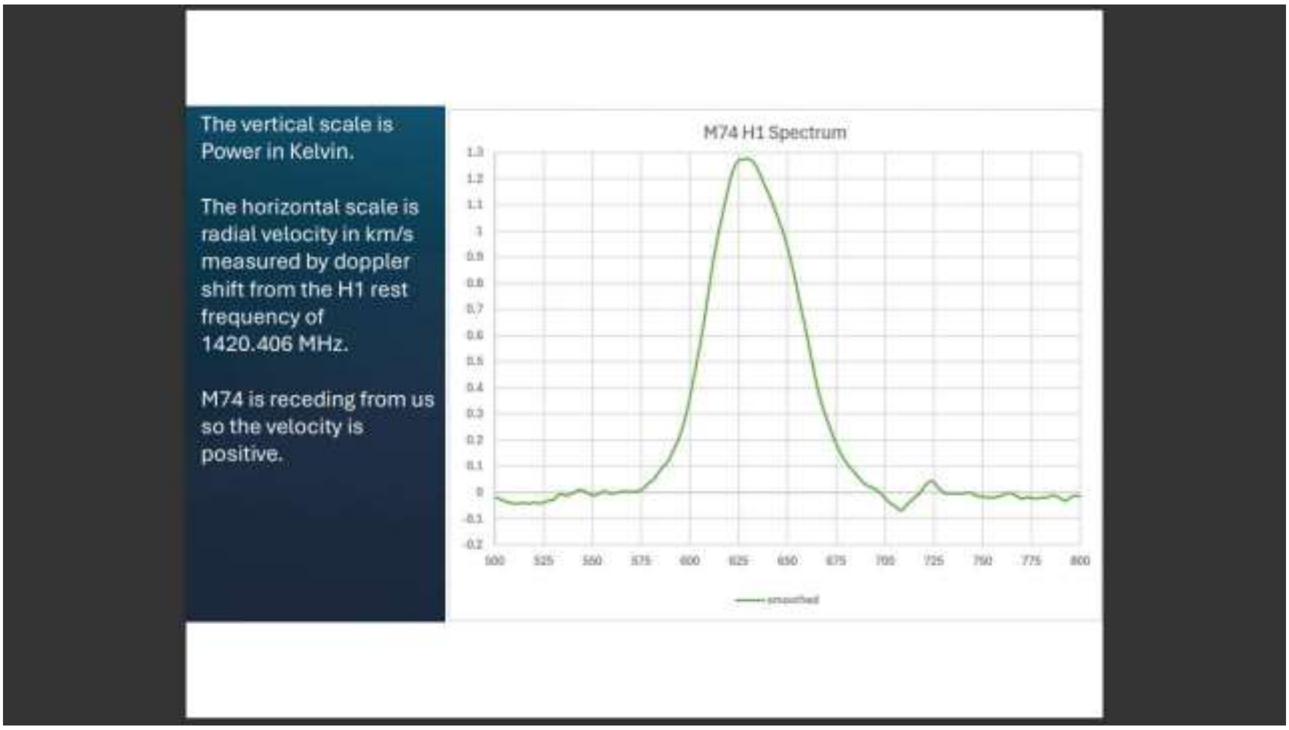
The vertical scale is Power in Kelvin.
The horizontal scale is radial velocity in km/s measured by doppler shift from the H1 rest frequency of 1420.406 MHz.
M74 is receding from us so the velocity is positive.
M74 H1 Spectrum
1.3 1.2 1.1 1 0.9 0.8 0.7 0.6 0.5 0.4 0.3 0.2 0.1 0 -0.1 -0.2
500 525 550 575 600 625 650 675 700 725 750 775 800

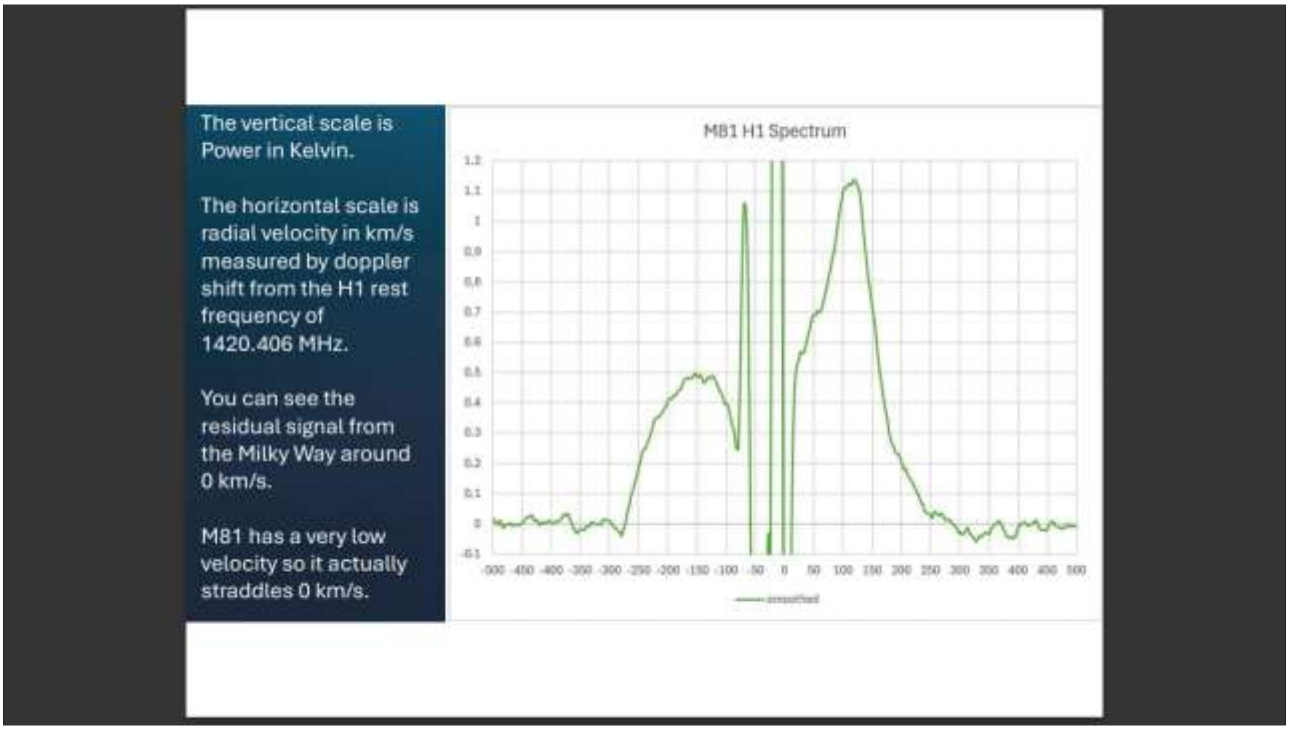
The vertical scale is Power in Kelvin.
The horizontal scale is radial velocity in km/s measured by doppler shift from the H1 rest frequency of 1420.406 MHz.
You can see the residual signal from the Milky Way around 0 km/s.
M81 has a very low velocity so it actually straddles 0 km/s.
M81 H1 Spectrum

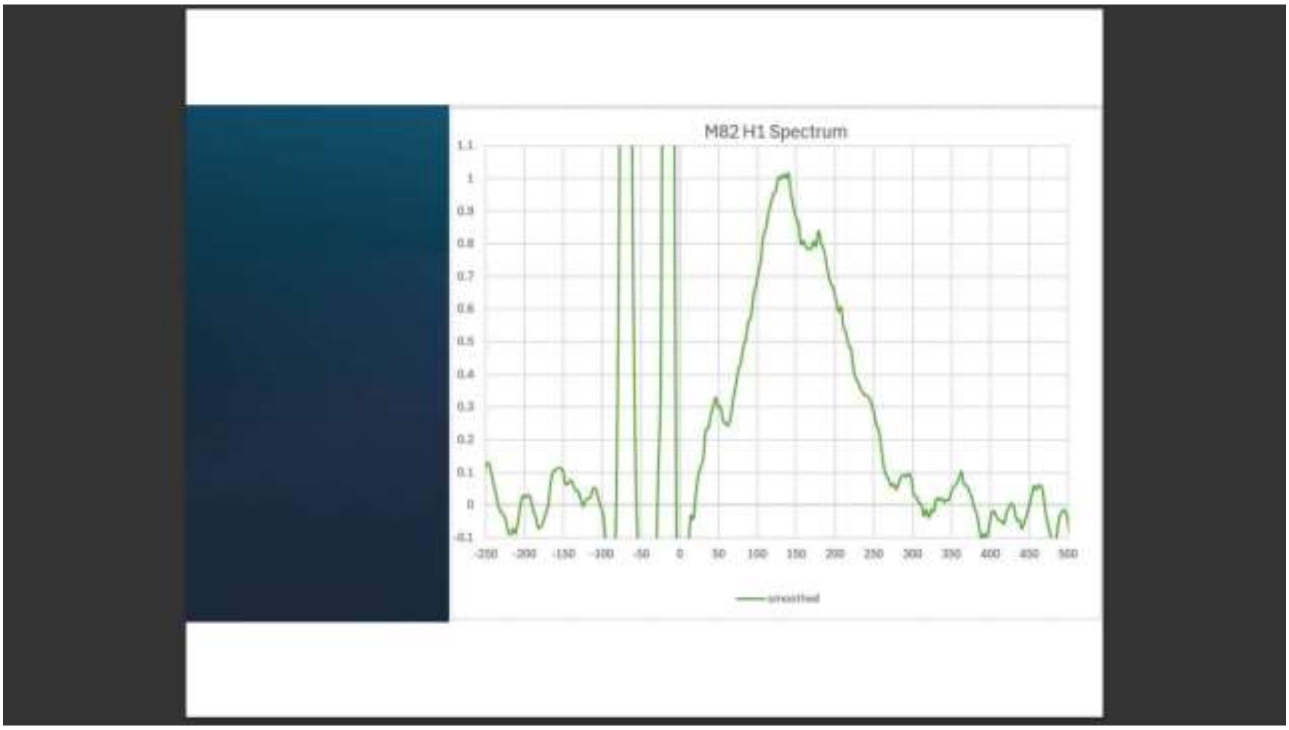
M82 H1 Spectrum
smoothed

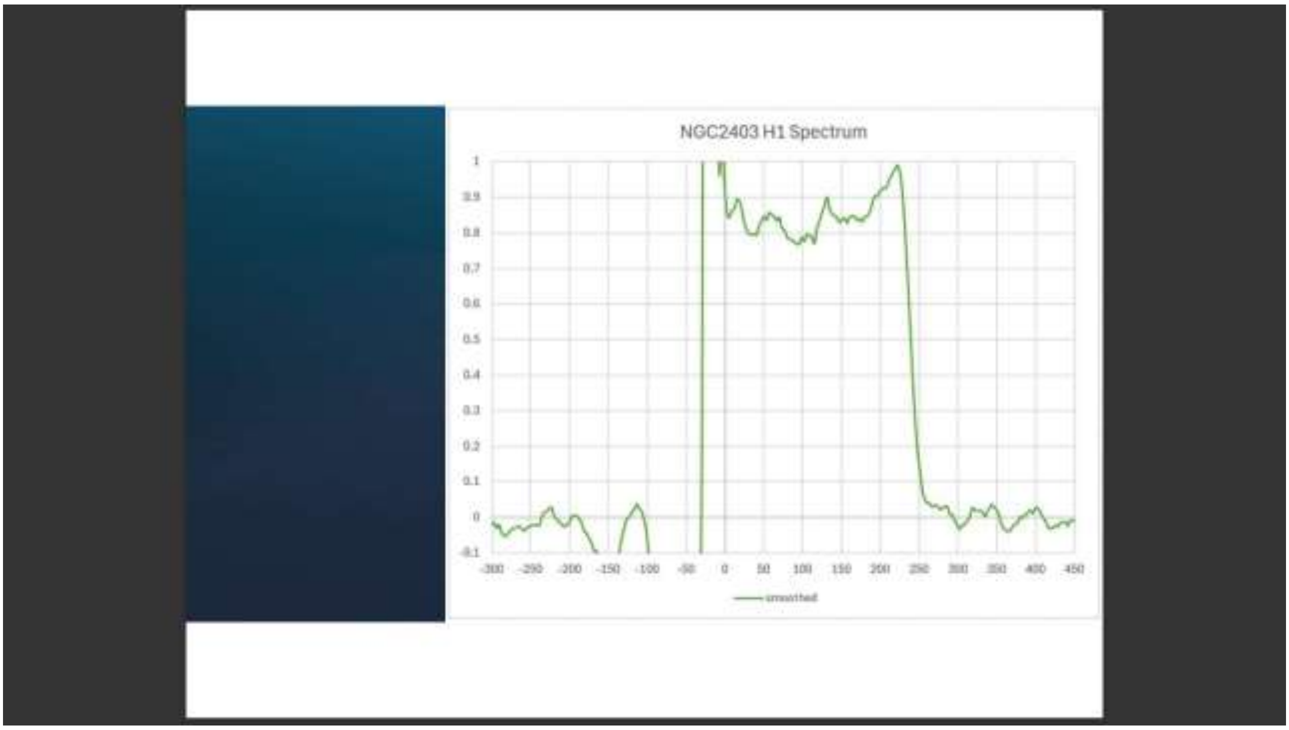
NGC2403 H1 Spectrum
smoothed

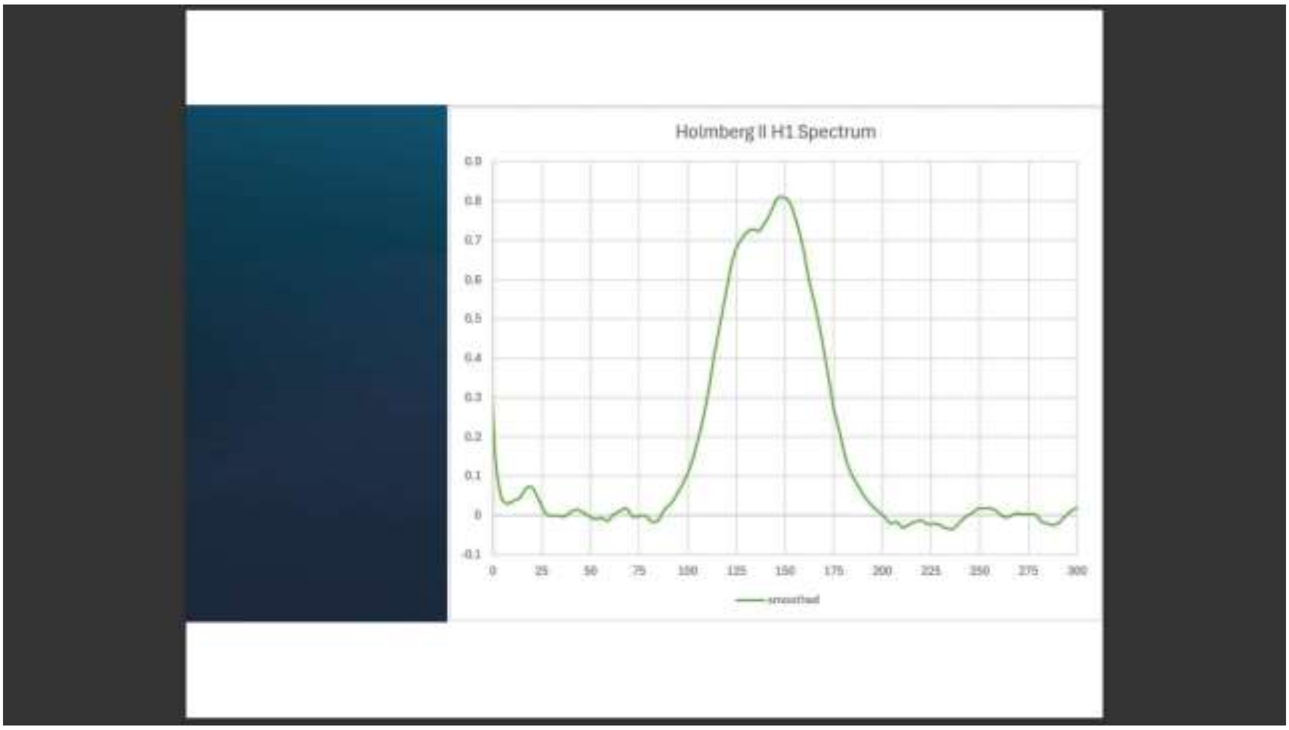
Holmberg II H1 Spectrum
smoothed

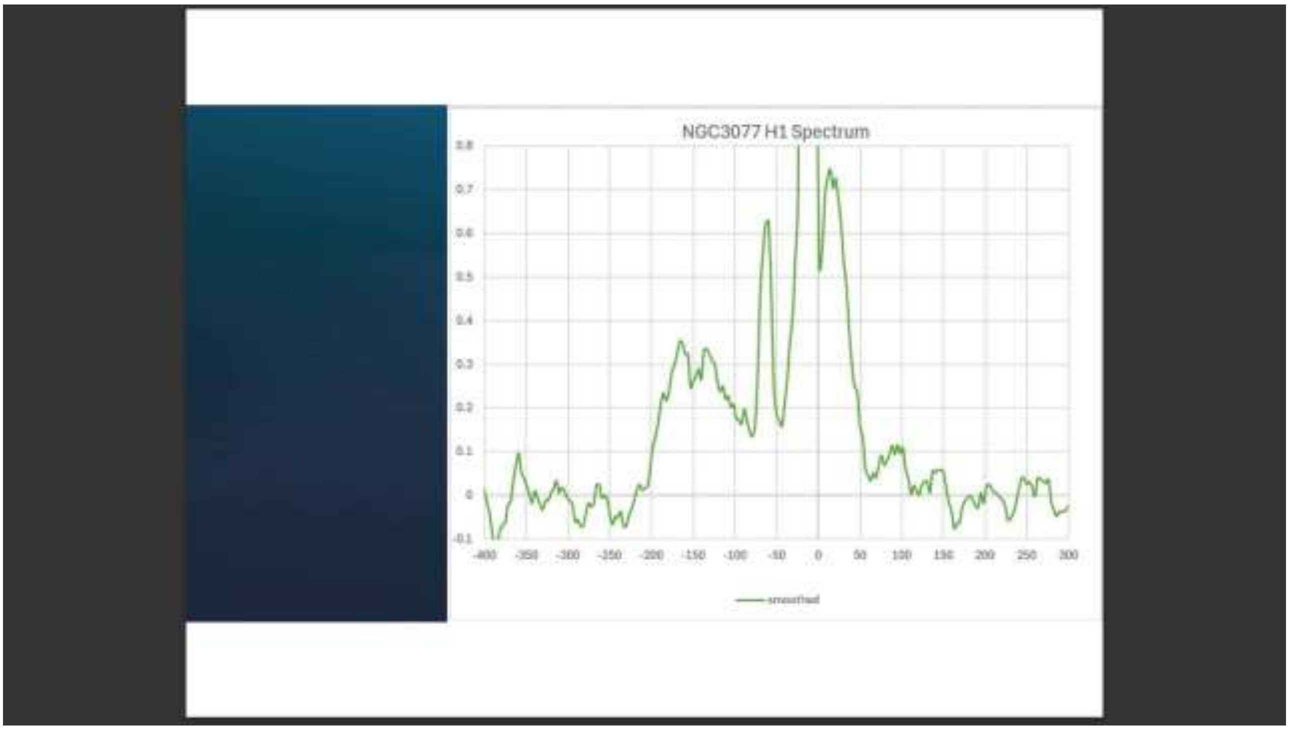
NGC3077 H1 Spectrum
smoothed

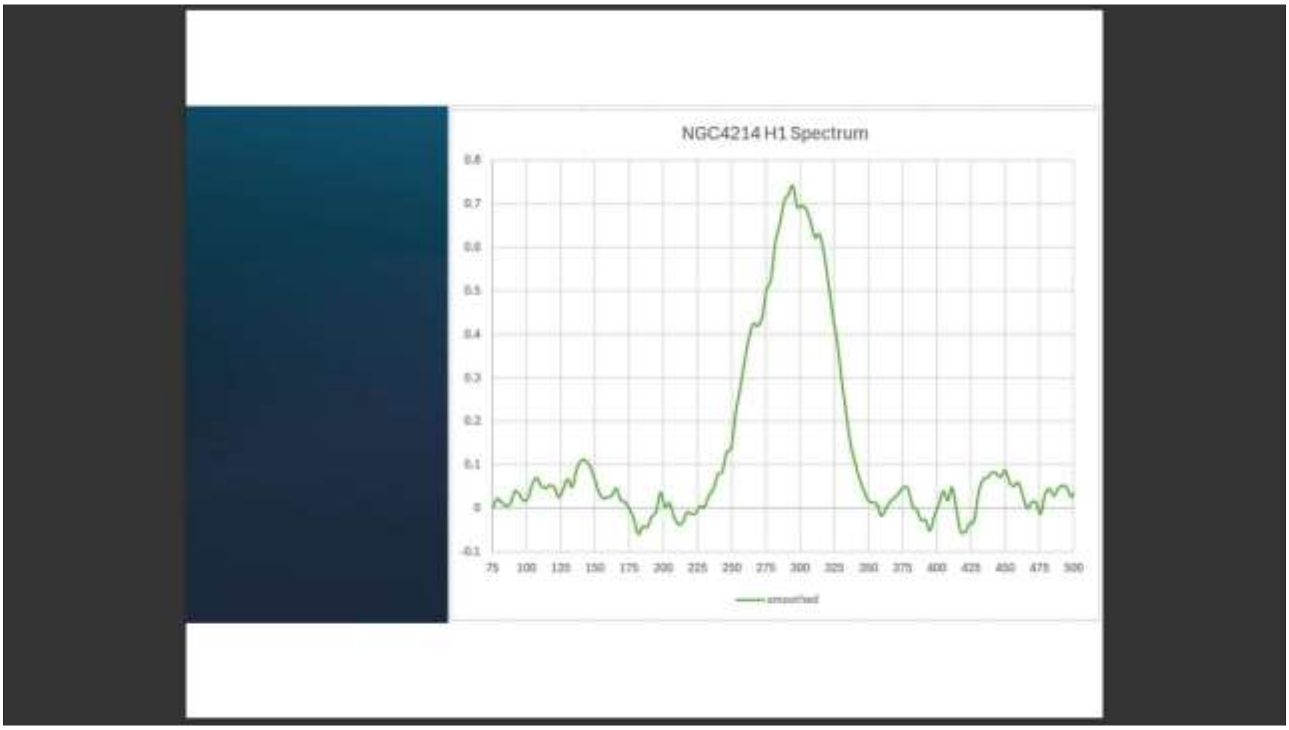
NGC4214 H1 Spectrum
0.7
0
75 100 125 150 175 200 225 250 275 300 325 350 375 400 425 450 475 500

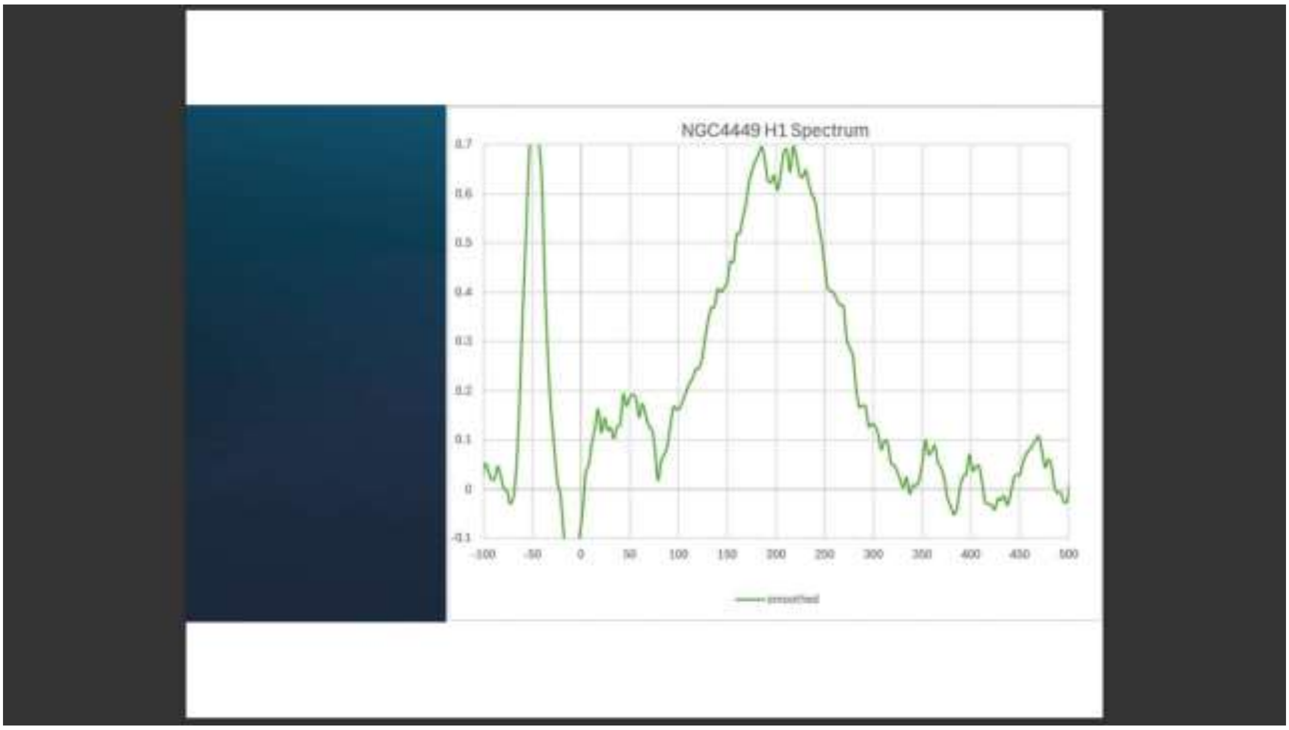
NGC4449 H1 Spectrum
0.7
0.6
0.5
0.4
0.3
0.2
0.1
0
-0.1
-100 -50 0 50 100 150 200 250 300 350 400 450 500

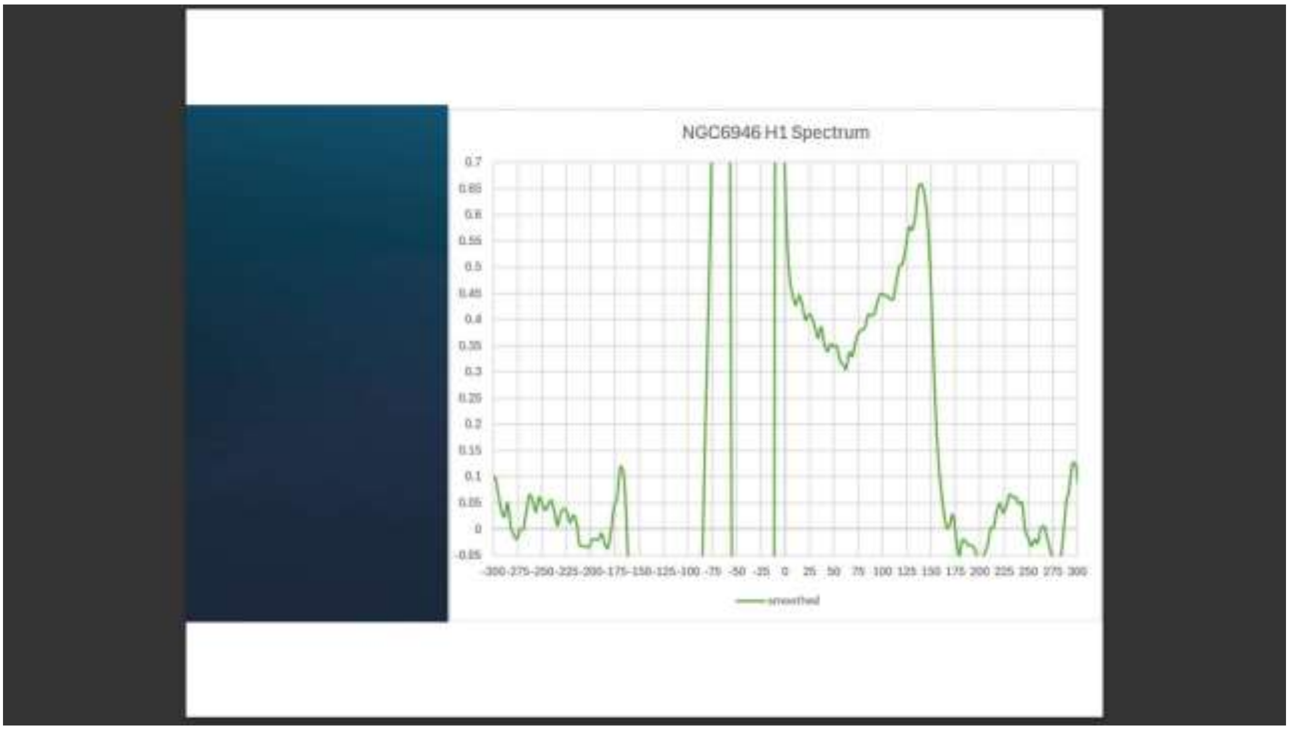
NGC6946 H1 Spectrum
smoothed

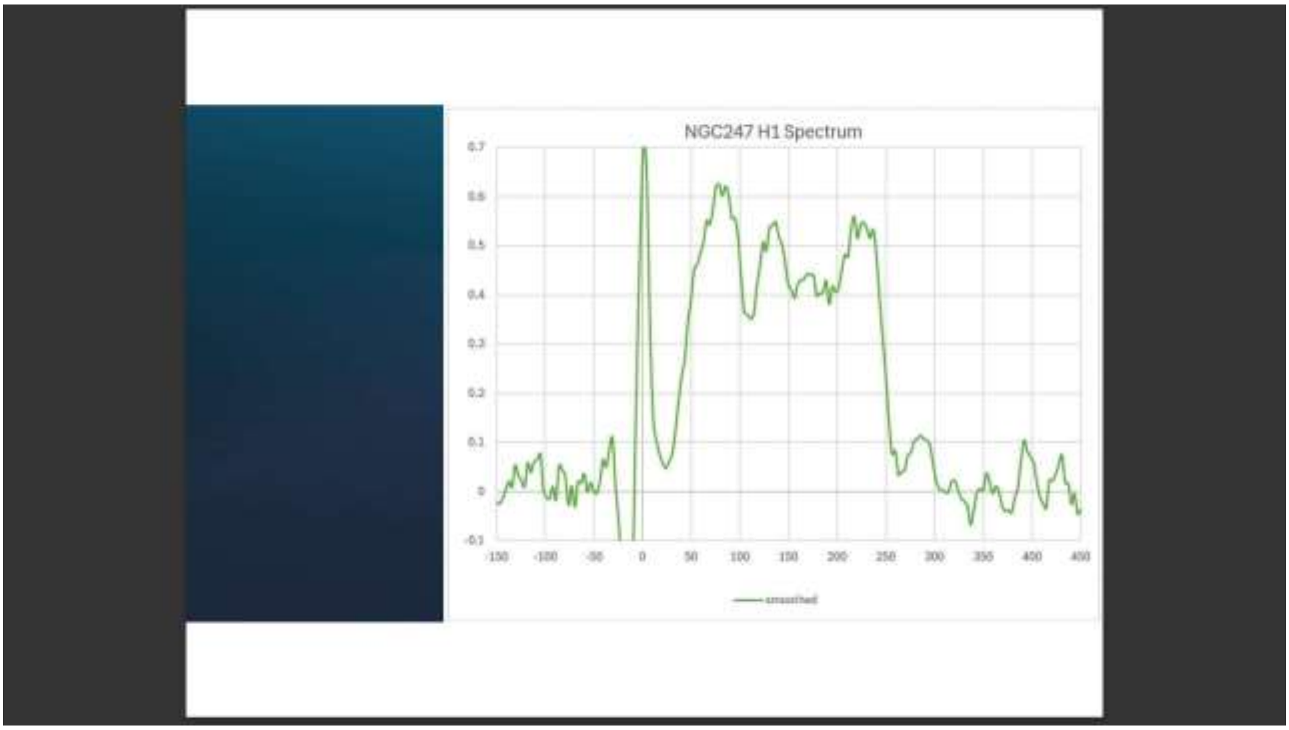
NGC247 H1 Spectrum
smoothed

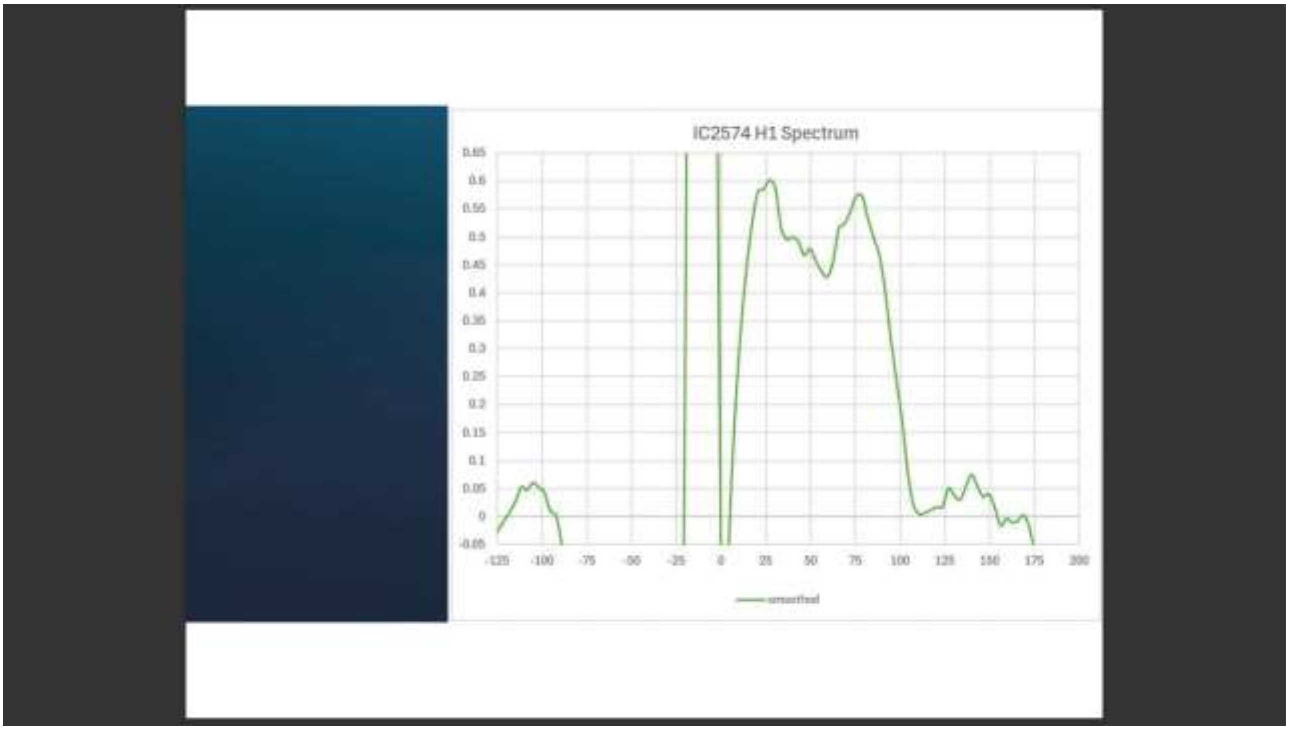
IC2574 H1 Spectrum
0.65
0.6
0.55
0.5
0.45
0.4
0.35
0.3
0.25
0.2
0.15
0.1
0.05
0
-0.05
-125 -100 -75 -50 -25 0 25 50 75 100 125 150 175 200
smoothed

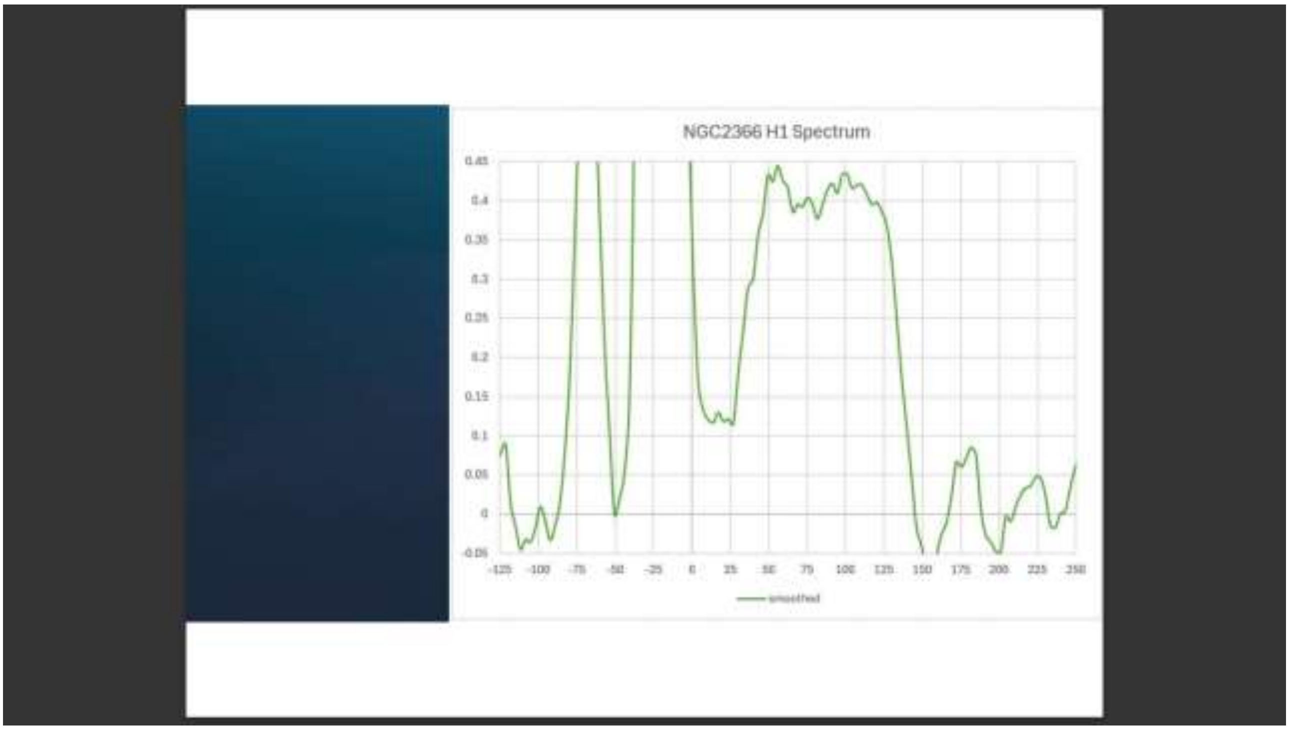
NGC2366 H1 Spectrum
0.45
0.4
0.35
0.3
0.25
0.2
0.15
0.1
0.05
0
-0.05
-125 -100 -75 -50 -25 0 25 50 75 100 125 150 175 200 225 250
smoothed

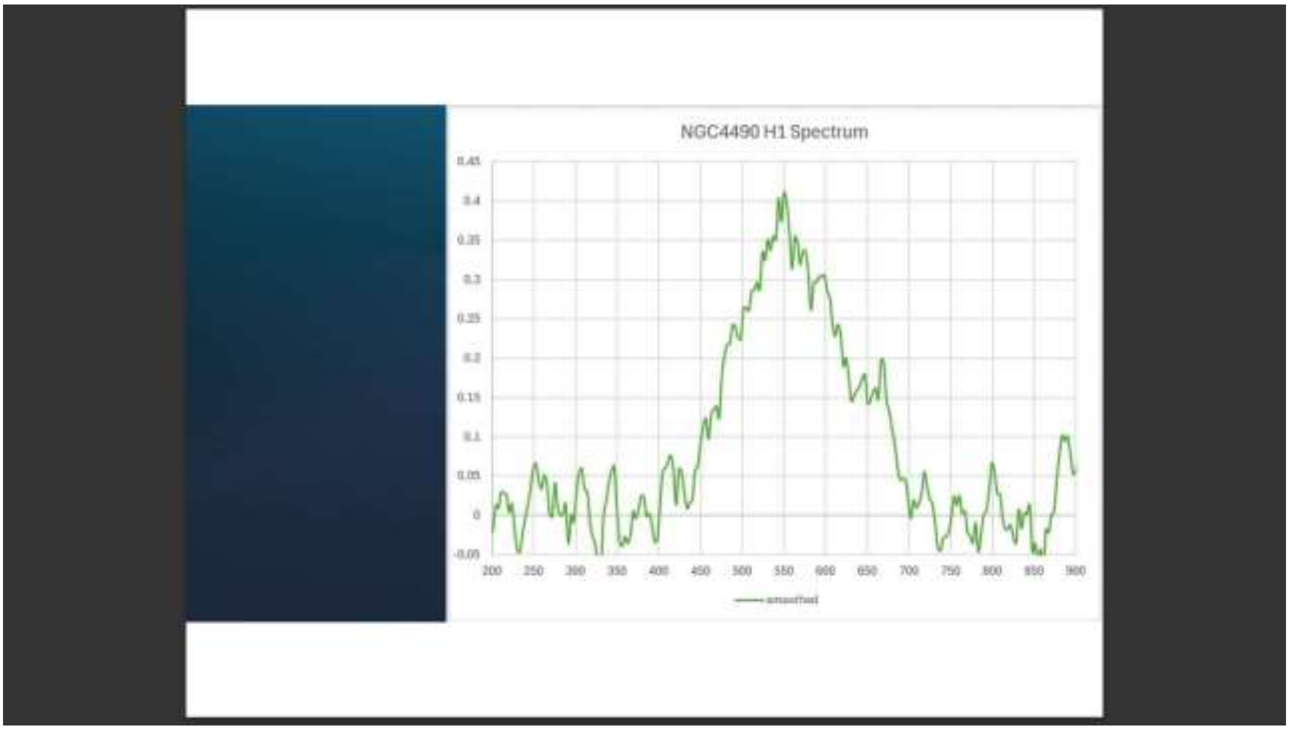
NGC4490 H1 Spectrum
0.45
0.4
0.35
0.3
0.25
0.2
0.15
0.1
0.05
0
-0.05
200 250 300 350 400 450 500 550 600 650 700 750 800 850 900
smoothed

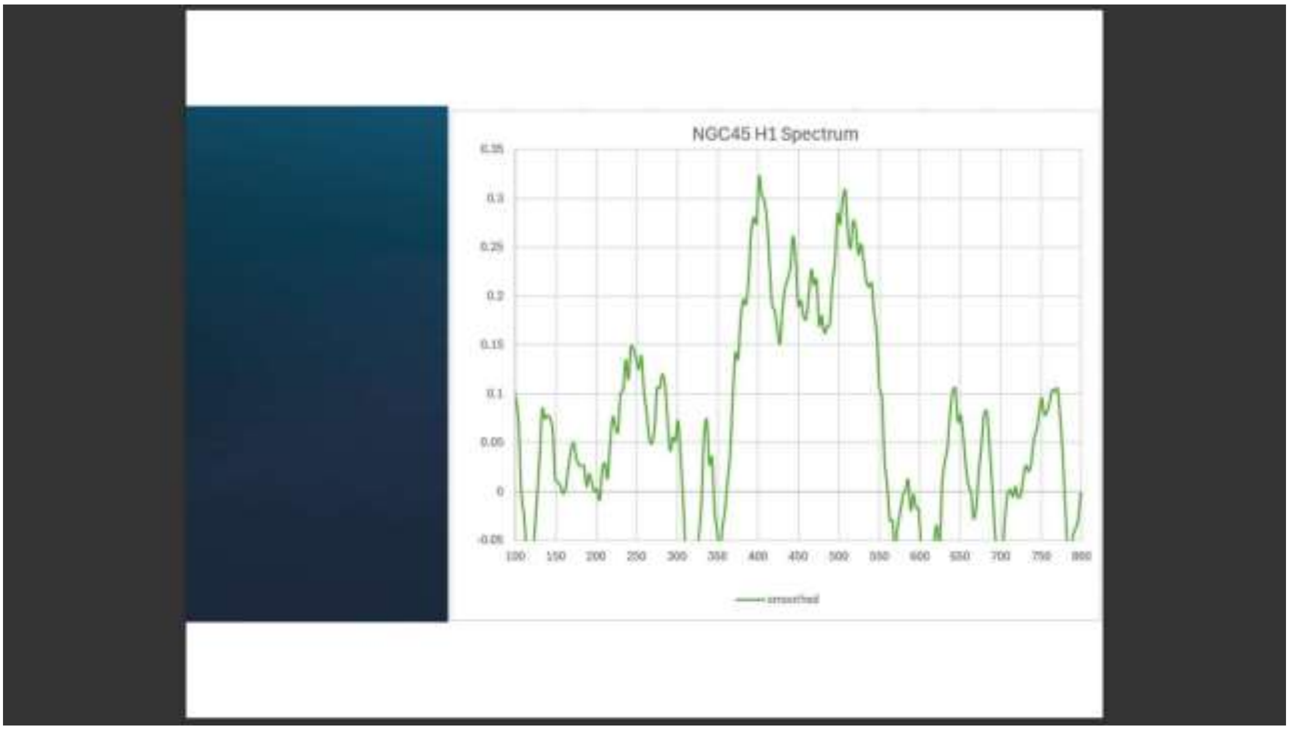
NGC45 H1 Spectrum
0.35
0.3
0.25
0.2
0.15
0.1
0.05
0
-0.05
100 150 200 250 300 350 400 450 500 550 600 650 700 750 800
smoothed

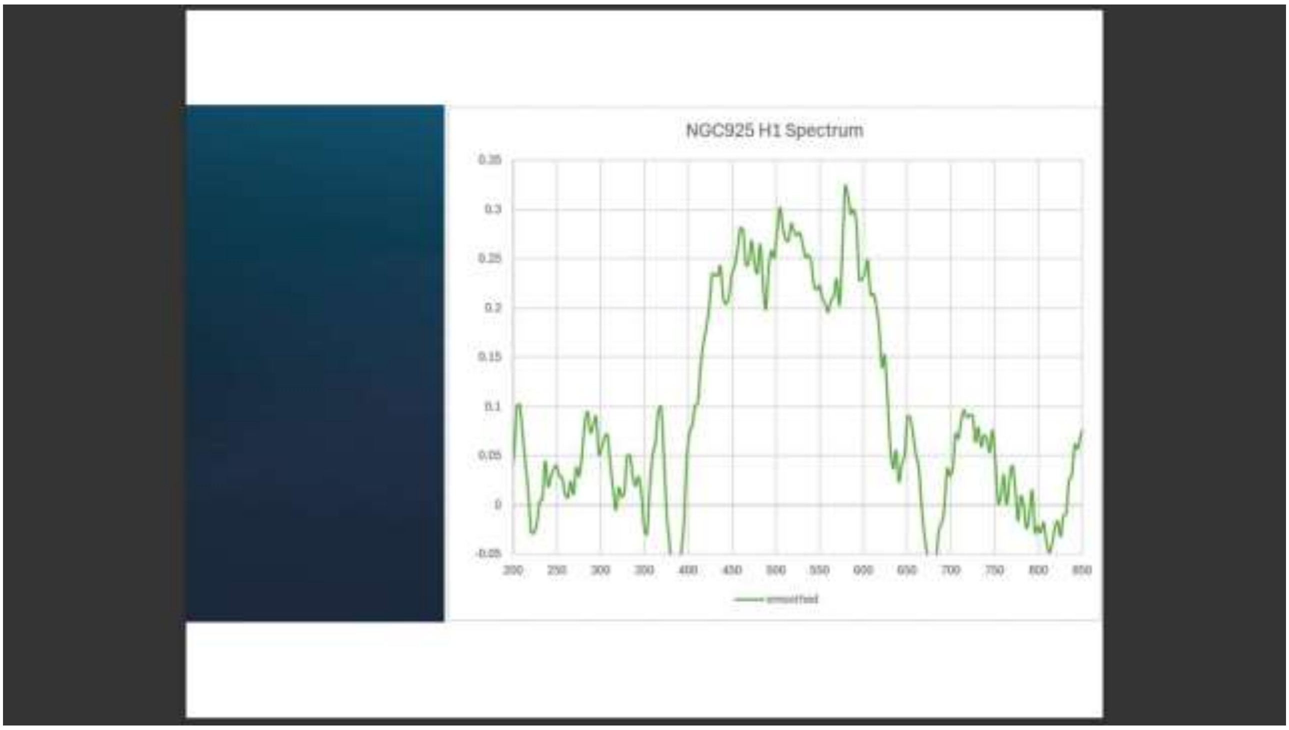
NGC925 H1 Spectrum
0.35
0.3
0.25
0.2
0.15
0.1
0.05
0
-0.05
200 250 300 350 400 450 500 550 600 650 700 750 800 850

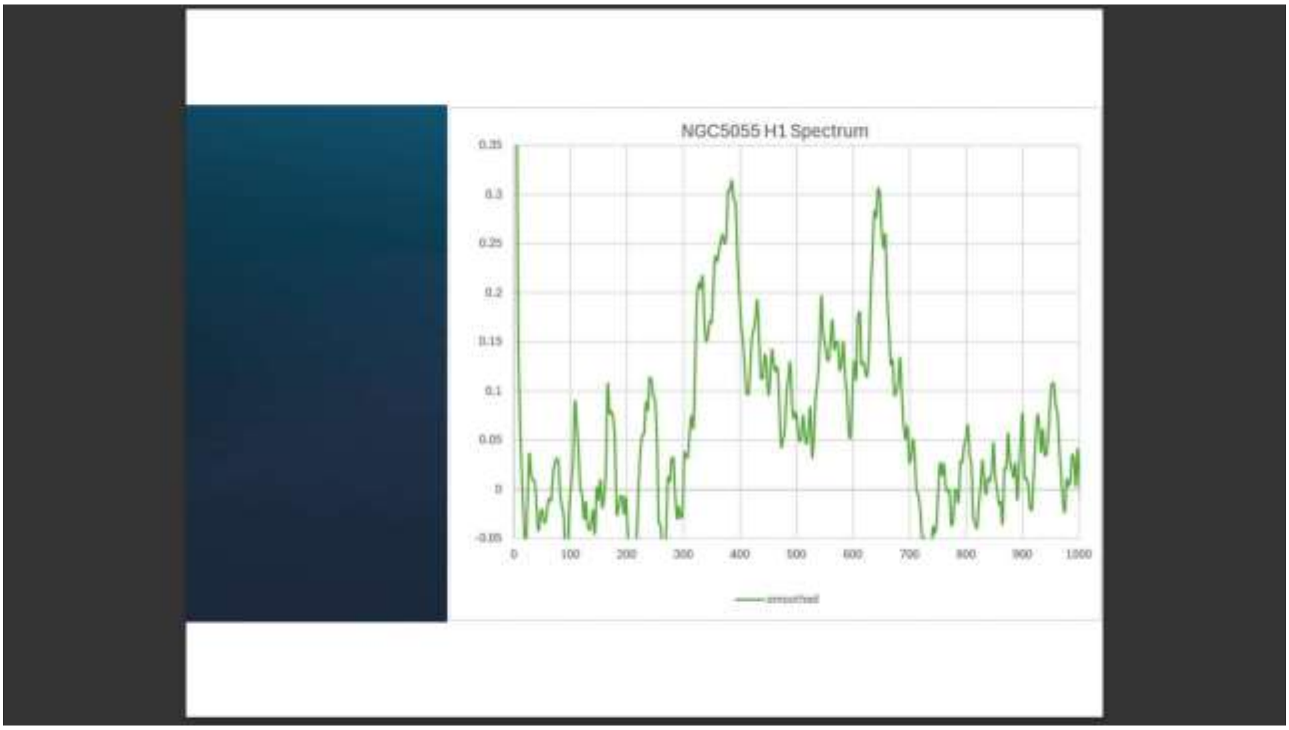
NGC5055 H1 Spectrum
0.35
0.3
0.25
0.2
0.15
0.1
0.05
0
-0.05
0 100 200 300 400 500 600 700 800 900 1000

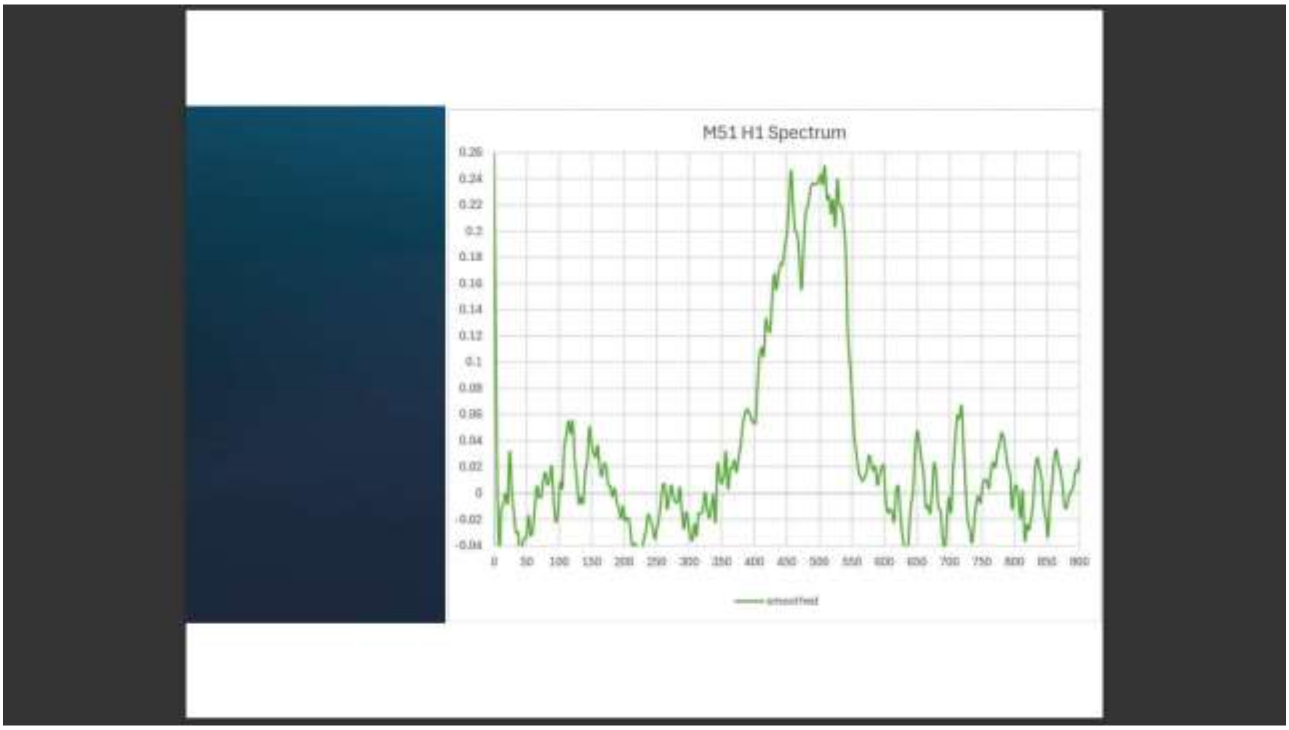
M51 H1 Spectrum
0.26
0.24
0.22
0.2
0.18
0.16
0.14
0.12
0.1
0.08
0.06
0.04
0.02
0
-0.02
-0.04
0 50 100 150 200 250 300 350 400 450 500 550 600 650 700 750 800 850 900

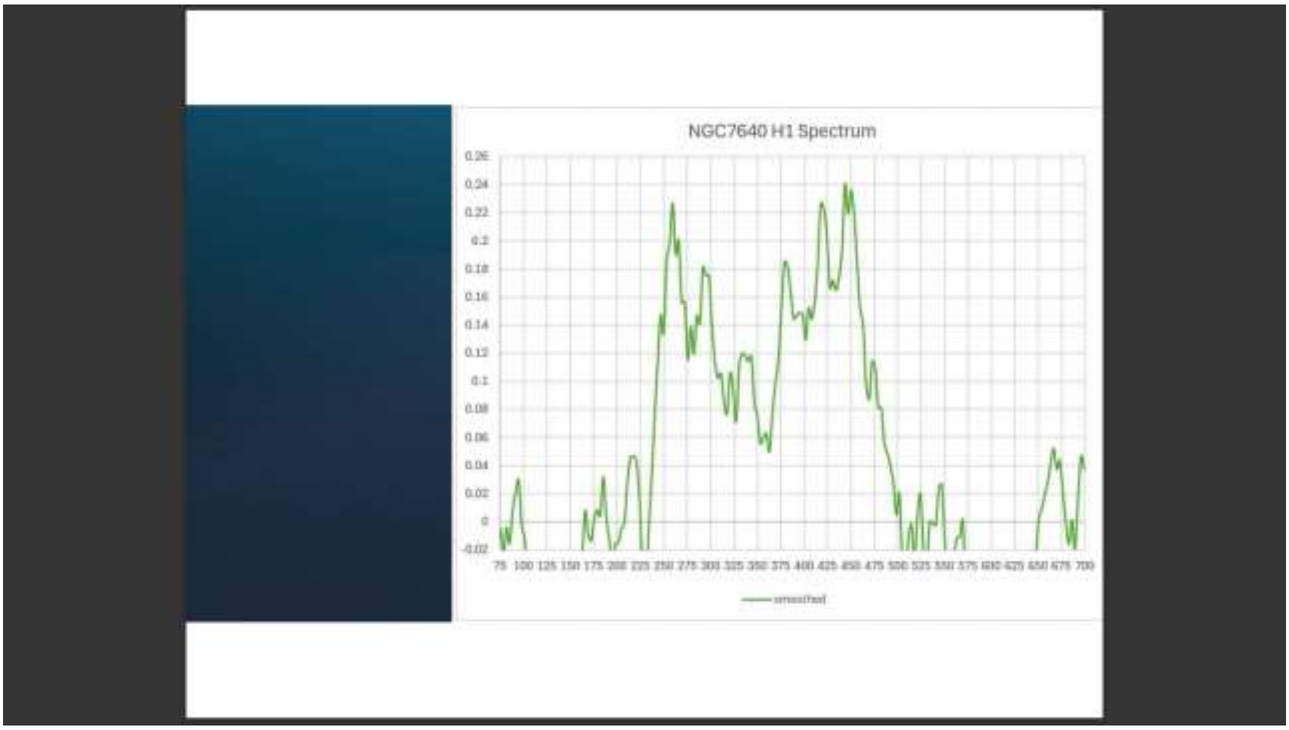
NGC7640 H1 Spectrum
0.26
0.24
0.22
0.2
0.18
0.16
0.14
0.12
0.1
0.08
0.06
0.04
0.02
0
-0.02

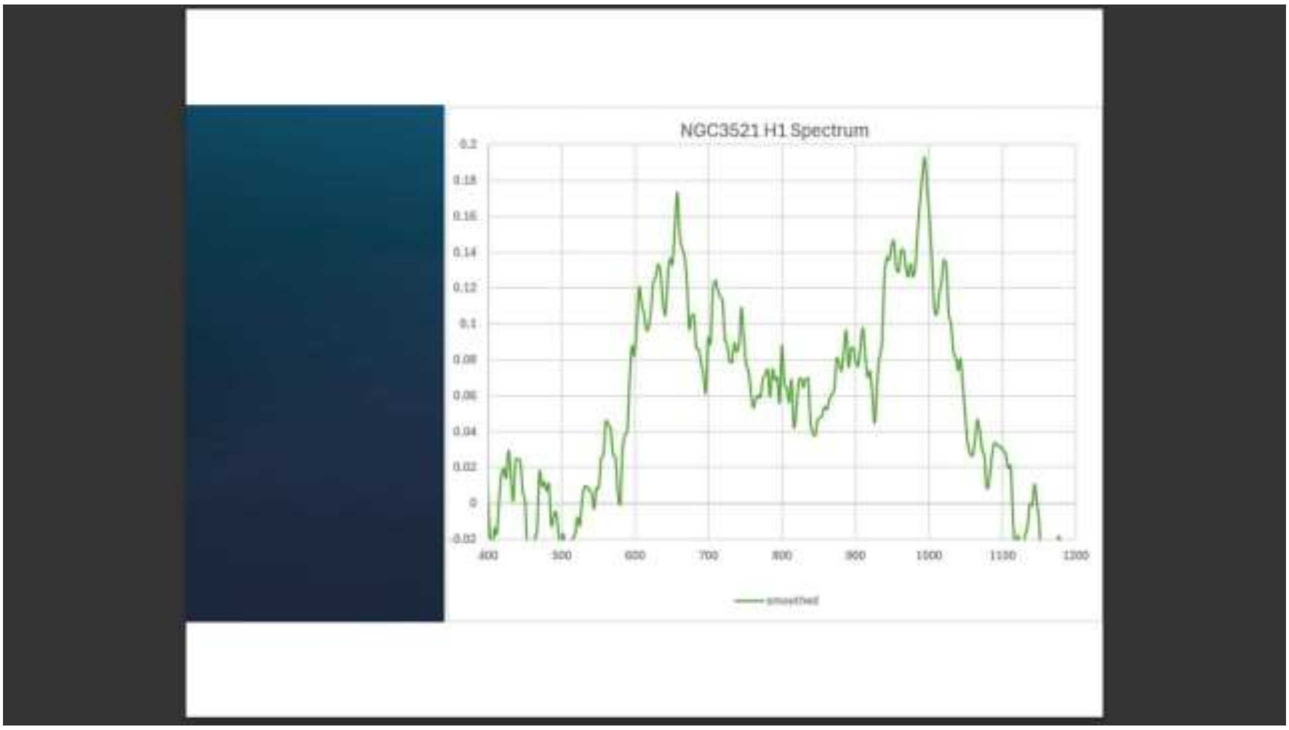
NGC3521 H1 Spectrum
0.2
0.18
0.16
0.14
0.12
0.1
0.08
0.06
0.04
0.02
0
-0.02
400
500
600
700
800
900
1000
1100
1200
smoothed

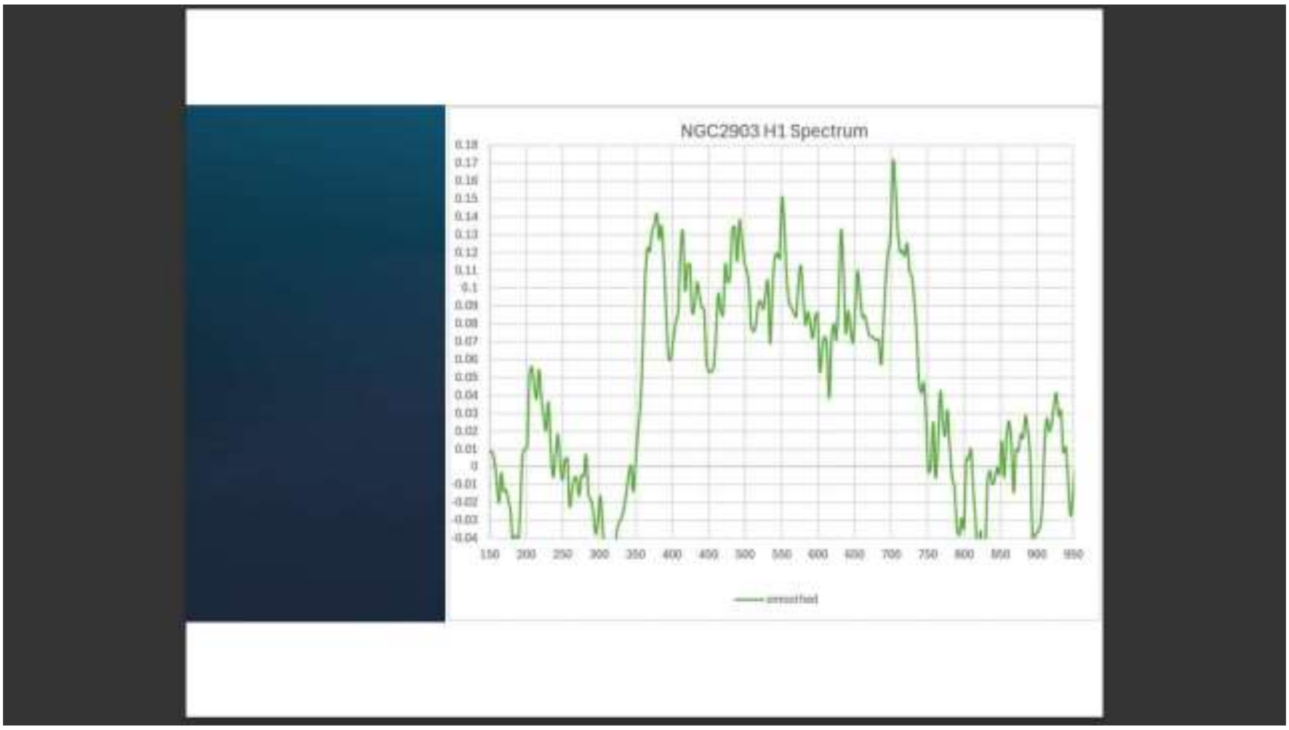
NGC2903 H1 Spectrum
150
200
250
300
350
400
450
500
550
600
650
700
750
800
850
900
950
smoothed

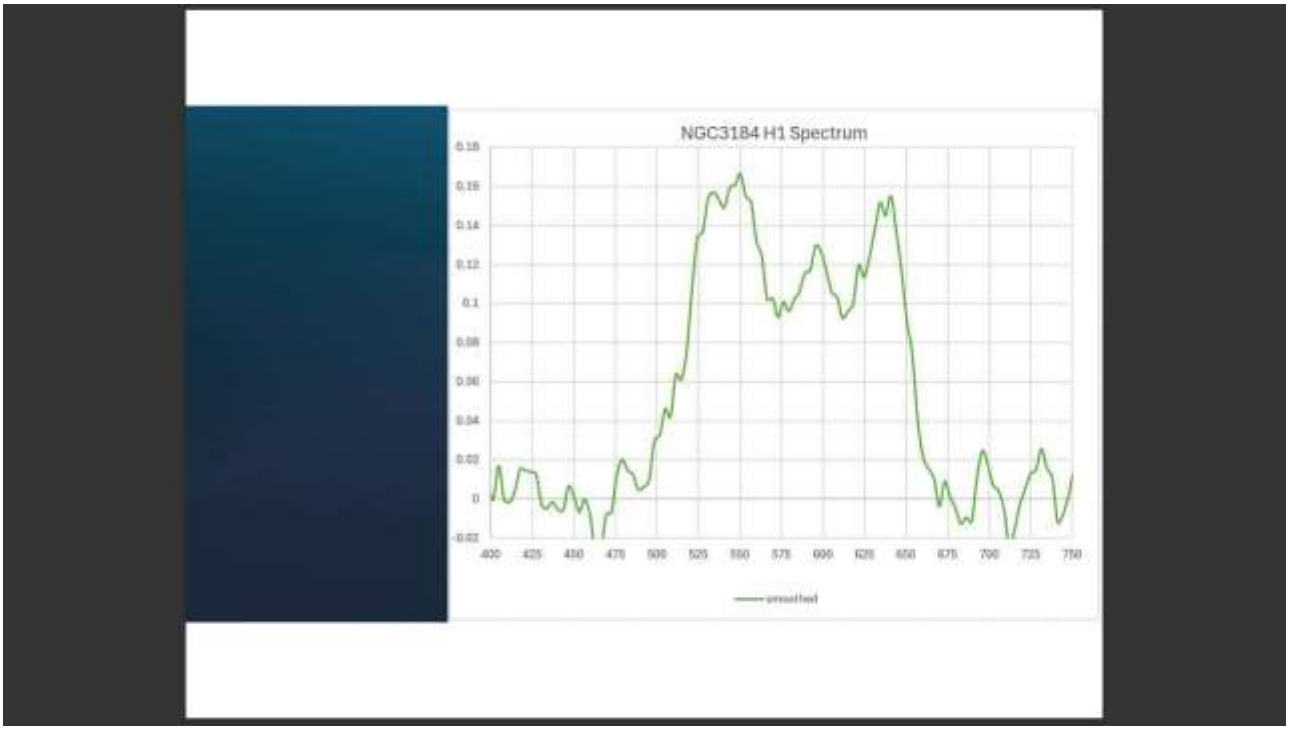
NGC3184 H1 Spectrum
0.18
0.16
0.14
0.12
0.1
0.08
0.06
0.04
0.02
0
-0.02
400 425 450 475 500 525 550 575 600 625 650 675 700 725 750
smoothed

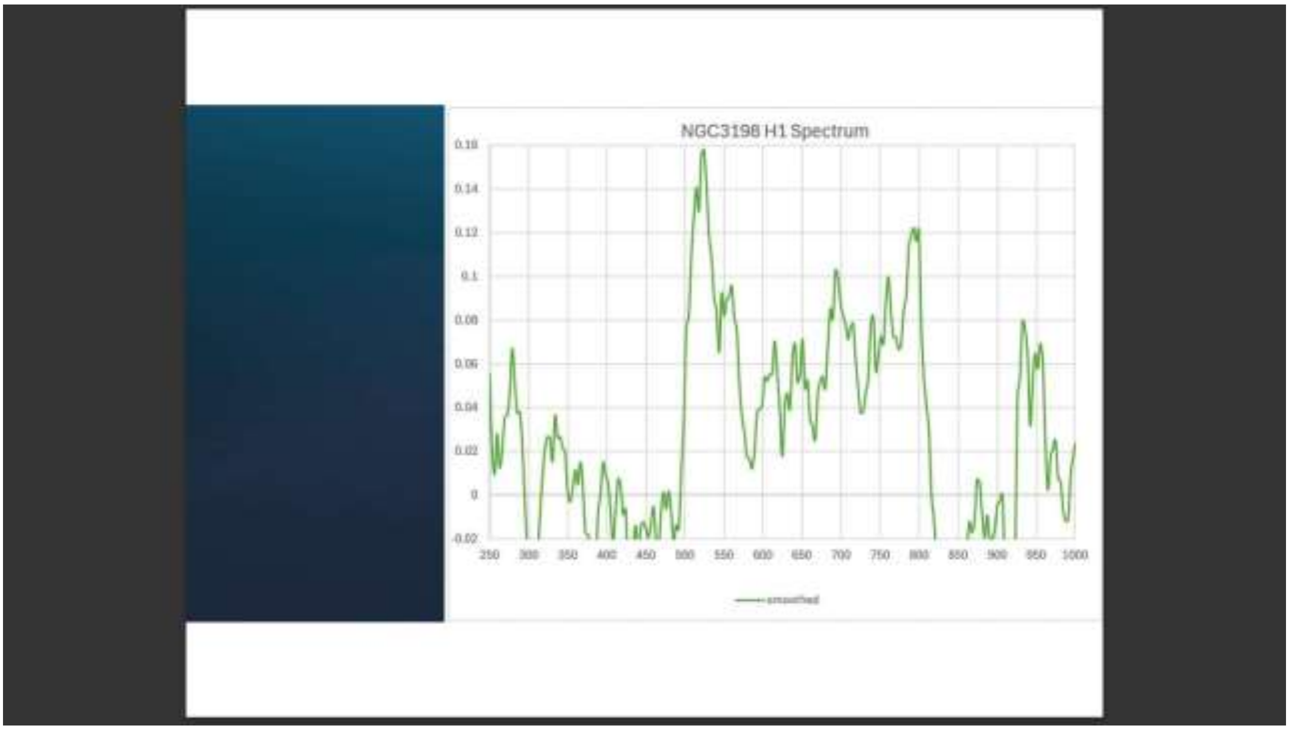
NGC3198 H1 Spectrum
0.16
0.14
0.12
0.1
0.08
0.06
0.04
0.02
0
-0.02
250 300 350 400 450 500 550 600 650 700 750 800 850 900 950 1000
smoothed

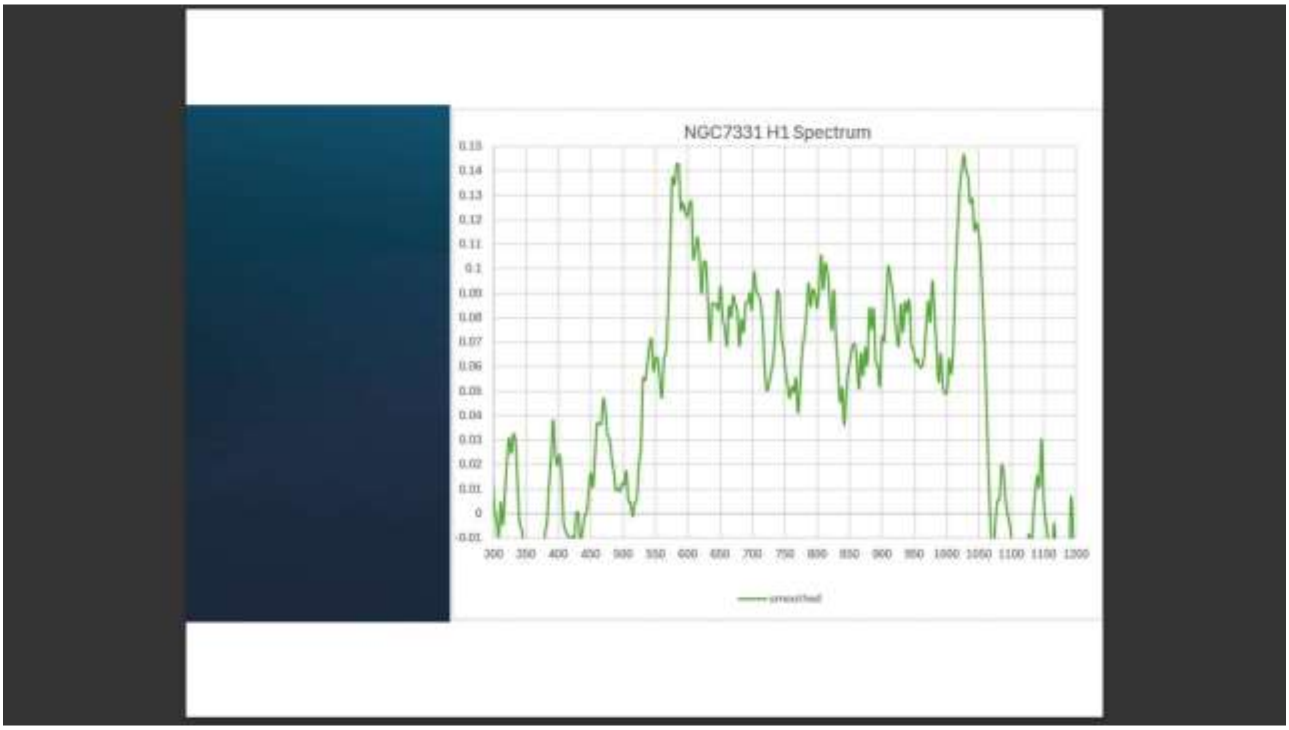
NGC7331 H1 Spectrum

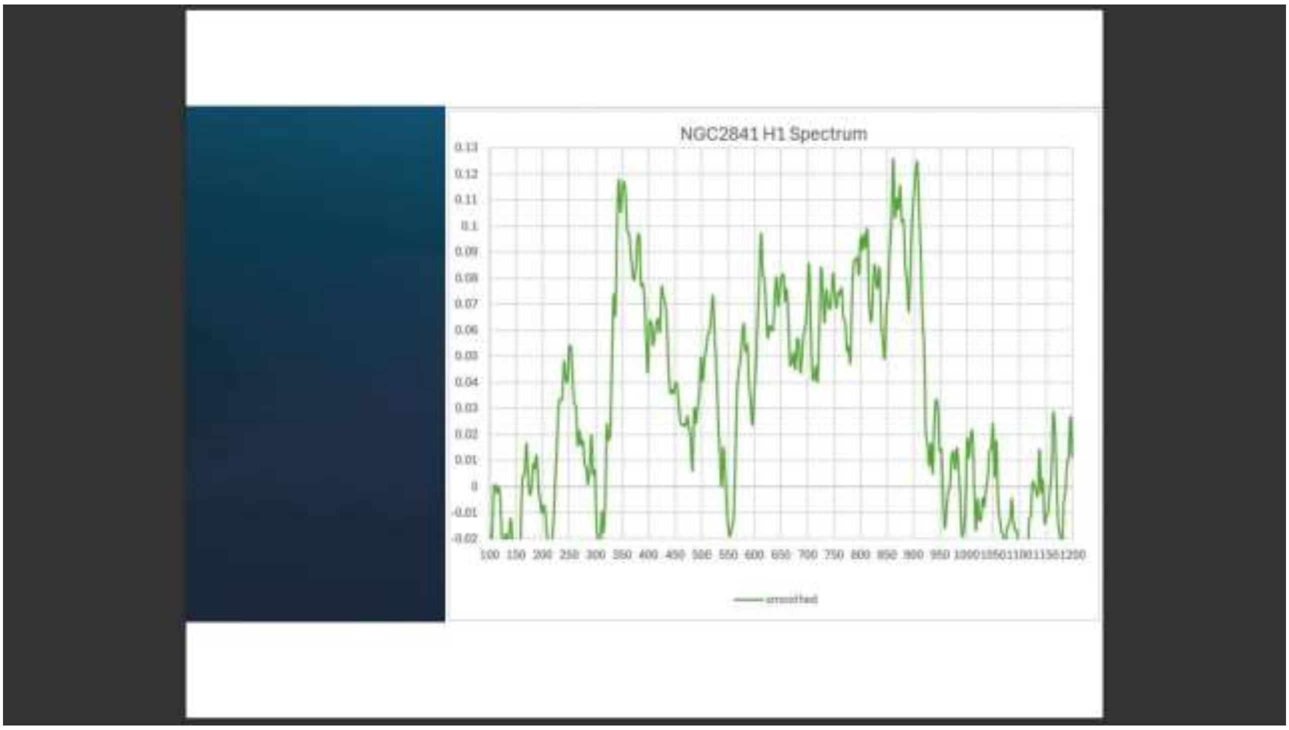
NGC2841 H1 Spectrum


References
1. Fabian Walter, Elias Brinks, W.J.G. De Bolk, Frank Bigel, Robert C. Kennicutt, Jr., Michele D. Thornley, Adam K. Leroy – THINGS: The HI Nearby Galaxy Survey
https://arxiv.org/abs/0810.2125
2. J.F. Dean and R.D. Davies - The Integrated Neutral Hydrogen Properties of Nearby Galaxies
https://academic.oup.com/mnras/article/170/3/503/961865

LMRO Radio Survey

Discone Antenna Scan Results Plus Other Tests 20th July 2024

Written: Stephen Bentley

Date: 26th July 2024

1.0 Preamble

Using the RAS discone antenna and RSPDX software defined radio, a survey was performed over a range of frequencies to assess the level of background radio signals present at the location of the RAS laboratory.

2.0 Equipment Setup

Shown in Figure 1 is an image of the RAS discone antenna located approximately 6 meters above ground near the south-west corner of the radio laboratory.

Figure 2 shows the receiving equipment setup inside the laboratory to perform the observations and screen captures.

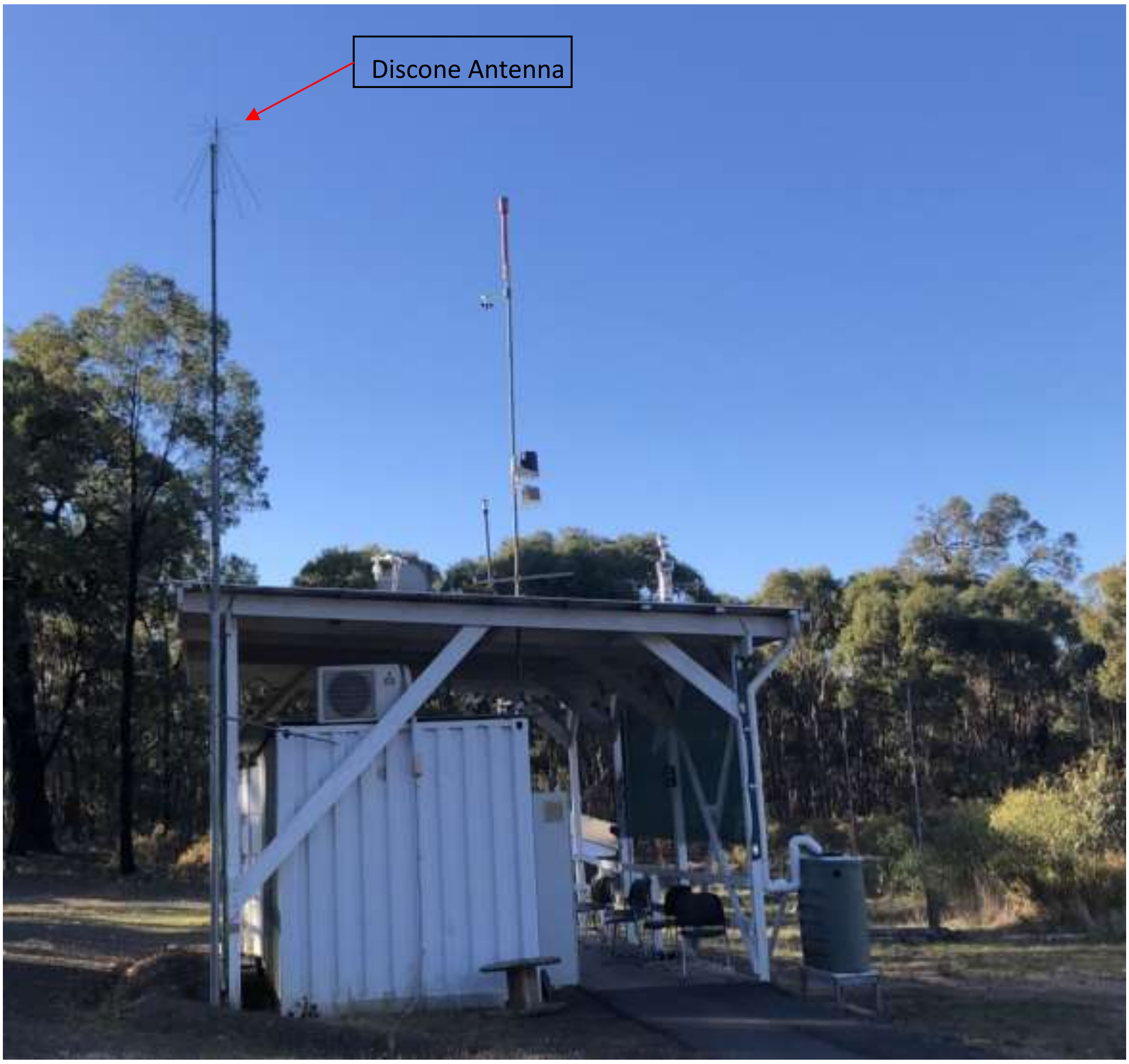

Figure 1. RAS Discone Antenna

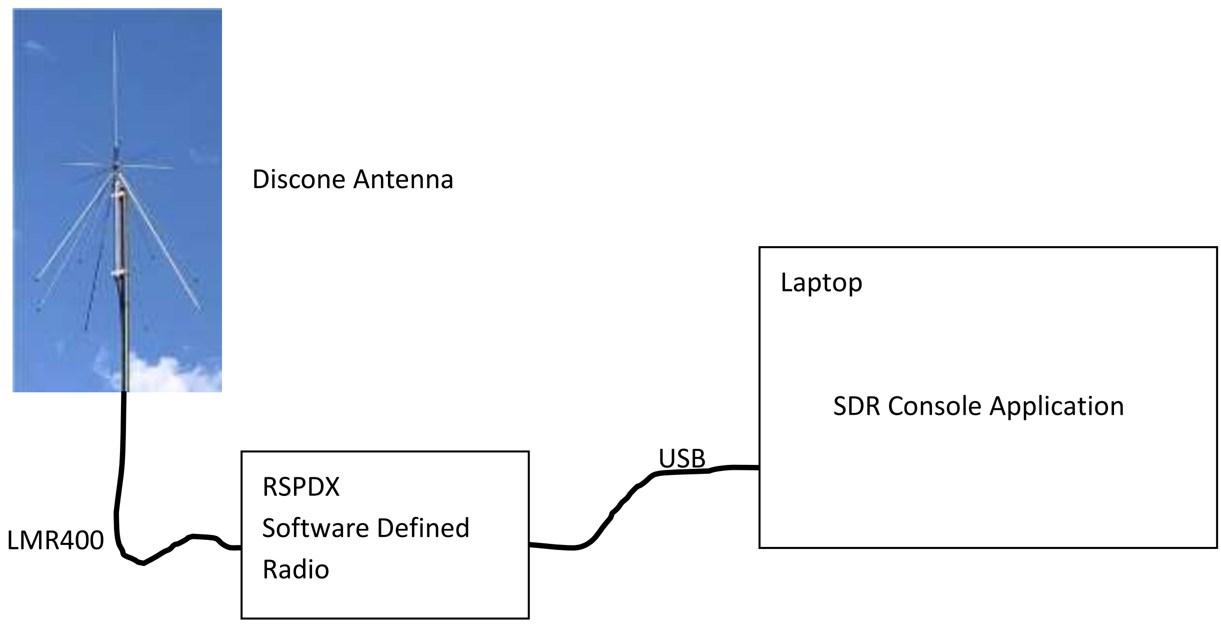

Figure 2. RF Survey Equipment Setup

3.0 Measured Results

A comprehensive assessment of the radio spectrum is difficult to obtain, however an overview survey was performed predominantly using the radio amateur bands. This was done for a number of reasons. Firstly the author's SDR Console program already had the amateur bands pre-programmed thereby enabling a quick re-configuration of the settings to obtain an observation. Secondly, the nature of the signals that should be present on the amateur frequencies is predictable and the "signature" and appearance of the signals are usually easy to identify compared to an unwanted interference signal.

The discone antenna is designed to operate over the frequency range of 30 to 3000 MHz. However, the antenna still provides useful observations of radio frequency (RF) signals down to the medium wave band around 0.5-2 MHz. The RSPDX range of operation is limited to the frequency range of 1 KHz to 2000 MHz. Figures 3 to 18 provide screen captures of the SDR Console at the various frequencies. Each display provides a spectrum and a waterfall display which reveals RF signals in a more visual manner. Notes have been added to the screen captures when an unusual interfering signal is present.

Aperiodic signals such as voice in either the AM mode or single sideband mode can easily be identified as a band of RF with typically 3 KHz bandwidth and an intermittent transmission. Morse code or CW are on/off carrier waves and easily identified. The digital modes are similar to Morse code except there are usually numerous signals very close to each other.

Interference signals

1) **Continuous carrier waves**. It is unusual for a radio amateur to continuously transmit an unmodulated carrier wave. It can be assumed a continuous unbroken vertical line in the waterfall display is a form of interference.

2) **Wobbling vertical lines**. These look like Morse code however when listened to sound like an unstable tone. A common source of these noisy interference lines are harmonics of a switched mode power supply. 3) Bands of noise which appear and disappear in time but repeat. These are potentially RF emissions from a data generator of some form, such as a digital camera which updates the image capture

periodically, or a sensor device which sends its output periodically. There may also be embedded vertical lines within the broadband noise bursts.

0

3) **SDR internal**. The RSPDX like any receiver be it analog or digital, can suffer from internally generated spurious responses. Examples of the SDR internally generated interference signals were observed on several screen captures. The frequency where these products appear will vary as the centre frequency of the receiver is re-tuned or the receiver bandwidth or RF gain is changed.

4.0 Discussion

The SDR Console receiver settings were adjusted to obtain the best contrast on the waterfall display for each observation. The bandwidth was set to 4 MHz but may have been adjusted to 1 MHz for the medium frequency and lower section of the High Frequency band. The RF gain was usually set to 25 dB however at the 1296 MHZ and 1420 MHz band the gain was set to maximum, 27 dB. For the MF and HF bands, the MW/FM notch was set to ‘on’. Above 30 MHz the notch filter was set to ‘off’.

1.8 MHz

At the MF band around 1.8 MHz the discone antenna has a low sensitivity, however the observation indicates very low levels of interference. The random horizontal lines in the waterfall display are created by lightning static.

3.6 MHz

This band is exhibiting more activity which can be seen by several active amateurs using SSB voice and CW Morse code. Lightning static is evident however new phenomenon are apparent being the short bursts in time of a broadband signal.

7 MHz

The amateur activity on this band is extensive with SSB voice, CW Morse code and digital transmission modes of communication all present. There were not many forms of interference observed with the exception of a few feint continuous vertical lines on the waterfall display.

14 MHz

On this amateur band we see similar communication activity as 7 MHz with SSB voice, CW Morse code and digital modes. However, the presence of many more feint vertical lines on the waterfall display indicate interference and there is also a “noisy”, wobbly line which is also an interfering signal.

18 MHz

This band has very little in the way of amateur communications, but the number and strength of interfering signals is more evident seen by the vertical lines on the waterfall display. The “noisy” line interferer is also present.

20 MHz

This band is not an amateur band in Australia. The observation is provided as the frequency of 20.1 MHz is used to study radio emissions from Jupiter using the RAS radio Jove project. Unfortunately, there is evidence of various forms of radio interference around the Jove receive frequency. There are numerous continuous carrier wave lines on the display, the “noisy” interferer and repeating patterns of broadband noise interference.

21 MHz

At this frequency band there is a small amount of amateur communication mainly in the form of the digital modes. However, we also see the same pattern of interference as seen at 20 MHz.

25 MHz

On this band we see the spectrum clear up to some extent. The strong signal centered on 24.98 MHz appears to be a commercial data communication signal.

28 MHz

This band has very little in the way of amateur communications but contains numerous interfering signals seen by the vertical lines on the waterfall display. There are approximately 6 lines for every 100 KHz on the display indicating the interference signal may have a fundamental frequency of about 17 KHz.

52 MHz

Like 28 MHz this band has little or no amateur communications but contains numerous interfering signals seen by the vertical lines on the waterfall display.

70 MHz

This is not an amateur band but includes the 70 MHz downlink frequency of the neutral hydrogen receivers of the horn and dish antenna. Here there are numerous lines on the waterfall display, however it is not known if some of these are for commercial communications. What can also be seen is a grouping of vertical lines which disappear near the top of the screen. This was observed and timed, and the interfering pattern was active for 23 seconds and inactive for 7 seconds. This might be evidence of a data burst where for instance, a digital image is sent from one of the several security cameras or the all sky camera on the lab roof. The "noisy" interferer can also be seen on this display.

146 MHz

Not much amateur communication can be seen however once again, the on-off pattern of interference can be seen above 146.5 MHz. The pattern or lines also appear to be independent of the other broadband interference. **220 MHz**

This is not an amateur band in Australia. Interference signals are also present on this band.

430 MHz

This UHF amateur band is not showing much activity and many of the interfering lines are much fainter now at this higher frequency. The broadband repeating pattern interference however is still very evident and quite strong.

1296 MHz

Not much activity or interference can be seen on this display.

1400 MHz

This is not an amateur band but includes the neutral Hydrogen frequency of 1420.405 MHz. Fortunately, not much interference can be seen at these frequencies.

5.0 Additional RF Survey

The author performed a field RF survey at the radio Jove antenna system. The Jove antenna was disconnected from the coax cable running back to the laboratory. The author's IC706 amateur radio transceiver was connected directly to the Jove antenna and used in receive only mode to observe off-air signals around the Jove emission frequency of 20.1 MHz. The receiver was operated on battery power and had no other connection apart from the antenna.

No written record of the observation was obtained however short videos were captured. The receiver was set to both the AM mode and the SSB mode of demodulation. The receiver was tuned from about. 19.87 MHz to 20.56 MHz to observe any notable signals.

There were several terrestrial signals observed such as the WWV time clock on 20.000 MHz, a few intermittent commercial data transmissions and the spectrum sweeper. However, an unusual signal on 20.113 MHz contained several closely spaced carrier signals and was unexpected although at the time of the observations was not considered significant. There was also a strong carrier wave signal on 20.96 MHz. The problem will be that these interferers are very close to the NASA inspire Jove receiver frequency of 20.1 MHz and are likely to appear in the receiver.

A more detailed follow up, field observation using this method is required.

6.0 Conclusion

From this overview it is clear there are several forms of strong radio interference signals around the RAS laboratory. The interference is present over a very wide range of frequencies from 3 MHz to 430 MHz. The interference can appear as listed below.

1) Continuous carrier wave lines on the waterfall display.
2) Continuous wobbly lines on the waterfall display.
3) Broadband intermittent but repeating noise bursts.
4) Broadband intermittent but repeating noise bursts with embedded continuous carrier wave lines.

The character of the interfering signals with wobbly carrier waves, and continuous carrier waves are typical of switched mode power supplies. The intermittent or repetitive noise bursts or repetitive broadband noises bursts with embedded carrier waves are typical of a data transmission source. Prime suspects for the latter are the all sky camera, the Blitzortung lightning detector, the security cameras and the weather station sensors.

The fundamental frequency of the interference is most likely in the low frequency band or the very low frequency band from 20 KHz to 300 KHz. The interference observed with the software defined radio is therefore harmonics of these fundamentals. The harmonic energy normally reduces at higher frequencies however it is possible to see peaks in harmonic energy from an interference generator if the connected wiring of the equipment becomes a more efficient radiating antenna. This was evident on the 430 MHz band for instance.

Data burst interference may be created by a microcontroller or microcomputer such as a Raspberry Pi (used on the all sky camera). These computers may operate with clock frequencies such as 16 MHz Arduino Uno, 84 MHz Arduino Due, 1.5 GHz Raspberry Pi 4, 2.4 GHz Raspberry Pi 5.

7.0 Future Action

To track down the source of the interfering signals, it will be necessary to repeat the RF survey however this time deactivate all the experiments connected to the RAS laboratory. Then activate each experiment in turn to observe if interference is generated from the experiment.

If interference is still evident it may be necessary to arrange for the new astrophotographic domes to be temporarily deactivated. If the observations were performed during daylight hours the disruption should in principle have no impact on astrophotography.

Remedial action for identified interference may take the form of improved shielding and grounding, in-line filters to the equipment cabling, or re-location of the equipment to another location on the LMDSS, particularly if the experiment/equipment is not related to radio astronomy.

The field test at the Jove antenna using a battery powered receiver is also recommended once the RAS laboratory experiments are all deactivated. A record of the Jove receiver antenna results should then be obtained and as a preference, it should be arranged that the new astrophotographic dome equipment be deactivated at the same time to ensure the northern end of the LMDSS is very much inactive from any potential source of radio interference generators.

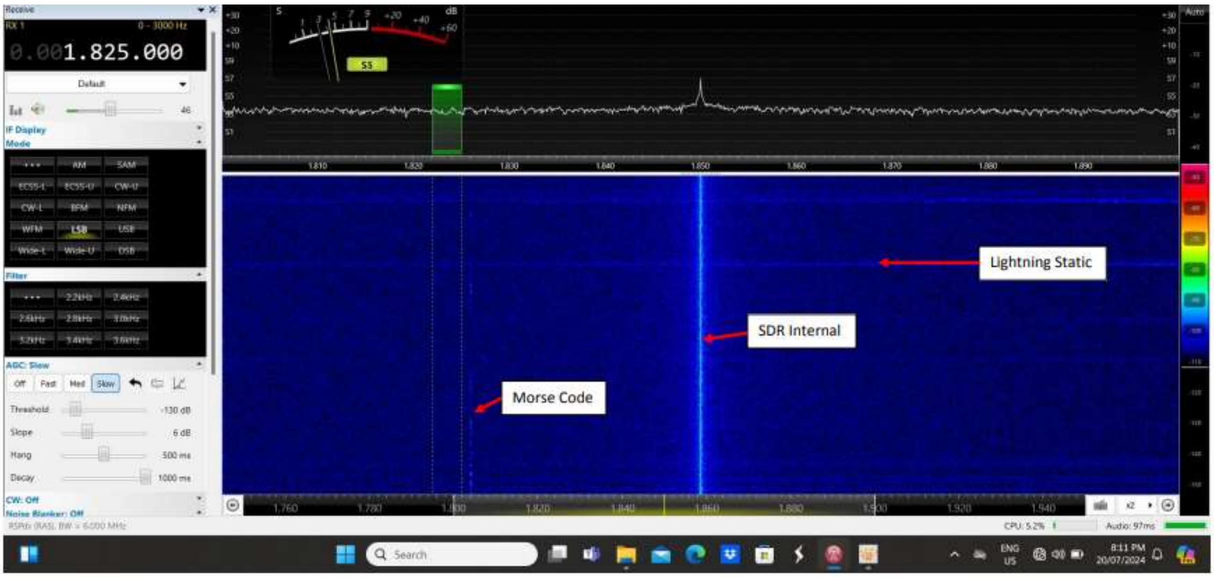

Figure 3. Screen Capture 1.8 MHz Band

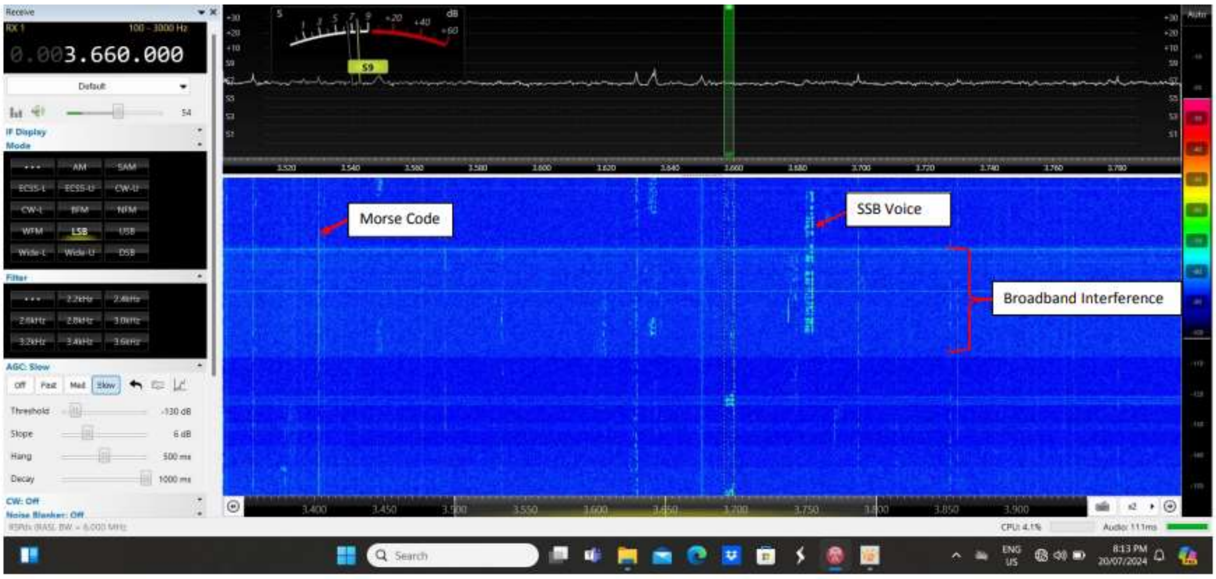

Figure 4. Screen Capture 3.6 MHz Band

Figure 5. Screen Capture 7 MHz Band

Figure 6. Screen Capture 14 MHz Band

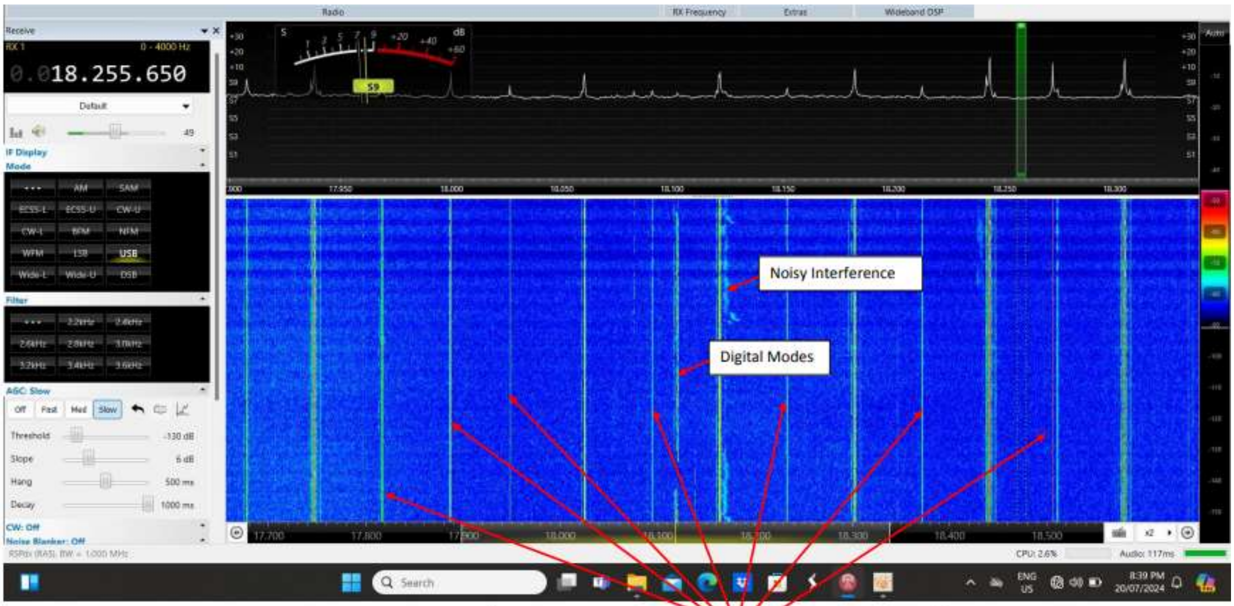

Figure 7. Screen Capture 18 MHz Band

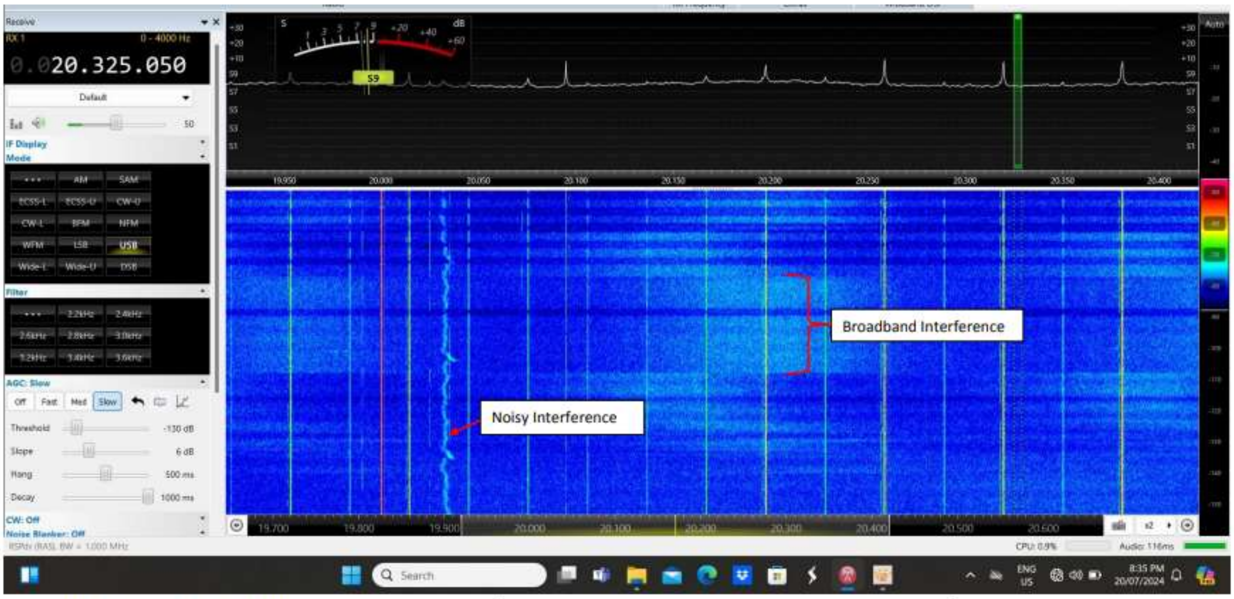

Figure 8. Screen Capture 20 MHz Band

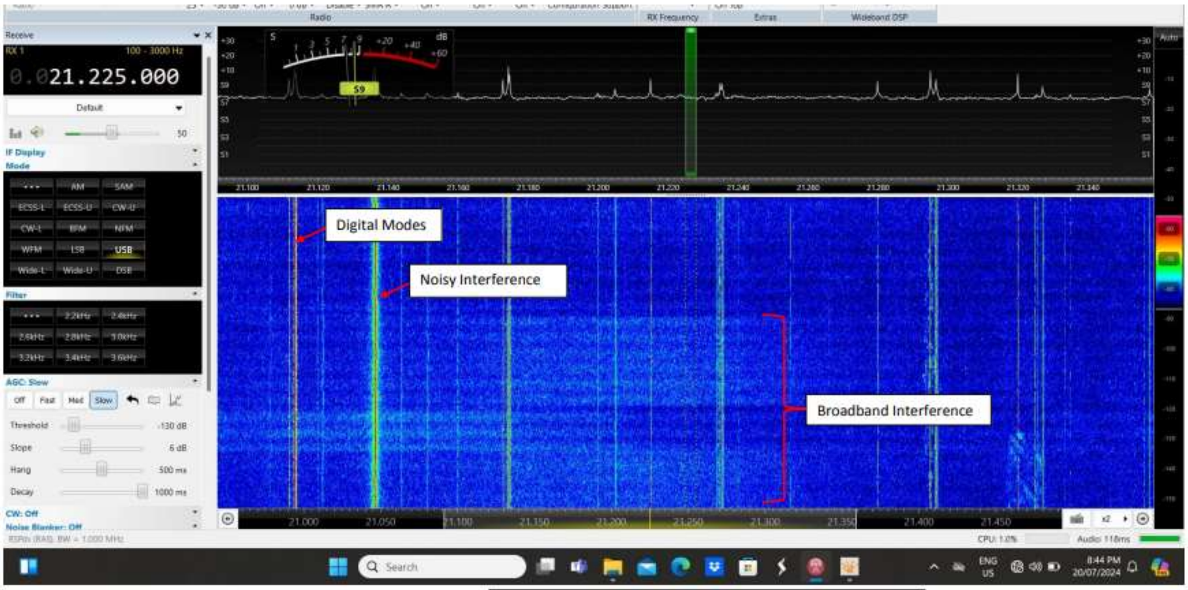

Figure 9. Screen Capture 21 MHz Band

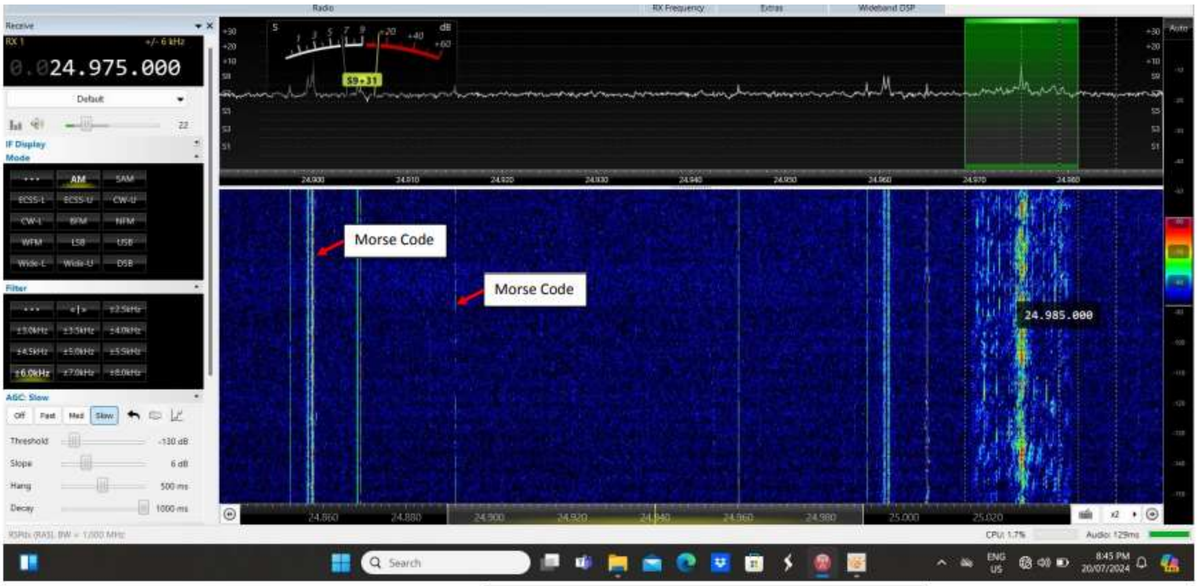

Figure 10. Screen Capture 25 MHz Band

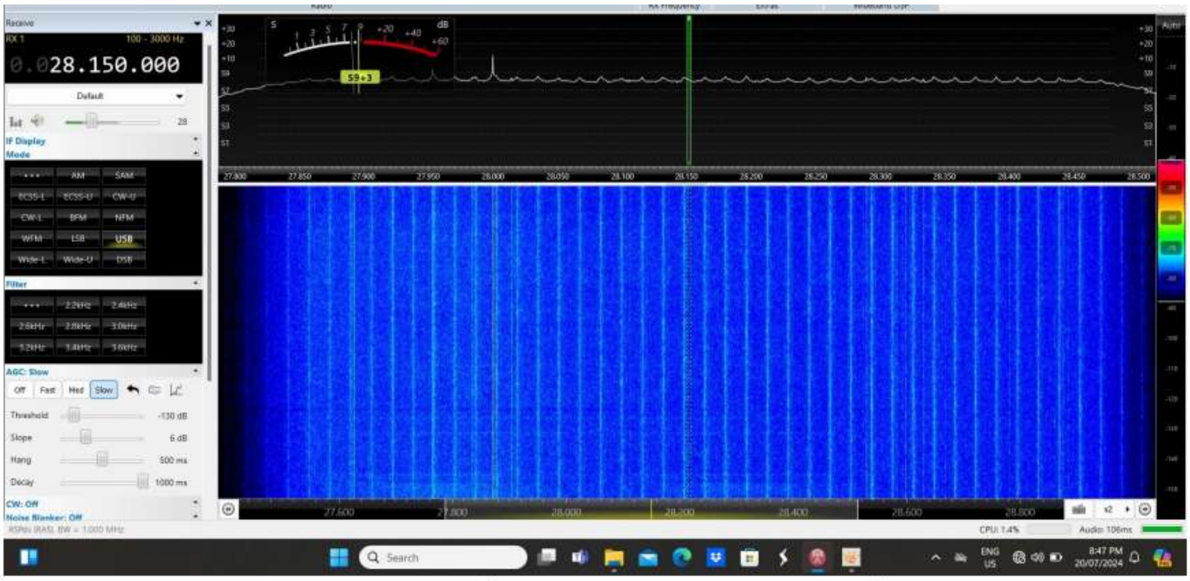

Figure 11. Screen Capture 28 MHz Band

Vertical Lines Potential Carrier Wave Type Interference

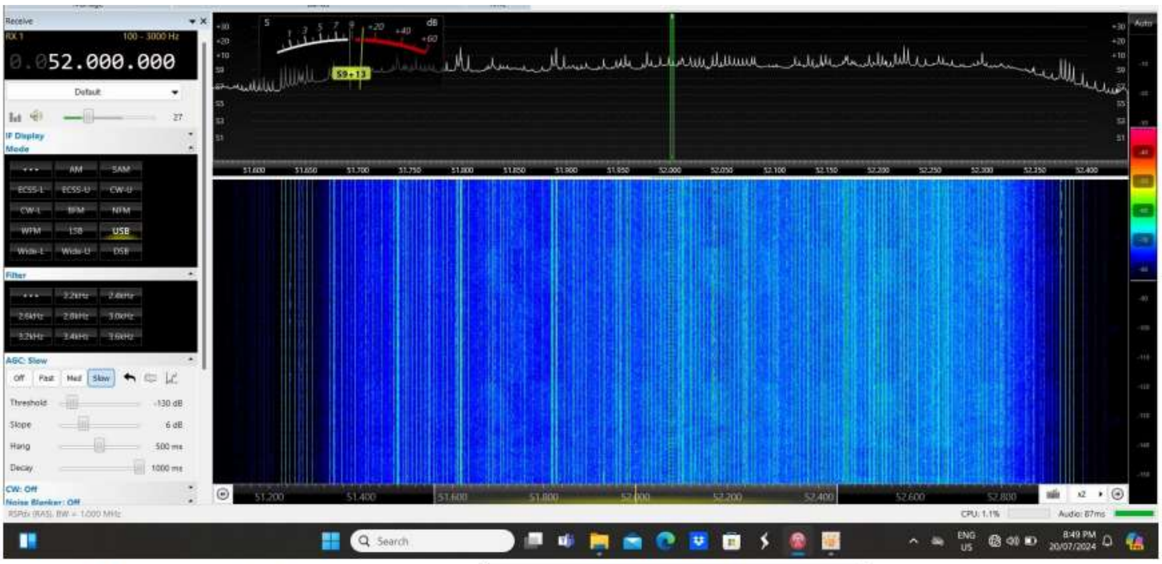

Figure 12. Screen Capture 52 MHz Band

Vertical Lines Potential Carrier Wave Type Interference

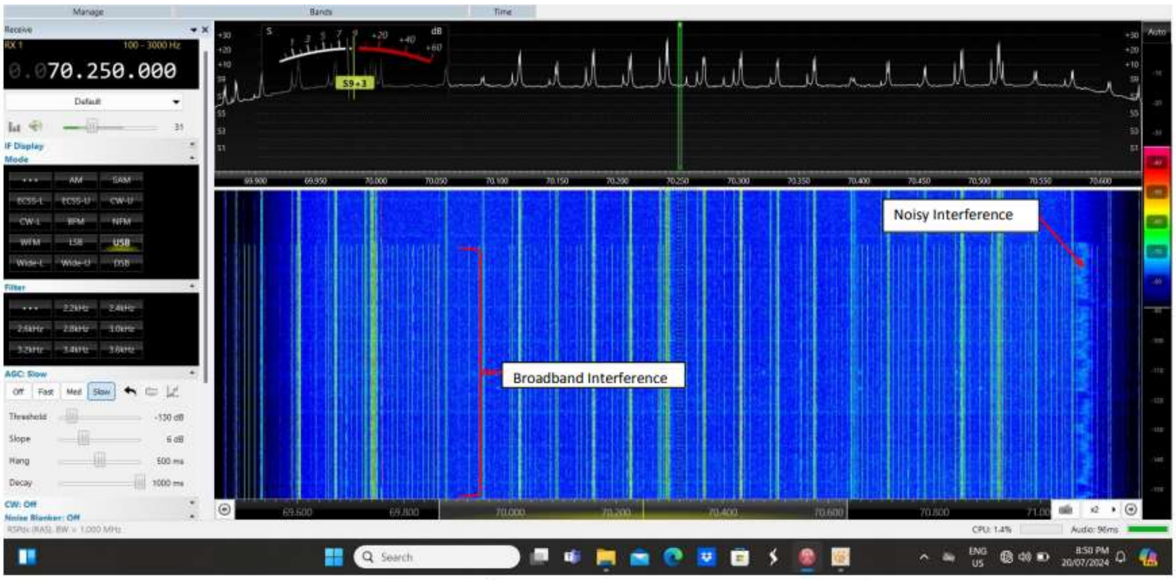

Figure 13. Screen Capture 70 MHz Band

Vertical Lines Potential Carrier Wave Type Interference

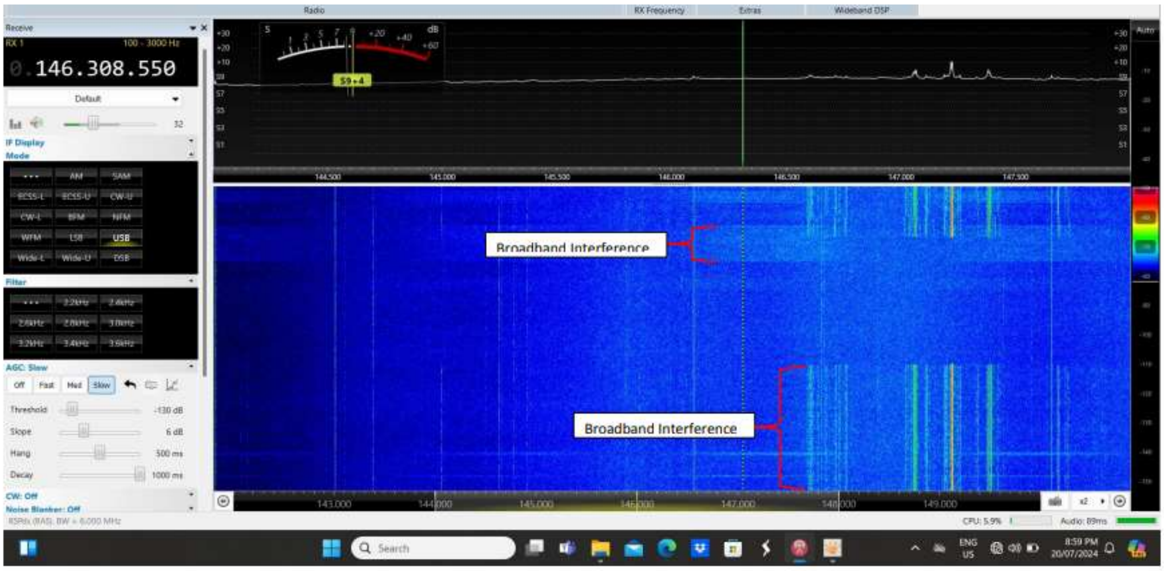

Figure 14. Screen Capture 144 MHz Band

Vertical Lines Potential Carrier Wave Type Interference

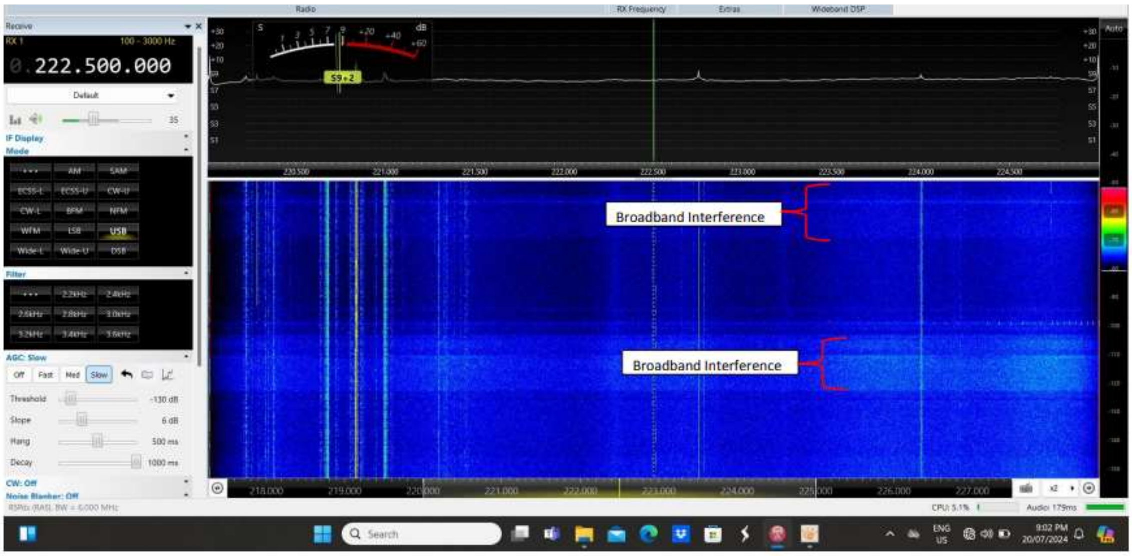

Figure 15. Screen Capture 220 MHz Band

Feint Vertical Lines Potential Carrier Wave Type Interference

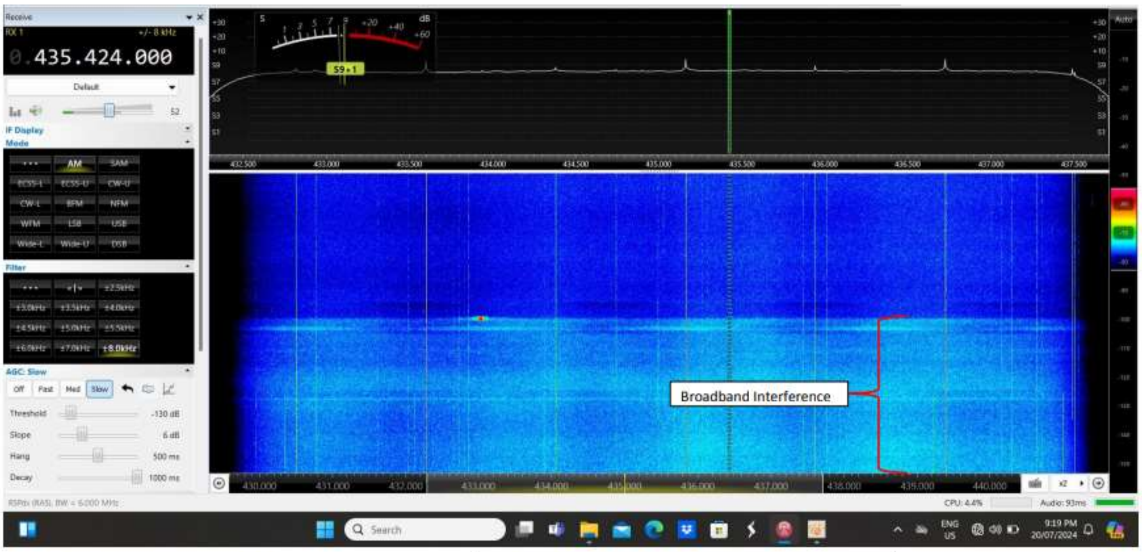

Figure 16. Screen Capture 432 MHz Band

Feint Vertical Lines Potential Carrier Wave Type Interference

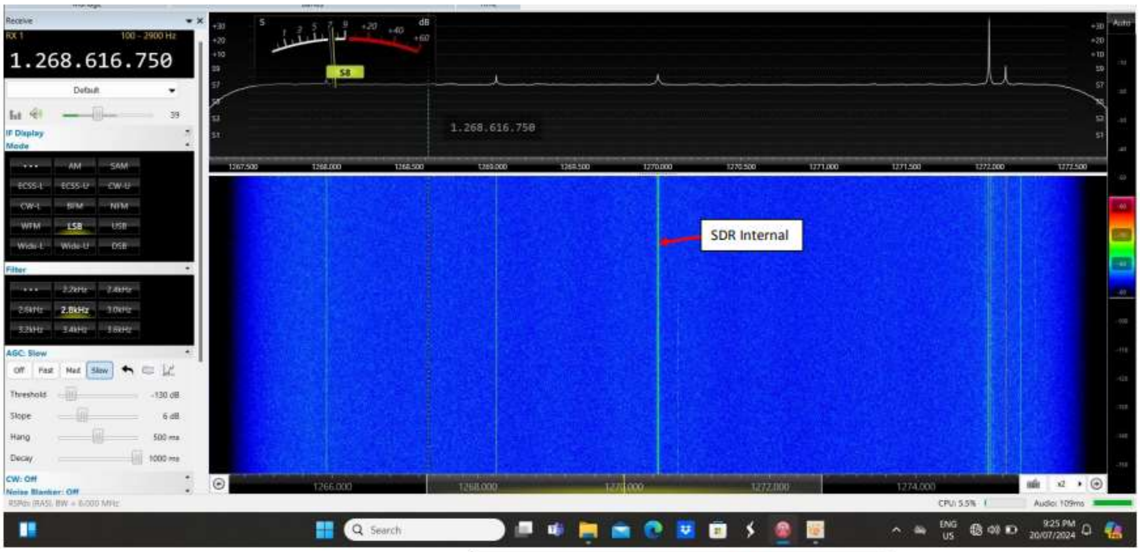

Figure 17. Screen Capture 1296 MHz Band

Feint Vertical Lines Potential Carrier Wave Type Interference

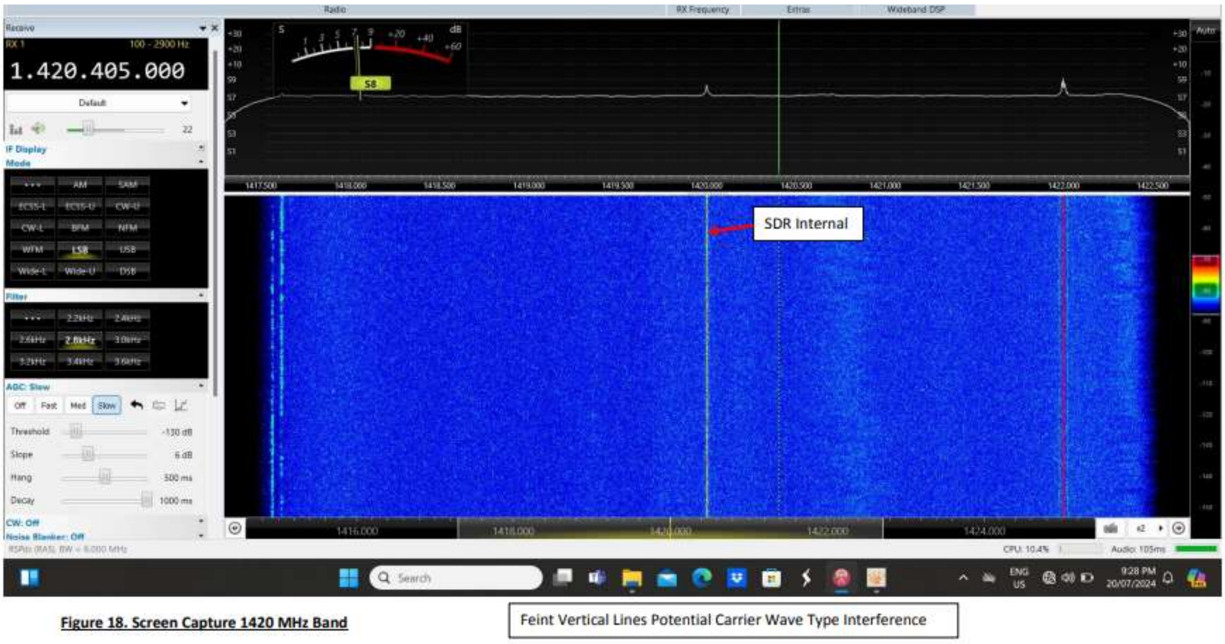

Figure 18. Screen Capture 1420 MHz Band

RAS Discone Antenna

Written: Stephen Bentley

Date: 1st Feb. 2024

1.0 Preamble

The RAS (Radio Astronomy Section) has purchased a wideband receiving (and transmitting) antenna for use at the LMRO (Leon Mow Radio Observatory). The author was interested in owning a similar antenna for home use and also purchased one and performed a range of tests. This report provides an assessment of the antenna and its capabilities and practical applications at the LMRO.

2.0 LMRO Applications

As well as the discone antenna, the RAS has also obtained a software defined radio (SDR) receiver, the RSPDX. An image of the RSPDX may be seen in Figure 1. This receiver product was obtained some time ago in 2023 and has been used to demonstrate the neutral hydrogen signals on 1420 MHz at star parties. The very sensitive SDR has the receive frequency range of 1 KHz, to 2000 MHz. Yes, it's an extraordinary receiver and has many high performance capabilities. SDR technology is the latest in terms of radio frequency receivers (and transmitters) and has also become a key component in modern radio astronomy systems. The author believes the RAS team needed a comparable receive antenna that made the most of the SDR capabilities. A summary of the applications of the SDR and discone antenna combination is presented below in Table 1.

1. Demonstration of modern receiver technology (SDR), also applicable to radio astronomy.
2. Tracking down local radio interferers that may degrade the various radio astronomy experiments operating at the LMRO.
3. Observation and demonstration of terrestrial communications such as commercial, broadcast, emergency services, aircraft and amateur radio communications.
4. 2-way amateur radio communication demonstrations using local VHF/UHF amateur repeater systems.

3.0 The Discone Antenna 3.1 Antenna Description

The discone antenna is self-described by its name, disc – cone. The antenna is constructed using a disc structure above a cone structure. Ideally both the disc and the cone should be solid, however in practice this is unnecessary and creates a higher weight and wind loading. Therefore, the typical discone antenna is constructed using wire radials and performs just as well as a solid antenna provided the range of operation is limited to the wavelengths formed by the wire structure.
Figure 2 provides a photograph of the author's discone installed at the home location.

The model the RAS has purchased is the D3000N. The frequency range of operation specified by the manufacturer is from 25 to 3000 MHz. The antenna has an omni-directional radiation pattern which is vertically polarized and has a nominal gain of 2 dBi (0 dBd). The additional feature of this antenna is that the tuning has been optimized for transmitting on specific amateur radio frequency bands of 6m (52 MHz), 2m (144 MHz), 70cm (432 MHz) and the 23cm band (1296 MHz) where transmit input power of up 200 Watts is possible.

The version the author has obtained is the D130NJ which has a frequency range of 25 to

1300 MHz. This report will mainly provide performance information relating to this version. The RAS version has the capability of receive up to 3GHz which may be of interest since it will allow observation of the radio spectrum around the neutral Hydrogen frequency of 1420.405 MHz.

Figure 1. RSPDX Software Defined Radio

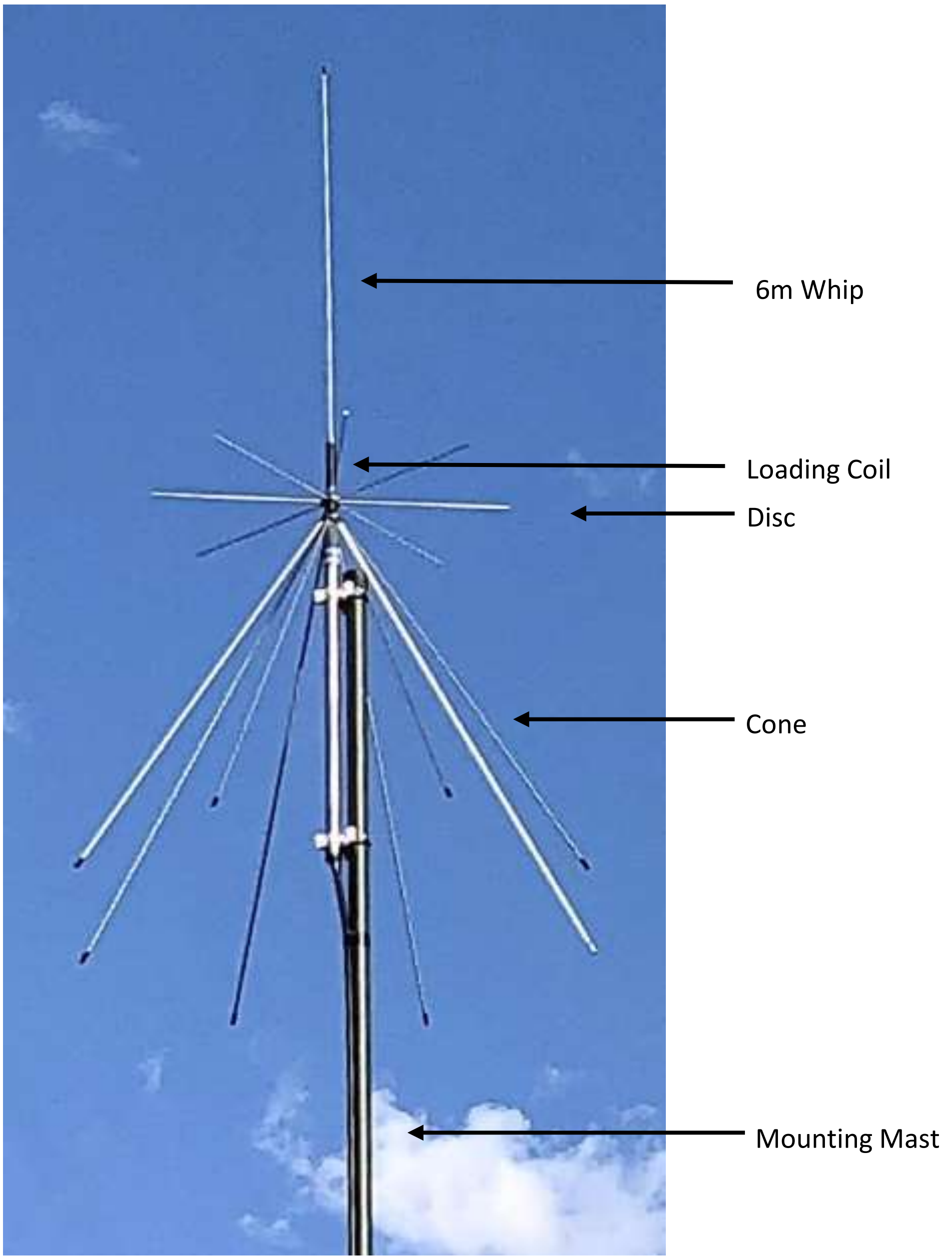

Figure 2. D130NJ Discone Antenna

The author's D130NJ discone is really 2 antennas in one. As can be seen in Figure 2, the antenna has the disc section realized by 4 cross radial wires which are horizontal and parallel to the ground. The cone is realized by 8 downward sloping radials. The additional vertically polarized whip with base loading inductor (coil) above the disc is provided for the 6m (52 MHz) amateur radio frequency band. This part of the antenna is an optional extra and it may be removed if the user does not require operation over the frequency range of 25 to 50 MHz.

Figure 2 also indicates the discone antenna is mounted on a vertical mast or pole. Because the main operational performance of the antenna is on the VHF and UHF frequency bands, the discone should be mounted as high above ground as practical. This is because most terrestrial communication on VHF and UHF is "line-of-sight" and range will be greatly improved by mounting the antenna as high as possible in order for the antenna to project out to the horizon as much as possible.

3.1 Antenna Theory

To help understand how the discone antenna works it may be worthwhile providing a brief discussion on antenna theory. What is an antenna? An antenna is a device that provides an optimum coupling of radio frequency energy between a receiver or a transmitter to free space. It is often better to express how an antenna works as a transmitting antenna. This way the language is more in terms of input feed impedance and radiation pattern rather than the reverse which is for a receiver. However, the antenna is reciprocal so transmitting language is valid. The other component of an antenna system is the feeder cable. The aim of the feeder cable is to transfer energy from the transmitter (or receiver) with a minimum loss of power. This is achieved by defining the characteristic impedance of the feeder to have an impedance equal to both the transmitter and the antenna. An impedance matched feeder cable will therefore exhibit no "standing waves". If a feeder is mismatched to the antenna a reflection occurs and standing waves will develop in the feeder cable and transmission loss will occur. A small impedance mismatch will not cause a significant transmission loss. For example, a 2:1 VSWR will only cause a transmission loss of about 0.5dB (11% power loss). To put this into perspective, for most communication systems a 3 dB loss or a drop of power by one half, is considered significant. The formula for transmission loss is shown in equation i) below.

i) Mismatch Loss dB = $-10 \times \text{Log}_{10}(1 - R^2)$

Where R is the reflection coefficient.
R = (VSWR – 1) / (VSWR + 1)

Example: A 2:1 VSWR, R = (2 -1) / (2 +1) = 0.33
Therefore, mismatch loss = $-10 \times \text{Log}_{10}(1 - (0.33)^2) = -0.51$ dB

Figure 3 shows the classic half wavelength dipole (λ/2) antenna illustrated by the solid black lines. This is a well-known antenna design and is currently being used with the radio Jove receiver. The λ/2 dipole requires a balanced feeder cable illustrated by the solid orange lines. At resonance the half wave dipole will exhibit the voltage (V) and current (I) distribution along the wires as indicated. The current maxima will occur in the centre of the dipole and diminish to a minimum at the ends of the dipole. The voltage will be at a minimum in the centre and increase to a maxima at each end of the dipole and there will be a phase reversal of the voltage from one end of the dipole to the other. At the dipole centre (feed point) the input impedance will be a real resistance without any imaginary or reactive component and is defined by Ohms law R = V/I. For the case of the λ/2 dipole the input impedance is **73 Ohm**.

As indicated also in Figure 3, the λ/2 dipole is typically oriented horizontally as shown on the left or vertically as shown on the right. The radiation pattern emerging from a λ/2 dipole has a maximum at the centre where the current is also at maxima. Figure 4 helps illustrate the radiation pattern. Therefore, the horizontally polarized dipole has an omni-directional radiation pattern which delivers a maximum energy in a doughnut shape that aims energy to the ground as well as the hemisphere of the sky. The antenna pattern however has nulls in the directions aimed out in the direction of the ends of the wires.

The requirement of a balanced feeder to the λ/2 dipole is often inconvenient therefore a "balun" is typically used. A balun is an abbreviation of "balanced to unbalanced". A balun may take a number of forms such as a transformer where the input and output of the transformer are not directly connected but are mutually coupled therefore the RF energy is transferred and one side of the transformer can be symmetrically connected to the dipole and the other side may be connected to an unbalanced feeder such as a coaxial cable. A standard coaxial cable is available with a characteristic impedance of 75 Ohms. This is very close to the 73 Ohm of the antenna and therefore a 1:1 transformer will be required. Another form of balun is the choke balun where direct connection between the input and the output is maintained however the RF currents that would normally flow on the outer of the coaxial cable are choked off by a suitable inductance.

Figure 5 provides examples of a transformer balun and a choke balun. The choke balun has the advantage that at least one leg of the dipole may be grounded for the protection against static build up or lightning. In Figure 5 an example of a choke balun is shown where the 75 Ohm coaxial feeder cable is simply wound over a suitable ferrite toroid core creating a high inductance at radio frequencies.

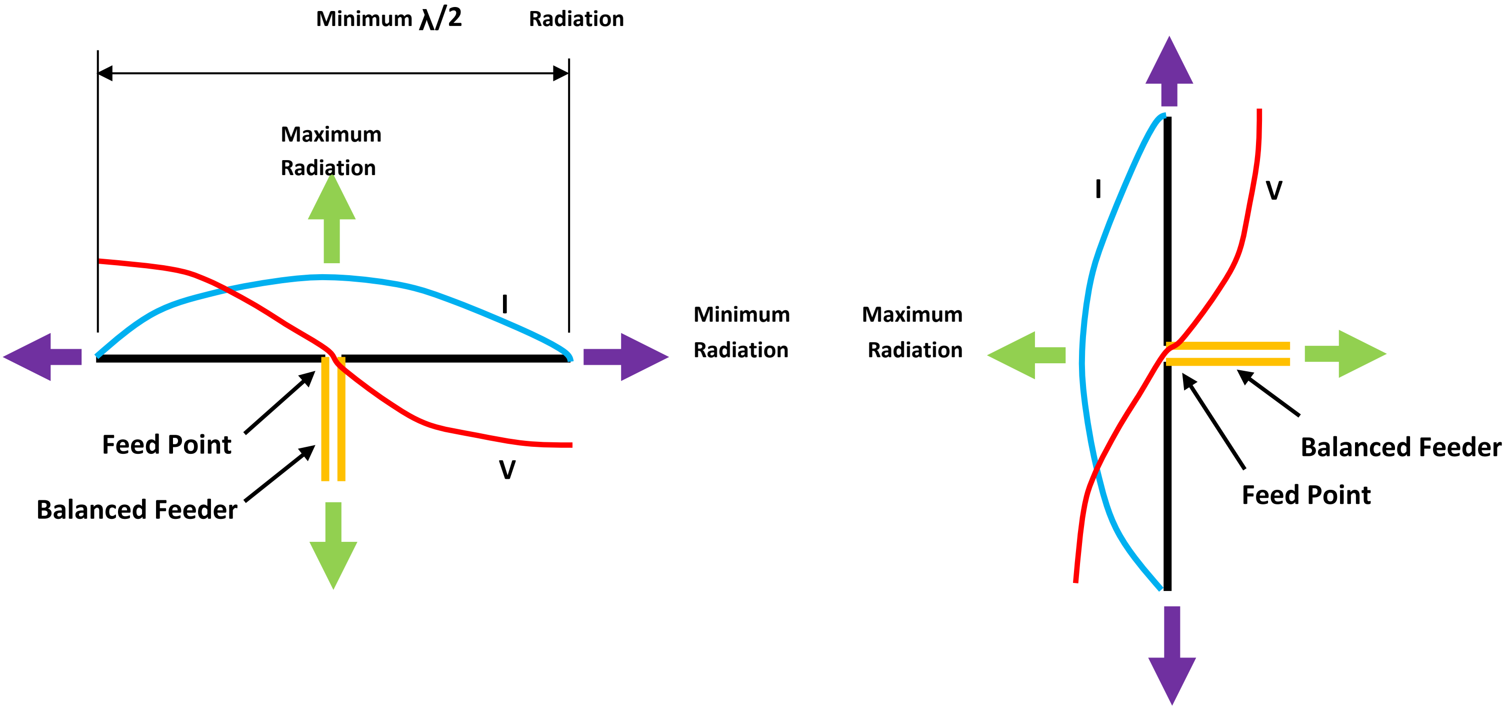

Horizontally Polarized λ/2 Dipole

Vertically Polarized λ/2 Dipole

Figure 3. Classic Half-Wave Dipole Antenna

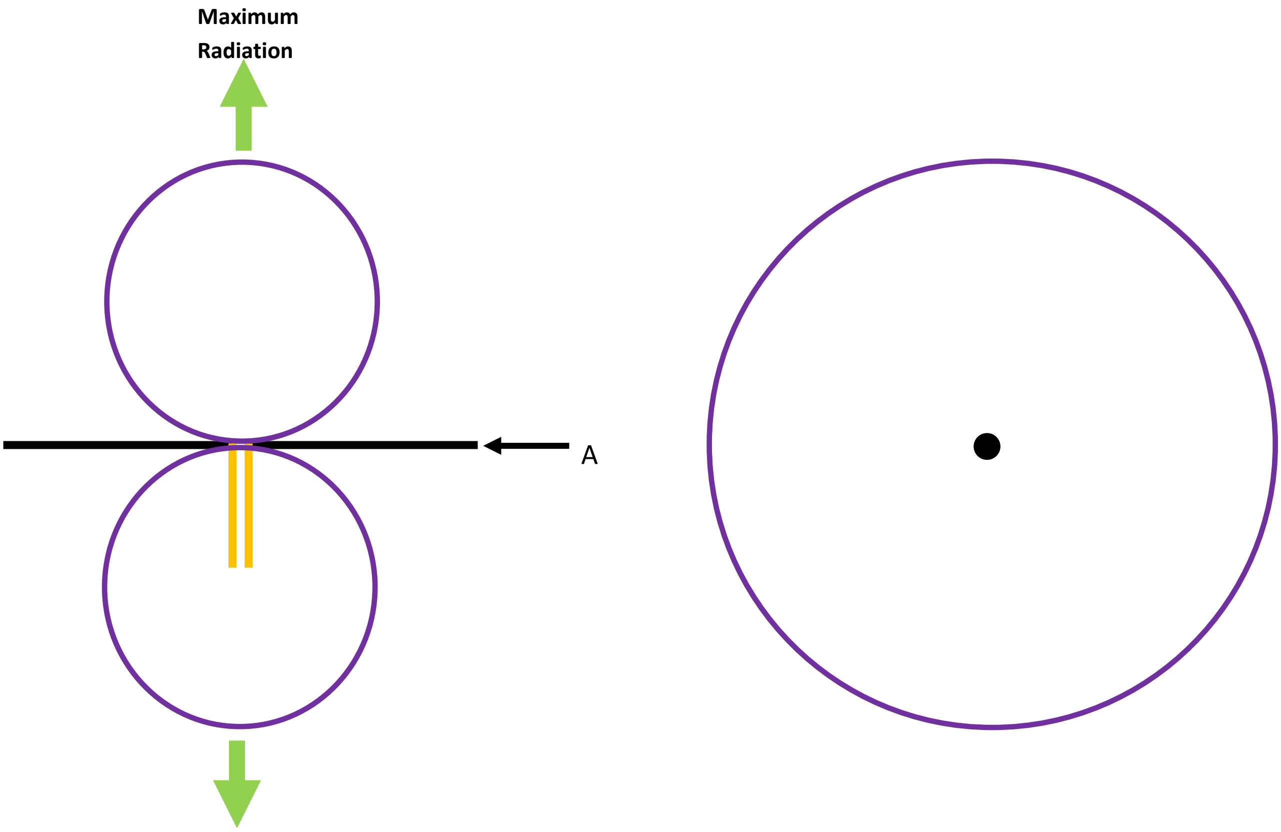

Side View

View A

Figure 4. Horizontal Half-Wave Dipole Antenna Radiation Pattern

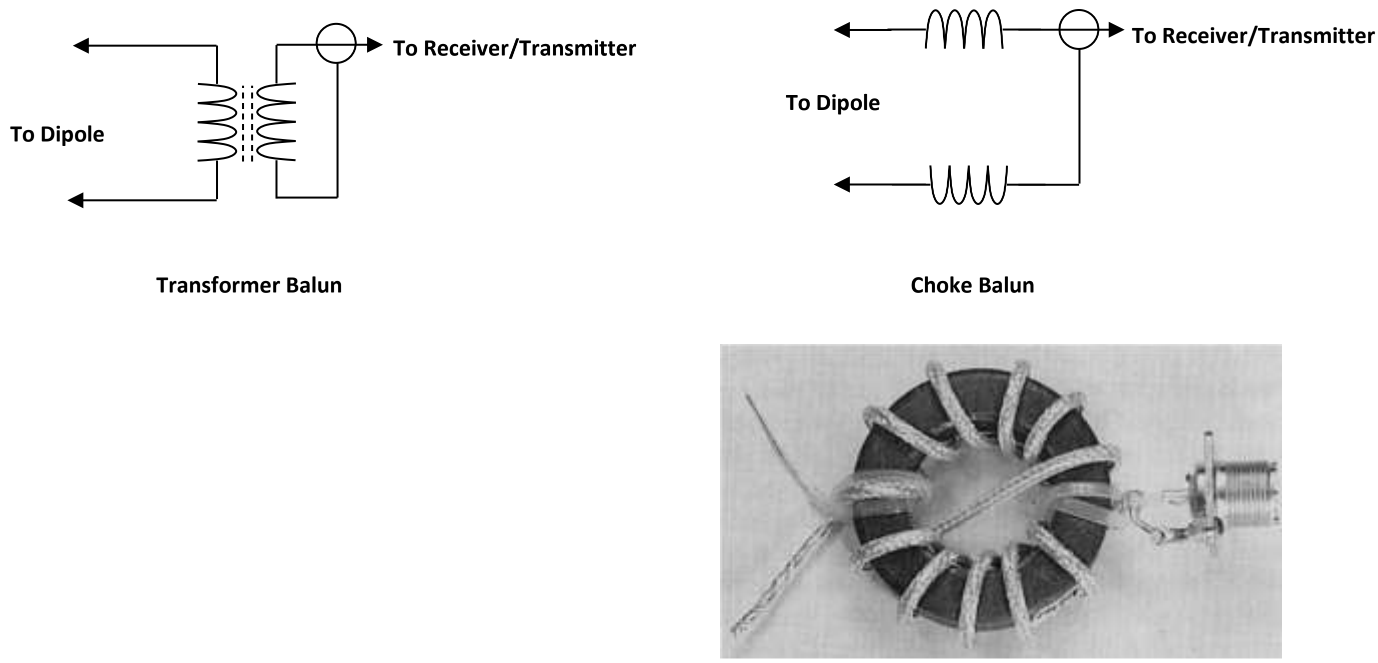

Figure 5. Balanced to Unbalanced Antenna Coupling

Another simple form of antenna is the monopole as opposed to the dipole. As the name suggests, the monopole consists of one half of a half wave dipole and is therefore one quarter wave (λ/4) long. The monopole requires a ground at right angles to the orientation of antenna. Shown in Figure 6 is a diagram of the quarter wave monopole antenna and the radiation pattern for the monopole is shown in Figure 7.

The λ/4 monopole is referenced to a ground plane which may be the earth for low frequency antennas however for VHF and UHF is typically realized by an artificial ground plane such as a flat metal sheet like a tin roof, the metal roof of a car, bus, truck or train or a simulated ground realized by radial wires instead of a solid metal sheet. An example of a quarter wave ground plane vertical antenna is shown in Figure 8. In this example the ground plane has been realized by 2 cross wires at the base of the vertical antenna section and provided the overall length of the ground plane wires are greater one half wavelength at the required frequency, this antenna will perform just as well as if the ground plane was an infinite flat sheet of metal.

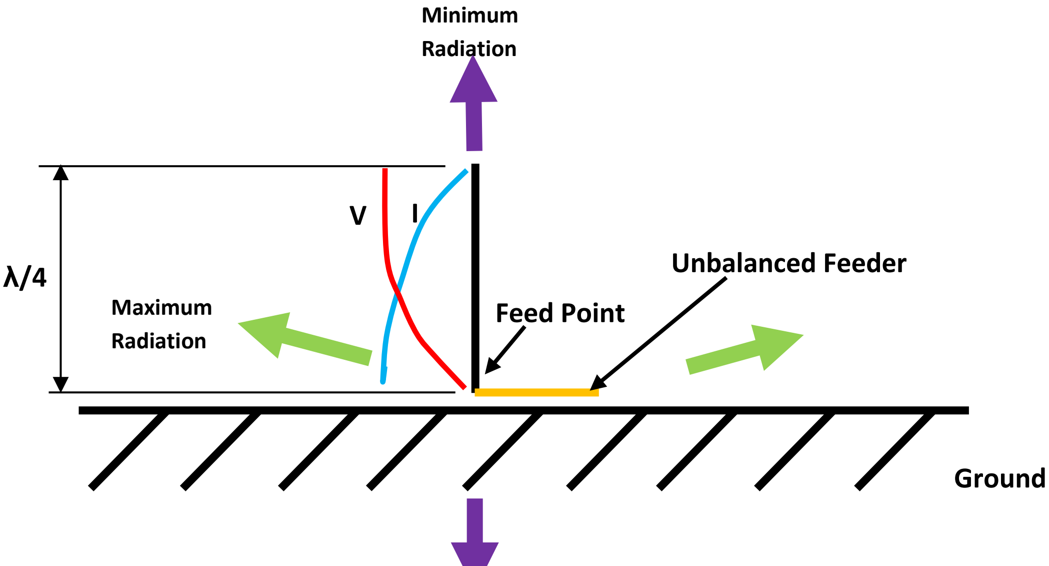

Figure 6:One Quarter Wave Vertical Antenna

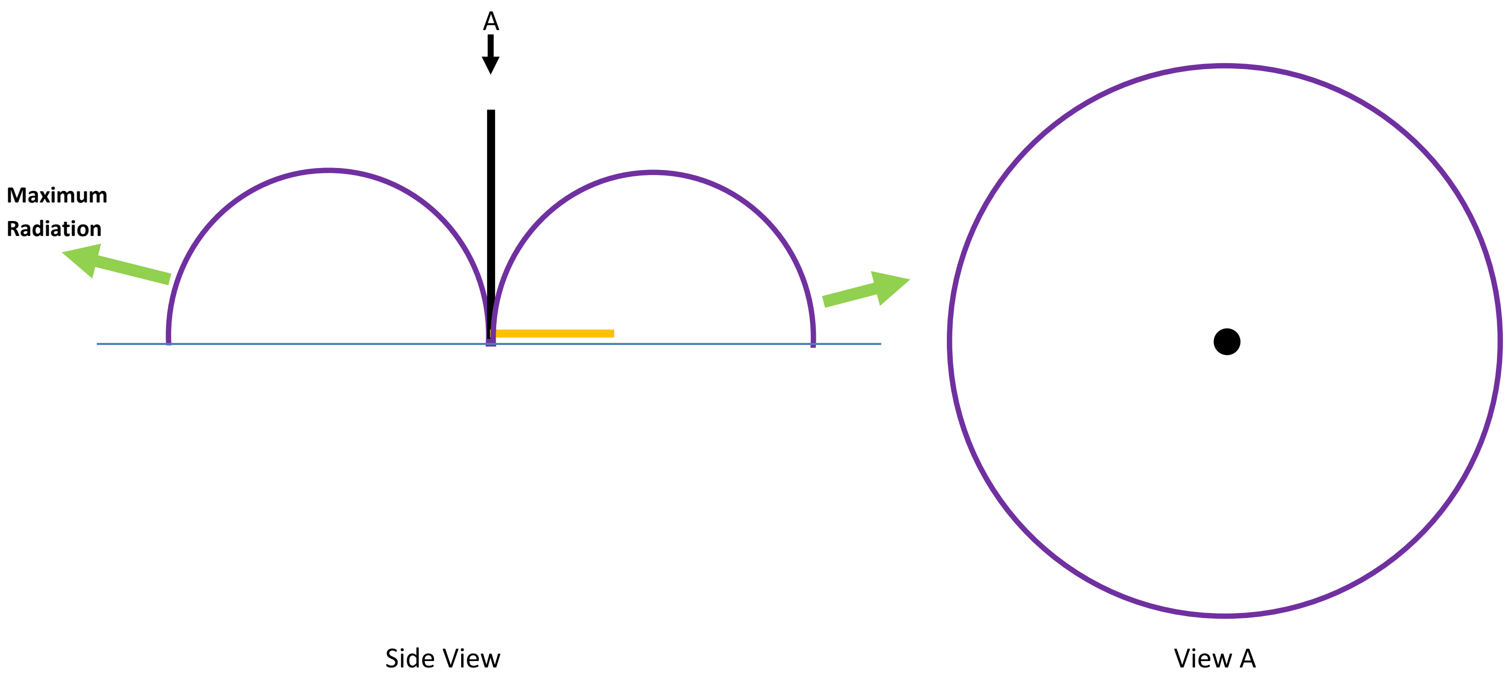

Figure 7. Quarter-Wave Monopole Antenna Radiation Pattern

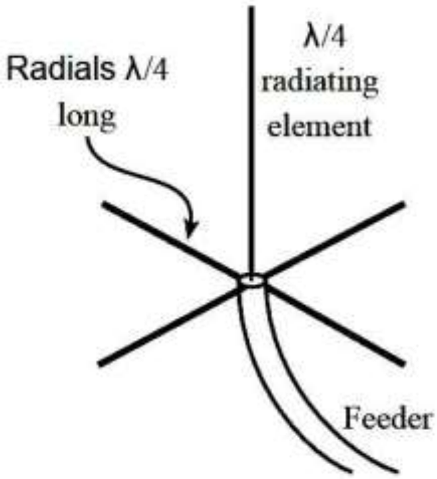

Figure 8. Example λ/4 Ground plane Vertical Antenna

The radiation pattern from the λ/4 ground plane vertical in practice has its maximum slightly above the horizon due to the imperfect nature of the ground plane. Some references claim the angle may be as high as 30 degrees. The feedpoint impedance of the λ/4 vertical is approximately **36.5 Ohm** which is half that of the λ/2 dipole. Coaxial cables are not manufactured with this characteristic impedance therefore an impedance mismatch will occur when using a 50 Ohm cable. The VSWR that results is about 1.4 : 1 however the transmission loss is only -0.1 dB. A neat trick which raises the feedpoint impedance is to bend the groundplane radials down at an angle of about 45 degrees as shown in Figure 9.

When using the downtilted radials the feedpoint impedance is raised and becomes very close to a 50 Ohm match.

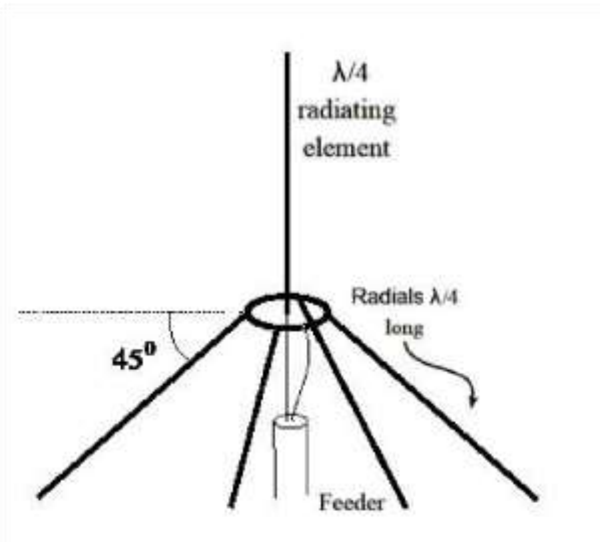

Figure 9. Example λ/4 Vertical Antenna with Down Sloping Groundplane Radials

If it is inconvenient to have a full scale quarter wavelength vertical it is possible to shorten the vertical wire. The input feed point will however become capacitively reactive and also lower in real resistance at the required frequency. To cancel the capacitance an inductance can be placed in series with the vertical element as shown in Figure 10. This is often referred to as a loading coil. The discone antenna has included a vertical element above the discone part of the antenna for the lower frequency range and specifically for optimum impedance match at 52 MHz. The length of the vertical whip is 725 mm which is a quarter wavelength at 103 MHz hence the loading coil at the base of the whip to make the input impedance a correct match at 52 MHz.

The shortened vertical will still have much the same radiation pattern as shown in Figure 7 however the gain of the shortened vertical will be slightly less than a full quarter wave antenna.

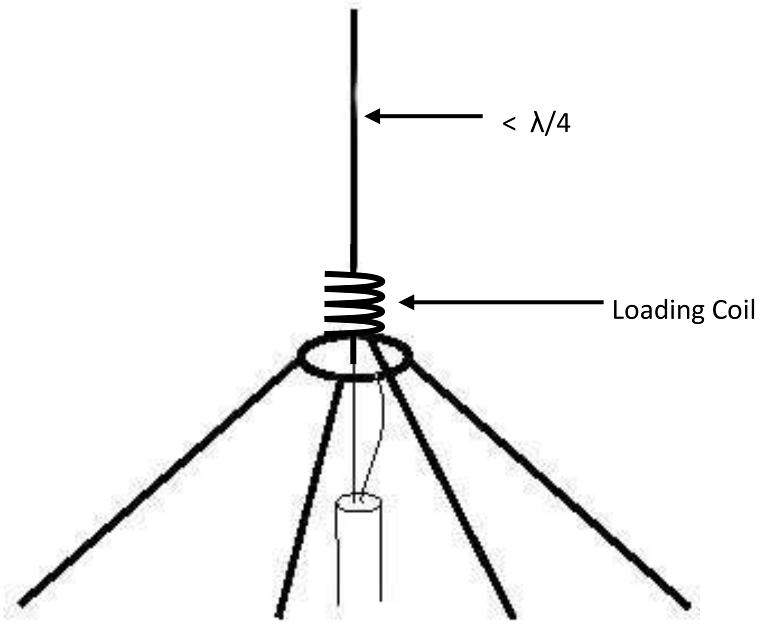

Figure 10. Example Shortened λ/4 Vertical Antenna with Base Loading Coil

Bicone Antenna

Before the discone is explained, it is best the bicone antenna is first addressed. Shown in Figure 11 is an example of a bicone antenna.

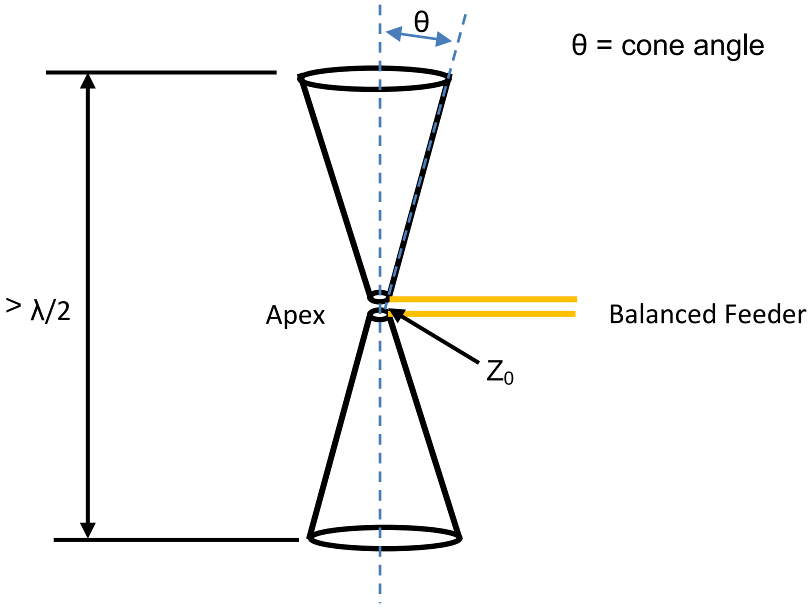

Figure 11. Bicone Antenna Configuration

The bicone antenna has a symmetrical configuration and looks similar to the dipole. The exception being that the antenna elements are cones rather than wires.
The input impedance of the bicone may be calculated using the formula shown in ii)

ii) Input Impedance = Z_0 = 120 Log_e Cotangent (θ/2)
(Formula obtained from Electromagnetic Waves and Radiating Systems by E. C. Jordan and K. G. Balmain)

for example: θ = 30 degrees

Therefore Z_0 = 120 x Log_e (1/ Tan (30/2)) = **158 Ohm**.

The characteristic input impedance should remain constant over a wide frequency range provided the length of the cones are greater than λ/4 of the lowest frequency of the antenna's operation. Therefore, the bicone antenna is inherently a wideband antenna. The bicone antenna radiates like a half wave dipole and in the example shown in Figure 11 the antenna is vertically polarised.

The bicone may be realized by rolled solid sheets of metal or by radial elements as shown in Figure 12. The more radials the better however most technical references recommend at least 8 for each half of the bicone.

Figure 12. Bicone Antenna using Radials

Conical Monopole or Monocone Antenna

There is another obvious configuration of the bicone antenna, that being the monocone. Shown in Figure 13 is diagram of the monocone which is placed above an infinite groundplane. Like the monopole, the monocone has an unbalanced feedpoint. The input impedance of the monocone is half that of the bicone. See equation ii). Therefore, the input impedance is 158/2 = 79 Ohm.

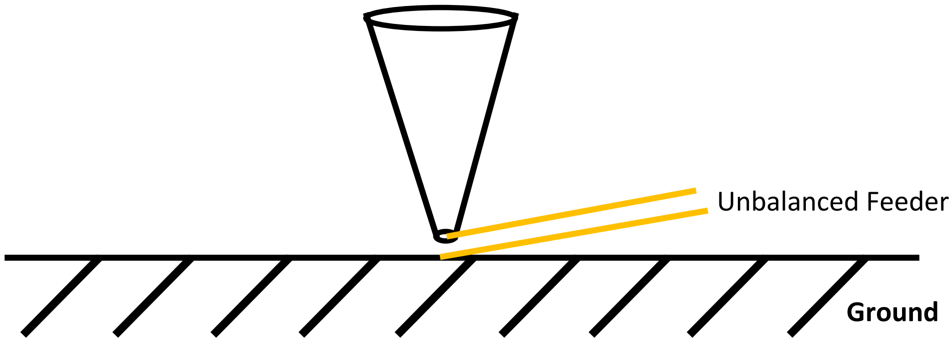

Figure 13. Monocone Antenna

The monocone may also be realized by wire radials and the infinite flat groundplane may also be realized by a truncated set of radials as shown in Figure 14. The overall length of the groundplane radials must also be greater than one half the wavelength of the lowest antenna operating frequency.

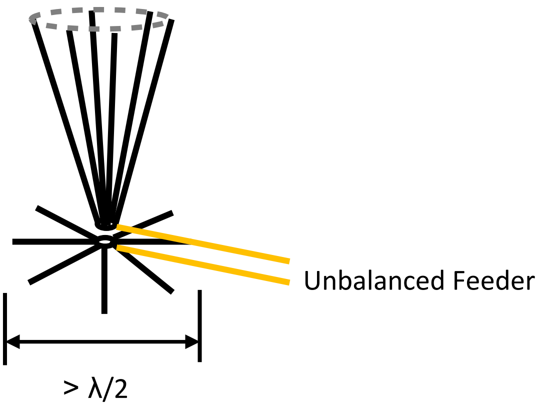

Figure 14. Monocone Antenna Using Radial Wires

It's not too much of a stretch of the imagination to visualize the monocone in the inverted configuration. See Figure 15 for the inverted monocone antenna configuration with radial wires. The antenna then has the same visual appearance of the discone however the similarities almost end there. The top radials of the inverted monocone must form a groundplane whereas in the discone this becomes the radiating element and the downward sloping radials become the groundplane. **Therefore, the discone is really a special case indeed of an inverted monocone.**

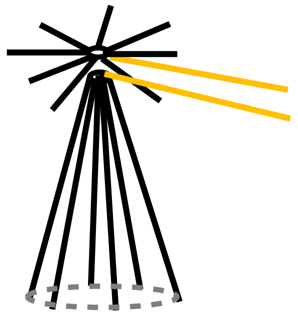

Figure 15. Inverted Monocone Antenna Using Radial Wires

Discone Antenna - Theory of Operation
Sergei Alexander Schelkunoff of Bell Labs published a paper in 1941 which covered the theory of operation of the biconical antenna and asymmetric variants such as the discone. Then in 1943 Armig Kandoian of the Federal Telephone and Radio Corporation in New York applied for a patent on his version of the discone. A patent was issued in 1945. An excellent reference on the discone can be found from an article written by Steve Stearns Jan/Feb 2007. A link to this paper is provided below:-

https://antena.fe.uni-lj.si/literatura/Razno/Antene/knjige/All_About_the_Discone_Antenna,_QEX,_JanFeb-2007.pdf

Several formulae and references used in the author's report are derived from Stern's paper. Steve Stearns himself also refers to the historic reference of Schelkunoff and Kandoian and a collegue of Kandoian, J.J. Nail. Schelkunoff also published a book in 1952 titled "Advanced Antenna Theory" which may be found at the weblink below. The book is thorough however has a high density of complex mathematics.

https://ia903004.us.archive.org/6/items/AdvancedAntennaTheory1952/Advanced%20Antenna%20Theory%201952_text.pdf

Figure 16 provides a diagram of the discone and its essential parameters. The measured dimensions of the author's discone are also shown and highlighted.

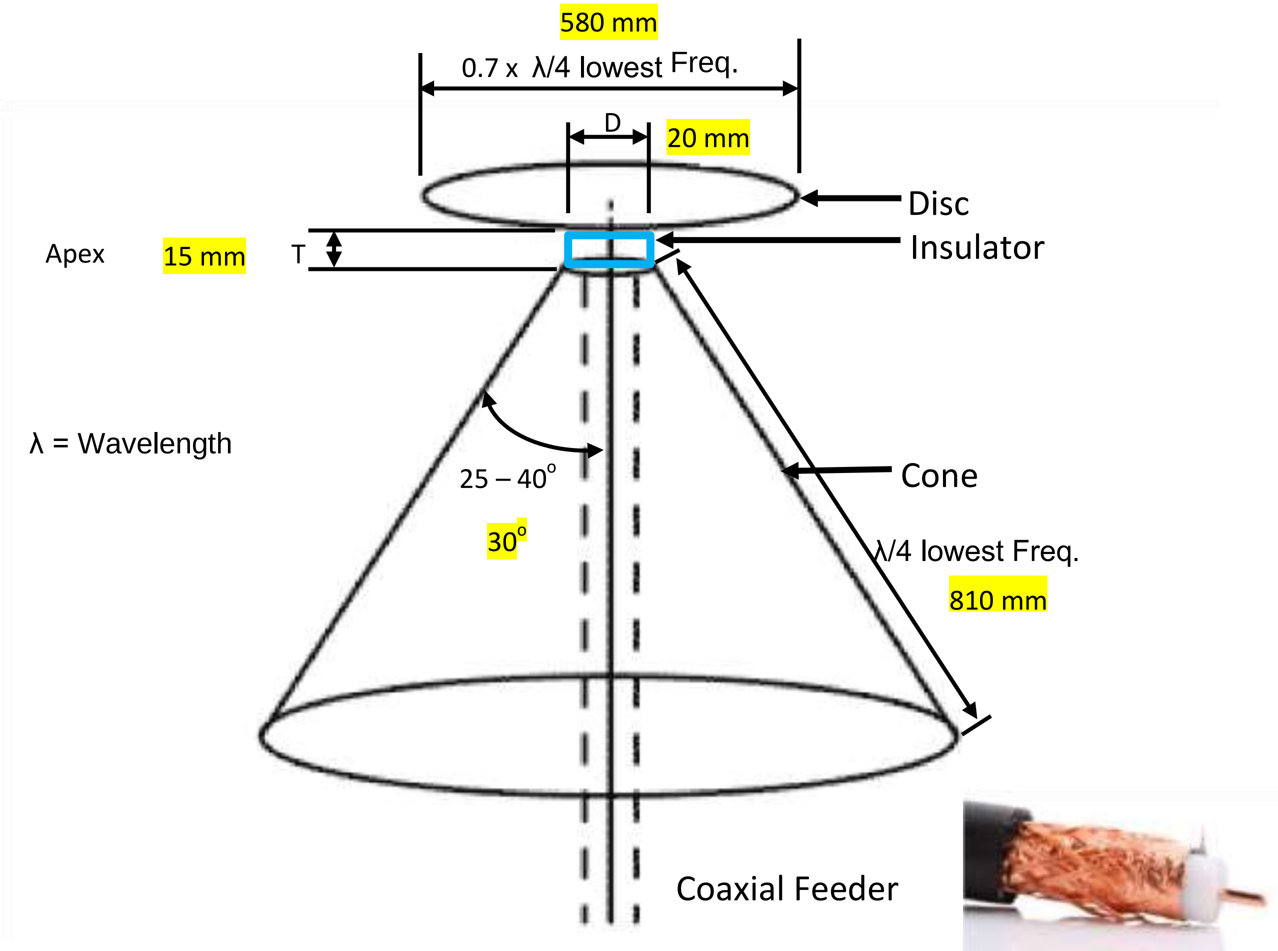

Figure 16. Discone Antenna Configuration

As shown in Figure 16, the discone antenna is connected to the receiver (or transmitter) via a coaxial cable with an example coax cable shown. As mentioned, the discone antenna is an unbalanced antenna. The inner conductor of the coaxial feeder is connected to the disc and the outer conductor (shield or "ground") of the coaxial feeder is connected to the cone. An insulator is placed between the disc and the cone. It may be worth performing a bit of reverse engineering of the author's discone to understand how it has been designed.

The overall diameter of the disc should be about 0.7 x λ/4 of the lowest frequency. In our case this is 25 MHz therefore the disc diameter may be calculated using Equation iii).

iii) Disc diameter = 0.7 x ¼ x ($3^8/25^6$) = 2.1 m

The elements provided for both the D3000N and the author's D130NJ disc are 580 mm long overall and therefore are a departure from the optimum size for operation down to 25 MHz. The diameter of 580 mm would suggest the disc is better suited to a lower frequency of about **90.5 MHz**.

The length of the cone should be λ/4 of the lowest frequency. Therefore equation iv) may be used to calculate the required length to operate down to 25 MHz.

iv) Cone Length = ¼ x ($3^8/25^6$) = 3m

Once again, the actual elements provided for the discone have a cone radial length of 810 mm which would be more suited to a lower frequency of **92.6** MHz.

These calculations indicate the discone on its own without the added vertical whip above the disc, is suitable for the higher frequency ranges only, a fact which is stated in the manufacturer's specifications.

From the fundamental theory of the discone, the characteristic input impedance of a conical monopole may be calculated using equation v). See also Figure 13.

v) $Z_0 = (\eta / 2 \times \pi) \times \text{Log}_e \text{ Cotangent}(\theta/2)$

Equation is obtained from Sterns who was quoting Schelkunoff paper from 1941.

The value η = 377 Ohm which is the impedance of free space.

Solving this equation based on θ = 30 degrees as used on our discone yields:

Z_0 = **79 Ohm**.

This result is also intuitively correct since it is half the impedance of a bicone as shown in equation ii).

Similarly, for an optimum discone designed for an input impedance of 50 Ohm the equation vi) may be used.

vi) R/L = 0.72 x sine θ

Equation obtained from Sterns who was quoting a paper by Nail a colleague of Kandoian from articles published 1946 – 1953.

R = radius of the disc = 580/2 = 290 mm L
= length of cone = 810 mm θ = 30 degrees

Therefore R/L = 0.72 sine 30 = **0.36**

Based on the actual elements R/L = 0.36 and is therefore consistent.

We therefore have an inconsistency where one theoretical determination for the input impedance determines 79 Ohm and the other determines the configuration is more optimum for 50 Ohm.

To determine the optimum cone angle the equation vii) is used.

vii) $\theta = 2 \tan^{-1} \exp(-Z_0/60)$ Equation from Sterns.

For a nominal 50 Ohm input impedance:-

Therefore $\theta = 2 \tan^{-1} \exp(-50/60)$ = **47 degrees**.

Since we have θ = 30 degrees, vii) may be used to determine Z_0.

Therefore Z_0 = **79 Ohm**.
The conclusion of this implies the discone configuration may have been constructed for a 50 Ohm input impedance however cone angle is more optimized for a 75 Ohm impedance. The author is confused!

As mentioned for Figure 15, the inverted monocone case, the horizontal radials were considered to be at lease $\lambda/2$ long. This was to form a groundplane. However, in the case of the discone when the horizontal elements become the radiating element instead of the ground plane, the length also becomes significantly shorter and may be as short as 0.7 x $\lambda/4$ overall. When the radiating element is shorter than $\lambda/4$ it will become capacitively reactive as previously mentioned (Figure 10). The input impedance also becomes lower than the nominal. For the case of a standard $\lambda/4$ vertical the impedance was 36.5 Ohm however can be raised to near 50 Ohm by bending the groundplane radials down at 45 degrees. Therefore, the discone is a kind of hybrid of a $\lambda/4$ wave vertical with downtilted groundplane radials. The input impedance of a normal monocone antenna was 79 Ohm therefore it is consistent that the impedance will become less than 79 Ohm and get closer to 50 Ohm if the main radiating element of the antenna (the disc) becomes shorter than $\lambda/4$.

The missing link in these calculations is the effect of the dimensions of the insulating element between the disc and the cone. From the paper by Nail in 1953, he determined the thickness of the insulator should be approximately 0.3 x insulator diameter. In our case the insulator is 20 mm dia. therefore the thickness should be 0.3 x 20 = 6 mm. Since the thickness is actually 15 mm we appear to depart from this recommendation. It may however be part of the secret with this discone which has been optimized for 50 Ohm. The dimensions of the discone antenna near the apex are also how it performs up to its highest frequency of operation. One can assume the D3000N version has also been adjusted in this region to perform at 3 GHz.

Shown in Figure 17 is an illustration of how the RF field emerging from the coaxial feeder cable, propagates out along the surface of the cone (or the simplified wire equivalent) to the point where the distance between the apex and point on the cone and the disc is a quarter wavelength. At this point the antenna is resonant and will radiate with maximum efficiency. With careful design, the feedpoint impedance will also be close to 50 Ohm across the whole frequency range however the antenna has also been optimized for a better impedance match at the amateur bands and it is not uncommon to obtain better than 1.2: 1 VSWR on 2m, 70cm and 23 cm. A typical discone radiation pattern is similar to the quarterwave monopole however some slight down-tilting of the pattern occurs at higher frequencies.

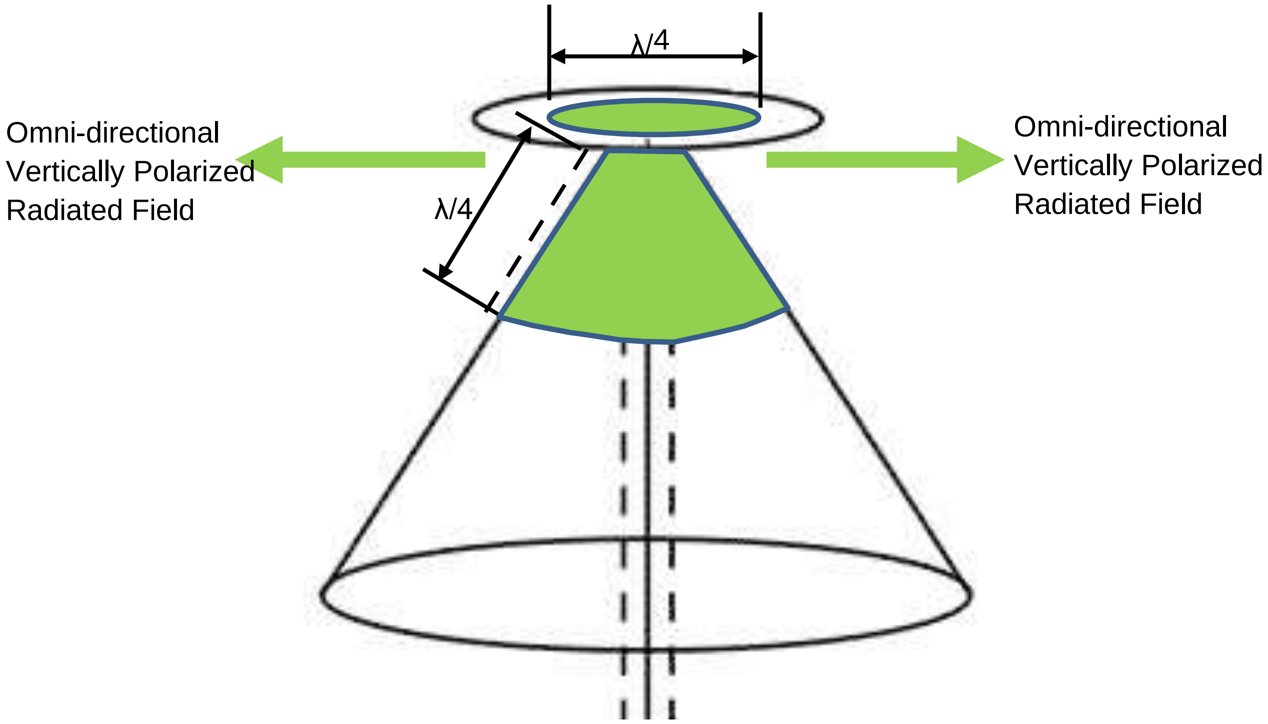

Figure 17. Discone Resonance Illustration

4.0 Discone Measured Performance

The Author's discone antenna was measured over a wide range of frequencies. Shown in Figures 18 to 23 are the input return loss measurements of the discone using a calibrated NanoVNA relative to a 50 Ohm reference. The return loss is a measure of the input impedance match or VSWR. A return loss of 10 dB corresponds to a VSWR of about 2:1. The higher the return loss the better the impedance match.

In Figure 18 the return loss measurement indicates poor performance with a variation between 2 to 10 dB over the range 25 to 50 MHz. This result is not unexpected based on the calculated performance determined by the actual dimensions of the antenna. A similar result can be seen in Figure 19 where the return loss does not consistently become higher than 10 dB until the frequency is above about 125 MHz.

Shown in Figure 24 is a detailed return loss measurement over the frequency range 40 to 60 MHz. As can be seen, the marker is placed at 52 MHz which indicates a return loss of 18.45 dB. This corresponds to a VSWR of 1.27: 1 and also represents a mismatch loss of about -0.06 dB. The vertical whip above the discone was trimmed in length (shortened) in increments until this tuned result was obtained. The performance is quite acceptable, however an antenna tuning unit at the transmitter end of the transmission line may assist to obtain 1:1 VSWR if that is considered necessary for the 6m amateur band.

Shown in Figure 25 is a detailed return loss measurement over the frequency range 140 to 150 MHz. At 146 MHz the value is 15.7 dB and corresponds to a VSWR of 1.4: 1 or a mismatch loss of 0.12 dB. Again, a result that is more than acceptable for the 2m amateur band.

Shown in Figure 21 the trace marker has been placed on the frequency of 432 MHz and the return loss of 18.11 dB is indicated. This is also another amateur band where it is suitable to transmit into the discone and based on the high return loss this also seems acceptable.

Shown in Figure 23 the return loss has been indicated with the marker set to 1295 MHz. The value is 7.17 dB. The amateur band covers the range from 1240 to 1300 MHz and from the return loss sweep over this range the discone does not appear to be consistently low and it appears an antenna tuning unit at the transmitter end of the transmission line would be recommended.

The general performance of the discone at other frequencies other than the amateur radio bands has a varying return loss fluctuating between 2 dB and 30 dB, however, is better than 10 dB from about 125 MHz to 1000 MHz. This is consistent with the calculated tuning range of the antenna based on the measured lengths of the radial elements. As mentioned, the 2 :1 VSWR only represents about 0.5 dB loss which is also considered acceptable for receive.

The antenna was also connected to the author's RSPDX SDR and evaluated below 25 MHz. The antenna was able to receive amateur radio transmissions on 28 MHz down to 1.8 MHz. In addition, the local Metro Melbourne AM broadcast stations could be received with very high signal strength down to 621 KHz.

5.0 Conclusion

A detailed investigation has been provided on the discone antenna the RAS has obtained. The study has concluded that theoretical calculations do not always match the specified and measured performance of the antenna. This is due to a number of reasons. The antenna is complex and in reality, is characterized by complex mathematics based on solutions of Maxwell's differential equations in spherical coordinates which result in Bessel functions and Legendre polynomials! Many of the formulae are simplifications or generalized relationships based on measured antennas.

The discone has some similarities with the inverted monocone antenna and some of the mathematics related to that variant come close to describing the discone.

However, the discone is more like the quarter wave groundplane antenna with the vertical whip replaced by a flat disc. Commercially the discone has been optimized by measurement to be an optimum impedance match to 50 Ohm and the manufacturer has also included tricks in the design to ensure the best impedance match occurs on several amateur radio bands.

The specific product the RAS has obtained is really 2 antennas combined, a discone from 50 MHz to 3000 MHz and a groundplane vertical whip for frequencies below 50 MHz.

Based on the author's version of this antenna, it is evident the antenna certainly has a wide range for reception. The ability to provide a close impedance match to 50 Ohm on several amateur radio bands provides the added advantage this antenna can be used for transmit as well.

A perfect impedance match, however, was not obtained for all parts of the amateur bands specified for transmit. It is therefore recommended to include an antenna tuning unit to ensure a 1:1 impedance match is obtained for all transmit frequencies. Although the actual transmission loss is quite low even with a 2:1 VSWR, avoiding a mismatch is not so much for minimizing transmission loss but to ensure the transmitting equipment does not become loaded excessively particularly where the mismatch causes the transmitter to consume a higher current consumption than normal. This will result in potentially overheating the transmitter.

The measured return loss of the discone indicates the antenna performs much better above 125 MHz which is consistent with the calculated tuning based on the dimensions of the antenna. Although the manufacturer has specified the antenna to perform down to a frequency of 25 MHz, the input impedance departs significantly from the required 50 Ohm. However, on-air live tests of the antenna has proven this does not matter significantly in receive mode and indeed the antenna may be used down to very low frequencies including the AM broadcast frequencies as low as 621 KHz.

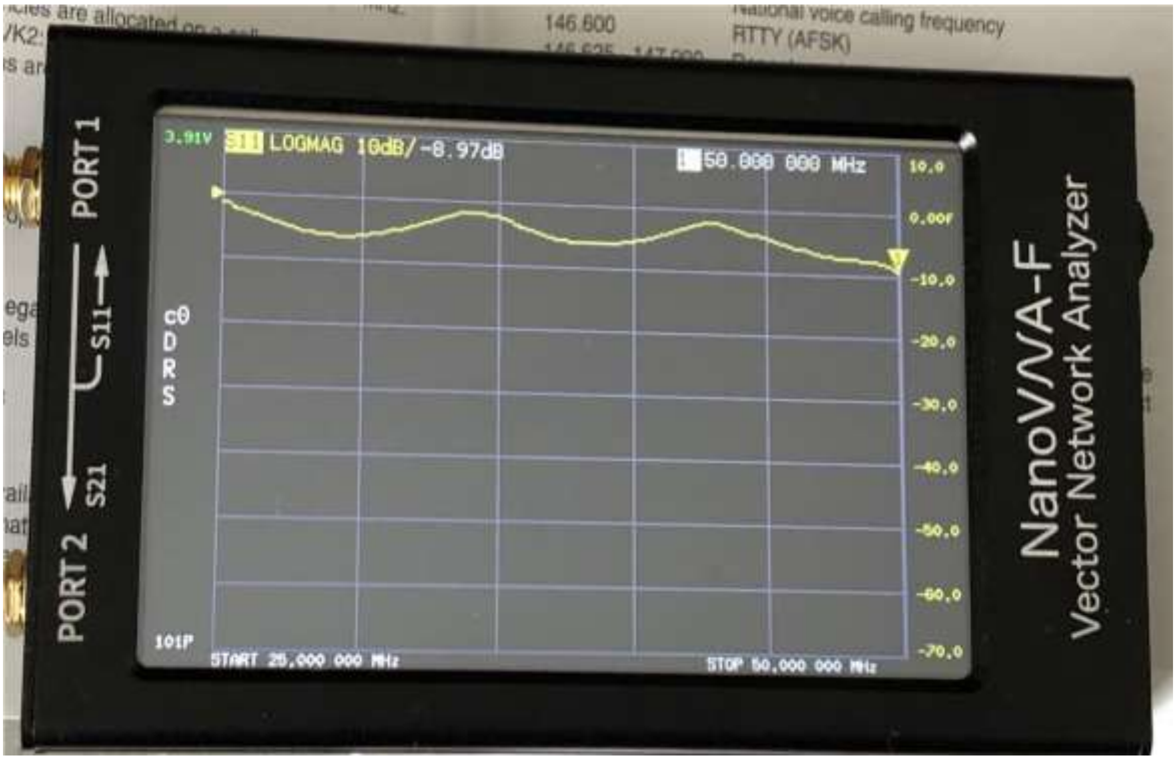

Figure 18. Discone Input Return Loss 25 to 50 MHz

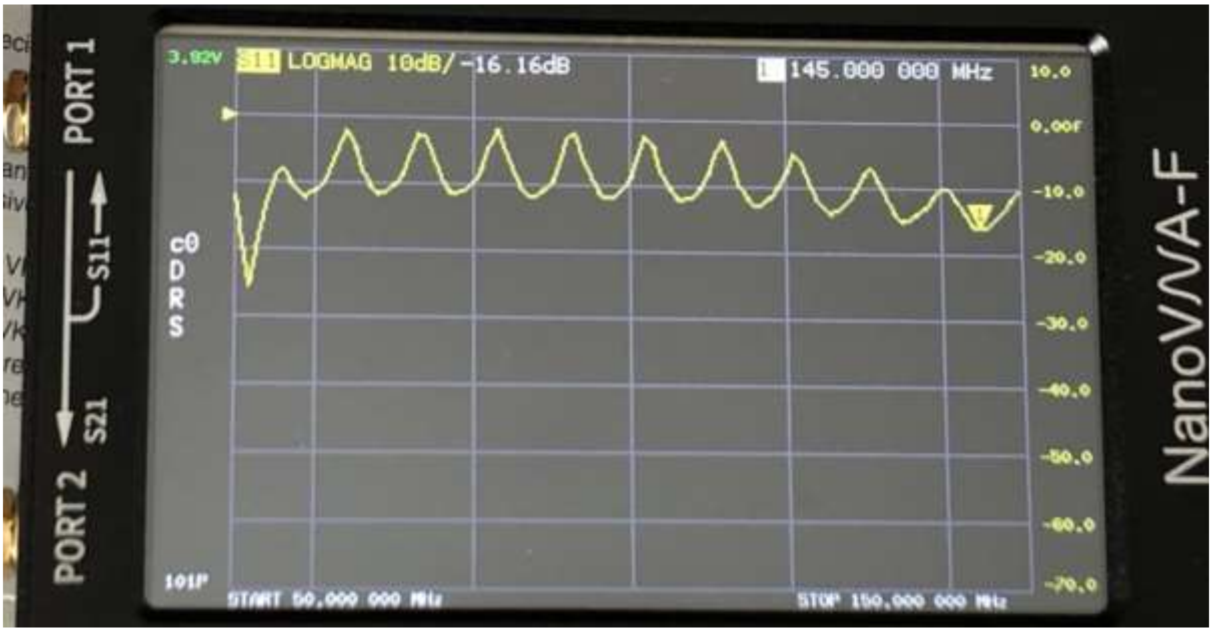

Figure 19. Discone Input Return Loss 50 to 150 MHz

Figure 20. Discone Input Return Loss 150 to 300 MHz

Figure 21. Discone Input Return Loss 300 to 500 MHz

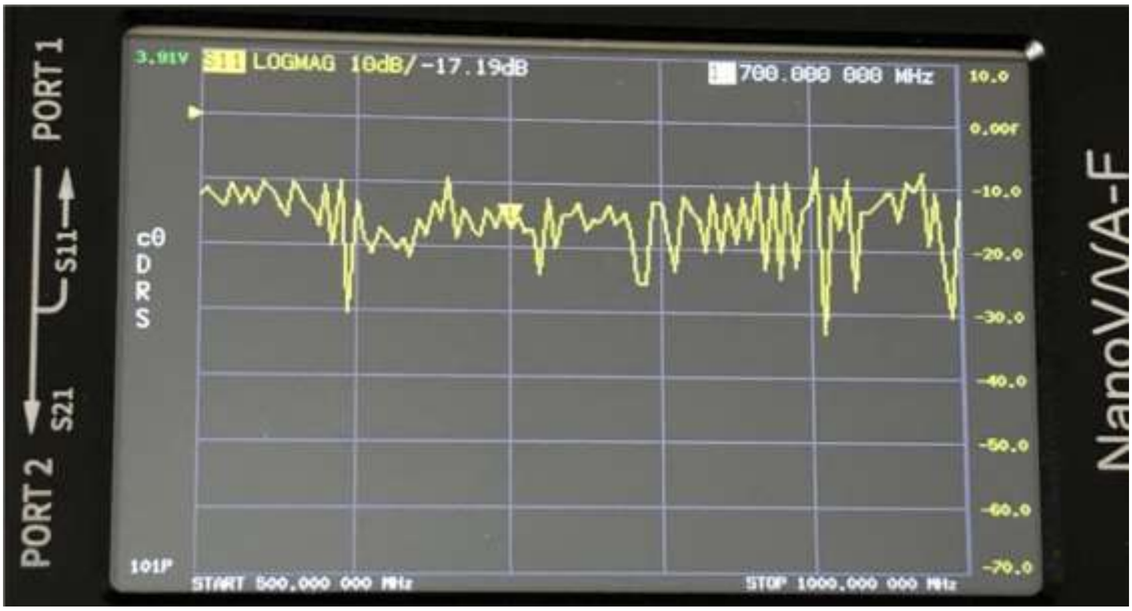

Figure 22. Discone Input Return Loss 500 to 1000 MHz

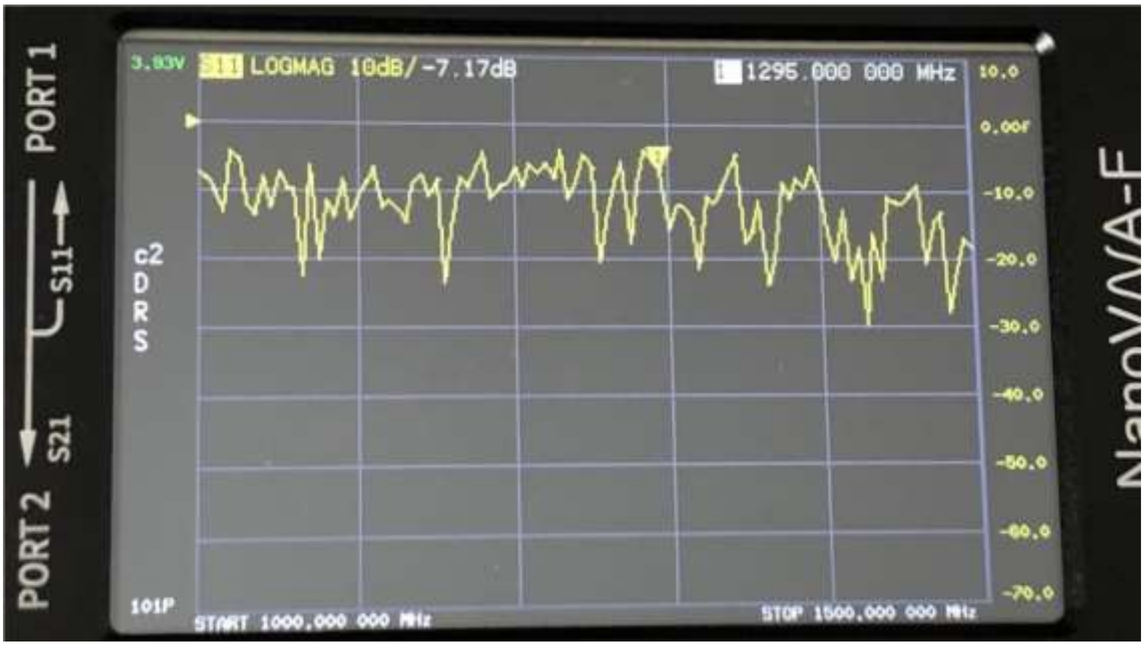

Figure 23. Discone Input Return Loss 1000 to 1500 MHz

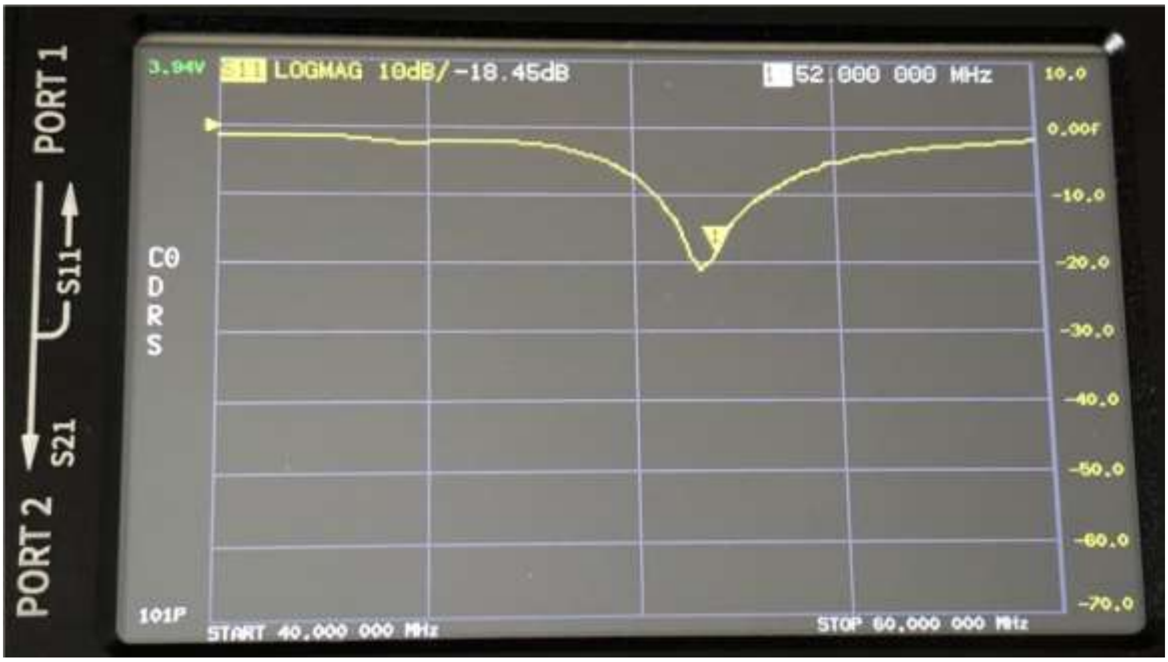

Figure 24. Discone Input Return Loss 6m band

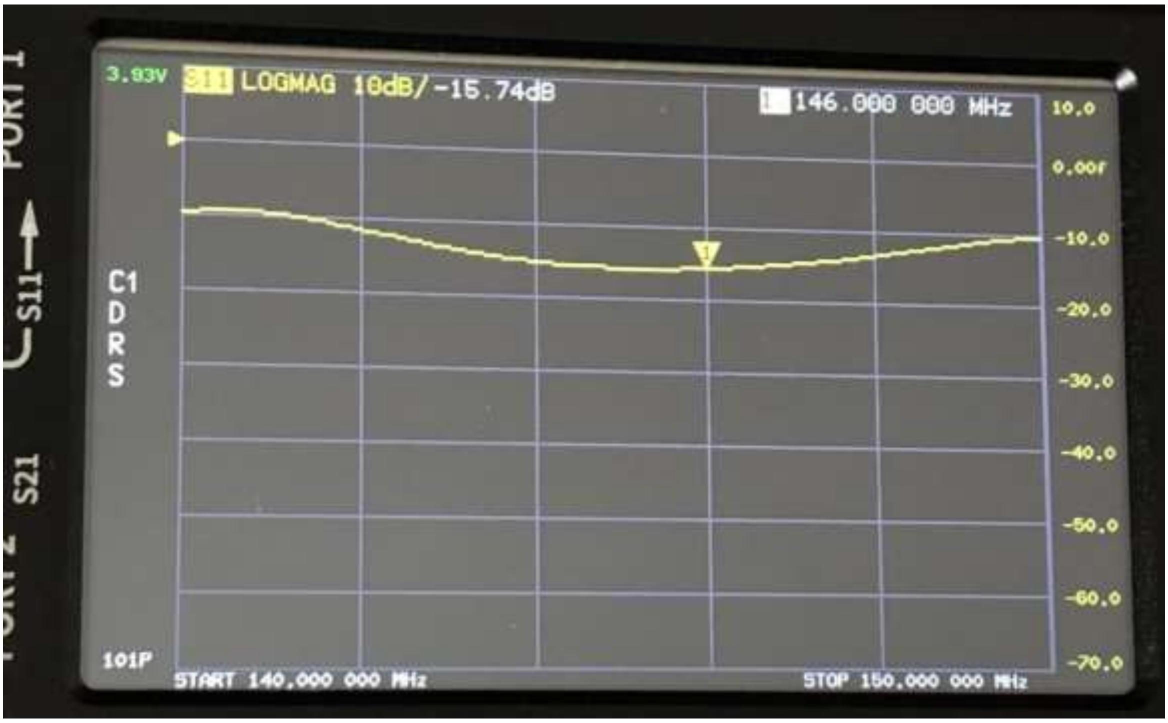

Figure 25. Discone Input Return Loss 2m band

Geomagnetic Sudden Impulse Observations

Whitham D. Reeve

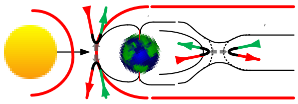

Sudden Impulses result from the impact of an Earth-directed coronal mass ejection (CME) on, and the rapid compression of, Earth's magnetosphere {Reeve13}. However, depending on the interplanetary magnetic field (IMF) direction and the plasma speed and density associated with the CME, the after-effects widely vary. CMEs are part of *space weather*, the overall effects on spacecraft and Earth's inhabitants by variations in solar activity. The persistently high level of solar activity during the first couple of weeks in September 2024, including an almost continuous stream of Earth-directed coronal mass ejections, provided plenty of bad space weather.

This article describes three Sudden Impulses during September that resulted in significantly different effects. Sudden Impulses are only part of a geomagnetic event and do not occur in isolation. What happens before and after are just as interesting and also discussed here. The times and intensities of the September Sudden Impulses are listed in table 1. The first impulse, on 4 September, was not followed by a significant disturbance to Earth's magnetic field but storm conditions followed the impulses on 12 and 16 September within 3 hours. Storm conditions are defined by a K-index ≥ K5 as measured by ground magnetometers. The three impulses were detected and recorded by the SAM-III magnetometers at Anchorage Radio Observatory and HAARP Radio Observatory (figure 1). The magnetometers are described later in terms of block diagrams.

Figure 1 ~ Map of Southcentral Alaska showing the locations of Anchorage Radio Observatory (left marker) and HAARP Radio Observatory (right). The great circle distance between the two, shown by the black line, is 286 km. HAARP is 2° farther north in magnetic latitude than Anchorage and 4° east in longitude.

Geomagnetic coordinates:
Anchorage: 61.72° N : 94.41° W (2022)
HAARP: 63.62° N : 90.42° W (2024)

Note: Geomagnetic coordinates change over time because of the wandering nature of Earth's internal dipole field.

Image source: http://www.movable-type.co.uk/scripts/latlong.html

Coronal mass ejections: A CME can consist of a billion tons of charged matter, mostly protons, electrons and helium nuclei, blasted away from an active region in the Sun's corona by magnetic instabilities. The CME is a plasma cloud. It is highly conductive and, consequently, the Sun's magnetic field is frozen in and carried along with it. As the CME moves away from the Sun to the surrounding solar system, the embedded solar magnetic field is called the *Interplanetary Magnetic Field*.

CMEs can travel at speeds above 2000 km s^{-1} and, if Earth-directed, can reach Earth in less than 1 day but most CMEs are much slower and require around 2 to 3 days to reach Earth. A CME may overtake or fall behind the ambient solar wind, coronal hole high-speed streams or other CMEs, further complicating their effects on Earth's magnetosphere. After leaving the Sun, CMEs spread out in an expanding cloud, so only a fraction of a typical Earth-directed CME actually intercepts Earth's magnetosphere.

Table 1 ~ Summary of Sudden Impulses on 4, 12 and 16 September 2024. The Shock Times are from SWPC reports of the measurements at ACE or DSCOVR spacecrafts. The Impulse Times also are from SWPC reports for the Boulder USA (4 and 16 September) and Canberra AU (12 September) ground magnetometers. The Sudden Impulse Amplitudes are from the Anchorage / HAARP observatories and are estimated from graphical Bx and By data that are added vectorially to find the horizontal amplitude.

Date (2024)	Type	Shock time (UTC)	Impulse time (UTC)	Amplitude (nT)	Remarks
4 September	SI	0940	1030	56 / 58	Amplitude 40 nT at Boulder
12 September	SSC	0254	0350	76 / 90	Amplitude 32 nT at Canberra
16 September	SSC	2249	2329	63 / 120	Amplitude 39 nT at Boulder

Not all CMEs are Earth-directed and sometimes only the flanks of a CME interact with Earth's magnetosphere and cause transient effects or disturbances. These interactions may last for days. Because CME speed and density are important parameters in space weather forecasting, NOAA uses spacecraft measurements to model CMEs for alert and warning purposes (figure 2). The modeling is not yet perfect but is under continuous improvement. For example, the plasma density and speed associated with the 16 September impulse were predicted to peak at 1300 but actually occurred about 10 hours later. Note that, according to the model for 16 September, a good part of the CME was predicted to miss Earth.

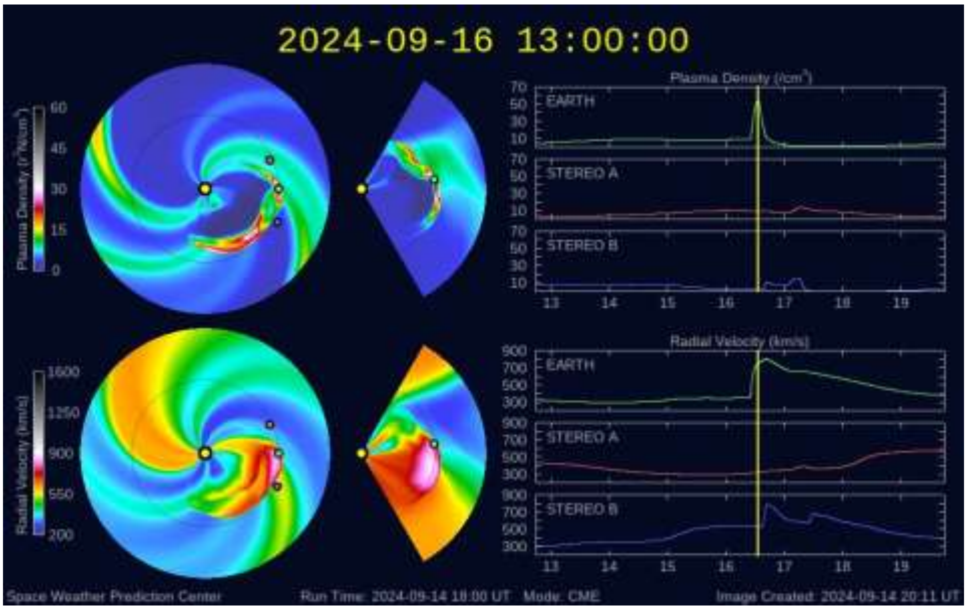

Figure 2 ~ WSA-ENIL model of the 16 September CME showing predicted arrival at Earth (yellow cursor). In this case, the predicted time was early by about 10 hours. The actual arrival time at Earth was 2329. The circles at left depict density (upper) and wind speed (lower) from an overhead view. The pies depict the same properties from an orbital plane view. Earth is the middle of three dots to right of the Sun at center. Image source: https://www.ngdc.noaa.gov/enlil/

Interplanetary magnetic field: The IMF component aligned with Earth's magnetic dipole field has great importance in space weather. It and other properties are measured by the ACE and DSCOVR sentinel spacecrafts located about 1.5 million km from Earth along the Sun-Earth line. The IMF component that is aligned with Earth's dipole field is labeled Bz. This is not to be confused with the component of Earth's magnetic field also labeled Bz but measured by ground magnetometers. The terrestrial Bz points from Earth's surface to its center.

If the IMF Bz component is opposite in polarity to Earth's magnetic field, that is, the Bz component is southward or negative, the two fields can easily merge, and a geomagnetic storm will follow almost immediately if the IMF remains southward for roughly an hour or more. The storm typically is stronger the longer the southward component persists and the higher its amplitude. On the other hand, if the IMF Bz component has the same polarity as the geomagnetic field (northward or positive), little or no merging takes place and a storm is unlikely to follow.

If a storm follows almost immediately, the impulse more accurately is called a Sudden Storm Commencement (SSC) rather than Sudden Impulse (SI). However, in this article, the Space Weather Prediction Center's (SWPC) simplified terminology will be used wherein both types of impulses are labeled Sudden Impulses. SWPC provides near-real-time warnings and alerts of space weather phenomena, and it is not known at the first sign of an impulse whether a storm follows or not.

An IMF and geomagnetic field merging event generally follows a sequence called the *Dungey Cycle*, which is described in the following numbered narrative keyed to figure 3 (Reeve21}:

1. When the interplanetary magnetic field embedded in the solar wind has a southward component, opposite to Earth's magnetic field, the two fields merge on the dayside of the magnetosphere in a process called *magnetic reconnection*;
2. The formerly closed geomagnetic field lines facing the Sun open as they merge with the IMF. The IMF and magnetosphere are now linked and solar wind plasma can enter the magnetosphere at high latitudes;
3. The open field lines are carried over the Earth's poles by the solar wind. The field lines are stretched out on Earth's nightside in the region called the *magnetotail*;
4. As they stretch out, the open-field lines move toward the center plane of the tail where they reconnect again, closing the magnetic flux that was opened on the dayside. The time from 1 to 4 is on the order of 1 hour;
5. Part of the magnetic flux moves down-tail away from Earth, but part of the flux returns by internal flows to their origin;
6. This process carries plasma resident in the magnetotail toward Earth;
7. The highly energized electrons in the plasma are trapped by the magnetic field and are further energized when they arrive within a few Earth radii by voltage variations along the magnetic field lines. The cycle may repeat in a quasi-periodic process called a *substorm* with a period of roughly 1 to 3 hours. If the IMF is northward, it is deflected around Earth and there is no reconnection.

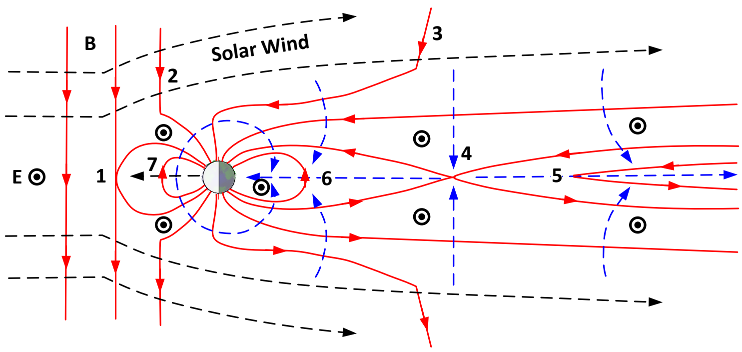

Figure 3 ~ Conceptual drawing of magnetic merging and reconnection called the Dungey Cycle. The numbers indicate the sequence described in the text. The Sun is to the left out of view, and the solar wind is shown by the black dashed lines flowing left-to-right. The magnetic field (B) is shown in red; the IMF is southward. Earth is the circle with the sunlit side facing the Sun and has a northward magnetic field. Current flow (E) is into the page shown by the circled dots. Magnetic flux movement is shown by blue arrows. Diagram adapted from: [Seki]

<u>Spacecraft data</u>: Data plots from the ACE or DSCOVR spacecrafts are shown in this section. Note that the time spans shown by these plots are 1 or more days and are chosen to aid the discussion of events that may span several days. The plots have been annotated to clarify dates and times of the events described, and a black vertical arrow has been added to indicate the time of the CME shock at the spacecraft. Each image contain numerous graphs and traces and those relevant to the discussion are (from top):

1st graph: Bt (black trace) and Bz (red trace) which are the total IMF and IMF component aligned with Earth's dipole field, respectively. The ambient Bt near Earth (1 AU) is on the order of 5 to 8 nT and values above 10 nT can be considered to be elevated. Shocks are usually indicated by a step-change in Bt whereas Bz can change more slowly or more erratically. A shock observed at the spacecraft will not be observed in terrestrial magnetic field data until the CME has traveled from the spacecraft to Earth's magnetosphere; the travel time depends on the speed but is on the order of 40 to 60 minutes.;

3th graph: Solar wind density (orange trace). The ambient solar wind density at 1 AU is on the order of 3 particles cm^{-3}. CMEs typically raise the density while coronal hole high-speed streams (CHHS) lower it;

4th graph: Solar wind speed (magenta trace). The ambient solar wind speed is on the order of 350 to 450 km s^{-1} and elevated values may be due to a CME or CHHS. Speeds associated with CMEs vary widely and usually are slower near Earth than when they are ejected from the Sun's corona.

It was mentioned above that a geomagnetic storm did not follow the Sudden Impulse on 4 September. The traces for Bt and Bz received from the ACE spacecraft have been circled. Examination of data shows that the IMF Bz component (red trace, figure 4) is positive for most of the period after the CME shock passage was observed there at 0940. The density and speed measurements indicate the solar wind remained near background levels although they both appear slightly elevated compared to the pre-shock time.

In the case, of the 12 September impulse event, which was followed by a geomagnetic storm, the ACE data shows a sustained negative Bz component not only for the day of the impulse but for a few days afterwards (figure 5). Geomagnetic storms persisted throughout this period. The ACE plots include other interesting information, which is described in the captions. The situation was similar on 16 September (figure 6) in which the Bz component was negative for two days afterwards. The ACE data clearly shows when the CME shock passed the spacecraft – see the step increase in the black trace in the graph near the top of the data plots, which corresponds very closely to the time the Bz component, shown by the red trace, turned negative.

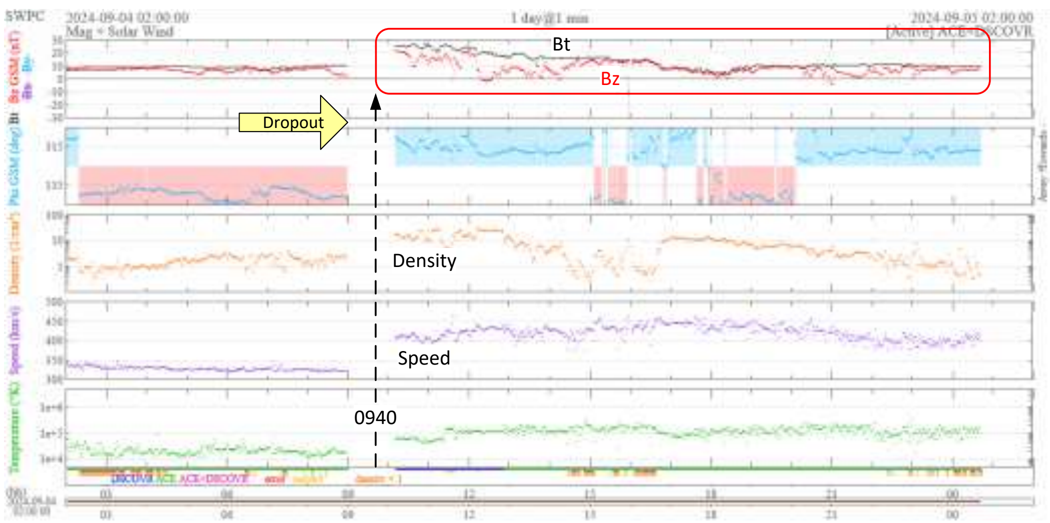

Figure 4 ~ ACE + DSCOVR spacecraft solar wind data for 4 September. The shock, measured by Bt and Bz, and density and speed increases occurred at 0940 during the data dropout period between 0900 and 1000. Image source: https://www.swpc.noaa.gov/products/real-time-solar-wind

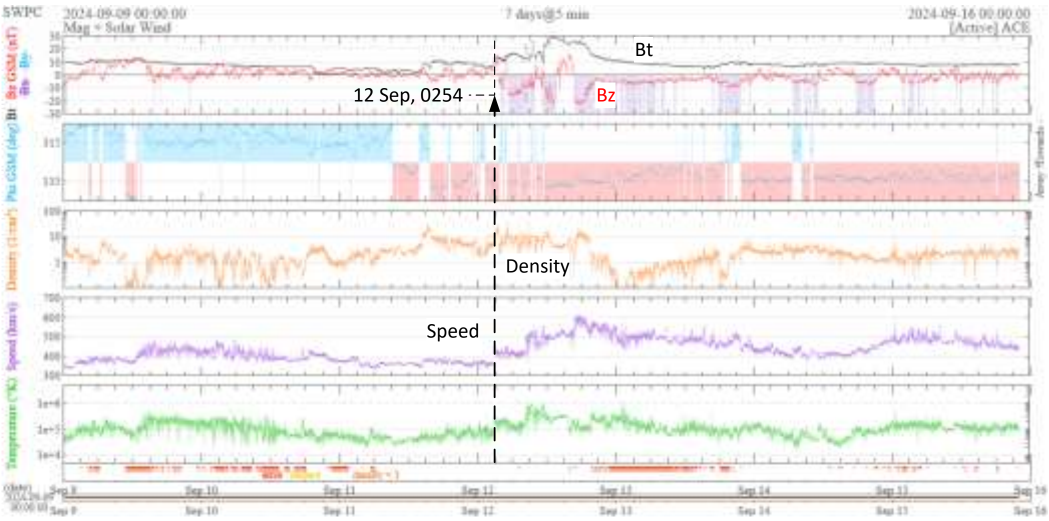

Figure 5 ~ ACE spacecraft data for the 7-day period 9 – 15 September. Bz moved negative starting early on 12 September with periods of sustained negative values days afterwards. The solar wind speed peaked about midday and then slowly decreased. Image source: Same as previous.

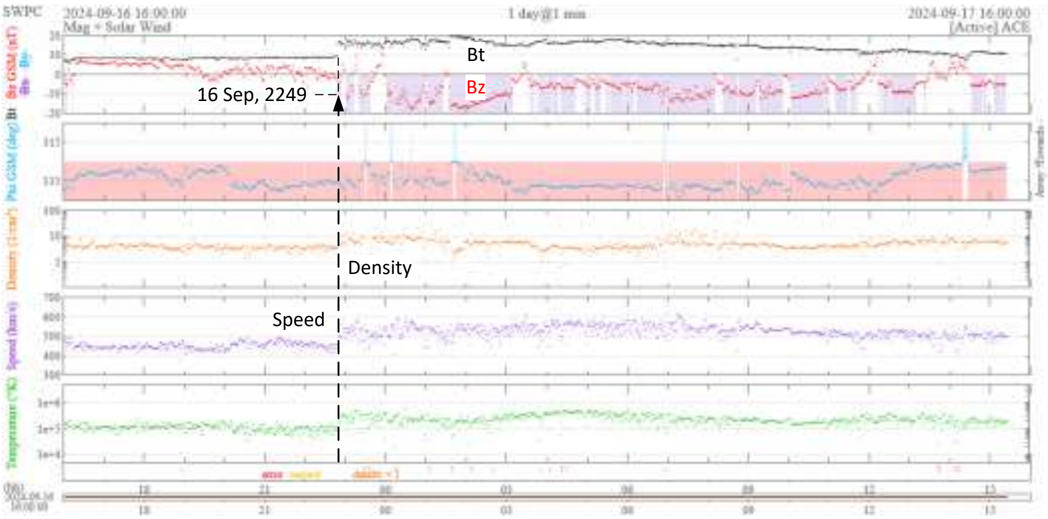

Figure 6 ~ ACE spacecraft data for the 24 hour period starting 1600 on 16 September. Bt increased rapidly at 2249 upon shock arrival. Bz turned negative at the same time and remained mostly negative until 18 September. Image source: Same as previous.

Auroral Electrojets: A result of IMF and geomagnetic field merging is an opening in the magnetosphere that allows energetic charged particles in the solar wind to enter high latitude areas in Earth's northern and southern hemispheres. These donut-shaped areas are called *Auroral Ovals* and mark the high latitudes regions where open magnetic field lines have their footprint on Earth. Generally horizontal current systems flow in the Auroral Oval between about 100 and 150 km altitude (E-region ionosphere). These currents are called the *Auroral Electrojets* (figure 7).

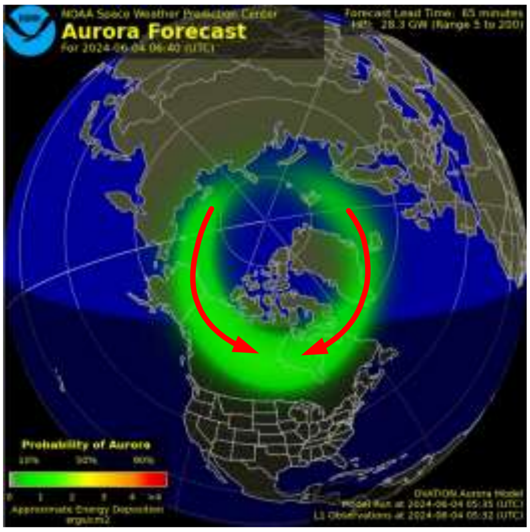

Figure 7 ~ The Auroral Oval is the green donut-shaped area centered on the geomagnetic north pole in this forecast image from NOAA. Magnetic field lines thread the oval and enter Earth's surface directly below. The red arrows indicate the eastward and westward Auroral Electrojets that flow at 100 to 150 km altitude. The Auroral Oval expands during geomagnetic disturbances, carrying the electrojets to lower latitudes. Underlying image source: https://www.swpc.noaa.gov/products/aurora-30-minute-forecast

The particles from the solar wind follow the magnetic field lines down toward Earth where they collide with the atoms and molecules in the atmosphere. The collisions increase the ionization – electron density – in the ionosphere. The increased density and associated conductivity is accompanied by increased Auroral Electrojet currents. The currents are measured by their effects on the local magnetic fields at high latitude observatories around the world and summarized in the AE, AU, AL and AO indices (figure 8, 9, 10 and 11). The magnetic fields measured by the ground magnetometers at both Anchorage and HAARP are influenced by the associated current systems. Magnetic disturbances push the ovals to lower latitudes and the Auroral Electrojets can then flow directly above the two observatories.

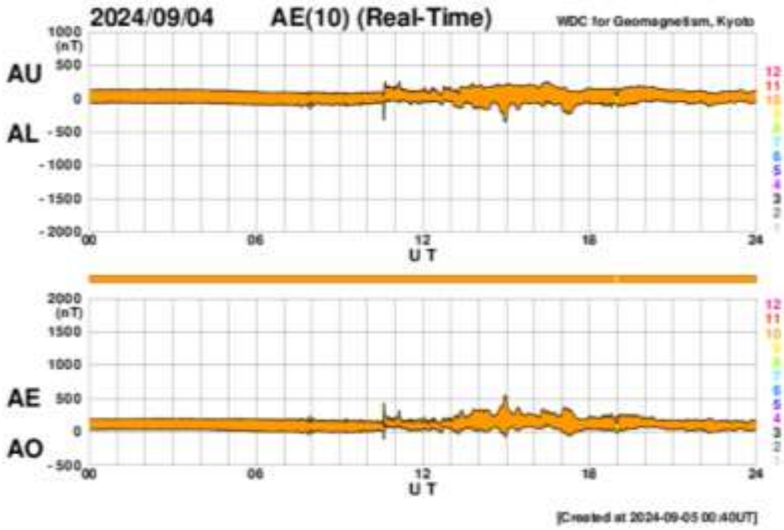

Figure 8 ~ AE indices for 4 September. The Sudden impulse at 1030 UTC was captured in these measurements, and there was a little activity afterwards. However, the AE index only exceeded 500 nT for a very brief period about 4.5 hours after the impulse. The trace envelope color indicate the number of stations reporting (see right scale). Image source: https://wdc.kugi.kyoto-u.ac.jp/ae_realtime/

Because of their low altitude, the Auroral Electrojets can produce large ground disturbances. A typical range of these disturbances is 100 to 1000 nT but much larger disturbances are possible during strong magnetic storms. The Auroral Electrojet index plots during the events in September reached moderately high levels up to about 1500 nT. It is important to remember that these plots are global representations of the AE indices. An individual magnetometer at high latitudes will record the effects of localized Auroral Electrojet currents, which are indicated by the local magnetic field variations.

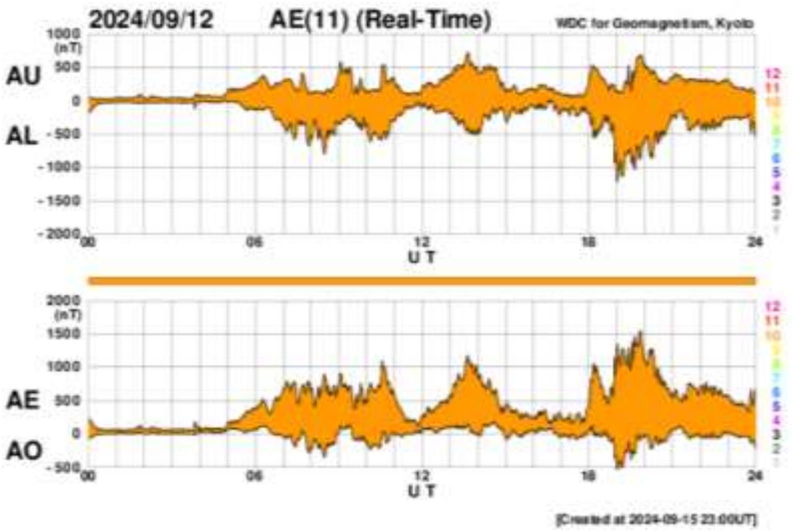

Figure 9 ~ AE indices for 12 September. In contrast to 4 September, the impulse at 0350 UTC on 12 September was followed by far higher electrojet currents throughout the day with the AE index approaching 1000 nT a few hours later and exceeding 1500 nT for a brief period about 16 hours later. Image source: same as previous.

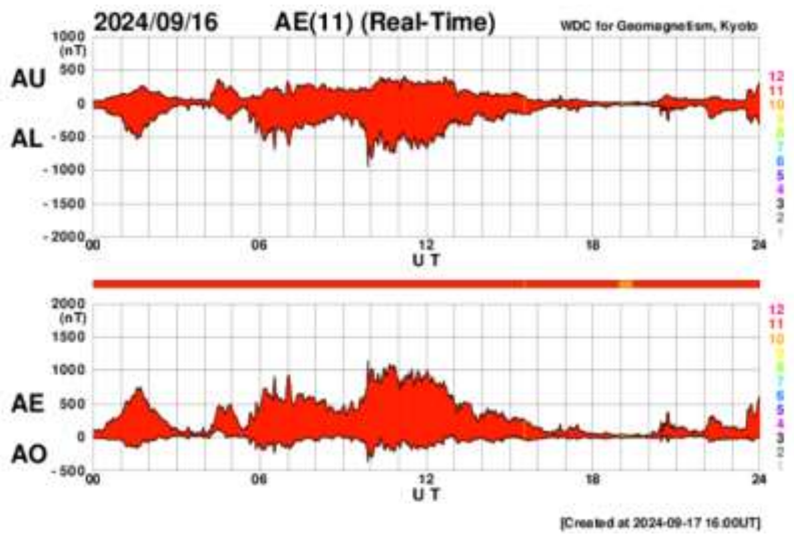

Figure 10 ~ AE indices for 16 September. The impulse late in the day at 2329 UTC was preceded several hours before by relatively high Auroral Electrojet activity due to a coronal hole high-speed stream and its embedded IMF. Since the Sudden Impulse occurred almost at the end of the day, its effects spilled over to the next day as shown in the following figure. Image source: Same as previous.

The AU and AL define the upper and lower envelopes of magnetic measurements from selected northern hemisphere high-latitude stations and express the strongest current intensity of the eastward and westward Auroral Electrojets, respectively, at any given time.

AE is the difference between AU and AL and AO is the average of AU and AL at any given time. Thus, AE represents the overall or peak-to-peak activity of the electrojets and is always positive. AO provides a measure of the equivalent current flows and may be positive or negative at any given time. AO was weak but positive during 4 September, indicating a small eastward current flow in the Auroral Oval. AO was primarily negative during the disturbances on 12 and 16 September, indicating a westward current flow.

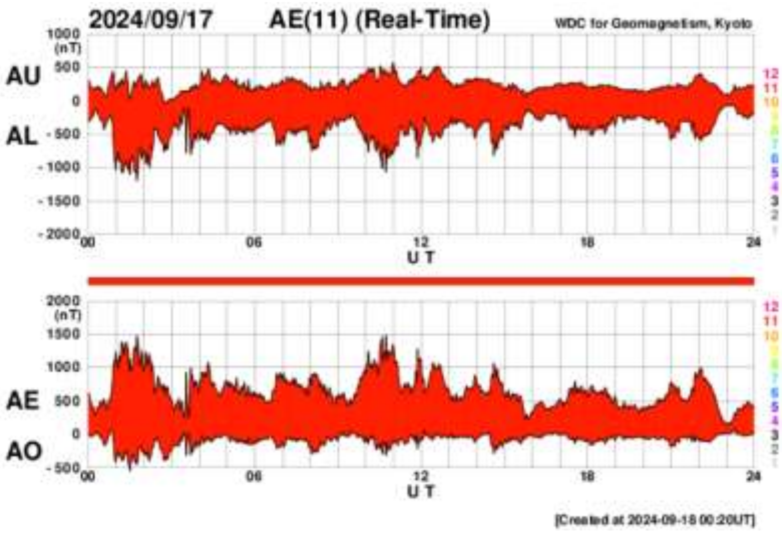

Figure 11 ~ AE indices for 17 September to show the after-effects of the late 16 September Sudden Impulse. The AE index reach 1500 nT within a couple hours of the Sudden Impulse and exceeded 500 nT for almost the entire 24 hour UTC day. Image source: Same as previous.

Magnetograms: The relatively weak eastward electrojet on 4 September produced little magnetic effect at the Anchorage and HAARP observatories (figure 12). The east-west component of the local magnetic fields (By, red trace) at these observatories usually swells each day as the Sun heats up the ionosphere above the stations from about 1200 to 1800 UTC each day. In this case, the pattern was little affected by the electrojets. However, as seen in the north-south component (Bx, blue trace), the Sudden Impulse immediately raised the magnetic flux density, which then slowly tapered off for several hours afterwards.

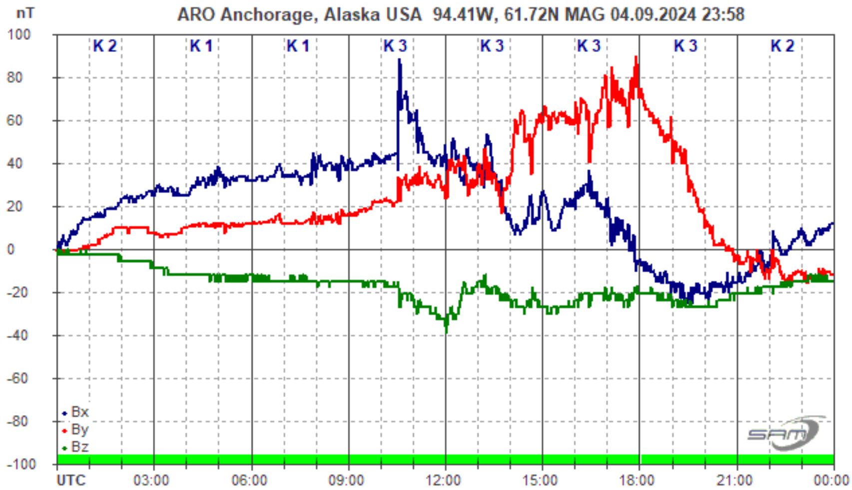

Figure 12.a ~ Magnetic field measurements at Anchorage Radio Observatory for 4 September. Note the vertical scale is 20 nT div^{-1}. The sudden impulse primarily affected the north-south component (blue trace, Bx) with a step-change at 1030 UTC followed by a slow decrease. Smaller step-changes are visible in the east-west component (red trace, By) and vertical component (green trace, Bz). The sudden impulse amplitude at Anchorage (vector sum of Bx and By) was approximately 56 nT. Image credit: © 2024 W. Reeve

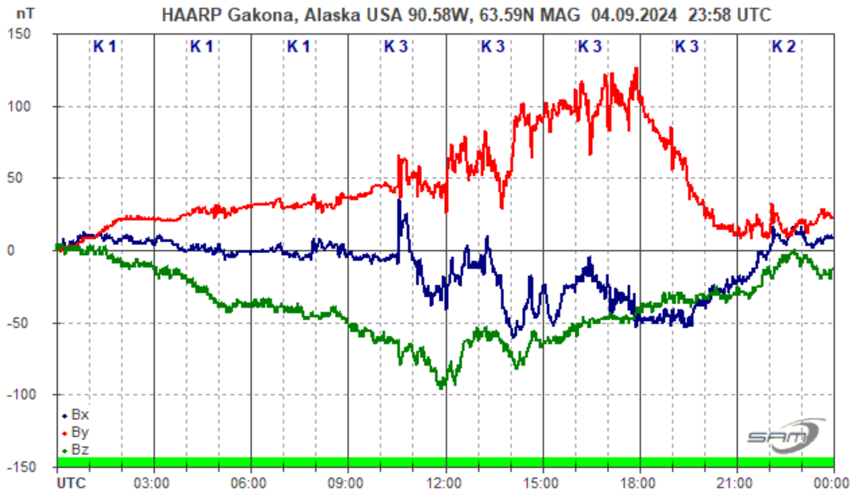

Figure 12.b ~ Magnetic field measurements at HAARP Radio Observatory for 4 September. Note the vertical scale in this plot is different than Anchorage at 50 nT div^{-1}. The sudden impulse effects are similar to Anchorage except that the east-west (By) component has higher amplitude, but the overall amplitude is 58 nT, only slightly higher than Anchorage. Image credit: © 2024 W. Reeve

The Auroral Electrojets on 12 September were much stronger, producing both bays and peaks in the local magnetic field components and indicating the complexity of the effects (figure 13). The event on 16 September produced a relatively large bay the next day (figure 14). A bay, or decrease, indicates that the magnetic field produced by the Auroral Electrojets opposed the local magnetic field while a peak indicates an enhancement. The SAM-III magnetograms at both Anchorage Radio Observatory and HAARP Radio Observatory displayed elevated K-indices throughout most of the day after the impulses on 12 and 16 September, although the K-index did not reach the highest possible value of K9 at either location.

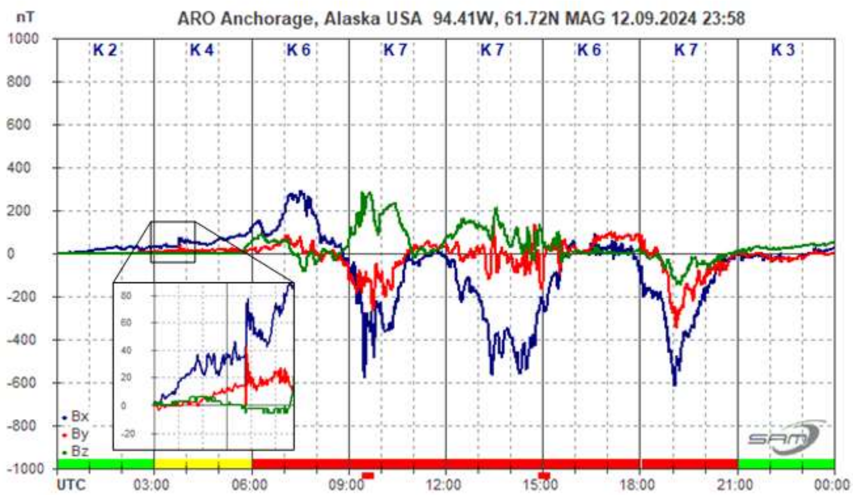

Figure 13.a ~ Anchorage magnetogram for 12 September. The vertical autoscale function of the SAM_VIEW software stepped to 1000 nT due to the high magnetic flux density at about 0930 following the Sudden Impulse. The impulse was almost invisible at this scale so the time from about 0300 to 0415 has been expanded in the inset to show more detail. The sudden impulse amplitude at Anchorage (vector sum of Bx and By) was approximately 76 nT.

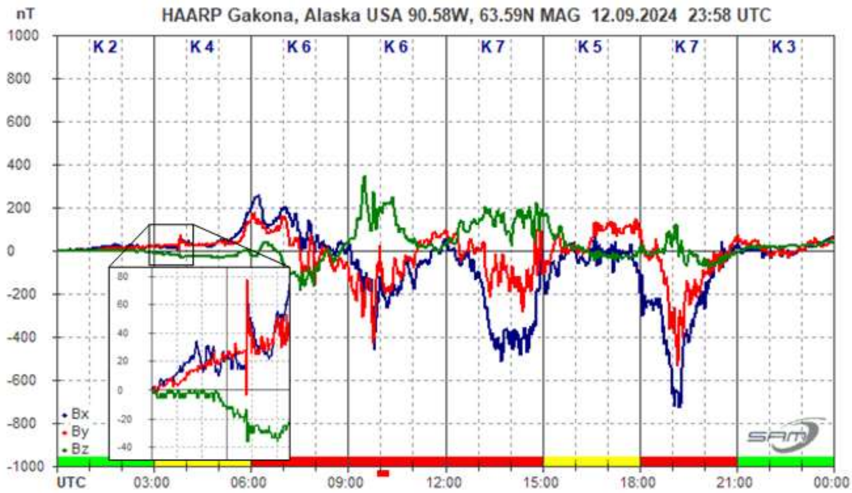

Figure 13.b ~ HAARP magnetogram for 12 September. As at Anchorage, the Sudden Impulse was almost invisible, so the time range from about 0300 to 0415 has been zoomed-in. All three components show evidence of the impulse, including about 10 nT in the vertical component Bz. The sudden impulse amplitude at HAARP (vector sum of Bx and By) was approximately 90 nT. Note the very similar but imperfect match between the impulse and full day field variations at Anchorage and HAARP. Part of the difference is due to different magnetic environments, including magnetic latitude, but some differences could arise because of the different models of fluxgate sensors at each site (FG3+ at HAARP and FGM-3 at Anchorage).

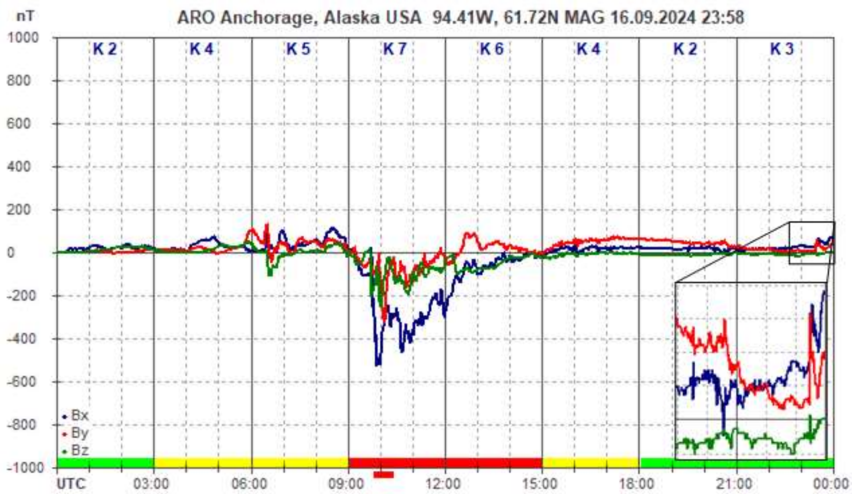

Figure 14.a ~ Anchorage magnetogram for 16 September annotated with the last three hours of the UTC day zoomed-in. All three components show evidence of the impulse (near right edge), including about 15 nT in the vertical component Bz. The sudden impulse amplitude at Anchorage was approximately 63 nT. Note the bay seen in the inset in the east-west component (By, red trace) during the 3-hour period leading up to the Sudden Impulse.

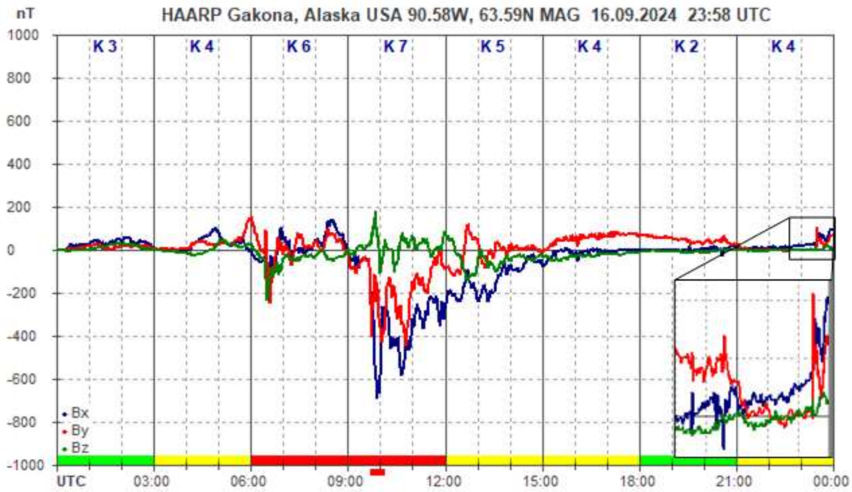

Figure 14.b ~ HAARP magnetogram for 16 September annotated with the last three hours of the UTC day zoomed-in. The scale in the inset is 50 nT Div^{-1}. The sudden impulse amplitude at HAARP was approximately 120 nT. Note the periodicity in variations of both Bx and By during the 0900-1200 and 1200-1500 synoptic periods prior to the Sudden Impulse. Similar periodicities appear in the Anchorage magnetogram but are lower amplitudes. The periods are too long to be classified as Ultralow Frequency (ULF) Waves and could be caused by *Periodic Density Structures* in the solar wind or substorm energy loading and unloading in the magnetosphere (step 7 in the Dungey Cycle described in the Interplanetary Magnetic Field section).

Discussion: Although storms (≥ K5) occurred at both observatories after the impulses on 12 and 16 September, the magnetic deflections only reached about 600 and 700 nT in Bx and By for a short time. Nevertheless, these peak deflections were significant fractions (~5% of Bx and ~10% By) of the ambient magnetic field components (table 2).

Table 2 ~ Ambient magnetic flux densities for September 2024 at the Anchorage and HAARP stations based on World Magnetic Model (2019-2024). Data source: https://www.ngdc.noaa.gov/geomag/calculators/magcalc.shtml#igrfwmm

Observatory	**Bx, north-south (nT)**	**By, east-west (nT)**	**Bz, vertical (nT)**
Anchorage	14 665	3 821	52 857
HAARP	13 416	3 910	53 838

The active regions on the Sun responsible for the CMEs discussed in the present article eventually rotated out of view and the space weather substantially calmed down on 18 September. However, during the last 12 days of September there were several brief storm intervals that involved CME trailing influences or near-misses and coronal hole high-speed streams.

The AE index variations shown previously are moderate compared to the very strong storm on 10 to 13 May 2024 (often called the *May Superstorm*) during which the AE index went off-scale (> 2000 nT). Not surprisingly, both Anchorage and HAARP magnetometers displayed a K-index of K9 (the highest on the K-index scale) on those same days. The May storm was unique because of its high and sustained intensity and will be the subject of a future article.

Readers may refer to several previous articles about Sudden Impulses recorded by the SAM-III magnetometers in Alaska:
https://reeve.com/RadioScience/Radio%20Astronomy%20Publications/Articles_Papers.htm#Observations

Instrumentation: The block diagrams for the SAM-III Magnetometers at Anchorage and HAARP show that the two installations are nearly identical (figure 15). The differences are listed in table 3. Both stations use the SAM_VIEW software to display and log the three magnetic components. Real-time magnetograms are available at: https://reeve.com/SAM/SAM_simple.html (Anchorage) and https://reeve.com/SAM/SAM-HAARP/SAM-HAARP_simple.html (HAARP).

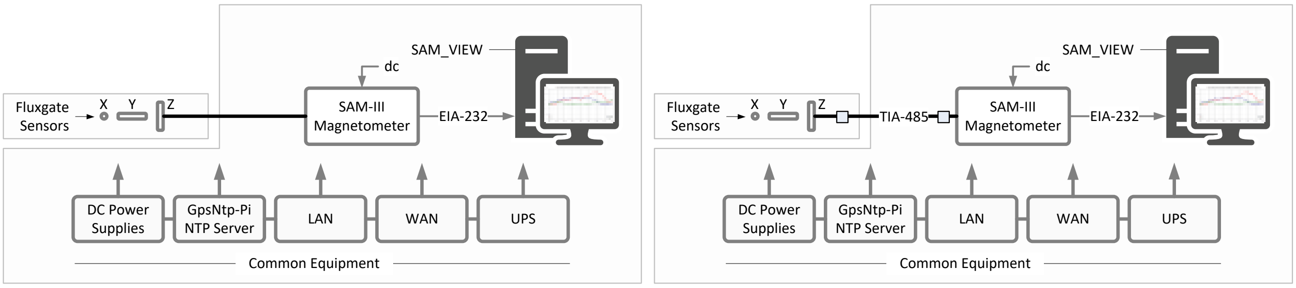

Figure 15 ~ SAM-III Magnetometer block diagrams for Anchorage (left) and HAARP (right). The two are operationally identical and differ only in a few technical details (see text).

Table 3 ~ Differences between magnetometer stations.

Observatory	**Anchorage**	**HAARP**	**Remarks**
Sensor type	FGM-3	FG-3+	Performance nearly identical
Sensor voltage	12 Vdc	5 Vdc	Anchorage has 5 V voltage regulators at the sensors whereas HAARP has them on the controller
Sensor transmission	Cable only	TIA-485 + Cable	HAARP uses CAT5E cable and TIA-485 transmission interfaces

References:

{Reeve13} Reeve, W., Geomagnetic Sudden Impulses, 2013: https://reeve.com/Documents/Articles%20Papers/Observations/Reeve_GeomagSuddenImpulses.pdf

{Reeve21} Reeve, W., Summary of Geomagnetic Effects Observed During a Solar Cycle, 2021: https://reeve.com/Documents/Articles%20Papers/Reeve_SolarMagneticCycle25.pdf

[Seki] Seki, K., et al, A Review of General Physical and Chemical Processes Related to Plasma Sources and Losses for Solar System Magnetospheres, Space Science Reviews, August 2015, DOI 10.1007/s11214-015-0170-y

Taking the Guesswork out of Antenna Ground and Spillover Noise

Peter W East

Abstract
Radio telescope antennas intercept ground radiation in their side- and back-lobes or via reflector spillover with a consequent loss in system sensitivity. Rough estimations, given average side- and back-lobe levels, are generally used [1,2]. With standard antenna co- and cross-polar E and H patterns it is possible to integrate over offending regions to fully determine ground effects on the system noise temperature [3,4]. This note describes a simple spreadsheet approach for antennas with circular symmetry using measured E/H plus co- and cross-polar averaged patterns. This technique can, not only produce a realistic value for ground noise of most small aperture and traveling-wave-type antennas at various orientations but also optimize sensitivity performance of large reflector antennas based just on the feed antenna patterns and dish physical parameters. The analysis confirms the recommended reflector edge illumination guidance but shows that optimum dish parameters for best antenna gain differs from those for best system sensitivity.

1. Introduction
In general, amateur radio astronomers estimate the antenna ground and spillover components of their receiver system noise temperature by subtracting known temperature contributions, such as low noise amplifiers and front-end losses, from calibrations made using the Y-Factor measurement method [5]. This is reasonable providing the calibration can be carried out with sources within the operational situation of interest.

An early approximation was described by Kraus splitting the antenna pattern into 3 regions; the main beam, an orthogonal side-lobe and a back-lobe. Assuming suggested temperatures proposed for these, he arrived at a coarse estimate for the antenna noise temperature [1, p410].

Reference 4 shares an antenna noise calculator based on measured antenna azimuth/elevation patterns and a defined noise temperature environment.

The methods outlined here also rely on antenna polar pattern measurements, assumes these are bore-sight rotationally symmetric and quantizes these sufficient to describe the pattern detail. The analysis is carried out automatically using a spreadsheet and provides a realistic indication of ground noise variation with antenna pointing direction and horizon. The process is also suitable for predicting reflector spillover with only a knowledge of the feed antenna pattern and so is useful for predicting the performance of large dish reflectors. Section 2 describes the mathematical background theory for the calculations and Section 3 interprets this suggesting a simpler quantized digital approach.

Section 4 demonstrates the analysis technique for ground noise estimation with some examples; the second more detailed example quantifies the variation of ground noise when tilting the antenna towards the horizon. Section 5 extends the technique to evaluate spillover noise for large dishes using just the feed antenna polar patterns together with the dish physical parameters at the frequency of operation.

The analysis spreadsheets are available via the referenced links and have been encoded and all that is needed is for users to enter their antenna pattern data.

2. Definitions

2.1. *Antenna Noise Temperature*

The antenna noise temperature equation, accounting for both co- and cross-polarization, placed in a non-zero temperature environment is,

$$T_A = \frac{\int_0^{2\pi}\int_{-\pi/2}^{\pi/2}\left[P_C(\theta,\phi)T_{bC}(\theta,\phi) + P_X(\theta,\phi)T_{bX}(\theta,\phi)\right]\sin\theta \, d\theta \, d\phi}{\int_0^{2\pi}\int_{-\pi/2}^{\pi/2}\left[P_C(\theta,\phi) + P_X(\theta,\phi)\right]\sin\theta \, d\theta \, d\phi} \qquad (1)$$

where, $\theta \ and \ \phi$, are the azimuth and elevation terms and $P_C(\theta,\phi)$ and $P_X(\theta,\phi)$ are power gain per unit solid angle for co-polar (*c*) and cross-polar (*x*) antenna responses respectively.

$\theta = 0 \ and \ \phi = 0$, represents the main beam bore-sight direction.

$T_{bC}(\theta,\phi)$ and $T_{bX}(\theta,\phi)$ represent the corresponding surrounding brightness temperatures per unit solid angle.

This is equation can be implemented in a simpler quantized form as below, by dividing the 4π observation sphere into *M* rotationally symmetric regions to allow a good working estimate of the ground temperature contribution to the telescope system temperature.

$$T_A = \frac{\sum_{m=1}^{M}\left(T_{Cm}G_{Cm}SA_{Cm} + T_{Xm}G_{Xm}SA_{Xm}\right)}{\sum_{m=1}^{M}\left(G_{Cm}SA_{Cm} + G_{Xm}SA_{Xm}\right)} \qquad (2)$$

G_{Cm} and G_{Xm} represent antenna co- and cross-polar pattern power gain levels, assumed constant over *M* solid angles, SA_{Cm} and SA_{Xm} (steradians)

2.2. ***Antenna Directivity (Gain)***

Given a spherical set of antenna polar pattern measurements, the antenna directivity, *D*, can be calculated from,

$$D = \frac{4\pi\left[P_C(0,0) + P_X(0,0)\right]}{\int_0^{2\pi}\int_{-\pi/2}^{\pi/2}\left[P_C(\theta,\phi) + P_X(\theta,\phi)\right]\sin\theta \, d\theta \, d\phi} \qquad (3)$$

As before, this equation can be simplified using the quantized integration technique to,

$$D = \frac{4\pi\left(G_{C0} + G_{X0}\right)}{\sum_{n=1}^{N}\left(G_{Cn}SA_{Cn} + G_{Xn}SA_{Xn}\right)} \qquad (4)$$

This directivity figure includes pattern focusing efficiency and will exceed the measured gain by resistive and mismatch losses.

3. Antenna Side-lobe Defining Concept

Ignoring resistive losses and loss due to illumination profile, the maximum gain *G* of an aperture antenna, area *A*, is given by the well-known formula,

$$G = \frac{4\pi A}{\lambda^2} \qquad (5)$$

where λ is the signal wavelength.

For a square aperture side *D*, the aperture area, $A = D^2$.

Now λ/D is a measure of the antenna half power beamwidth = *BW* in radians. So, we can re-write the gain equation as,

$$G = \frac{4\pi}{\left(\frac{\lambda}{D}\right)^2} = \frac{4\pi}{BW^2} \qquad (6)$$

Now observe that there are 4π steradians in a sphere and *BW* is approximately the antenna main beam solid angle, also in steradians.

Similarly, for a circular reflector, *G*, becomes,

$$G = \frac{\pi^2 D^2}{\lambda^2} = \frac{4\pi}{\left(\frac{\lambda}{D}\right)^2 \cdot \frac{4}{\pi}} = \frac{4\pi}{BW^2} \qquad (7)$$

So, the gain equation is also telling us that the antenna can be considered as producing a number of radial lobes, *G'*, roughly equal to the linear gain figure *G*, over the 4π sphere. One, of course, is the main directional beam and the *G'*-1 remainder can be thought of as much lower level side- and back-lobes equi-spaced over the surface of the sphere; each lobe emanating from the center of the sphere.

This is a useful concept as it gives a measure to the extent of practical side-lobes when determining power radiated or temperature sensed in side-lobes. We can set a level to the *G* - 1 side-lobe beams from antenna power pattern measurements and just sum the side-lobe/equivalent beam contributions over their relevant solid angles using a standard spreadsheet.

3.1. Calculating Side-lobe Temperature Contributions

If the antenna pattern is assumed rotationally symmetric, a particular side-lobe region can be thought of as a number of equivalent side-lobe beams occupying a spherical sector of a sphere as shown in Figure 1.

The solid angles covered by a particular side-lobe level region of Figure 1 are calculated from the spherical sector, solid angle formula,

$$SA_{12} = 4\pi\left[\left(\sin\frac{\phi_2}{2}\right)^2 - \left(\sin\frac{\phi_1}{2}\right)^2\right] = 2\pi(\cos\phi_1 - \cos\phi_2) \qquad (8)$$

where, ϕ_1 *and* ϕ_2 represent the specified side-lobe sector (elevation) limits.

Dividing the sphere into *M* solid angle sectors, then from each solid angle sector, we can calculate the equivalent number of side-lobe beams within it.

So, the number of side-lobe beams in the m^{th} *SA* sector = $\eta_m = \frac{SA_m . G}{4\pi}$ (9)

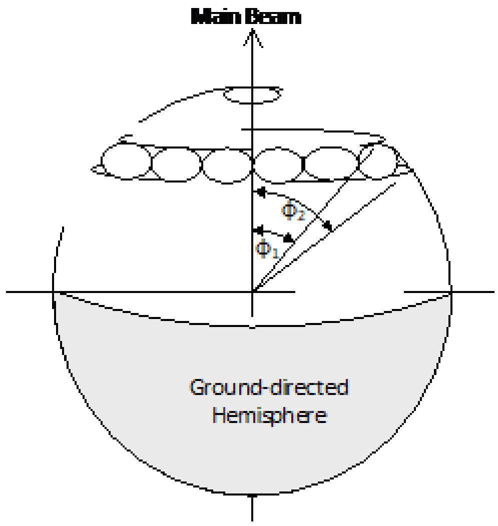

Figure 1 Side-lobe Solid Angle (SA) Spherical Sector Definition, $\phi_2 - \phi_1$

Adapting Equation (2), and assuming the antenna is singly polarized and placed in a closed environment with the walls at ambient temperature, 290°K, the equivalent temperature seen by the m^{th} lobe sector is,

$$T_m = \frac{290 . S_m . \eta_m}{\sum_{m=1}^{M} S_m . \eta_m} \quad (10)$$

where, S_m is a nominated side-lobe power gain over the sector SA_m ; the denominator represents the sum of the power levels of all *M* sectors. Setting the enclosed environment allows quantifying the ground temperature seen by ground-pointing antenna lobe/sectors.

4. Examples

The method is first demonstrated with a basic example. In this case, based on an 8 degree beamwidth reflector antenna with published gain 23dB (~x200). The maximum possible gain using the specified beamwidth = 27dB ~ x506.

The overall efficiency then, is 40%, (-4dB gain from maximum = 1/2.5). Efficiency losses of a focus fed parabolic dish include feed losses, illumination profile loss. Directivity losses include spillover and power lost in side-lobes.

4.1 Example 1, Basic Application

The basic example of a co-polar antenna pattern of a parabolic reflector antenna is shown in Figure 2. For the following calculations, it is assumed that this pattern is preserved over the bore-sight axis of revolution.

Here, the pattern is first divided into a number of angular regions by eye, in this case, where the side-lobe levels appear roughly constant, (Column 1, Figure 3). Column 2 represents the mean side-lobe level over each region. Column 3 is the calculated solid angle (Equation 8) whilst Column 4 lists the equivalent number of beams (Equation 9), in this case totaling 506.2, the calculated maximum gain.

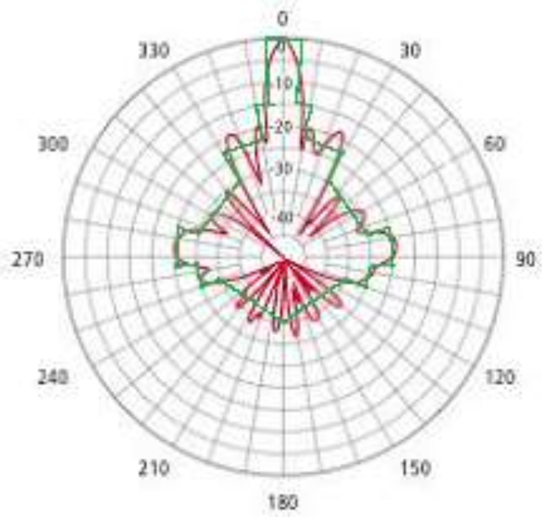

Figure 2 Polar Pattern of Parabolic Dish Example (red), and Approximation (green)

Figure 3 table shows that 49%, (290-148.9)/290, of the power enters through the side-lobes and the antenna pattern efficiency is 51% (=148.9/290) and accounts for 3 dB gain loss from the ideal.
The other 1 dB (ideal gain 27dB, published gain 23dB in the example is reflector illumination loss, feed antenna efficiency etc:

Angle (deg)	SL Level (dB)	Solid Angle (Steradians)	No. Beams	Lobe Sector Temp
0-4	0	0.019	0.8	148.9
4 -10	-15	0.76	3.1	18.5
10-30	-25	0.747	30.1	18.1
30-75	-30	3.817	153.7	29.3
75-95	-25	2.174	87.6	52.8
95-110	-30	1.602	64.5	12.3
110-180	-35	4.133	166.5	10.0
Totals		**12.566**	**506.2**	**290**

Figure 3. Lobe-Sector Temperature Contributions (blue font entries are spreadsheet calculated)

The lobe-sector temperature contributions, Column 5 are calculated using Equation 10.

Figure 3 shows that with the rear hemisphere facing the ground, side/back-lobes (90 to 180 degrees) can contribute 25° or more to a radio telescope system temperature. Also, the side-lobe region 75° - 95° should be kept well clear of horizon/building/tree obstructions.

4.2 Example 2, Estimating System Ground Temperature with Tilted Yagi Antenna

Figure 4 antenna spreadsheet file (Side-lobeTempYagi.xls) applies; measurements in black type (columns F and G) were taken from a professionally designed 22-element Yagi antenna tuned to 595 MHz [6]. The measured co- and cross-polar azimuth patterns are inset with a measured beamwidth of 28.8 degrees. Data listed in blue type are either pre-set or automatically calculated in the referenced Excel spreadsheet using formulae stored in the spreadsheet file; changing values in columns F and G automatically change the calculated values and results.

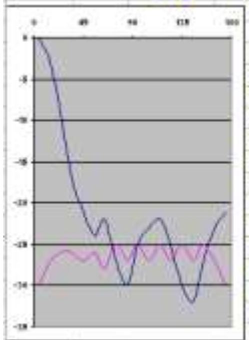

A	B	C	D	E	F	G	H	I	J	K	L	M	N	O
BW-Az	BW-El	Max. Gain	Min Angle	Max Angle	Mean level (dB)	Xpol level	SA (sterads)	No: of Beams	CPxT	XPxT	C Power	X Power	C Temp: °K	C+X Temp: °K
28.8	28.8	15.92	0	10	0	-30	0.095	0.30	86.072	0.086	0.297	0.000	81.99	75.25
			10	20	-3	-27	0.284	0.88	128.104	0.510	0.442	0.002	122.02	112.33
		39.1	20	30	-10	-26	0.463	1.44	41.736	1.048	0.144	0.004	39.75	37.37
			30	40	-17	-26	0.628	1.95	11.302	1.423	0.039	0.005	10.77	11.11
			40	50	-21	-27	0.775	2.41	5.547	1.393	0.019	0.005	5.28	6.06
			50	60	-24	-26	0.897	2.79	3.220	2.032	0.011	0.007	3.07	4.59
			60	70	-22	-28	0.993	3.09	5.647	1.418	0.019	0.005	5.38	6.17
			70	80	-27	-25	1.058	3.29	1.903	3.016	0.007	0.010	1.81	4.30
			80	90	-30	-27	1.091	3.39	0.984	1.963	0.003	0.007	0.94	2.57
			90	100	-25	-25	1.091	3.39	3.111	3.111	0.011	0.011	2.96	5.43
			100	110	-23	-27	1.058	3.29	4.780	1.903	0.016	0.007	4.55	5.84
			110	120	-22.0	-25	0.993	3.09	5.646	2.830	0.019	0.010	5.38	7.40
			120	130	-25.0	-27	0.897	2.79	2.557	1.614	0.009	0.006	2.44	3.64
			130	140	-30.0	-25	0.774	2.41	0.698	2.207	0.002	0.008	0.66	2.54
			140	150	-32.0	-27	0.628	1.95	0.357	1.130	0.001	0.004	0.34	1.30
			150	160	-27.0	-25	0.463	1.44	0.832	1.319	0.003	0.005	0.79	1.88
			160	170	-23.0	-27	0.283	0.88	1.279	0.509	0.004	0.002	1.22	1.56
			170	180	-21.0	-30	0.095	0.30	0.681	0.086	0.002	0.000	0.65	0.67
	Totals						12.6	39.1	304.455	27.597	1.050	0.095	290.00	290.00
Notes:	1. Adjust black bold font entries only													
	2. Max linear gain = (180/BW)^2						39.1							
	3. Number of beams in 4pi steradians = linear gain													
	4. Side/backlobe temp: from rear hemisphere (90-180) in Tsys =						30.26	deg K						
	5. Antenna pattern efficiency =						81.3	%						

Figure 4 Side-lobe Spreadsheet Table - Yagi 22-element Example

The method of estimating the system temperature due to ground illumination of the antenna side-lobes is to assume that ground temperature source (assumed here as 290 °K) only occupies the lower hemisphere as seen by the antenna pattern. With this stipulation, when the pointing direction of the antenna is tilted from the vertical new halves of the side-lobe sectors fall within this region whilst on the opposite side, the other half-sectors enter the forward hemisphere. Using this simple algorithm, and summing the lower hemisphere sectors, an estimate of how the ground influences the system temperature with tilting is realized. Figure 5 shows the tilting ground system temperature using the data of Figure 4.

Tilt °K	Tilted Temp:	Incl: Cross Pol:
0	18.99	30.26
10	17.98	28.83
20	16.61	28.06
30	16.61	27.44
40	16.93	27.92
50	19.24	29.68
60	24.45	34.59
70	43.93	52.33
80	104.33	107.71
90	145.00	145.00

Figure 5 System Ground Temperature Variation with Antenna Tilt from Vertical

When tilting the antenna away from the vertical, the proportion of relevant angle ranges directed at ground/warm structures can be estimated and side-lobe sections summed to obtain a new side-lobe temperature result. Pointing an antenna horizontally towards the horizon for example, theoretically, half the antenna pattern hemisphere is now ground-directed, which would result in a ground temperature contribution of 290/2 = 145°K.

Figure 5. Columns 2 and 3 list ground-directed hemisphere noise temperature; column 2, co-polar response only, column 3 including a simulated cross-polar response.

As an example of calculating the values in Figure 5, the result for a 10° tilt using just co-polar data from Figure 5 ('C Temp' column) by examining the tilted sector geometry is,

17.98 = SUM(C Temp: 100° to 180°) + ½.SUM(C Temp: 80° to 100°) (XL1)

Refer to the .xls file in Reference 6 for more detail.

Figure 5 shows that antenna cross-polar performance can have a significant effect on the ground-induced system noise temperature. The cross-polar figures for this antenna show that they need to be much lower than the co-polar side-lobes to minimize their effect. It is interesting to note that the ground system temperature component does not change significantly for tilts up to 50°. This may not be true for sites with positive horizons due to in-leaf trees or buildings: Figure 5 is still relevant in this case and can be used to estimate the increased system noise temperature expanding the range by adapting Equation XL1.

5. Estimating Parabolic Dish Performance

Measurement of large dish antenna patterns requires long antenna ranges, and expensive rotation gear and test equipment. The performance of even very large dishes can however be estimated with well-characterized antenna feed data together with dish physical focus and diameter parameters. With this information, this note describes a method of determining the dish system performance parameters including, optimum *F*/*D* (dish focal length/dish diameter) ratio, beam pattern, gain, efficiency, spillover and *G*/*T* figure ($10.\log_{10}$(antenna gain/system noise)). The previous sections outline the procedure for extracting useful information from the feed antenna patterns. For this example, measurements on a 1420MHz Cantenna antenna are used [7].

5.1. Parabolic Dish Parameters

The profile of the dish is defined by a parabola (see Figure 6) given by,

$$y = \frac{x^2}{4F} \qquad (11)$$

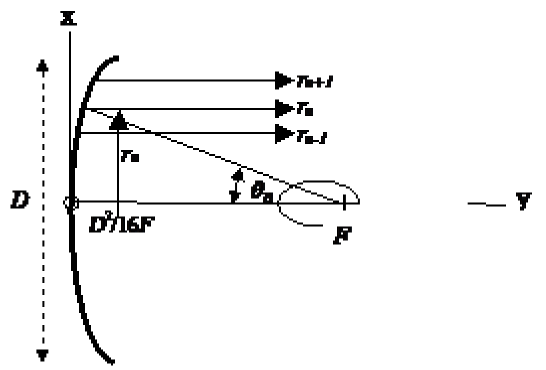

Figure 6. Parabolic Dish + Feed Schematic

Used as an antenna reflector, it has the property that placing a feed antenna at the focal point *F* ensures that all waves generated align in phase at the dish front plane to produce a focused beam with a beamwidth defined by the dish aperture *D* and illumination profile.

The distance from the dish center r_n corresponding to a feed angle offset of ϑ_n is given by,

$$r_n = 2F \frac{[1 - \cos(\theta_n)]}{\sin(\theta_n)}$$

When $r = D/2$, $\tan(\theta)=\dfrac{D/F}{2\left(1-(D/4F)^2\right)}$ (12)

so, given the dish focal distance/dish diameter (*F/D*) ratio, the feed subtended half-angle ϑ, at the dish focal distance *F* can be found.

Maximum gain is achieved if the feed could illuminate the dish with a constant amplitude profile, the beam gain and shape are then defined by,

$$G(\alpha)=\frac{\pi^2 D^2}{\lambda^2}\left[\frac{2J1\left(\frac{\pi}{\lambda}D\alpha\right)}{\left(\frac{\pi}{\lambda}D\alpha\right)}\right]^2 \quad (13)$$

where, *D* is the dish diameter, α is the beam offset angle in radians, λ is the signal wavelength and *J*1 is the Bessel function of the first kind, first order. Bessel functions are available in most mathematical CAD packages and also conveniently in Excel (using the inbuilt function, BESSELJ()).
Maximum bore-sight gain occurs when $\alpha = 0$.

Generally, the feed antenna will not provide a constant illumination over the dish aperture, but will show a more profiled response, preferably rotationally symmetrical. For the purposes of this application, where the feed pattern equivalent temperatures, T_n can be described in spherical sector form, this gain equation can be modified (see Appendix A.1) accordingly to,

$$G(\alpha)=\left(\frac{2\pi}{\lambda}\right)^2\left[r_1\sqrt{T_1}\,j1+\sum_{n=2}^{N} jn\sqrt{T_n\left(r_n^2-r_{n-1}^2\right)}\right]^2/290 \quad (14)$$

where,

$$j1=\left[\frac{2J1\left(\frac{2\pi}{\lambda}r_1\alpha\right)}{\frac{2\pi}{\lambda}r_1\alpha}\right] \quad \text{and,} \quad jn=\left[J0\left(\frac{\pi}{\lambda}(r_n+r_{n-1})\alpha\right)\right]$$

*J*0 is the Bessel function of the first kind, zero order, and is used to approximate the pattern shape contributions of the various annulus rings across the dish aperture, other than the first inner circle, radius r_1. The annulus illumination amplitudes, T_n apply over the radius range r_n to r_{n-1}, and, n = 1 to N where, $r_N = D/2$.

5.2. Cantenna Feed Data

It is recommended that 360° feed patterns should be taken for *E* and *H* planes at 5° intervals, plus intermediate planes if possible, and the results linearly averaged and then partitioned as described above.

To ensure best efficiency estimation, cross-polar patterns should also be available. Together with feed amplitude/temperature pattern measurements.

In practice, it is important to determine the feed aperture phase center (usually just inside the physical aperture) so that it can be accurately placed physically at the dish focal point. The analysis assumes correct alignment.

	A	B	C	D	E	F	G	H	I	J
1					**Feed Antenna**					
2										
3	**theta**	**Amp**	**mean LR**	**SA**	**G.SA**	**Tsa**	**SQRT(Tsa)**	**Xpol**	**D**	**Feed Gain**
4								-40	8.21	
5	0	**0.00**	0	0						8.21
6	5	**-0.17**	-0.086	0.024	0.023	3.58	1.89			8.12
7	10	**-0.32**	-0.249	0.072	0.068	10.32	3.21			7.96
8	15	**-0.58**	-0.448	0.119	0.107	16.35	4.04			7.76
9	20	**-0.90**	-0.733	0.165	0.139	21.27	4.61			7.47
10	25	**-1.37**	-1.126	0.210	0.162	24.73	4.97			7.08
11	30	**-1.94**	-1.643	0.253	0.173	26.49	5.15			6.56
12	35	**-2.49**	-2.206	0.295	0.177	27.08	5.20			6.00
13	40	**-3.16**	-2.815	0.334	0.175	26.66	5.16			5.39
14	45	**-3.89**	-3.510	0.370	0.165	25.22	5.02			4.70
15	50	**-4.90**	-4.363	0.404	0.148	22.61	4.76			3.84
16	55	**-5.88**	-5.361	0.435	0.127	19.33	4.40			2.85
17	60	**-6.89**	-6.356	0.462	0.107	16.35	4.04			1.85
18	65	**-8.39**	-7.578	0.486	0.085	12.98	3.60			0.63
19	70	**-9.81**	-9.042	0.507	0.063	9.65	3.11			-0.84
20	75	**-11.32**	-10.496	0.523	0.047	7.13	2.67			-2.29
21	80	**-12.99**	-12.075	0.535	0.033	5.08	2.25			-3.87
22	85	**-14.63**	-13.737	0.54	0.023	3.52	1.88			-5.53
23	90	**-16.61**	-15.511	0.55	0.015	2.36	1.54			-7.30
24	95	**-17.95**	-17.229	0.55	0.010	1.59	1.26			-9.02
25	100	**-18.79**	-18.352	0.54	0.008	1.22	1.11			-10.15
26	105	**-19.58**	-19.168	0.54	0.007	1.00	1.00			-10.96
27	110	**-20.53**	-20.028	0.52	0.005	0.80	0.90			-11.82
28	115	**-21.27**	-20.887	0.51	0.004	0.64	0.80			-12.68
29	120	**-21.10**	-21.183	0.49	0.004	0.57	0.76			-12.98
30	125	**-21.04**	-21.070	0.46	0.004	0.56	0.75			-12.86
31	130	**-21.09**	-21.068	0.43	0.003	0.53	0.73			-12.86
32	135	**-21.19**	-21.139	0.40	0.003	0.48	0.69			-12.93
33	140	**-21.37**	-21.277	0.37	0.003	0.43	0.65			-13.07
34	145	**-21.90**	-21.627	0.33	0.002	0.36	0.60			-13.42
35	150	**-23.19**	-22.497	0.29	0.002	0.26	0.51			-14.29
36	155	**-23.34**	-23.264	0.25	0.001	0.19	0.43			-15.06
37	160	**-22.24**	-22.756	0.21	0.001	0.17	0.42			-14.55
38	165	**-21.05**	-21.604	0.16	0.001	0.18	0.42			-13.40
39	170	**-19.24**	-20.051	0.12	0.001	0.18	0.42			-11.84
40	175	**-19.30**	-19.268	0.07	0.001	0.13	0.36			-11.06
41	180	**-19.25**	-19.271	0.02	0.000	0.04	0.21			-11.06
42			**Col. Sums**	12.568	1.899	290.00				

Figure 7. 6" Cantenna Feed Pattern Analysis Spreadsheet

Figure 7 shows a typical feed analysis summary in the spreadsheet *DishCalcsF.xls* [8]. The input data is of an L-band 6 inch diameter, 80 degree beamwidth Cantenna measured at 1420MHz.

The first three columns in the spreadsheet *A*, *B*, *C* list the input data. Column *B* corresponds to the left and right linear averages of the measured pattern plot.

Column C is the sector mid-level,
'Mean' -> 10*LOG((10^(B2/10)+10^(C2/10))/2) (XL2)

Column D is the Sector spherical area from Equation 8
'SA' -> 2*3.142*(COS(A5*3.142/180)-COS(A6*3.142/180)) (XL3)

Column *E*, is the equivalent side-lobe level,
'G.SA' -> =(10^((C6)/10)+10^((H$4)/10))*D6 (XL4)

Column *F,* describes each spherical sector equivalent temperature assumed placed in a 290 K container
'Tsys' -> =290*E6/E42 (XL5)) °

If cross-polar data relative to the co-polar data amplitudes is available for a better directivity and efficiency estimate, then further columns need adding and combined as required by Equation 2. Failing this, in this example a constant cross-polar level of -40dB (column J2) is assumed.

From this data, we can calculate the Directivity = $4\pi/\Sigma(G.SA)$ = 8.21dB and the ground noise temperature assuming the Cantenna is pointed vertically and the lower side-lobe hemisphere is = $\Sigma T_{sal(95\text{-}180)}$ = 9.3°.

Now that the feed antenna is characterized in this way, the forward-looking sector data is suitable for estimating the performance of any feed-reflector dish combination.

5.3. Estimating Parabolic Dish plus Feed Performance.
The parabolic dish focal distance-to-dish diameter ratio *F*/*D* defines the angle subtended by the feed antenna from Equation 12. This angle in turn, defines which feed spherical sectors illuminate which circular ring sections in the dish. Feed antenna spherical sectors that exceed the dish aperture can be used to estimate spillover. The cut-off for ground noise due to spillover is the angle of the dish edge to the horizon angle of 90°, assuming the dish aperture is pointing to the zenith.

5.4. Results.
The analysis spreadsheet *DishCalcsF.xls* uses the Cantenna feed data in the analysis equations of Section 5.1 to synthesize the dish antenna pattern and calculate the various dish parameters as a function of dish focal length to diameter ratio to determine the optimum *F*/*D* ratio.

Figure 8, extracted from the analysis spreadsheet, summarizes the key parameters and performance figures for the feed antenna of Figure 7 when driving a 1.2m dish at 1420 MHz for various *F*/*D* ratios (Row 1). Row 2 lists the corresponding feed-dish subtended angle, chosen to match ranges listed for the feed in Figure 7.

The dish illumination efficiency is calculated by summing the spherical sector temperatures of Figure 7, lying within the feed subtended angle as a ratio of 290 °K. As the focal distance reduces, more of the feed spherical sectors illuminate the dish.

The spillover temperature is calculated by summing the sector temperatures over the range between the *F*/*D* subtended half-angle and 90° - this assumes the dish is directed vertically and ground noise temperature angle is limited by the horizon. The variation of spillover noise with antenna tilting follows the method outlined in Section 4.2.

The feed+dish maximum gain *G*(0), is calculated using Equation 14, setting the Bessel terms, *j0* and *jn* equal to unity; full evaluation is required to calculate the dish antenna polar pattern.

Row 7, estimates the antenna combination radiation efficiency, taking the ratio of dish + feed maximum gain to the aperture maximum gain $= \pi^2 D^2 / \lambda^2$ = 322.3 (for D = 1.2m, λ = 0.21m).

F/D	5.73	2.86	1.90	1.42	1.13	0.93	0.79	0.69	0.60	0.54	0.48	0.43	**0.39**	0.36	0.33	0.30	0.27
Subt: Angle(°)	10.0	20.0	30.0	40.0	50.0	60.0	70.0	80.0	90.0	100.0	110.0	120.0	**130.0**	140.0	150.0	160.0	170.0
Illumination Effy.	0.01	0.05	0.10	0.18	0.26	0.35	0.45	0.54	0.63	0.70	0.77	0.83	**0.87**	0.91	0.93	0.95	0.96
Spillover (°K)	277.1	266.8	250.4	229.2	204.4	178.0	150.9	124.2	99.0	76.4	57.1	40.7	**27.7**	18.1	11.0	5.9	2.4
Edge Illumination	0.1	0.2	0.4	0.7	1.1	1.6	2.2	2.8	3.5	4.4	5.4	6.4	**7.6**	9.0	10.5	12.1	13.7
Max Gain	4.0	15.4	33.6	57.2	84.5	113.5	142.7	170.7	196.2	217.4	233.1	243.7	**248.1**	246.2	239.3	228.2	214.0
Radiation Effy.	0.01	0.05	0.10	0.18	0.26	0.35	0.44	0.53	0.61	0.67	0.72	0.76	**0.77**	0.76	0.74	0.71	0.66
G/T+40K	-19.01	-12.98	-9.37	-6.73	-4.61	-2.83	-1.26	0.17	1.50	2.71	3.81	4.80	**5.64**	6.27	6.72	6.97	7.03
G/T+100K	-19.77	-13.76	-10.18	-7.60	-5.57	-3.89	-2.45	-1.18	-0.06	0.91	1.72	2.38	**2.88**	3.19	3.34	3.34	3.20

Figure 8. Feed+Dish Parameter Summary v Dish *F/D*

The final two rows offer an indication of the overall system *G/T* sensitivity assuming receiver noise temperatures of 40 °K and 100 °K respectively. The Figure 8 tabulated figures also seem to confirm the conventional rule-of-thumb for an optimum feed antenna producing a dish edge illumination of -10dB.

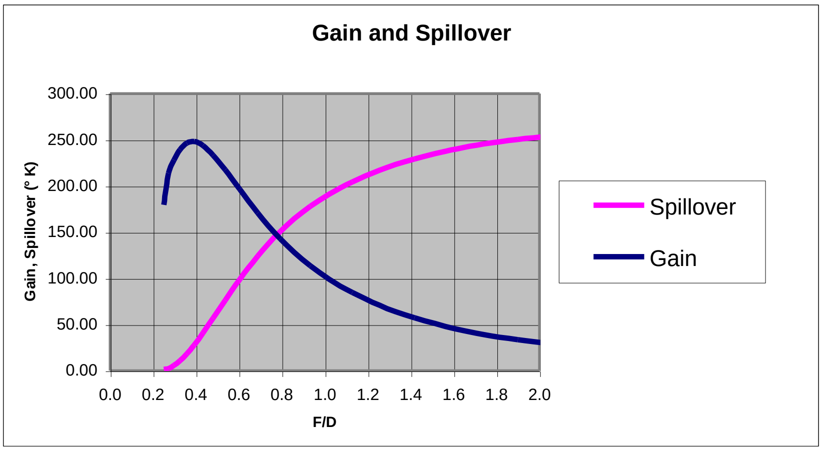

Figure 9. Feed+Dish Gain and Spillover Estimates

Two parameters of primary interest in this tabulated data are plotted in Figure 9. This indicates that for this Cantenna feed, the optimum parabolic dish *F/D* ratio producing maximum gain is 0.39. However, in this case the spillover noise temperature appears quite large at 27.7 °K .

The optimum dish *F/D* for the chosen feed is tested in Figure 10 using the antenna gain/system noise temperature ratio figure of merit, 10.log(*G/T*). To explore this region, Figure 10 also calculates the system *G/T* sensitivity for several likely receiver noise temperatures and these show that either a narrower beamwidth feed or a modified dish *F/D* ratio down to 0.3 should provide a better system sensitivity result for most practical receiver noise levels. It shows, however, that only the lowest receiver system noise levels benefit significantly from this change.

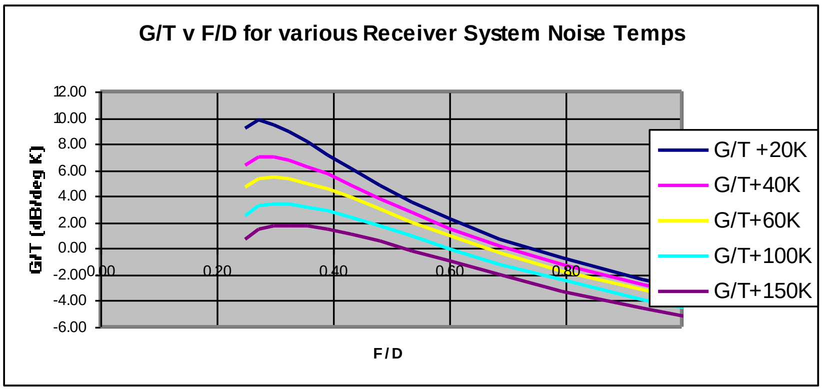

Figure 10. System Sensitivity v F/D Ratio

In Figure 11, the antenna pattern for the feed is plotted together with the predicted dish patterns for *F/D* = 0.39 derived by applying Equation 14. The patterns are produced using the Excel spreadsheet, *DishCalcsF.xls*, using the spreadsheet sub-panels to calculate the dish ring illuminated contributions and corresponding Bessel terms.

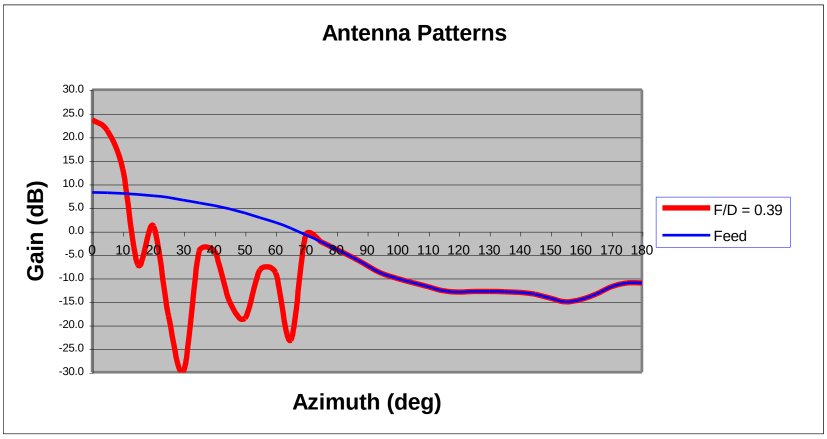

Figure 11. Feed and Predicted Feed+Dish Patterns for *F/D* = 0.39 with 0.8 λ, Feed Blockage

Figure 11 dish pattern at angles greater than 65° should be only taken as a rough guide since the geometrical optics approach adopted ignores diffraction that normally dominates in the rear hemisphere. In practice, diffraction and phasing effects tend to increase side-lobe rippling and complexity and also enhance the 180 degree back-lobe.

Figure 11 is the result of removing the first two center ring terms corresponding to a blockage of 0.164m or 0.8 λ. The effect is to slightly lower the directivity/gain and efficiency, but significantly modify the near side-lobes.

Also note that efficiency figures do not include feed match or resistive losses.

6. Spreadsheet Use

The spreadsheets associated with this paper, References 6 and 8, may be used to estimate the performance of custom antennas if suitable antenna pattern data are available. The required computations have been encoded and all that is needed is to enter users pattern data.

Allowed pattern data entries are indicated in black type consistent with the preset angles listed.

7. Conclusions and Discussion

This article describes a simple working spreadsheet method of estimating the effect of side/back-lobes and cross-polar performance on degrading the system noise temperature of a radio telescope over most practical tilting angles and dish geometries. Prediction of large dish antenna performance based on feed antenna radiation pattern measurements is demonstrated including spillover, optimizing F/D and G/T plus ratification of the -10dB dish edge illumination popular recommendation. The importance of low antenna cross-polar performance to minimize ground and spillover noise is demonstrated. The spreadsheets are structured to allow entry of custom antenna data for performance prediction of user's antennas.

The method predicts that the optimum parabolic dish antenna F/D ratio for maximum system sensitivity may not be the same as that for maximum gain due to spillover noise degradation. In the case of this 80 degree beamwidth Cantenna feed example, it appears that the best system sensitivity for sub-50 °K receiver noise temperature systems is possible with a lower dish F/D ratio of 0.3 rather than 0.4, the value demonstrating maximum gain (see Figure 10). Alternatives here are to reduce the feed beamwidth and corresponding edge illumination or if the situation allows, extend the dish diameter with a suitable reflecting skirt matching the parabola trend. This both reduces the F/D ratio and increases aperture and gain. Diffraction effects have not been taken into account which tend to increase the back-lobe, but these would also reduce with lower edge illumination.

Yagi and helical antenna types have the advantage of size and portability and can be tuned to improve efficiency, so reducing back-lobes at the expense of bandwidth. As basically traveling-wave type antennas, the antenna phase center is near the forward end so that local ground screening is of limited effectiveness. For these antenna types, system sensitivity is best improved by increasing gain and aperture by employing multiple antennas in an array.

8. Acknowledgement

The Yagi and Cantenna Pattern measurement data was provided by, Prof. P.N Wilkinson, School of Physics & Astronomy, University of Manchester.

References

1. Kraus JD. "Radio Astronomy" McGraw-Hill, 1966. p 401.
2. Nikolova N. "Lecture 7: Antenna Noise Temperature and System Signal-to-Noise Ratio", https://www.ece.mcmaster.ca/faculty/nikolova/antenna_dload/current_lectures/L07_Noise.pdf
3. Lambert, K. M., and R. C. Rudduk, ‘‘Calculation and Verification of Antenna Temperature for Earth-Based Reflector Antennas,’’ *Radio Science*, Vol. 27, No. 1, January–February, 1992, pp. 23–30.
4. Galuščák R, Galuščáková P, Mazánek M, Hazdra P, Macáš M. " Antenna Noise Temperature Calculator" http://www.om6aa.eu/Antenna_Noise_Temperature_Calculator.pdf. http://www.om6aa.eu/antc.php
5. Agilent Technologies. "Application Note 57-2, The Y-Factor Method". https://testworld.com/wp-content/uploads/noise-figure-measurement-accuracy-the-y-factor-method.pdf
6. http://www.y1pwe.co.uk/RAProgs/Side-lobeTempYagi.xls
7. Cantenna Calculator, https://www.changpuak.ch/electronics/cantenna.php
8. http://www.y1pwe.co.uk/RAProgs/DishCalcsF.xls
9. Jull, EV. ‘Aperture Antennas and Diffraction Theory’. IET/Peter Peregrinus Ltd, 1981.

Appendix 1. Bessel Functions for Circular Aperture Reflector Beam Patterns

For a circular aperture, diameter *D* and a uniform illumination, the antenna beam pattern shape is defined by the first order Bessel function and given by Reference [9],

$$G(\alpha) = \frac{\pi^2 D^2}{\lambda^2}\left[\frac{2J1\left(\frac{\pi}{\lambda}D\alpha\right)}{\left(\frac{\pi}{\lambda}D\alpha\right)}\right]^2 \qquad \text{(A1)}$$

It is convenient in this application to compute the beam shape of the dish with a profiled illumination to split the aperture into a number of ring or annulus sections, assume that the illumination is constant within the ring, and then sum the voltages of these to determine the beam shape.

For any one ring, radius r_1 to r_2, the power is,

$$G_{12}(\alpha) = \frac{4\pi^2}{\lambda^2\left(r_2^2 - r_1^2\right)}\left[\frac{2J1\left(\frac{2\pi}{\lambda}r_2\alpha\right)}{\left(\frac{2\pi}{\lambda}r_2\alpha\right)}r_2^2 - \frac{2J1\left(\frac{2\pi}{\lambda}r_1\alpha\right)}{\left(\frac{2\pi}{\lambda}r_1\alpha\right)}r_1^2\right]^2 \qquad \text{(A2)}$$

Since the differential, $\frac{\partial}{\partial x}\left(xJ1(x)\right) = xJ0(x)$

With this identity, Equation (A2) can now be simplified to,

$$G_{12}(\alpha) = \frac{4\pi^2}{\lambda^2}\left(r_2^2 - r_1^2\right)\left[J0\left(\frac{2\pi}{\lambda}\left(\frac{r_1 + r_2}{2}\right)\alpha\right)\right]^2 \qquad \text{(A3)}$$

Extension to *n* rings is based on the summing of ring voltages derived from Equation A3, and this leads to Equation 14 in the main text.

Peter East, *pe@y1pwe.co.uk* is retired from a Defense Electronics career in radar and electronic warfare system design. He has authored a book on Microwave System Design Tools, is a member of the British Astronomical Association since 1975 and joined SARA in 2013. He is active in amateur detection of pulsars using SDRs and researching low SNR pulsar recognition and analysis. He has recently written two other books, 'Galactic Hydrogen and Pulsars' and 'Small Aperture Pulsar Detection', based on articles written for the BAA RA Group and SARA Journal, describing his work in Radio Astronomy.
He maintains an active RA website at *http://www.y1pwe.co.uk/RAProgs/*

Observation Reports

AD8302 September 2024 Sky Survey

Otte Observatory mike.otte96@gmail.com 10/6/2024

The AD8302 is a phase measure/ detector chip here being used in an interferometer setup. Measurements on common radio sources seemed to be doing well after putting it together again after the SARA Eastern Conference. I was seeing some weaker sources than I had seen before including 3C353 and 3C290. Time for a survey. What else is out there!

The system consists of 2 x 3M south facing dishes, 2x Sawbird LNA's in each feed line, AD8302 phase detector feeding a 12bit A/D which is logged every 2 secs into a file. The system is further described in an article in SARA journal June 2024. Measurements were recorded and examined every day September 3, 2024 to October 7, 2024.

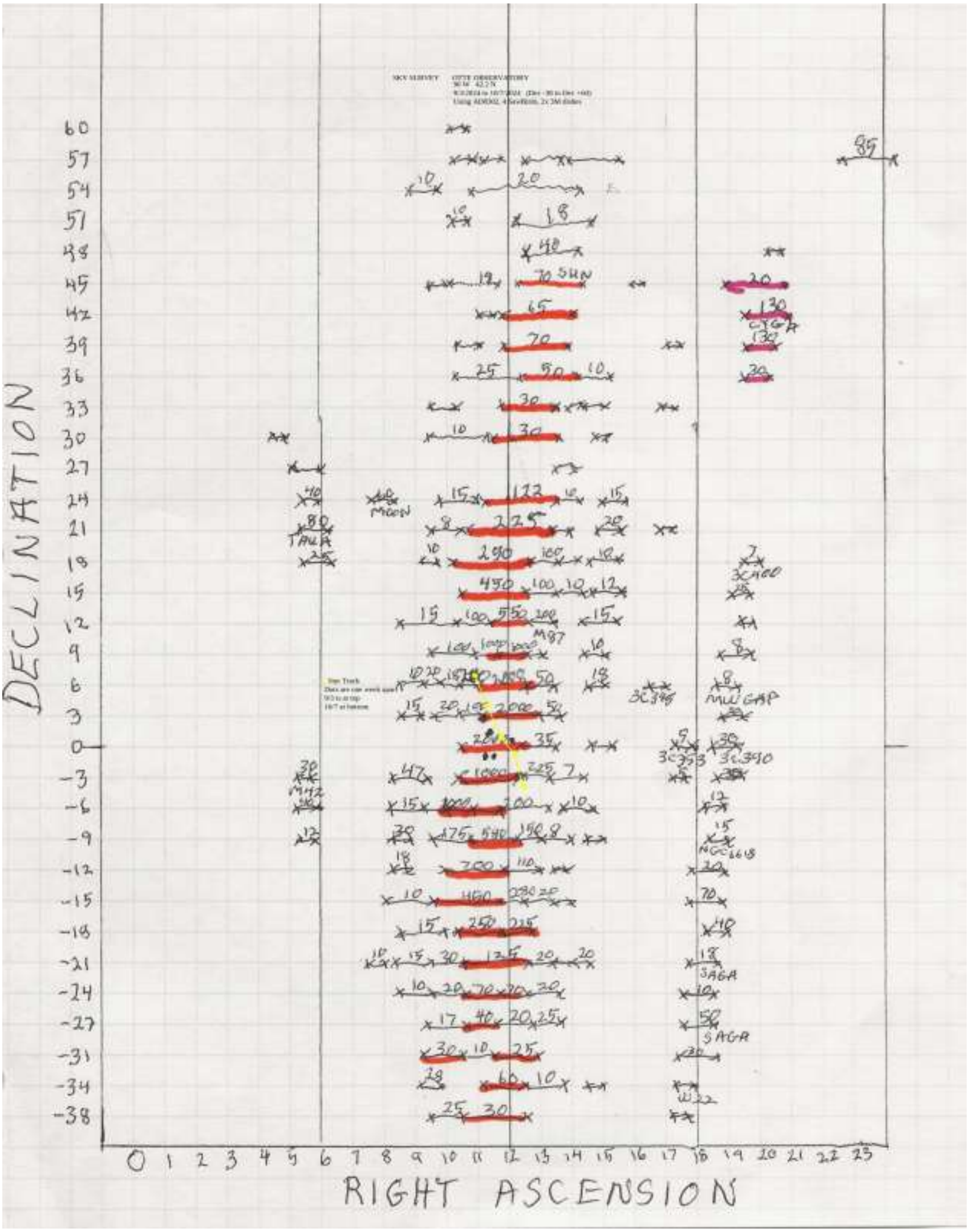

Figure 1: Graphical summary of the daily observations from 9/3 to 10/7 of 2024.

As you can see the Sun is a big influencer for 40 deg in declination and 4-6 hours in Right Ascension. I drew in the position of the Sun (yellow dots) 1 week apart for the 5 weeks of observation.

I set the dishes at 3 degree increments because I wanted the survey to get done quickly. Hoping to discover some new to me sources. There was a lot more interference to the signals but the detection of the interference patterns were done by eye and in some cases spliced through the noise. Most of the detections were familiar but there were some new ones and at Declination 24 one night the Moon showed up.

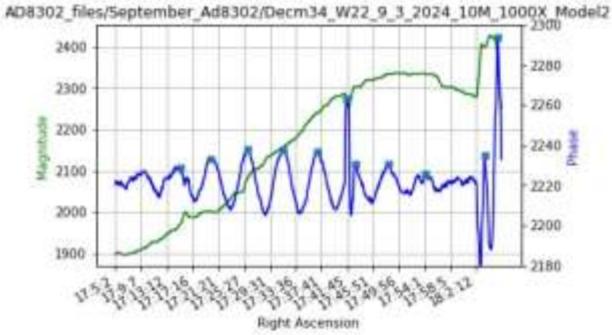

Figure 2: W22

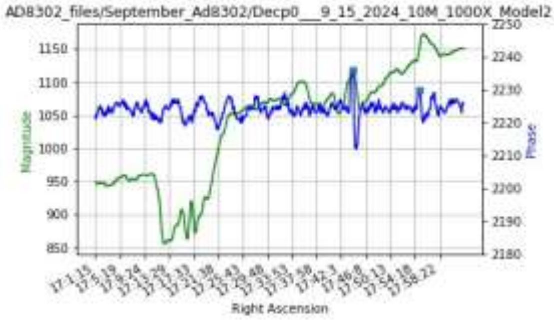

Figure 3: 3C353

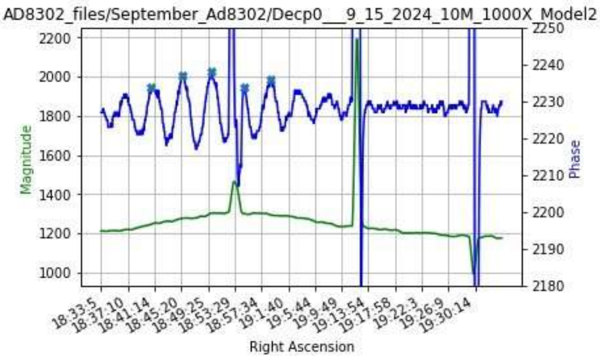

Figure 4: 3C390

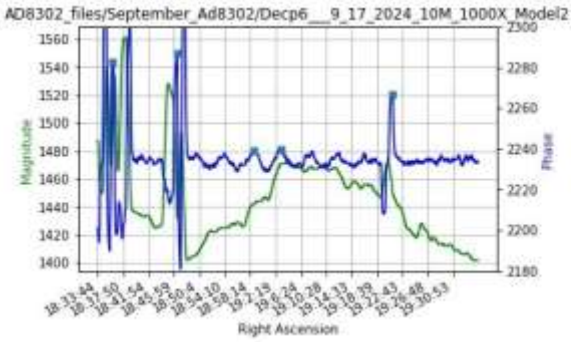

Figure 5: MW Gap

Figure 6: 3C348

Figure 7: Unknown

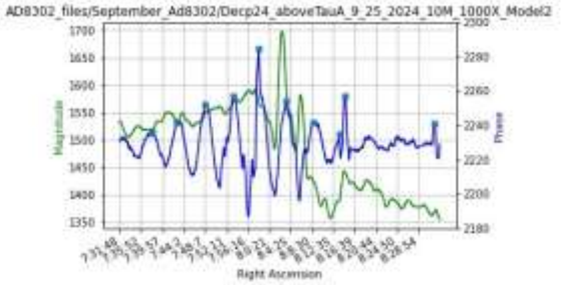

Figure 8: Moon

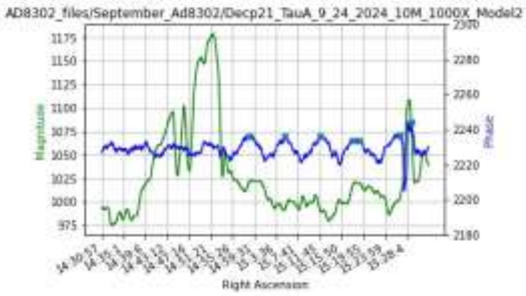

Figure 9: Unknown

So, the figures are the rarer sources that were detected. The 3 degree increment I used may be too much because my antennas are ~6 deg HPBW. But it was a good exercise and I was lucky the equipment continued to work for this length of time. It is obvious the Sun is in the way for much of the day and the survey should be repeated every 3 months to be able to see behind the Sun.

Interferometry increases your sensitivity and shows more sources than measuring the continuum strength. It is different than measuring the hydrogen spectrum. I continue to find my way to the next step "imaging" with the interferometer and have been reading good articles on interferometry in the SARA journal 1997 and 1998.

Journal Archives and Other Promotions

The rich and diverse legacy of member contributed content is available in the SARA Journal Archives. Table of contents for journals is available online at: SARA-Journal-Master-Index.xlsx (live.com)

The entire set of The Journal of The Society of Amateur Radio Astronomers is available by online download. It goes from the beginning of 1981 to the present (over 6000 pages of SARA history!)

All SARA journals and conference proceedings are available through the previous calendar year.

SARA Store (radio-astronomy.org/store.)

SARA Online Discussion Group

SARA members participate in the online forum at http://groups.google.com/group/sara-list. This is an invaluable resource for any amateur radio astronomer.

SARA Conferences

SARA organizes multiple conferences each year. Participants give talks, share ideas, attend seminars, and get hands-on experience. For more information, visit http://www.radio-astronomy.org/meetings.

What is Radio Astronomy?

Radio Astronomy is just what the name implies…. Astronomy observed at radio wavelengths instead of optical. But why do radio astronomy? Radio astronomy has expanded the knowledge of the universe about as much since its discovery in 1932 as optical has since humans first looked up at the sky. (The sky in the different frequencies or colors of radio are as different and varied as all of the flowers on Earth. Each frequency has its own information about what is happening in the universe.) This knowledge has been gained by both professional astronomers as well as amateurs, with amateurs contributing to this day.

Do I need a big dish and expensive equipment?
No. Complete beginner projects are available at the SARA store at very reasonable prices. You can monitor the Sun's effects upon our planet with SuperSID. This information is gathered for Stanford for research into our ionosphere and radio signal propagation. Another project is the detection the hydrogen line just like Dr. Ewen had done in 1951 for a fraction of the cost using the Scope in a Box kit.

That said, radio astronomy is like optical astronomy in that you can spend as much as you want to. Many amateurs push the lower boundaries of cost by using very low-cost receivers and low-noise low-cost amplifiers that were not available even a few years ago. (See the Scope in a Box kit in the store for examples of both.)

Is everything 'plug and play' and boring?
The kits mentioned above are a starting point which are mostly plug-and-play… that gets you started. After you have mastered the basics, where you go from there depends upon your interests. Monitoring pulsars is done by amateurs. (One even noticed a pulsar glitch before the professionals!) These amateurs are pushing the boundaries of what can be done. Papers are being published and discussions had about pulsar detection as well detection of a MASER with a 50-inch dish. Techniques on new detection methods are posted in the SARA forum and elsewhere. You are free to build your own equipment to receive the signals as well as software to collect and analyze the data.

What is SETI?
SETI is the Search for Extra-Terrestrial Intelligence. Some amateurs scan the sky and search for signals that might be from aliens. To date no one has received a definitive alien signal (professional or amateur), but the search continues. The search has resulted not just in better receiving equipment but also wide and lively discussions about how aliens might communicate and how they might be trying to contact us. Some of these techniques have interesting ideas for our own communication techniques here on Earth!

What should I do to get started?
You should start with reading our Introduction to Radio Astronomy and joining our online SARA Forum. Look at the SARA store to get a project to get your feet wet without much expense and minimal risk. We will work with you so you can succeed.

Administrative

Officers, directors, and additional SARA contacts

The Society of Amateur Radio Astronomers is an all-volunteer organization. The best way to reach people on this page is by email with SARA in the subject line SARA Officers.

President: Dr. Rich Russel, AC0UB, https://www.radio-astronomy.org/contact/President
Vice President: Marcus Fisher, https://www.radio-astronomy.org/contact/Vicepresident
Secretary: Bruce Randall, NT4RT, https://www.radio-astronomy.org/contact/Secretary
Treasurer: Tom Jacobs, https://www.radio-astronomy.org/contact/Treasurer
Asst. Treasurer: Donna Hallin, https://www.radio-astronomy.org/contact/Treasurer
Past President: Dennis Farr
Founder Emeritus and Director: Jeffrey M. Lichtman, KI4GIY, jeff@radioastronomysupplies.com

Board of Directors

Name	Term expires	Email
Dennis Farr	2026	dennisfarr@verizon.net
Dr. Wolfgang Herrmann	2025	messbetrieb@astropeiler.de
Paul Butler	2025	paul.butler.melbourne@gmail.com
Charles Osborne	2025	k4cso@twc.com
Don Latham	2026	djl@montana.com
Steve Tzikas	2026	Tzikas@alum.rpi.edu
Ted Cline	2025	TedClineGit@gmail.com
Jay Wilson	2026	jwilson@radio-astronomy.org

Other SARA Contacts

All Officers	http://www.radio-astronomy.org/contact-sara	
All Directors and Officers	http://www.radio-astronomy.org/contact/All-Directors-and-Officers	
Eastern Conference Coordinator	http://www.radio-astronomy.org/contact/Annual-Meeting	
All Radio Astronomy Editors	http://www.radio-astronomy.org/contact/Newsletter-Editor	
Radio Astronomy Editor	Dr. Richard A. Russel	drrichrussel@radio-astronomy.org
Contributing Editor	Bogdan Vacaliuc	bvaculiuc@iee.org
Educational Co-Chairs	Ken Redcap, Tom Hagen: http://www.radio-astronomy.org/contact/Educational-Outreach	
Grant Committee	Tom Crowley	grants@radio-astronomy.org
Membership Chair	http://www.radio-astronomy.org/contact/Membership-Chair	
Technical Queries (David Westman)	http://www.radio-astronomy.org/contact/Technical-Queries	
Webmaster	Ciprian (Chip) Sufitchi, N2YO	webmaster@radio-astronomy.org

Resources

Great Projects to Get Started in Radio Astronomy

Radio Observing Program

The Astronomical League (AL) is starting a radio astronomy observing program. If you observe one category, you get a Bronze certificate. Silver pin is two categories with one being personally built. Gold pin level is at least four categories. (Silver and Gold level require AL membership which many clubs have membership. For the bronze level, you need not be a member of AL.)

Categories include.
1) SID
2) Sun (aka IBT)
3) Jupiter (aka Radio Jove)
4) Meteor back-scatter
5) Galactic radio sources

This program is a collaboration between NRAO and AL. Steve Boerner is the Lead Coordinator and a SARA member.

For more information:
Steve Boerner
2017 Lake Clay Drive
Chesterfield, MO 63017
Email: sboerner@charter.net
Phone: 636-537-2495
http://www.astroleague.org/programs/radio-astronomy-observing-program

Radio Jove

The Radio Jove Project monitors the storms of Jupiter, solar activity and the galactic background. The radio telescope can be purchased as a kit, or you can order it assembled. They have a terrific user group you can join. http://radiojove.gsfc.nasa.gov/

INSPIRE Program

The INSPIRE program uses build-it-yourself radio telescope kits to measure and record VLF emissions such as tweeks, whistlers, sferics, and chorus along with man-made emissions. This is a very portable unit that can be easily transported to remote sites for observations.
http://theinspireproject.org/default.asp?contentID=27

SARA/Stanford SuperSID

Stanford Solar Center and the Society of Amateur Radio Astronomers have teamed up to produce and distribute the SuperSID (Sudden Ionospheric Disturbance) monitor. The monitor utilizes a simple pre-amp to magnify the VLF radio signals which are then fed into a high-definition sound card. This design allows the user to monitor and record multiple frequencies simultaneously. The unit uses a compact 1-meter loop antenna that can be used indoors or outside. This is an ideal project for the radio astronomer that has limited space. To request a unit, send an e-mail to supersid@radio-astronomy.org

Radio Astronomy Online Resources

SARA YouTube Videos: https://www.youtube.com/@radio-astronomy	Pisgah Astronomical Research Institute: www.pari.edu
AJ4CO Observatory – Radio Astronomy Website: http://www.aj4co.org/	A New Radio Telescope for Mexico - ORION 2021 01 20. Dr. Stan Kurtz https://www.youtube.com/watch?v=Q9aBWr1aBVc
Radio Astronomy calculators https://www.aj4co.org/Calculators/Calculators.html	National Radio Astronomy Observatory http://www.nrao.edu
Introduction to Amateur Radio Astronomy (presentation) http://www.aj4co.org/Publications/Intro%20to%20Amateur%20Radio%20Astronomy,%20Typinski%20(AAC,%202016)%20v2.pdf	NRAO Essential Radio Astronomy Course http://www.cv.nrao.edu/course/astr534/ERA.shtml
RF Associates Richard Flagg, rf@hawaii.rr.com 1721-1 Young Street, Honolulu, HI 96826	Exotic Ions and Molecules in Interstellar Space -- ORION 2020 10 21. Dr. Bob Compton https://www.youtube.com/watch?v=r6cKhp23SUo&t=5s
RFSpace, Inc. http://www.rfspace.com	The Radio JOVE Project & NASA Citizen Science – ORION 2020.6.17. Dr. Chuck Higgins https://www.youtube.com/watch?v=s6eWAxJywp8&t=5s
CALLISTO Receiver & e-CALLISTO http://www.reeve.com/Solar/e-CALLISTO/e-callisto.htm	UK Radio Astronomy Association http://www.ukraa.com/
Deep Space Exploration Society http://DSES.science	CALLISTO software and data archive: www.e-callisto.org
Deep Space Object Astrophotography Part 1 -- ORION 2021 02 17. George Sradnov https://www.youtube.com/watch?v=Pm_Rs17KIyQ	Radio Jove Spectrograph Users Group http://www.radiojove.net/SUG/
European Radio Astronomy Club http://www.eracnet.org	Radio Sky Publishing http://radiosky.com
British Astronomical Association – Radio Astronomy Group http://www.britastro.org/baa/	The Arecibo Radio Telescope; It's History, Collapse, and Future - ORION 2020.12.16. Dr. Stan Kurtz, Dr. David Fields https://www.youtube.com/watch?v=rBZIPOLNX9E
Forum and Discussion Group http://groups.google.com/group/sara-list	Shirleys Bay Radio Astronomy Consortium marcus@propulsionpolymers.com
GNU Radio https://www.gnuradio.org/	SARA Twitter feed https://twitter.com/RadioAstronomy1
SETI League http://www.setileague.org	SARA Web Site http://radio-astronomy.org
NRAO Essential Radio Astronomy Course http://www.cv.nrao.edu/course/astr534/ERA.shtml	Simple Aurora Monitor: Magnetometer http://www.reeve.com/SAMDescription.htm
NASA Radio JOVE Project http://radiojove.gsfc.nasa.gov Archive: http://radiojove.net/archive.html https://groups.io/g/radio-jove	Stanford Solar Center http://solar-center.stanford.edu/SID/
National Radio Astronomy Observatory http://www.nrao.edu	https://www.csiro.au/ There's a wealth of info on this site of the Australian National Science Agency. It's much more than just radio astronomy. Looking under "Research" opens a real family tree of interesting pages of things they are involved with.

Found an interesting Grote Reber link: https://www.utas.edu.au/groterebermuseum Their gallery is interesting, but sure wish they had some captions to indicate who and what some of it is about. I can guess, knowing some of Grote's stories, but others might need more info. Several pictures show the University of Tasmania 26m dish that was once one of the NASA worldwide Satellite Tracking and Data Network (STDN) dishes like the ones at the Pisgah Astronomical Research Institute (www.pari.edu). PARI's dishes were the first qualification units for that network.

For Sale, Trade and Wanted

At the SARA online store: radio-astronomy.org/store.

New on-demand store for SARA SWAG! https://saragifts.org/

Scope in a Box

radio-astronomy.org/store.

Kit of parts and software to build a working Radio Telescope to detect Hydrogen Line emissions. Available to USA addresses only at this time.

SuperSID Complete Kit

radio-astronomy.org/store.

SARA Publication, Journals and Conference Proceedings (various prices)

radio-astronomy.org/store.

SARA Journal Online Download

radio-astronomy.org/store.

The Journal archive covers the society journal "Radio Astronomy" from the founding of the organization in 1981 through the present. Articles cover a wide range of topics including cosmic radiation, pulsars, quasars, meteor detection, solar observing, Jupiter, Radio Jove, gamma ray bursts, the Itty Bitty Telescope (IBT), dark matter, black holes, the Jansky antenna, methanol masers, mapping at 408 MHz and more.

New! **SARA On-Demand Store: https://saragifts.org**

These are the current items – more to come in the future!

(Note: No returns or refunds possible because of the on-demand production approach)

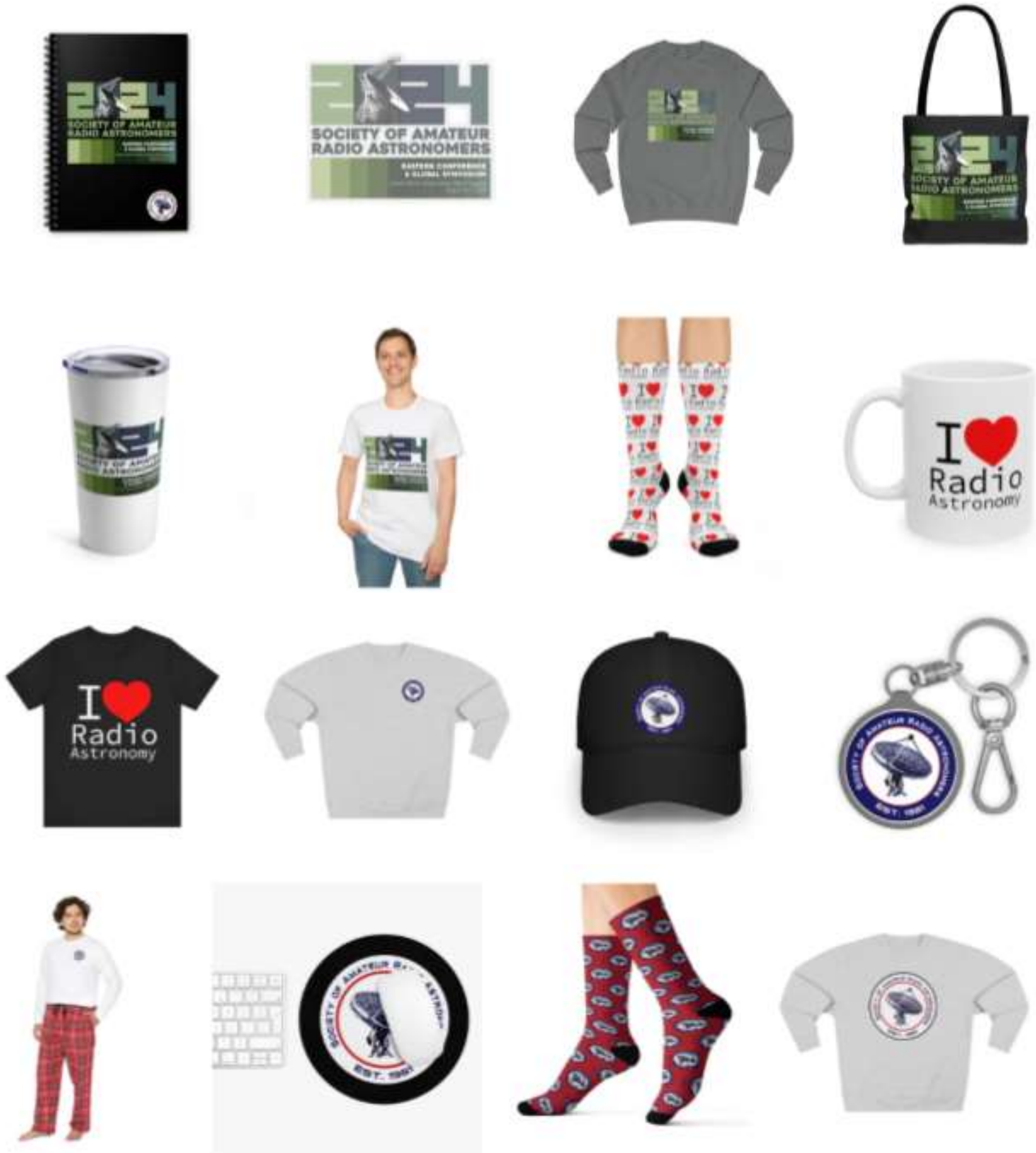

SARA Brochure

Membership Information

Annual SARA dues Individual $20, Classroom $20, Student $5 (US funds) anywhere in the world. Membership includes a subscription to Radio Astronomy, the bimonthly Journal of The Society of Amateur Radio Astronomers, delivered electronically (via a secure web link, emailed to you as each new issue is posted). We regret that printing and postage costs prevent SARA from providing hardcopy subscriptions to our Journal.

We would appreciate the following information included with your check or money order, made payable to SARA:

Name: ____________________

Email Address : ____________________
(required for electronic Journal delivery)

Ham call sign: ____________________ (if applicable)

Address: ____________________

City: ____________________

State: ____________________

Zip: ____________________

Country: ____________________

Phone: ____________________

Please include a note of your interests. Send your application for membership, along with your remittance, to our Treasurer.

For further information, see our website at:
http://radio-astronomy.org/membership

How to get started?

SARA has a made a kit of software and parts to detect the Hydrogen line signal from space. This is an excellent method to get started in radio astronomy. It teaches the principles of antenna design, signal detection, and signal processing. Read more about this and other projects on our web site.

Society of Amateur Radio Astronomers, Inc.
Founded 1981

Membership supported, nonprofit [501(c) (3)] Educational and Radio Astronomy Organization

Knowledge through Common Research, Education and Mentoring

SARA members have been privileged to use this forty foot diameter drift-scan hydrogen line radio telescope every year at their annual meeting in Green Bank.

http://radio-astronomy.org

Why Radio Astronomy?

Because about sixty five percent of our current knowledge of the universe has stemmed from radio astronomy alone. The discovery of quasars, pulsars, black holes, the 3K background from the "Big Bang" and the discovery of biochemical hydrogen/carbon molecules are all the result of professional radio astronomy.

The Society of Amateur Radio Astronomers

SARA was founded in 1981, with the purpose of educating those interested in pursuing amateur radio astronomy.

The society is open to all, wishing to participate with others, worldwide.

SARA members have many interests, some are as follows:

SARA Areas of Study and Research:

- Solar Radio Astronomy
- Galactic Radio Astronomy
- Meteor Detection
- Jupiter
- SETI
- Gamma Ray/High Energy Pulse
- Detection
- Antennas
- Design of Hardware / Software

The members of the society offer a friendly mentor atmosphere. All questions and inquiries are answered in a constructive manner. No question is silly!

SARA offers its members an electronic bi-monthly journal entitled Radio Astronomy. Within the journal, members report on their research and observations. In addition, members receive updates on the professional radio astronomy community and, society news.

Once a year SARA meets for a three-day conference at the Green Bank Observatory in Green Bank West Va.

There is also a spring conference held at various cities in the Western USA. Previous meeting have been at the VLA in Socorro, NM and at Stanford University.

How do I get started?

Just as a long journey begins with the first step, the project you elect must start with a clear idea of your objectives. Do you wish to study the sun? Jupiter? Make meteor counts? Do you wish to engage in imaging radio astronomy? What you decide will not only determine the type of equipment you will need, but also the local radio spectrum.

How do amateurs do radio astronomy?

Radio astronomy by amateurs is conducted using antennas of various shapes and sizes, from smaller parabolic dishes to simple wire antennas. These antennas are connected to receivers and most of these receivers are software defined radios these days. Data from the receivers are collected by computers, and the received signals will be displayed as charts, graphs or maybe even sky maps. As diverse as the observed objects, so is are the instruments and tools used. SARA members will always be supportive to find good solutions for what one wishes to observe.

Is amateur radio astronomy instrumentation expensive?

Technical information freely circulated in our monthly journal helps amateurs to obtain good low noise equipment from off the shelf assemblies, or to build their own units. The actual cash investment in radio astronomy equipment need not exceed that of any other hobby.

What are amateurs actually looking for in the received data?

The aim of the radio amateur is to find something new and unusual. Just as an amateur optical observer hopes to notice a supernova or a new comet, so does an amateur radio observer hope to notice a new radio source, or one whose radiation has changed appreciably.

The Reber Telescope at NRAO. Constructed by Grote Reber in 1937 in his back yard in Wheaton, Illinois

SARA Members discussing the IBT (Itty Bitty Telescope)